UNIVERSITY COLLEGE LONDON

Faculty of Mathematical and Physical Sciences

Department of Physics & Astronomy

THE IMPACT OF INTERIOR PLASMA DYNAMICS ON THE SHAPE AND SIZE OF SATURN'S MAGNETOSPHERE

Thesis submitted for the Degree of Doctor of Philosophy of University College London

by

Nathan M. Pilkington

Supervisors:
Nicholas A. Achilleos
Anasuya L. Aruliah

Examiners:
Geraint H. Jones
Jonathan D. Nichols

December 27, 2015

For Elia and Holly, my whole universe;

And for Boo, who makes it shine bright

I, Nathan M. Pilkington, confirm that the work presented in this thesis is my own. Where information has been derived from other sources, I confirm that this has been indicated in the thesis.

I would also like to declare that the work presented in this thesis has been published in peer reviewed journals, resulting in the following articles:

Pilkington, N. M., N. Achilleos, C. S. Arridge, A. Masters, N. Sergis, A. J. Coates and Dougherty, M. K. (2014). Polar confinement of Saturns magnetosphere revealed by in situ Cassini observations. Journal of Geophysical Research, 119. doi:10.1002/2014JA019774

Pilkington, N. M., N. Achilleos, C. S. Arridge, P. Guio, A. Masters, L. C. Ray, N. Sergis, M. F. Thomsen, A. J. Coates, and M. K. Dougherty (2015), Internally driven large-scale changes in the size of Saturns magnetosphere, Journal of Geophysical Research: Space Physics, 120, doi:10.1002/2015JA021290.

Pilkington, N. M., N. Achilleos, C. S. Arridge, P. Guio, A. Masters, L. C. Ray, N. Sergis, M. F. Thomsen, A. J. Coates, and M. K. Dougherty (2015), Asymmetries observed in Saturns magnetopause geometry, Geophysical Research Letters, 42, doi:10.1002/2015GL065477.

Abstract

This thesis explores the impact of rotational and plasma dynamics on the geometry and variability of the location of Saturn's magnetopause, using data obtained by the *Cassini* spacecraft. A significant departure was identified between the observed location of the high-latitude magnetopause and that predicted by the axisymmetric *Kanani et al.* (2010) model. This model was derived from equatorial measurements made earlier in the mission. The departure demonstrated for the first time that Saturn's magnetosphere is subject to significant 'polar flattening'.

It was found that variability in the suprathermal plasma pressure causes dramatic changes in the location of the magnetopause. Such variability had previously been attributed to changes in the solar wind dynamic pressure, but these observations showed that internally driven plasma dynamics imparts a similar degree of variability in the location of the standoff point (up to ∼10–15 planetary radii). This effect was incorporated into an empirical magnetopause model and significantly improved the agreement between the observations and the model predictions.

In the final part of this study, the structure of the magnetopause was examined in greater detail. Firstly, it was found that the magnetosphere extends further at dawn than dusk. This may be caused by the flow of plasma around the planet, which opposes the solar wind on the morning side of the magnetosphere, but flows in the same direction as the solar wind at dusk. The large dataset collected throughout this study also spans approximately nine years, a significant fraction of a Saturnian season. Additional analysis revealed that the geometry of the magnetopause changes with season, in agreement with

theoretical studies. Specifically, a north-south asymmetry is introduced away from equinox whereby the magnetopause is further flattened in the winter hemisphere relative to the north-south symmetric equinoctial magnetopause. This is in addition to the contribution from the centrifugally confined thermal plasma.

Acknowledgements

First of all, I would like to thank Nick for being the best possible supervisor. This thesis would not have been possible without your excellent guidance and advice. I would also like to thank Patrick for great advice; Jaf for countless answers to countless questions and Licia for great discussions, lots of laughs and many, many coffees!

Secondly, I would like to thank the myriad colleagues and co-authors that have helped me along the way. In particular, I would like to thank Chris Arridge, Fran Bagenal, Andrew Coates, Michele Dougherty, Xianzhe Jia, Margaret Kivelson, Adam Masters, Nick Sergis, Jim Slavin, Michelle Thomsen and all of the Journal Club guys for useful and invaluable discussions. I would also like to thank all of the folks over at Leicester without whom I certainly would not have pursued this thesis, particularly Emma Bunce, Stan Cowley, Jonny Nichols, Tom Stallard and Mike Watson.

Finally, and most of all, I must thank my amazing family. I must especially thank Beth for your incredible support and boundless patience throughout (and for bothering to learn the title of my first paper!); Ellie and Holly for making it all worthwhile and Mum, Dad, Haley and Katie for being ever supportive.

I know that I am mortal by nature, and ephemeral; but when I trace at my pleasure the windings to and fro of the heavenly bodies I no longer touch the earth with my feet: I stand in the presence of Zeus himself and take my fill of ambrosia

Claudius Ptolemy, *Ptolemy's Almagest*

It is not knowledge, but the act of learning, not possession but the act of getting there, which grants the greatest enjoyment

Carl Friedrich Gauss

Contents

This page was intentionally left blank

List of Figures

This page was intentionally left blank

List of Tables

This page was intentionally left blank

Chapter 1

Introduction

The Sun, with all those planets revolving around it and dependent upon it, can still ripen a bunch of grapes as if it had nothing else in the Universe to do.

Galileo Galilei, Astronomer

One of the biggest unresolved questions facing society and scientists alike is the possibility and implications of 'life in the universe' beyond our own planet. This question is of huge public interest and has spawned many works of fiction (explored throughout the making of this thesis for research purposes only) and is an important fundament of the field of exoplanet research. Indeed, an exact Google search for the aforementioned statement yields over 28 million results.

It has been suggested that one of the essential ingredients for a habitable planet is the presence of an internally driven magnetic field and an extended *magnetosphere* (e.g. *Khodachenko et al.*, 2007). The magnetosphere is thought to protect the planet and its atmosphere from direct interaction with a stream of particles that flows radially away from the Sun, known as the *solar wind*. Evidence supporting this suggestion arises when comparing Earth's atmospheric composition to its more magnetically challenged siblings,

Venus and Mars.

Thus far, a global magnetic field has not been detected at Mars (e.g. *Acuna et al.*, 1998), but *Acuna et al.* (1999) detected strong crustal magnetic fields using the magnetometer onboard *Mars Global Surveyor*. This is evidence that Mars once did have a substantial, internally driven magnetic field, of which the crust has retained a 'memory'. Likewise, a global magnetic field has not been detected at Venus, and this allows the solar wind to interact directly with its atmosphere. The ratio of deuterium to hydrogen in Venus' atmosphere is much larger than that of Earth's atmosphere, indicating that the lighter elements may have been preferentially 'stripped'. This suggests the solar wind has been allowed to erode the Venusian atmosphere over time (*de Bergh et al.*, 1991; *Fedorova et al.*, 2008), and similarly for Mars (*Jakosky and Phillips*, 2001). *Luhmann and Kozyra* (1991) found that heavier elements like O^+ could also be lost to the solar wind in this way, and *Jarvinen et al.* (2010) found that the orientation of the *interplanetary magnetic field* (IMF), which threads the solar wind, may organise this escape. In addition, there are many features and minerals present that indicate that substantial quantities of liquid water existed on the surface of Mars for long periods of time (e.g. see the overview by *Baker*, 2006), and this, in turn, would require a much larger atmospheric pressure than is present today. If that is the case, where did the atmosphere go? It is likely that it was lost to interplanetary space due to solar wind erosion over very long timescales.

The Earth's magnetic field and magnetosphere have been studied for many years, but to truly understand the interaction between the Sun and the planets and implications thereof for more exotic planets, we require a much richer dataset. Indeed, exploration of the outer planets has challenged the fundamental concepts that underpin the entire field of magnetospheric physics. Dynamo theory, for example, has long since been taken for granted but is challenged by observations made of Saturn's magnetospheric field (discussed in more detail in Section 1.3.1).

The Cassini spacecraft has been orbiting Saturn for over ten years, making detailed measurements of its magnetic and plasma environment. In this thesis, I use measurements taken over the majority of this time period by multiple instruments onboard Cassini to characterise Saturn's *magnetopause*. The magnetopause is the interface between the solar-dominated region of space and the region shielded from direct exposure to particles of

solar origin, known as the planet's magnetosphere. Clearly, then, the Sun is of immense importance to this study since it is ultimately responsible for the formation of planetary magnetospheres and exerts some degree of control over the shape and size of those within the solar system. But, as we shall explore, Saturn's magnetosphere is also controlled by internal drivers, in contrast to the terrestrial magnetosphere, for example, which is largely solar wind-driven.

In this chapter, I will introduce the fundamental electromagnetic processes that lead to the formation of the solar wind, the interplanetary magnetic field and planetary magnetospheres in general. The processes that occur within Saturn's magnetosphere that impact upon the magnetopause location will then be discussed, as well as previous studies concerning Saturn's magnetopause. In Chapter 2, I will give an outline of the Cassini mission and the instrumentation used to conduct this study. In Chapter 3, I will discuss the first element of this study: observations showing that Saturn's magnetosphere extends further from the planet at low latitudes than at high latitudes relative to the shape expected from an existing axisymmetric model of the magnetopause surface. This effect arises due to centrifugal confinement of magnetospheric plasma. In Chapter 4, I will describe how I have adapted previous empirical models to account for this effect and extended this study to incorporate coverage of most regions of Saturn's magnetopause. Furthermore, I will discuss observations that show that variations in the internal plasma pressure cause dramatic changes in the size of the magnetosphere, in addition to the control that the solar wind exerts. In Chapter 5, I will describe how an extended database of magnetopause crossings collected throughout this work has been used to study the structure of Saturn's magnetopause in unprecedented detail. Asymmetries in the extent of Saturn's magnetopause have been quantified for the first time. Finally, the results of this thesis will be summarised in Chapter 6 and suggestions for further exploration will be discussed.

1.1 Electrostatic Forces and Motion

Electromagnetism is one of the four fundamental forces of nature of which we know. All particles are configured such that they either have a net charge (*ions* and *electrons*) and are subject to the laws of electromagnetism, or are charge-neutral and thus exempt from these laws for as long as they remain so. All ions (defined throughout to be positively

charged) and electrons, including those that make up the Sun, are subject to the *Lorentz force*, which governs the interaction between charged particles and background magnetic and electric fields,

$$m\frac{d\mathbf{v}}{dt} = q(\mathbf{E} + \mathbf{v} \times \mathbf{B}), \tag{1.1}$$

where m, q and $\mathbf{v}$ are the mass, charge and velocity of the particle and $d\mathbf{v}/dt$ is the acceleration of the particle caused by the background electric and magnetic fields it experiences, $\mathbf{E}$ and $\mathbf{B}$ respectively. Hence, the Lorentz force only acts on particles with a net charge and leaves neutral particles entirely unaffected.

Electric fields energise and accelerate ions (electrons) in the same (opposite) direction as the field. In the electrostatic case, electric fields arise due to charge imbalances and the force imposed by an electric field on a charged particle is ultimately a restoring force. It acts to move negatively charged particles into regions of net positive charge and vice versa, in order to eliminate this charge separation. In this case, the electric field is conservative – the electric field changes the energy of a particle but it will return to its initial energy if it manages to return to its initial position, i.e., $\oint \mathbf{E} \cdot d\mathbf{l} = 0$. In general though, this is not the case as electric fields are also associated with changing magnetic fields in accordance with Faraday's law:

$$\nabla \times \mathbf{E} = -\frac{\partial \mathbf{B}}{\partial t}. \tag{1.2}$$

The magnetic force, on the other hand, is always conservative. It does not change the energy of the particle, only the direction in which it moves. This can be shown by starting with Equation 1.1 (with $\mathbf{E} = 0$) and taking the dot product of both sides with $\mathbf{v}$,

$$\begin{aligned} m\mathbf{v} \cdot \frac{d\mathbf{v}}{dt} &= m\frac{d}{dt}\left(\frac{1}{2}\mathbf{v} \cdot \mathbf{v}\right), \\ &= \frac{d}{dt}\left(\frac{1}{2}mv^2\right), \\ &= q\mathbf{v} \cdot (\mathbf{v} \times \mathbf{B}), \\ \therefore q\mathbf{v} \cdot (\mathbf{v} \times \mathbf{B}) &= 0, \end{aligned} \tag{1.3}$$

as $\mathbf{v}$, by definition, is perpendicular to $\mathbf{v} \times \mathbf{B}$. Hence, the magnetic field does not change

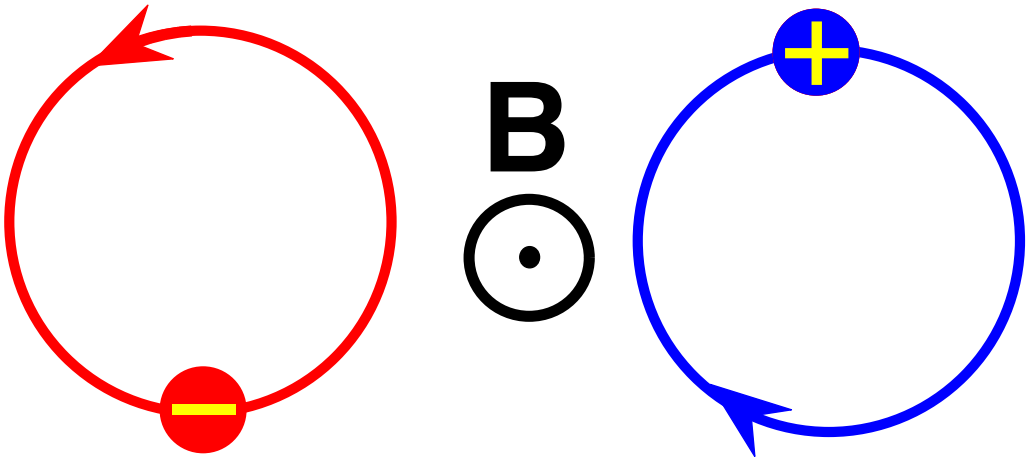

Figure 1.1. The gyration of positively and negatively charged particles in the presence of a uniform magnetic field. Note that this diagram is only to scale if the particles have the same mass – more massive particles have larger radii of gyration.

the kinetic energy ($\frac{1}{2}mv^2$) of the particle. The force imposed by the magnetic field acts perpendicular to both the velocity of the particle and the magnetic field itself. Thus, the magnetic field changes the direction of motion of the particle but not its energy. The magnetic force also acts in opposite directions for electrons and ions as shown in Figure 1.1.

It can be useful to separate the particle velocity into components parallel and perpendicular to the magnetic field, i.e. $\mathbf{v} = \mathbf{v}_{\parallel} + \mathbf{v}_{\perp}$, as the former (latter) is independent of (dependent on) a uniform magnetic field. However, this is not the case if the magnetic field is not uniform as discussed in Section 1.1.2. If the particle has a component of velocity in the direction parallel to the magnetic field, it is free to travel along the field and follows a helical path 'wound' around the magnetic field vector as shown in Figure 1.2. The radius of gyration is known as the *Larmour radius* and is given by,

$$r_L = \frac{v_{\perp}}{\omega_c} = \frac{mv_{\perp}}{|q|B}, \tag{1.4}$$

where,

$$\omega_c = \frac{qB}{m}, \tag{1.5}$$

is the frequency of gyration measured in radians per second, known as the *cyclotron frequency*. Hence, the radius of gyration depends on both the magnetic field strength and

Figure 1.2. The helical path taken by a particle gyrating in a uniform magnetic field with a finite component of velocity parallel to the magnetic field.

the microscopic properties of the particle. It is clear from Equation 1.4 that electrons have much smaller gyroradii than ions of the same $v_\perp$ since they are much smaller in mass. Equation 1.4 also shows that more energetic particles of the same mass have larger gyroradii than those of lower energy. The combination of these factors becomes important when considering large, energetic ions such as the water-group ions found within Saturn's magnetosphere as discussed in Section 1.3.4.

Magnetic fields are themselves associated with systems of electrical currents in accordance with Ampère's law,

$$\nabla \times \mathbf{B} = \mu_0 \mathbf{j}, \tag{1.6}$$

where μ_0 is the permeability of free space and $\mathbf{j}$ is the current density. Hence, a flowing electric current generates a magnetic field that encircles it. Equation 1.6 is only valid for as long as the background electric field remains steady. Rapidly changing electric fields are also associated with magnetic fields, just as Faraday found that rapidly changing magnetic fields are associated with electric fields (Equation 1.2). As a result, Maxwell generalised Ampère's law thusly,

$$\nabla \times \mathbf{B} = \mu_0 \left(\mathbf{j} + \epsilon_0 \frac{\partial \mathbf{E}}{\partial t} \right), \tag{1.7}$$

and Equation 1.7 is known as the Ampère-Maxwell relation.

It is clear, then, that the forces a particle experiences as it travels through any combination of electric and magnetic fields are ultimately the manifestation of the electromagnetic interactions between that particle and the charged particles responsible for generating those fields. Fundamental to this thesis is the interaction and time evolution of magnetic fields generated within the interior of the Sun and within the interiors of some planets, including Saturn. Essentially, complex motions within the electrically conducting interiors of these bodies convert mechanical energy into electromagnetic energy, which results in magnetic field generation. Motions, such as: convection due to the temperature differential between the deep interiors of the Sun and the planets and their surfaces; flow shears, which cause magnetic fields to stretch; and rotation, which organises motions on larger scales, all aid in the formation of a self-sustaining dynamo (e.g. *Miesch*, 2010).

Such dynamos are responsible for the magnetic fields that penetrate the surfaces of the Sun and the magnetised planets and interact with the plasma populations within their atmospheres and beyond. Far from the surface, dynamo magnetic fields are approximately dipolar since higher order field moments decrease more rapidly with distance, r, than the r^{-3} dependence of the dipole moment. However, as discussed in Section 1.3, these magnetic fields are modified by external influences such as plasma flows and interactions with external media. In the next section, the motion of individual particles within electromagnetic fields with different properties will be considered.

1.1.1 Particle motion

Consider the behaviour of an electron moving with velocity $\mathbf{v} = v_x\hat{\mathbf{x}} + v_y\hat{\mathbf{y}} + v_z\hat{\mathbf{z}}$ within a uniform magnetic field in the presence of no external electric field. Equation 1.1 can be used to deduce how a uniform magnetic field described by $\mathbf{B} = B\hat{\mathbf{z}}$ affects the motion of this electron,

$$\frac{dv_x}{dt} = \frac{qB}{m}v_y, \tag{1.8}$$

$$\frac{dv_y}{dt} = -\frac{qB}{m}v_x, \tag{1.9}$$

$$\frac{dv_z}{dt} = 0, \tag{1.10}$$

where subscripts denote components of the particle velocity in a Cartesian coordinate system. An important consequence of Equation 1.10 is that the magnetic field does not impose a force along its direction, in concurrence with Equation 1.3. Instead, it supplies the centripetal force that keeps the particle gyrating perpendicular to the direction of the magnetic field as can be seen by differentiating Equation 1.8 to yield,

$$\frac{d^2v_x}{dt^2} + \omega_c^2 v_x = 0, \tag{1.11}$$

and similarly for v_y. It can be seen that Equation 1.11 is the simple harmonic equation of motion, which charged particles are subject to in the presence of a magnetic field as shown in Figure 1.1. The solution to Equation 1.11 is,

$$v_x = v_\perp \cos(\omega_c t + \phi), \tag{1.12}$$

$$v_y = -v_\perp \sin(\omega_c t + \phi), \tag{1.13}$$

where t is the time at which the equations are evaluated and ϕ is the phase difference defined by the initial conditions. Integrating Equations 1.12 and 1.13 yields,

$$x = r_L \sin(\omega_c t + \phi) + x_0, \tag{1.14}$$

$$y = r_L \cos(\omega_c t + \phi) + x_0, \tag{1.15}$$

where x_0 and y_0 are the coordinates of the particle *guiding centre*, about which the particle gyrates.

Now consider the motion of the particle in the presence of a finite electric field of the form $\mathbf{E} = E_\perp \hat{\mathbf{y}}$, such that the electric field is perpendicular to the magnetic field. Equation 1.9 is modified thusly,

$$\frac{dv_y}{dt} = -\frac{q}{m}(v_x B - E_\perp). \tag{1.16}$$

One may deduce the effect of the electric field on the motion of the particle by following the same procedure as was used in the previous case with no external electric field. This procedure can be simplified by transforming into a frame of reference moving in the $\hat{\mathbf{x}}$ direction with speed $E_\perp/B$,

$$v'_x = v_x - \frac{E_\perp}{B}, \tag{1.17}$$

such that Equation 1.16 then becomes,

$$\frac{dv_y}{dt} = -\frac{qB}{m}v'_x, \tag{1.18}$$

which is analogous to Equation 1.9. Similarly, this yields,

$$v'_x = v_\perp \cos(\omega_c t + \phi), \tag{1.19}$$

and transforming back into the original frame of reference yields,

$$v_x = v_\perp \cos(\omega_c t + \phi) + \frac{E_\perp}{B}. \tag{1.20}$$

Equation 1.20 demonstrates that the presence of an external electric field causes charged particles to drift in the direction perpendicular to both the magnetic and electric fields. This is because the particle's gyroradius becomes larger (smaller) when the particle is moving in the same (opposite) direction to the force imposed by the electric field. In general terms, it can be demonstrated that the drift velocity of the particle's guiding

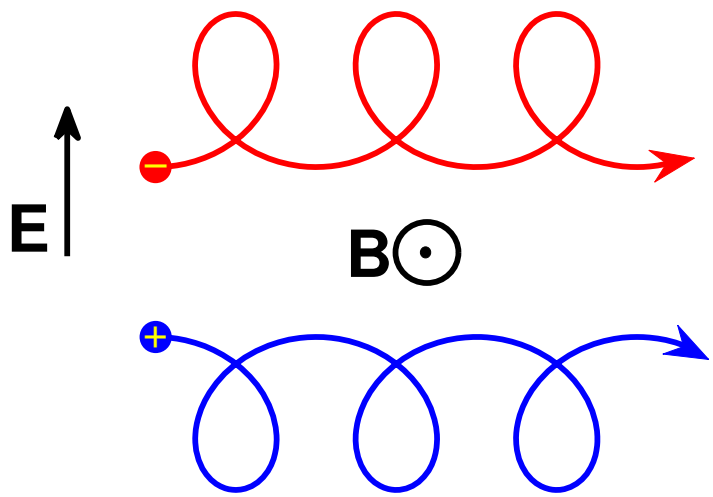

Figure 1.3. An electric field perpendicular to a background magnetic field causes positively charged and negatively charged particles to drift in the same direction.

centre introduced by such a perpendicular electric field is,

$$\mathbf{v_E} = \frac{\mathbf{E} \times \mathbf{B}}{B^2}. \tag{1.21}$$

This so-called '$\mathbf{E} \times \mathbf{B}$' drift is independent of charge – it causes electrons and ions to drift in the same direction because, although ions and electrons gyrate in opposite directions, they are also accelerated in opposite directions by the electric field. The combination of these two effects causes ions and electrons to drift in the same direction as shown in Figure 1.3. Hence, in the collisionless regime, this type of drift cannot cause a net current to flow. If collisions are significant, in the ionosphere for example, a current may flow because ions are impeded more than electrons.

If the electric field is, instead, parallel to or has a component parallel to the magnetic field, then electrons and ions will be accelerated along the magnetic field line in order to neutralise it. Hence, electric fields (or components of an electric field) parallel to a magnetic field are usually quickly negated. There are important and poorly understood exceptions to this such as the field-aligned voltages invoked to explain the acceleration of electrons from thermal energies to tens of keV into the the upper atmospheres of several of the planets, resulting in magnificent auroral displays (e.g. *Boström*, 1964).

Analogous to the $\mathbf{E} \times \mathbf{B}$ drift expressed in Equation 1.21 is the motion of a particle in the

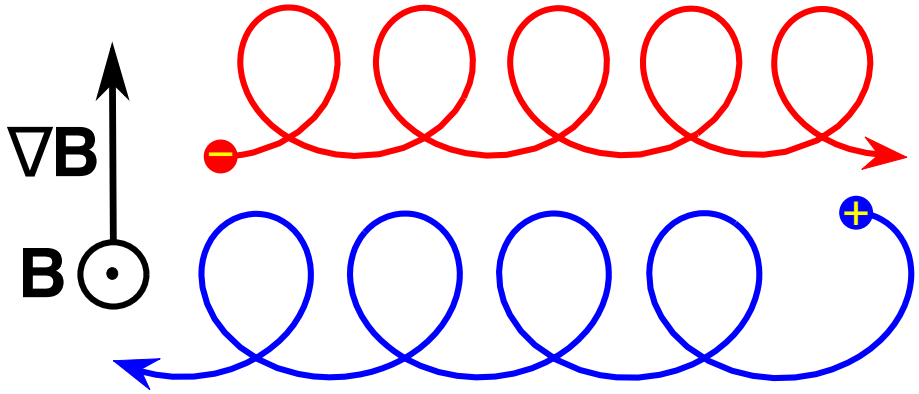

Figure 1.4. Particles drifting in the presence of a magnetic field gradient.

presence of a magnetic field gradient with no electric field. A particle moving into a region of stronger magnetic field will experience a stronger magnetic force so it will take less time for the particle to complete a full gyration. Hence, it will have a smaller gyroradius within the region of greater field strength in agreement with Equation 1.4. When the particle moves back into the region of weaker field strength, its gyroradius will increase and this cycle will repeat itself as the particle alternates between these regions. If the field changes on a distance scale comparable to the gyroradius, the particle will drift perpendicular to both the field and the gradient in the field strength. Furthermore, since electrons and ions gyrate in opposite directions, they also drift in opposite directions. This is illustrated in Figure 1.4. Such a situation occurs when particles gyrate within a planetary magnetic field in which the field strength decreases as the particles move further from the planet. In a dipole field, this causes them to drift orthogonally to both the radial direction and the field direction. As a result, they drift around the planet and contribute to the *ring current*, which flows around the magnetised planets. Perhaps of more immediate importance to this thesis is that the '$\nabla\mathbf{B}$' drift also contributes to the magnetopause current since magnetic field gradients exist in the vicinity of the magnetopause. The velocity with which the guiding centre of the particle drifts as a result of the magnetic field gradient is,

$$\mathbf{v}_{\nabla\mathbf{B}} = \pm\frac{r_L v_\perp}{2}\frac{\mathbf{B}\times\nabla\mathbf{B}}{B^2}, \tag{1.22}$$

the direction of which is charge dependent.

Another drift that contributes to the afore mentioned currents arises from the curvature of magnetic field necessary to achieve magnetic field closure. For example, the dipole field

of a planet emerges from one of its magnetic poles and must curve through space in order to reach the opposite pole and then close within the interior of the planet, in accordance with Gauss' 'no monopoles' law for magnetism,

$$\nabla \cdot \mathbf{B} = 0. \tag{1.23}$$

As a result, a particle gyrating along a planetary field line experiences a centrifugal force associated with the curved path it must take. At the extremum of its gyration closest to the planet, the radius of curvature is smaller than its counterpart furthest from the planet. Hence, the centrifugal acceleration also varies and causes a drift perpendicular to the magnetic field and the centrifugal force. In general, it can be shown that the drift velocity imposed by a generic force, $\mathbf{F}$, is of the form,

$$\mathbf{v_d} = \frac{1}{q}\frac{\mathbf{F} \times \mathbf{B}}{B^2}. \tag{1.24}$$

The centrifugal force takes the form,

$$\mathbf{F_c} = \frac{m v_{\shortparallel}^2}{r_c}\hat{\mathbf{r}}_\mathbf{c}, \tag{1.25}$$

where r_c is the radius of curvature of the magnetic field and $\hat{\mathbf{r}}_\mathbf{c}$ is directed from the centre of curvature to the particle. Applying Equation 1.25 to Equation 1.24 yields,

$$\mathbf{v_c} = \frac{m v_{\shortparallel}^2}{qB}\frac{\hat{\mathbf{r}}_\mathbf{c} \times \mathbf{B}}{r_c B}, \tag{1.26}$$

where $\mathbf{v_c}$ is the *curvature drift* velocity. Curvature drift is demonstrated in Figure 1.5, in addition to gyration and the bounce motion that will be discussed in the next section.

1.1.2 The magnetic bottle

Consider a particle moving into a region where the magnetic field strength is increasing along the field direction, said to be a converging magnetic field. Such a situation occurs, again, in planetary magnetospheres when a particle is gyrating in the presence of a dipole field and follows the magnetic field from the equatorial regions towards the magnetic poles. In the absence of a background electric field, the Lorentz force (Equation 1.1) acts

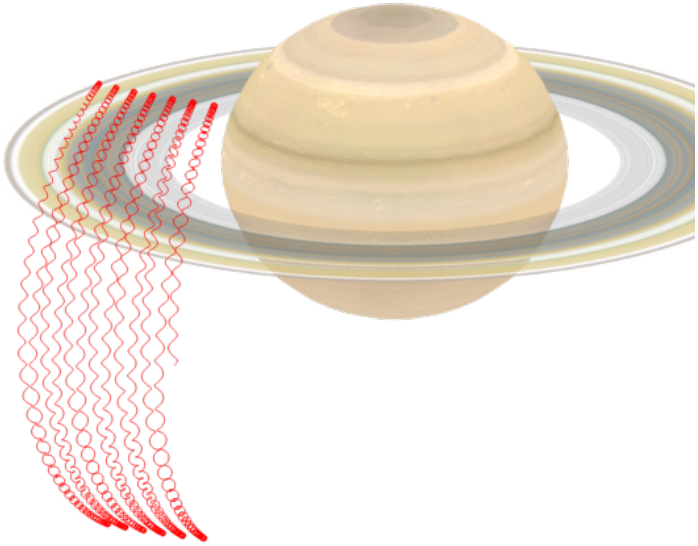

Figure 1.5. A simulation of a 100 MeV proton gyrating within a dipole magnetic field for one minute, starting from the equator at a radial distance of 4 R_S and a pitch angle of 45° (angle between the magnetic field vector and the velocity vector). It is subject to gyration, bounce motion and curvature and gradient drifts. The vast differences in the scale sizes and timescales of these motions is clearly visible. Saturn map created by Björn Jònsson. from 56 images taken by Cassini.

perpendicular to the magnetic field and points in the direction of the guiding centre. As a result, when the field begins to converge, a component of this force points in the $-\nabla\mathbf{B}$ direction. According to Equation 1.3, the magnetic field cannot change the total velocity of the particle so as $v_{\parallel}$ decreases, $v_{\perp}$ must increase until eventually $v_{\parallel} = 0$. At this point, known as the *mirror point*, the particle is reflected and will travel back down towards the opposite pole, only to be reflected again at the same field strength, provided that other processes do not change its kinetic energy in the interim. Such particles are said to be trapped in a 'magnetic bottle' and this is illustrated in Figure 1.5, along with other types of motion already discussed.

This interaction can also be considered in terms of the *magnetic moment* of a particle. Gyrating particles can be thought of as miniature circular current loops. This *diamagnetic current* generates a magnetic field that opposes that of the the external magnetic field and tends to reduce the magnetic field within the plasma. If one considers the magnetic moment of this current loop,

$$\mu = IA, \tag{1.27}$$

where μ is the magnetic moment of the particle, I is the diamagnetic current and A is the area of the circle traced by the gyrating particle perpendicular to the magnetic field. The diamagnetic current is equal to the charge of the particle divided by its period of gyration, or *gyroperiod*,

$$\tau_g = \frac{2\pi r_L}{v_\perp}, \tag{1.28}$$

where τ_g is the gyroperiod. Thus,

$$\mu = \pi r_L^2 \left(\frac{|q| v_\perp}{2\pi r_L} \right), \tag{1.29}$$

and using Equation 1.4, the definition of r_L, one finds that,

$$\mu = \frac{m v_\perp^2}{2B}. \tag{1.30}$$

As long as the timescale over which the particle experiences changes in the external magnetic field is large compared to its gyroperiod, the magnetic moment can be considered to be a conserved quantity, and is known as the *first adiabatic invariant*. If this is the case, according to Equation 1.30, for a charged particle gyrating within a converging magnetic field, as the magnetic field strength increases $v_\perp$ must also increase. Correspondingly, $v_\parallel$ must decrease and, hence, the particle is reflected at the mirror point where $v_\parallel$ drops to zero.

If $v_\parallel$ is large enough, the mirror point may be within the atmosphere of the planet, in which case it is likely that it will collide with atmospheric species, energising them and producing auroral emissions. One can define the *loss cone* as the region in velocity space within which particles will escape the magnetic bottle. If the perpendicular velocity of a particle is zero, the particle will escape no matter how small its parallel velocity is since a finite perpendicular velocity is necessary to initiate gyration. One can also define the *pitch angle* of the particle as the angle between the perpendicular and parallel velocity components,

$$\tan \alpha = \frac{v_\perp}{v_\parallel}, \tag{1.31}$$

where α is the particle pitch angle. Substituting $v_\perp = v \sin \alpha$ into Equation 1.30, one finds

that the quantity $\frac{\sin^2\alpha}{B}$ is conserved. This means that if the pitch angle is known at a reference magnetic field strength, the magnetic field strength at the mirror point can be calculated,

$$B_m = \frac{B_0}{\sin^2\alpha_0}, \tag{1.32}$$

where B_m is the magnetic field strength at the mirror point and B_0 and α_0 are the magnetic field strength and the pitch angle at the reference point. Hence, if B_m is suitably large, one may find that the mirror point is within the atmosphere of the planet, in which case it is likely to be scattered collisionally. If a particle occupies a position outside of the loss cone, it can be trapped within the magnetic bottle for long periods of time but such particles tend to diffuse into the loss cone over time scales comparable to the mean particle collision time.

1.1.3 The plasma state and frozen-in flux

The final, important, concept that will be discussed in this section is that of frozen-in flux, which arises when considering the time evolution of the magnetic field. Here, we move from the microscopic world of particles and their individual interactions with magnetic and electric fields to the macroscopic response of a fluid determined by the collective behaviour of its constituent charged particles.

The world we know consists almost entirely of three states of matter: solids, liquids and gases. In contrast to this, outside of our own little protective bubble most matter exists in what can be thought of as a fourth state: **plasma**. A plasma is essentially a gas with a substantial ionised component and can be thought of as the marriage between a gas and a highly conducting metal because it exhibits some of the key properties of both. The bulk motion of a plasma is well described by fluid dynamics, which has been studied for millennia, and key constructs such as buoyancy and the Navier-Stokes equations apply just as well to plasmas as they do to fluids. However, since plasmas are composed of charged particles, they are also influenced by the electromagnetic forces described earlier in this chapter. Most astrophysical plasmas are sufficiently tenuous that interactions are no longer in the form of particle-particle collisions but are now long-ranged electro-

magnetic interactions which can lead to organised motions and plasma waves. Important exceptions exist such as the ionosphere, through which a planet can exert control over its magnetosphere via ion-neutral collisions (and vice versa).

Furthermore, since the majority of space plasmas are essentially non-collisional, persistent hot plasma populations can arise since particles can be energised but, unlike collisional gases, do not have an efficient mechanism with which to lose energy. Hence, their velocity distributions are often non-Maxwellian with significant high-energy tails (e.g. *Baumjohann and Treumann*, 1996). A further consequence of their non-collisional nature is that, in general, space plasmas are also very highly conducting and can carry currents.

Instead, the plasma and magnetic field move together and are said to be 'frozen-in'. A parcel of plasma can change in shape and size, but the magnetic flux threading this parcel remains constant. This is known as *Alfvén's Theorem* (*Alfven*, 1942), or the frozen-in condition. In a dipole magnetic field, field lines map out a volume of plasma known as a *flux tube*. This is a useful concept when identifying and studying the time evolution of a given plasma population. However, when the magnetic field varies over length scales of the order of a particle gyroradius, the frozen-in theorem no longer holds. More energetic particles have larger gyroradii, so particles with adequately high energies drift in the presence of even relatively small magnetic field gradients as discussed in Section 1.1.1. Clearly the frozen-in theorem is violated in these cases. Despite these restrictions, the frozen-in theorem is a very important concept which has implications for the solar wind and the interplanetary magnetic field described in the next section.

Further important and fundamental properties of the interaction between magnetic fields and plasma can be demonstrated by taking the vector product of Ampère's law (Equation 1.6) with $\mathbf{B}$,

$$\mathbf{j} \times \mathbf{B} = \frac{1}{\mu_0}(\nabla \times \mathbf{B}) \times \mathbf{B}, \tag{1.33}$$

and using the the vector identity,

$$(\nabla \times \mathbf{B}) \times \mathbf{B} = (\mathbf{B} \cdot \nabla)\mathbf{B} - \nabla\left(\frac{1}{2}\mathbf{B} \cdot \mathbf{B}\right), \tag{1.34}$$

yields:

$$\mathbf{j} \times \mathbf{B} = \frac{1}{\mu_0}(\mathbf{B} \cdot \nabla)\mathbf{B} - \nabla\left(\frac{B^2}{2\mu_0}\right). \tag{1.35}$$

The two terms on the right hand side of Equation 1.35 reveal remarkable properties of all magnetic fields. A magnetic field can exert both a *magnetic pressure* and a *magnetic tension* force upon the plasma. In addition, if the magnetic field is frozen into the plasma, field lines will follow the plasma motion that results from these forces. The first term on the right hand side of Equation 1.35 is the magnetic tension force, which acts to straighten out curvatures in the magnetic field. It is analogous to the restoring force which acts to straighten out a plucked elastic string and return it back to its equilibrium position. The second term is the gradient of the magnetic pressure, which acts isotropically and acts to reduce non-uniformities in the magnetic field strength. The components of the magnetic pressure and the magnetic tension parallel to the magnetic field must cancel, as, by definition, $\mathbf{j}\times\mathbf{B}$ cannot have a component parallel to the magnetic field. The component of the magnetic tension perpendicular to the magnetic field is known as the *curvature force*. These force terms have direct consequences for the formation and dynamics taking place within and surrounding planetary magnetospheres, and their interactions with the solar wind.

1.2 The Sun and the Solar Wind

The Sun is an immense thermonuclear engine which supplies energy to the system of planetary bodies that surrounds it. It is essentially a huge ball of rotating plasma which is held together by gravity and has an internal heat source via the fusion of hydrogen nuclei. This internal heating causes turbulent motions within the upper levels of the Sun's interior, such as convection. The temperature of the plasma decreases from its core out towards its surface, known as the *photosphere*, but then increases from its photosphere out to the *corona* through poorly understood processes. The extreme temperatures that exist here mean that its upper atmosphere is constantly being liberated to interplanetary space. Approximately a million tonnes of matter are lost each second in an attempt to equilibrate the pressure gradient between the corona and the surrounding interplanetary

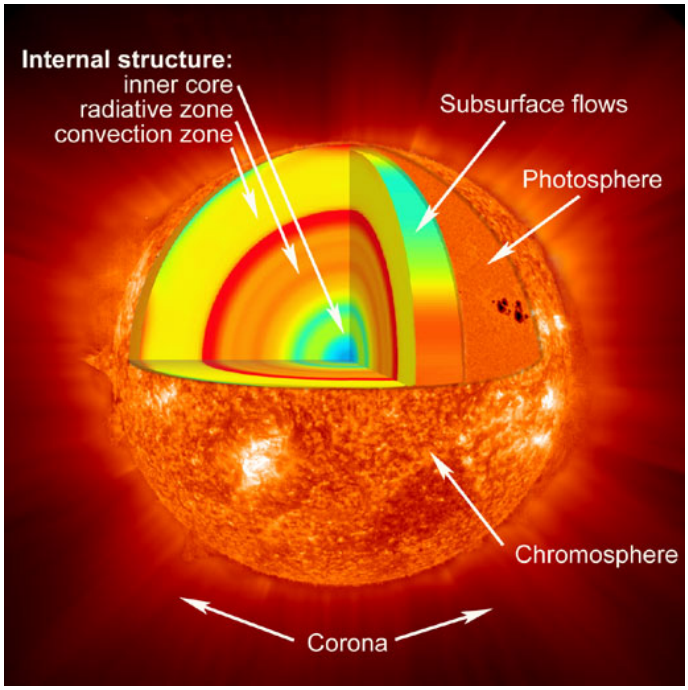

Figure 1.6. An artisitic impression of the different layers that make up the Sun. Credit: NASA

space (e.g. *Schrijver and Zwaan*, 2000). This sounds like an awful lot, but it would take several thousand times longer than the Sun's lifetime for the mass loss due to outflow alone to be significant.

Essentially, the Sun's atmosphere is so hot that not even the gravitational pull from the $\sim 10^{57}$ nuclei that reside below the surface can contain it. At these temperatures, ranging from several thousands of degrees at the photosphere and extending up to millions of degrees in the corona, matter exists primarily as plasma. This plasma is lost to interplanetary space and is then known as the solar wind. The solar wind pervades the entire region under the influence of the Sun, known as the heliosphere, and expands as it flows outwards supersonically. It continues to expand until its density becomes so low that the solar wind dynamic pressure can be balanced by the pressure of the tenuous interstellar medium at the termination shock. *Voyager 1* first encountered the termination shock at a distance of 94.0 AU on 16 December 2004 after a 27 year tour of the solar system (*Decker et al.*, 2005). As mentioned in Section 1.1, the Sun also has a large-scale magnetic field and this fact is of critical importance when considering the interaction between the solar wind and planetary magnetic fields.

1.2.1 Properties of the solar wind

The existence of the solar wind was first proposed by *Birkeland* (1896, 1908, 1913) in order to explain observations made in the arctic of the *aurora borealis*, or 'northern lights', in addition to laboratory studies. Several decades later, *Chapman and Ferraro* (1930) came to a similar conclusion in order to explain magnetic storms, which they theorised could be caused by the ejection of clouds of ions from the Sun. Additional evidence came in the form of cometary observations made by *Hoffmeister* (1943), who deduced that the solar wind flows with a finite velocity. *Hoffmeister* (1943) measured a few degrees lag between the direction in which the tails of comets point and the radial direction from the Sun due to the relative velocity between the comet and the solar wind. *Biermann* (1951) deduced that the Sun's electromagnetic radiation pressure alone is not large enough to account for this, which implies that some form of gas is continually streaming away from the Sun. Furthermore, *Parker* (1958) found that the solar corona could not be in hydrostatic equilibrium because the coronal pressure is non-vanishing as the distance from the Sun tends towards infinity. Like most paradigm-changing discoveries, this theory was not accepted for several years until the solar wind was directly observed by the Soviet *Luna 1* spacecraft. This discovery was verified by *Luna 2* and *Luna 3*, and again three years later by *Snyder and Neugebauer* (1963) using measurements taken by the *Mariner 2* spacecraft.

The solar wind consists mainly of protons and electrons with ∼4% abundance (by number) of He^+ (*Robbins et al.*, 1970). As *Biermann* (1951) first deduced, the solar wind travels supersonically away from the Sun. This has important consequences when it approaches magnetised planets as will be discussed in Section 1.3.1. The solar wind dynamic pressure can be approximated as,

$$D_P = 1.16 m_p n v^2, \tag{1.36}$$

where D_P is the solar wind dynamic pressure, m_p is the mass of a proton, n is the proton number density and v is the solar wind velocity. The factor of 1.16 accounts for the fact that there is a 4% abundance of He^+ in the solar wind (*Robbins et al.*, 1970). The solar wind density typically falls in proportion to r^{-2} since the solar wind expands to cover a larger spherical surface area as it travels away from the Sun. However, *Horbury and Balogh* (2001) used magnetic field data from the *Ulysses* spacecraft to find that high-speed solar

wind streams originating from coronal holes exhibit a degree of 'overexpansion'. Fast streams expand with altitude to fill a larger proportion of the surface area than that of the coronal hole with respect to the surface area of the Sun. As a result, the solar wind does not necessarily map precisely to the sources of the fast and slow solar wind at the Sun's surface. It accelerates as it leaves the Sun, but remains fairly constant in speed after a few tens of solar radii ($R_\odot$), beyond which gravitation and coronal acceleration are negligible (*Parker*, 1958). Hence, one can assume that $D_P \propto r^{-2}$ beyond this point.

As the solar wind flows away from the Sun, in accordance with the frozen-in condition it carries with it a remnant of the solar magnetic field, which is then known as the interplanetary or heliospheric magnetic field (I/HMF). In the absence of radial outflow, the large-scale solar magnetic field would be approximately dipolar. However, near the Sun's magnetic equator, the magnetic field is orthogonal to the radial flow direction, so there is competition between the magnetic field and the outflowing plasma (*Woo et al.*, 2004). Close to the Sun, the magnetic field is strong enough to dictate the direction of flow and inhibit the solar wind. But since the field strength of a magnetic dipole falls off as r^{-3}, its magnetic pressure according to Equation 1.35 falls as r^{-6}. *Parker* (1958) deduced that the energy density of a steady-state magnetic field from a rotating star falls as r^{-4}. On the other hand, the dynamic pressure only falls off as r^{-2}. As such, the plasma pressure soon dominates and, at a height of $\sim$1.5 $\mathrm{R}_\odot$ (*Hansteen*, 2009), is able to stretch the equatorial magnetic field outwards, allowing the solar wind to stream away from the Sun with a velocity of $\sim$400 $\mathrm{km\,s^{-1}}$ (*Woo and Habbal*, 2000). At high latitudes, the outflowing plasma does not face this opposition so it is able to stretch the field lines with relative ease such that they point radially inwards in one hemisphere and radially outwards in the opposite hemisphere. The solar wind is able to stream out of these high-latitude 'coronal holes' with a velocity in excess of $\sim$700 $\mathrm{km\,s^{-1}}$(*Phillips et al.*, 1995), though *Woo and Habbal* (2000) later showed that fast solar wind streams can also emerge from active regions at low latitudes. This quiescent picture of the Sun is shown in Figure 1.7a.

However, solar activity and the properties of the solar wind follow cycles of activity and vary over several different characteristic timescales. The most well known of these cycles is the $\sim$11-year activity cycle known as the *Schwabe cycle*. Solar activity is often quantified in terms of the number of *sunspots* present on its surface, regions where convection is inhibited by strong magnetic fields. This causes the sunspots to become cooler than the surrounding

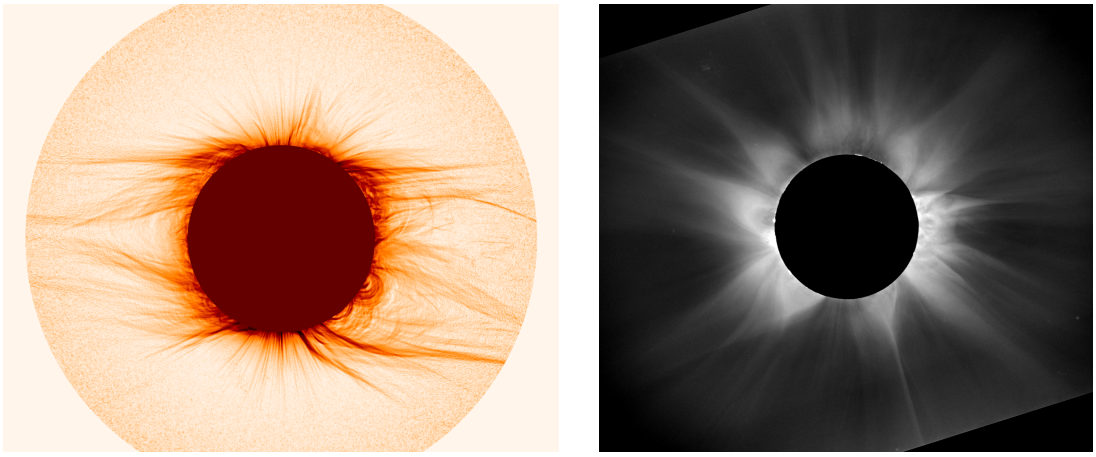

(a) Solar Minimum (b) Solar Maximum

Figure 1.7. Images taken of the solar corona close to solar minimum (a) and solar maximum (b). The plasma traces magnetic field lines and shows that at solar minimum the Sun's magnetic field is roughly dipolar with high-energy arcades at the equator, whereas it is less ordered and complex at solar maximum. Credit: High Altitude Observatory, National Center for Atmospheric Research, Boulder, Colorado.

region where the magnetic field is weaker. Schwabe detected a periodic variation in the number of sunspots present on the surface of the Sun as shown in Figure 1.8. When the number of recorded sunspots peaks at 'solar maximum', the magnetic field is no longer well ordered as it is during the 'solar minimum' case discussed previously. It becomes disorganised and complex as shown in Figure 1.7b.

Regular sunspot records stretch back to the early 17^{th} century but between approximately 1645–1715, a period of time known as the 'Maunder minimum', very few were recorded. *Eddy* (1983) showed that this minimum was a real effect and not the result of a measurement bias. He also showed that the solar minimum is consistent with C^{14} abundance data. C^{14} is produced in the upper atmosphere when cosmic rays interact with nitrogen. The number of cosmic rays that are able to reach the atmosphere varies with the level of solar activity. The abundance of C^{14} is anti-correlated with solar activity since the active Sun blocks more cosmic rays from entering Earth's atmosphere. *Eddy* (1983) also showed that the C^{14} abundance follows a regular cycle with a period of ∼1000 years, strongly indicating that another, much longer, cycle of solar activity exists. Many other such cycles of varying length have subsequently been found (e.g. *Sonett and Finney*, 1990; *Vasiliev and Dergachev*, 2002; *Braun et al.*, 2005; *Xapsos and Burke*, 2009). Hence, the properties of the solar wind may be very different depending on the epoch of observation.

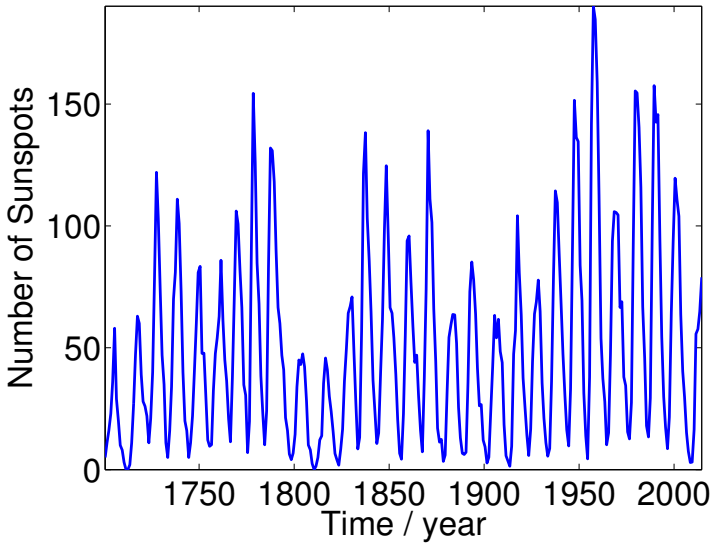

Figure 1.8. Shows the yearly sunspot tally since 1700. This number is a good proxy for the level of solar activity and follows a clear cycle with an average period of 11 years. One may also be able to identify what appear to be a much longer cycles superimposed upon the more obvious Schwabe cycle. Data from WDC-SILSO, Royal Observatory of Belgium, Brussels.

However, solar activity can vary over much shorter timescales. The Sun rotates with a sidereal period of 24.5 days at its equator so recurrence of activity may occur if active regions persist for at least this length of time, or longer if taken with respect to a co-moving observer like one of the planets. In addition, the geometry of the IMF is complicated by the rotation of the Sun since the IMF is anchored to the point on the solar surface where the solar wind originally left it. As such, solar rotation is imposed upon the IMF and the magnetic field is bent into an Archimedean spiral known as the *Parker Spiral* (*Parker*, 1958), as shown in Figure 1.9. The solar wind and the IMF that threads it continue to flow radially away from the Sun but are still magnetically connected to their source regions on the rotating solar surface. Hence, the configuration of the IMF evolves with distance from the Sun. Close to the Sun, it has been discussed that the solar magnetic field points radially outwards in one hemisphere and radially inwards in the opposite hemisphere. At the orbit of Earth, the angle between the IMF and the flow of the solar wind is typically expected to be $\sim 45°$ (*Wilcox*, 1968). At Saturn, *Jackman and Arridge* (2011) found that the solar wind dynamic pressure follows a lognormal distribution with a peak at ~ 0.01 nPa between $8 - 10$ AU (encompassing the orbit of Saturn). *Jackman and Arridge* (2011) also found that the average spiral angle was $\sim 86.8°$ within this range of distances.

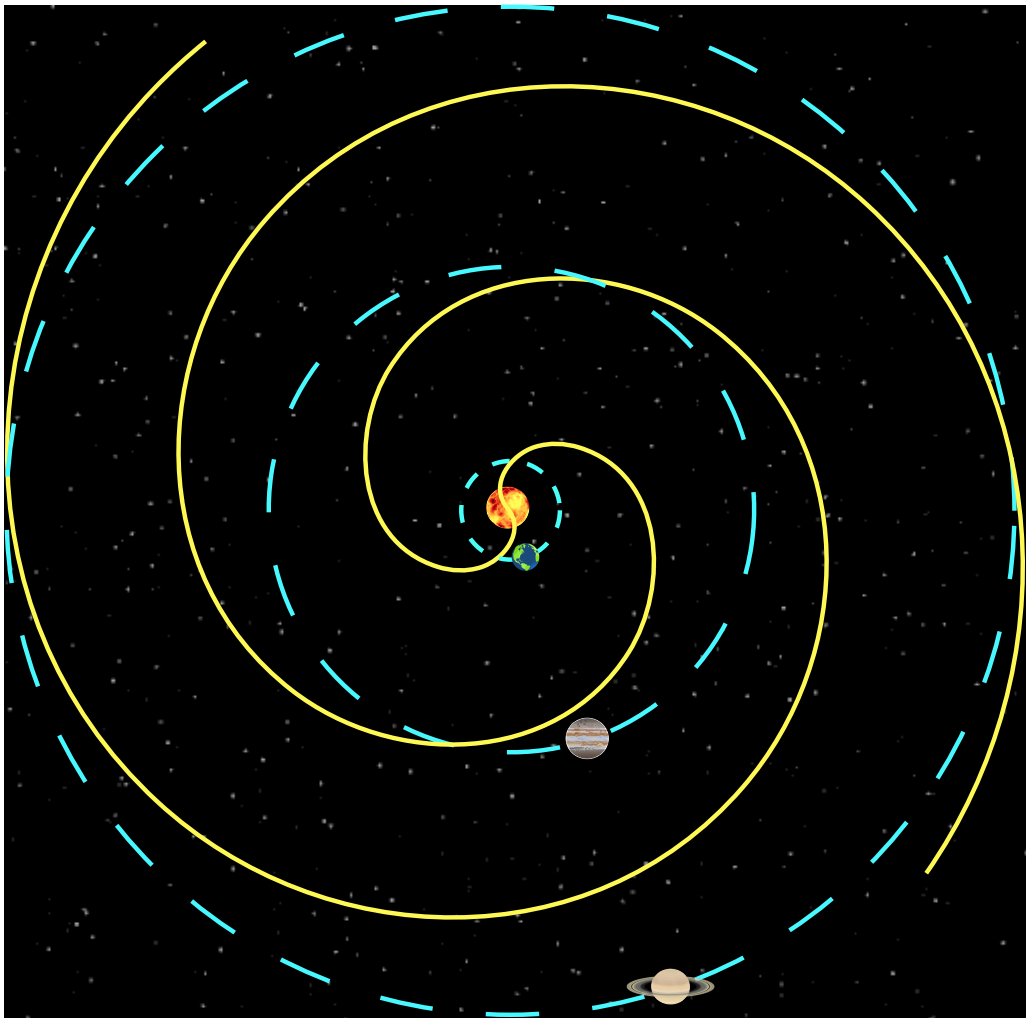

Figure 1.9. Depicts the approximate configuration of the IMF with respect to Earth, Jupiter and Saturn, known as the Parker spiral. The positions of the planets relative to the Sun are to-scale, but the sizes of the Sun and the planets have been exaggerated and are not to scale with each other. After *Parker* (1958)

.

Since the IMF is oppositely directed on either side of the solar magnetic equator, a gradient in the magnetic field must exist. A current must flow at this interface in accordance with Ampère's law and this interface is known as the *heliospheric current sheet*. The Sun's magnetic dipole axis is tilted with respect to its axis of rotation, so one may expect the heliospheric current sheet to pass over a stationary observer twice per solar rotation. A transition through the heliospheric current sheet is accompanied by a reversal in the direction of the IMF.

In addition to the heliospheric current sheet, further organised structure exists within the solar wind. Fast and slow solar wind streams can interact with each other to form

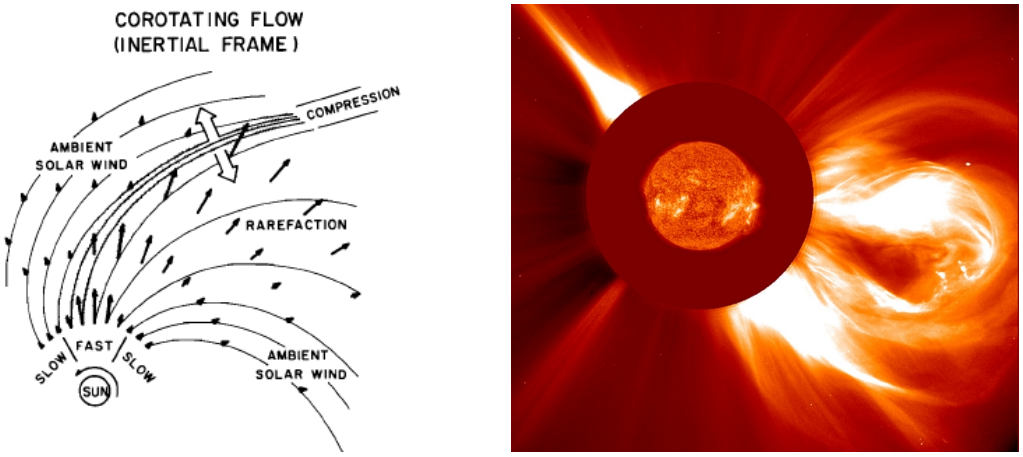

(a) CIR (b) CME

Figure 1.10. a) Shows the structure of a corotating interaction region (CIR). Fast solar wind streams build up behind slow solar wind streams, forming a compression region. From *Pizzo* (1978). b) An image of a coronal mass ejection (CME) leaving the Sun. This image is a composite taken by two instruments on board the Solar and Heliospheric Observatory on 2 December 2003. An image of the Sun taken by the Extreme ultraviolet Imaging telescope is overlaid on top of a chronograph image taken at the same time by the Large Angle and Spectrometric Coronagraph. Credit: ESA & NASA.

corotating interaction regions (CIRs), which form when a fast stream catches up to a slow stream as shown in Figure 1.10a. As the plasma and magnetic field are frozen together, the fast stream bumps into the slow stream, which acts as an obstacle to it. This causes a build up of fast solar wind behind the slow solar wind stream, leading to a compression and a possible shock. Coronal mass ejections (CMEs) occur when a loop of coronal material becomes distended, causing the anti-parallel field lines on either side of the loop to be drawn together and 'reconnect'. A loop of closed magnetic flux is 'pinched off' as a result, which is then propelled out into the heliosphere by magnetic tension (see *Low*, 2001 and the references therein). Magnetic reconnection occurs as a result of the breakdown of the frozen-in flux condition and is a process of fundamental importance to the dynamics taking place within planetary magnetospheres, so will be discussed more in Section 1.3.1. Both CIRs and CMEs can significantly perturb the ambient solar wind. *Lindsay et al.* (1995) found that CIRs in particular lead to enhancements in the dynamic pressure, though CMEs transfer more energy to the terrestrial magnetosphere due to their favourable magnetic configuration.

Since the solar wind and IMF are frozen together, the IMF travels along with the solar

wind during its passage through the heliosphere and interacts with magnetic fields and plasma populations originating elsewhere. For as long as the frozen-in condition remains valid, plasma populations tied to magnetic fields of different origins cannot mix. This is exemplified when the solar wind comes into contact with a planetary magnetic field, forming a magnetospheric cavity within which the solar wind cannot gain direct entry.

1.3 The Configuration of Saturn's Magnetosphere

To date, four spacecraft have sampled Saturn's magnetosphere in situ and all have detected a rather peculiar planetary magnetic field. *Smith et al.* (1980) found that Saturn's internal magnetic field is perfectly axisymmetric with respect to the planet's axis of rotation within the limitations of the *Pioneer 11* observations. This was a surprising result because such a configuration is forbidden by classical dynamo theory as shown by *Cowling* (1933). Subsequent observations made by Voyager 1 and *Voyager 2* (*Ness et al.*, 1981, 1982) supported the existence of this peculiarity. Two decades later, Cassini observations showed that the angle separating the planet's dipole and rotation axes is even smaller than previously thought (*Cao et al.*, 2011). Even after extensive study of the Kronian system with Cassini, it is still not known precisely how long it takes for Saturn to complete one rotation.

One could measure the length of a day by measuring the time it takes for persistent features to return back to the position at which they were first observed. For the gas giants though, this is complicated by the fact that the upper layers of the planet do not necessarily rotate with the same period as the lower levels, or the 'surface' of the planet (e.g. *Coroniti*, 1974; *Huang and Hill*, 1989). Instead, one could measure one revolution of the magnetic dipole as was done for Jupiter, first using ground based observations of the auroral radio emissions and later using in-situ magnetic field observations. But this relies on there being a measurable tilt between the magnetic dipole axis and the planet's axis of rotation, which does not seem to be the case for Saturn.

Furthermore, despite the internal field being almost perfectly axisymmetric, periodic modulation of the magnetic field, plasma parameters, radio emissions and auroral signatures is also observed (e.g. see the review by *Carbary and Mitchell*, 2013 and the references

therein). This is known as the 'rotational anomaly' and is said to cause 'planetary period oscillations' (PPOs). Such a modulation has also been observed at Jupiter but is caused by an offset between the magnetic dipole and the planet's axis of rotation. In the absence of such an offset for Saturn, a different mechanism must be responsible.

But *Gurnett et al.* (2005) observed that this period had increased by ∼6 minutes in the time between the Voyager detections and the arrival of Cassini in 2004. This suggests that this period cannot coincide with the true rotational period of the planet since such a large change in the angular velocity of an object as large as Saturn in such a short period of time is implausible. Subsequent measurements by *Kurth et al.* (2008) found that the PPO period is slowly drifting with time. Later, two distinct periods were discovered which have been identified as oscillations associated with rotating current systems occurring in the northern and southern hemispheres separately (e.g. *Gurnett et al.*, 2009a,b; *Carbary et al.*, 2009; *Andrews et al.*, 2010). *Clarke et al.* (2006, 2010) also found that the PPOs lead to periodic modulation of the magnetopause, and, hence, directly impact upon empirical studies of Saturn's magnetopause.

1.3.1 Formation of the magnetosphere

The planetary magnetic field of Saturn itself is of the utmost importance to this work since it is this property that gives rise to the magnetospheric cavity. The magnetised solar wind perceives a planetary magnetic field as an obstacle as a consequence of the frozen-in theorem. Under conditions where this theorem is valid, the solar wind exists separately to and cannot mix with plasma populations embedded within planetary magnetic fields. It is worth noting that even if the solar wind were unmagnetised, a magnetospheric cavity would still be expected as the solar wind is also deflected by the Lorentz force as described by *Chapman and Ferraro* (1930).

The quasi-static background dipole field is then modified by magnetic fields generated within the magnetosphere, such as the ring current described in Section 1.1.1. However, the largest modification to this field arises due to its interaction with the solar wind. The solar wind flows through the heliosphere supersonically so, when it comes into contact with such an obstacle, a *bow shock* is formed because information about the obstacle cannot be conveyed back to the approaching solar wind in time for it to reconfigure. The formation

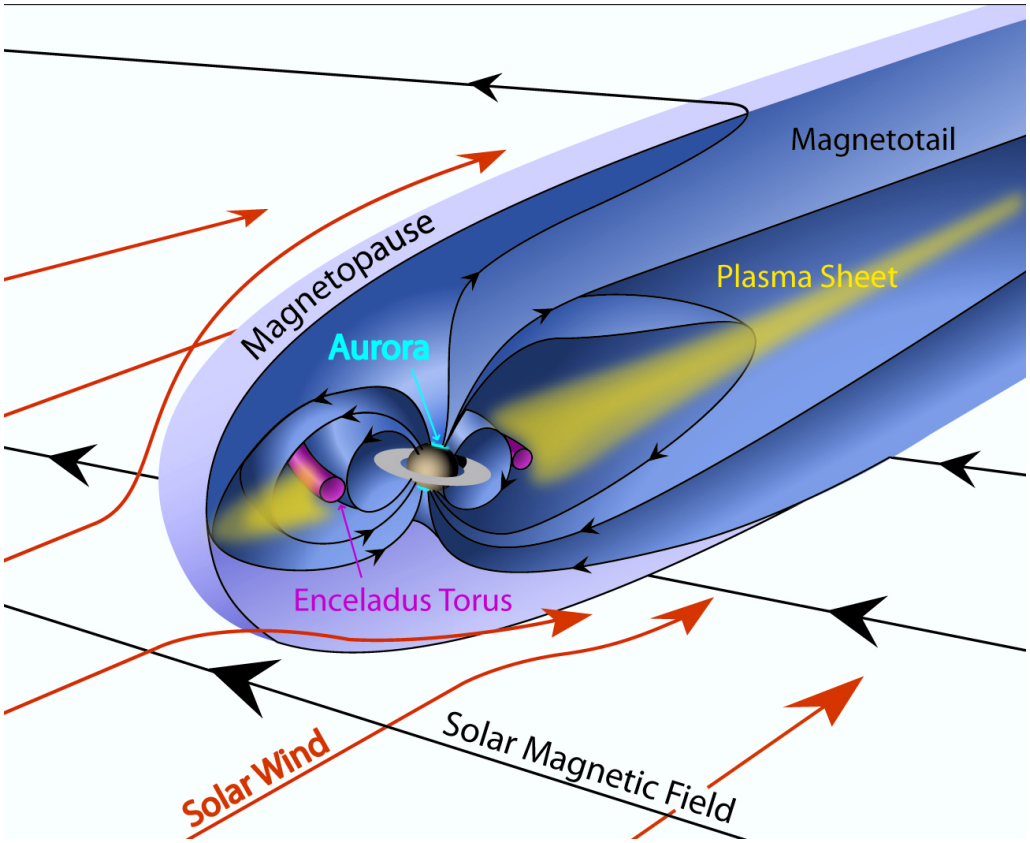

Figure 1.11. Shows the structure of Saturn's magnetospheric cavity that results from the interaction between the solar wind and the magnetospheric magnetic field. Also shown are the Enceladus plasma torus and the extended plasma sheet that forms as a result, and the location of the polar aurorae in both hemispheres. Credit: Fran Bagenal & Steve Bartlett.

of a bow shock upstream of the Earth was first postulated by *Axford* (1962) and *Kellogg* (1962) and was first observed by *Holzer et al.* (1966) using data from the magnetometer on board the *Ogo 1* spacecraft. When the solar wind transitions through this shock, it is slowed, heated and compressed to form a region of higher plasma density and magnetic field strength known as the *magnetosheath*, which envelops the magnetosphere.

The area within which the solar wind cannot gain direct access is known as the magnetosphere, and the boundary between the magnetosphere and the magnetosheath is known as the **magnetopause**. The terrestrial magnetopause was first directly observed by *Cahill and Amazeen* (1963) using the magnetometer on board *Explorer 12*. The solar wind exerts pressure upon the planetary magnetic field. This acts to compress the field on the dayside whilst allowing it to 'stretch out' on the nightside to form a bullet-shaped cavity as shown in Figure 1.11. Thus, the symmetry otherwise expected of a vacuum dipole magnetic field

is broken.

Since the magnetopause separates the compressed IMF from the magnetospheric magnetic field, a magnetic field gradient must exist across it. As a result, a current must also flow along the magnetopause in accordance with Ampères law (Equation 1.6). This current essentially acts to shield the magnetosphere from the solar wind. There are several contributions to the magnetopause current. *Chapman and Ferraro* (1930) described how a stream of unmagnetised electrons and ions incident upon Earth's magnetic field would be initially deflected in opposite directions by the magnetic field, which gives rise to a westerly current around Earth. In general terms, the solar wind need not be unmagnetised as a sharp magnetic field gradient experienced by a magnetised stream of ions and electrons would produce a similar response. As discussed in Section 1.1.1, particles gyrating in the presence of magnetic field gradients also give rise to a current in the direction perpendicular to the magnetic field and the magnetic field gradient, which is in the same direction as the Chapman-Ferraro current. Similarly, curvature drift also contributes to the magnetopause current. Finally, a density gradient typically exists across the magnetopause, which leads to the formation of a diamagnetic current and also contributes to the total magnetopause current.

1.3.2 The impact of magnetospheric plasma

Broadly speaking, when in equilibrium, the magnetopause forms where the solar wind dynamic pressure acting normal to the boundary is exactly balanced by pressure sources inside the magnetosphere. In reality, the solar wind dynamic pressure is highly variable and has a strong influence on the magnetosphere, whose size and shape can exhibit rapid variability in response. As such, the magnetopause is rarely, if ever, in true hydrostatic equilibrium (e.g. *Kaufmann and Konradi*, 1969). In most cases there will be some deviation between the true dynamic pressure and that estimated assuming pressure balance depending on how close the magnetopause actually was to equilibrium at the time of the observation. The average deviation may also change for each planet in response to the changing solar wind conditions.

For the Earth, the principal pressure source that holds off the solar wind is the magnetic pressure associated with the planetary dipole. However, there are large sources of plasma

within the magnetospheres of Saturn and Jupiter, and this plasma contributes significantly to the interior pressure resisting that of the solar wind. At Earth, the plasma source rate is low and is constrained observationally only by the amount of plasma leaving the system (e.g. *Hultqvist et al.*, 1999). However, within the magnetospheres of Saturn and Jupiter, volcanic activity within one of their respective moons injects their respective magnetospheres with large amounts of material.

Early in the Cassini mission, it was found that Enceladus ejects plumes of water-group molecules into Saturn's magnetosphere (e.g. *Dougherty et al.*, 2006; *Porco et al.*, 2006). A small fraction of these are ionised into a plasma, which forms a torus at the orbit of Enceladus, and this plasma can greatly influence the dynamics that drive Saturn's magnetosphere. Mass loading estimates vary substantially. *Tokar et al.* (2006) and *Pontius and Hill* (2006) estimated that $\sim$100 kg s^{-1} of the water molecules that are liberated by the moon are ionised. More recent estimates made by *Spencer* (2011) placed the mass outflow rate to be as high as 200 kg s^{-1} and *Bagenal and Delamere* (2011) found that the plasma source rates lie between $\sim 12 - 250$ kg s^{-1}. *Waite et al.* (2009) also found that smaller quantities of carbon dioxide, ammonia and hydrocarbons are also present within the Enceladus plume.

Similarly, Io is a large source of plasma within Jupiter's magnetosphere with typical plasma source rates exceeding those of Enceladus in absolute terms by at least an order of magnitude. However, *Vasylinas* (2008) used simple scaling relationships to show that, in relative terms, Enceladus may be a more significant plasma source to Saturn's magnetosphere than Io is to Jupiter's, primarily due to Saturn's weaker magnetic field. Note that there may be a significant degree of temporal variability associated with the mass loading rate within both magnetospheres. *Bagenal et al.* (1997), for example, noted that the Io plasma torus exhibited significantly different characteristics between the Voyager and Galileo eras.

Newly-formed plasma originating from the moons then begins to gyrate around magnetic field lines, with a typical Larmour radius of $\sim$1 R_S for O^+ in the vicinity of Enceladus for example. As flux tubes become loaded with mass, conservation of angular momentum dictates that they should slow down, resulting in a velocity differential between the flux tube and the atmosphere of the planet. Collisions between ionospheric neutral species

and ions within the flux tube impose a torque which acts to speed up the flux tube and slow down the neutral atmosphere (e.g. *Ferraro*, 1937; *Hill*, 1979). Essentially, angular momentum is transferred from the neutral atmosphere of the planet to this newly created plasma via a $\mathbf{j} \times \mathbf{B}$ force.

The thermal component of the plasma within the magnetosphere is largely equatorially confined due to the centrifugal forces it experiences (*Gledhill*, 1967). It forms an extended magnetodisc (or plasma sheet) structure, a region of dense plasma accompanied by radially stretched magnetic field. A magnetodisc has been detected at Saturn (e.g. *Arridge et al.*, 2007) and stretches all the way out to the dayside magnetopause (e.g. *Sergis et al.*, 2009). Similarly, a plasma sheet has been observed within Earth's magnetosphere (e.g. *Ness*, 1965; *Vasyliunas*, 1968). However, the large plasma sources within Saturn's magnetosphere make Saturn's magnetodisc far more dense than its terrestrial counterpart, and inflates the magnetosphere of Saturn beyond the size expected based on the strength of the magnetic dipole alone. The gravitational force of the planet can only exceed the centrifugal force acting on the plasma up to $\sim$1.7 R_S from the centre of the planet (e.g. *Achilleos et al.*, 2010a), which is inside of the orbital radius of Enceladus ($\sim$4.0 R_S). Hence, an additional force is required if plasma produced at Enceladus is to corotate with the planet.

1.3.3 Competing magnetospheric processes

The force required to impart centripetal acceleration of plasma comes in the form of a $\mathbf{j} \times \mathbf{B}$ force resulting from the azimuthal ring current. In addition, a set of radial corotation-enforcement currents first discussed by *Kennel and Coroniti* (1975) accelerate plasma in the azimuthal direction in the sense of corotation. These currents flow along magnetic field lines and close via Pedersen currents in the ionosphere (e.g. *Hill*, 1979), as shown in Figure 1.12. These currents are responsible for the ever-present auroral oval of Jupiter (*Cowley and Bunce*, 2001). A similar feature was observed at Saturn by *Stallard et al.* (2008) though it was approximately 75% less intense than Saturn's main auroral emissions, which are generated through a different mechanism discussed later.

As plasma diffuses out through the system, its angular velocity must drop to conserve angular momentum. In the outer magnetosphere, the magnetic field becomes 'stretched' relative to the magnetospheric configuration in the inner magnetosphere. Ultimately,

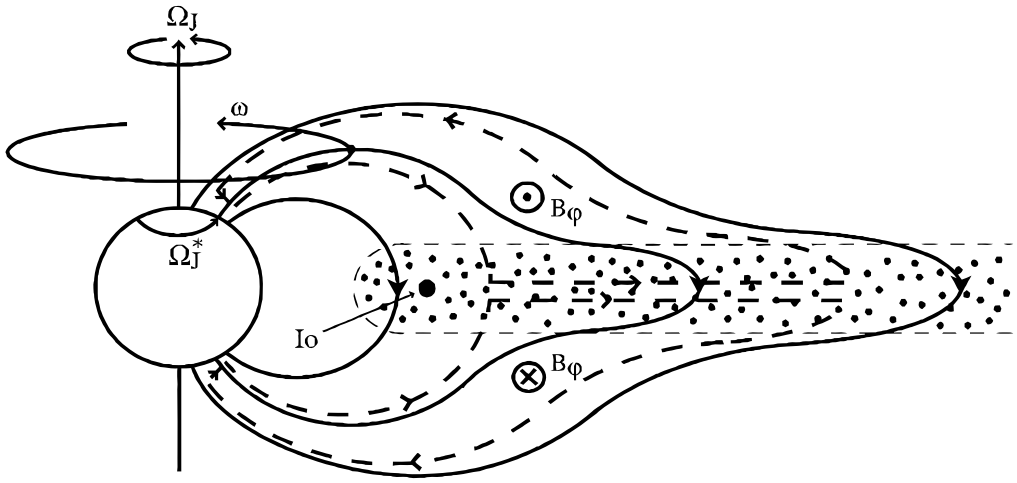

Figure 1.12. Shows the system of currents that enforce plasma corotation within Jupiter's magnetosphere up to tens of planetary radii away from the planet (and to a lesser extent in Saturn's magnetosphere). Currents (dashed) flow along magnetic field lines (solid) and close through the ionosphere via Pedersen currents and through the magnetodisc (shaded area). From *Cowley and Bunce* (2001).

this leads to the ejection of a plasmoid down into the magnetotail through magnetic reconnection, similar to the release of CMEs from the Sun as discussed in Section 1.2.1. The newly unloaded flux tube is then convected back around the planet, propelled by magnetic tension. This cycle was proposed by *Vasyliunas* (1983) and is illustrated in Figure 1.13.

Global magnetohydrodynamic (MHD) simulations of Saturn's magnetosphere are generally in good qualitative agreement with this theory. *Zieger et al.* (2010) showed that the periodic or quasi-periodic release of large-scale plasmoids results in periodic or quasi-periodic perturbations in the magnetopause standoff distance. Simulations by *Jia et al.* (2012) found that that magnetopause standoff distance can change by up to $\sim$10 R_S under low (< 0.005 nPa) solar wind dynamic pressure conditions as a result. After a plasmoid is pinched off, the depleted flux tube rotates around Saturn causing a negative pressure perturbation and consequently a perturbation in the magnetopause distance. The depleted flux rope is gradually filled up with internal plasma until it is suddenly depleted again during the next plasmoid release.

The picture of the magnetosphere described thus far is known as the 'closed' magnetosphere, whereby the solar wind and the magnetospheric plasma are separate so long

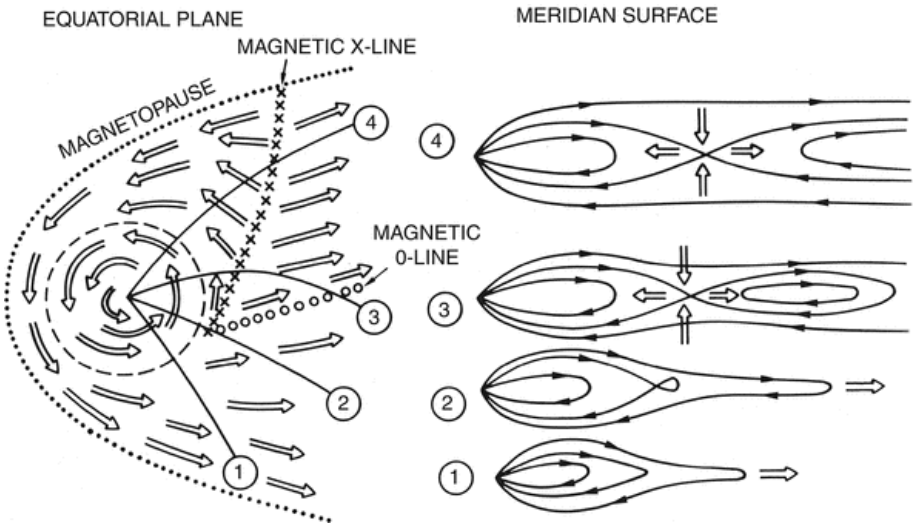

Figure 1.13. Shows the Vasyliũnas cycle of plasma transport. Close to the planet (within the dashed line) plasma corotates with the planet. As plasma moves out of this region, its angular velocity falls to conserve angular momentum and the plasma begins to subcorotate (region 1). As it moves further into the tail (region 2) flux tubes become distended and are eventually 'pinched-off' (region 3 and 4). From *Vasyliunas* (1983).

as Alfvén's theorem holds true. However, magnetic reconnection can also open up the magnetosphere to the solar wind, allowing plasma of solar origin to enter it as described by *Dungey* (1961). Through this process, oppositely directed magnetic field lines merge and connect the planet to the Sun magnetically. These 'open' magnetic field lines then convect across the poles of the planet and reconnect in the magnetotail to attain closure once again, propelling a parcel of plasma down into the magnetotail in the process through magnetic tension. Magnetic reconnection essentially excites plasma transport within the magnetosphere, and gives rise to a twin cell pattern of plasma flow.

This whole process is known as the Dungey cycle (Figure 1.14) and is not necessarily as steady a process as this description may imply. Magnetic flux can be opened on the dayside of the planet and can build up in the magnetotail, increasing the size of the polar cap – the ionospheric region to where these open field lines map *Russell and McPherron* (1973). This is known as the 'growth phase' of a geomagnetic substorm, named such since the auroral oval literally grows in size as more flux is added to the system (*Akasofu*, 1964). A large amount of energy is collected from the solar wind and is stored in the magnetotail and can then be released very rapidly (*Baker et al.*, 1997). It is primarily through this process that the auroral emissions are generated at Earth, though it is a matter of considerable

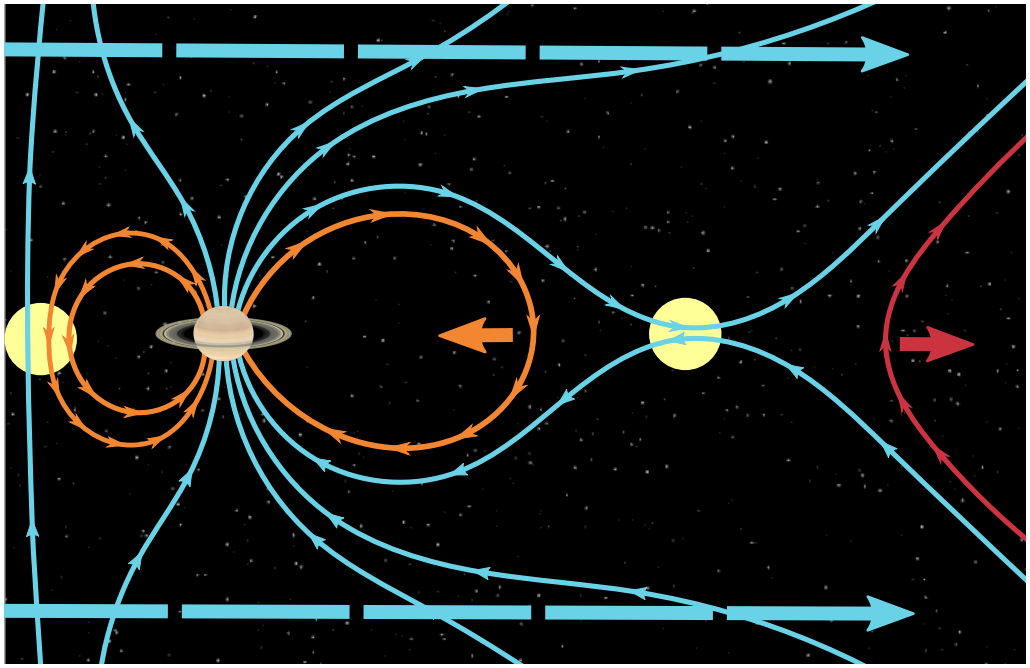

Figure 1.14. Illustrates the Dungey cycle under northward IMF (for Saturn) whereby magnetic flux is opened to the solar wind on the dayside of the planet and is closed in the magnetotail. Magnetic field lines are depicted as thin, arrowed lines: orange indicates closed planetary field lines; blue indicates field lines open to the solar wind and red corresponds to the plasmoid ejected into the magnetotail. The yellow regions indicate the magnetic field diffusion regions where reconnection takes place, and the large dashed arrows indicate plasma transport. Note that Earth's magnetic field is directed oppositely with respect to Saturn's magnetic field, so reconnection is most efficient under southward IMF. Reconnection is also expected when the IMF is parallel to the planetary field, but is less efficient under these conditions. After *Dungey* (1961).

debate as to what effect (if any) this has on Saturn's magnetosphere.

Magnetic reconnection is most efficient under conditions in which the magnetic field lines are antiparallel (otherwise known as a 180° magnetic 'shear'). But by the time the solar wind reaches Saturn, the IMF is rotated such that there is typically a ∼90° angle between the nominally southward dayside planetary magnetic field and the IMF, such that reconnection may be suppressed. Prevailing conditions across the magnetopause, such as the high magnetospheric plasma β (the ratio of plasma to magnetic pressure) and large difference in β across the boundary, may also inhibit reconnection at Saturn (e.g. *Masters et al.*, 2012a). Similarly, MHD simulations imply that Saturn's magnetosphere may be relatively insensitive to the orientation of the IMF (e.g. *Jia et al.*, 2012). However, similarities have been found between the auroral morphology and variability at Saturn

and Earth (e.g. *Badman et al.*, 2013, 2014), and it is well established that Earth's auroral emissions are solar wind-driven (e.g. *Paschmann et al.*, 2003).

The true pattern of plasma flow within a planetary magnetosphere is expected to resemble something akin to a summation of the Vasyliũnas flow and the Dungey flow cycles. The resulting cycle will depend on the relative importance of each process, which likely varies from planet to planet. It is likely to be a function of the magnetospheric plasma source rate, the planetary rotation rate, the planetary field strength, the solar wind conditions and the efficiency of magnetic reconnection at the dayside magnetopause.

1.3.4 Suprathermal plasma

Unlike the equatorially confined thermal plasma, energetic plasma is ubiquitous within Saturn's magnetosphere (e.g. *Krimigis et al.*, 1982, 2005) and can extend to high latitudes. Various mechanisms have been proposed for the energisation of plasma up to the suprathermal energies observed, ranging from $\sim$3 keV and exceeding 100 MeV. One such mechanism is the interchange instability (e.g. *André et al.*, 2005), which causes adiabatic energisation of plasma moving into the inner magnetosphere. It can be followed by non-adiabatic relaxation whereby energised plasma can move back into the outer magnetosphere via scattering processes without losing energy (e.g. *Hill et al.*, 1983 and the references therein).

Plasma interchange events have been observed within Saturn's magnetosphere via energetic neutral atom (ENA) imaging by the Ion and Neutral Camera (INCA) on board Cassini (e.g. *Krimigis et al.*, 2007; *Brandt et al.*, 2010; *Mitchell et al.*, 2015). Energetic ions interact with cold neutral gas through the process of charge-exchange, whereby the energetic ion captures an electron from a neutral particle and becomes an 'energetic neutral atom'. As such, it is no longer affected by the magnetic field so it then follows a ballistic trajectory. Hence, one can expect ENAs to be emitted isotropically from regions containing an abundance of energetic plasma, and these ENAs can be measured remotely in order to indirectly detect the presence of energetic plasma within Saturn's magnetosphere. This is precisely what INCA can do (described in more detail in Chapter 2).

Care should be taken with the interpretation of ENA images, however, as there are

several potential sources of observational bias. First of all, ENAs will only be emitted from regions that contain both hot plasma and cold neutral gas. A lack of ENAs from a particular region does not necessarily indicate the absence of energetic plasma, it could mean that there are relatively few neutrals in that region instead. In addition, *Paranicas et al.* (2005) described how the Compton-Getting effect also affects ENA observations if there is a relative velocity between the spacecraft and the source region. This is because the instrument will accumulate more (fewer) detections in a given time step if the spacecraft and the source region are moving towards (away from) each other. *Paranicas et al.* (2005) also presented a method by which this effect can be accounted for.

A sequence of ENA images of Saturn's magnetosphere taken by INCA is shown in Figure 1.15. Intensifications of the ring current are shown with 'warmer' regions indicating regions in which a lot of energetic plasma is present. These images are typical of those observed at Saturn: 'bubbles' of plasma are observed to rotate around the planet in the sense of corotation. They tend to begin in the post-midnight region and travel around the planet, generally diminishing as they enter the dusk sector (e.g. *Mitchell et al.*, 2009a). These bubbles are caused by plasma interchange, where hotter, less dense plasma in the outer magnetosphere replaces colder, denser plasma in the inner magnetosphere due to a centrifugally driven buoyancy instability. In addition, INCA has observed very large scale injections of plasma into the dayside magnetosphere through which a large fraction of the dayside magnetosphere is filled with energetic plasma as shown in Figure 1.16. It is possible that these events are the result of Vasyliũnas-style reconnection on the nightside of the planet, causing plasmoids to be ejected into the magnetotail along with return planetward transport of a relatively large body of energised plasma (e.g. *Vasyliunas*, 1983; *Bunce et al.*, 2005).

Both of these types of event are likely to lead to rapid changes in the interior plasma pressure, and are expected to significantly affect pressure balance at the magnetopause boundary as a result. The orbit of Titan is a useful marker in Figures 1.15 and 1.16 (the outer dashed ring) as it orbits close to (and sometime outside of) the magnetopause boundary (e.g. *Bertucci et al.*, 2008). Hence, energetic plasma that extends beyond the orbit of Titan in the dayside magnetosphere is likely to have a profound effect on pressure balance at the magnetopause. The ENA events discussed here are regularly observed to extend beyond the orbit of Titan.

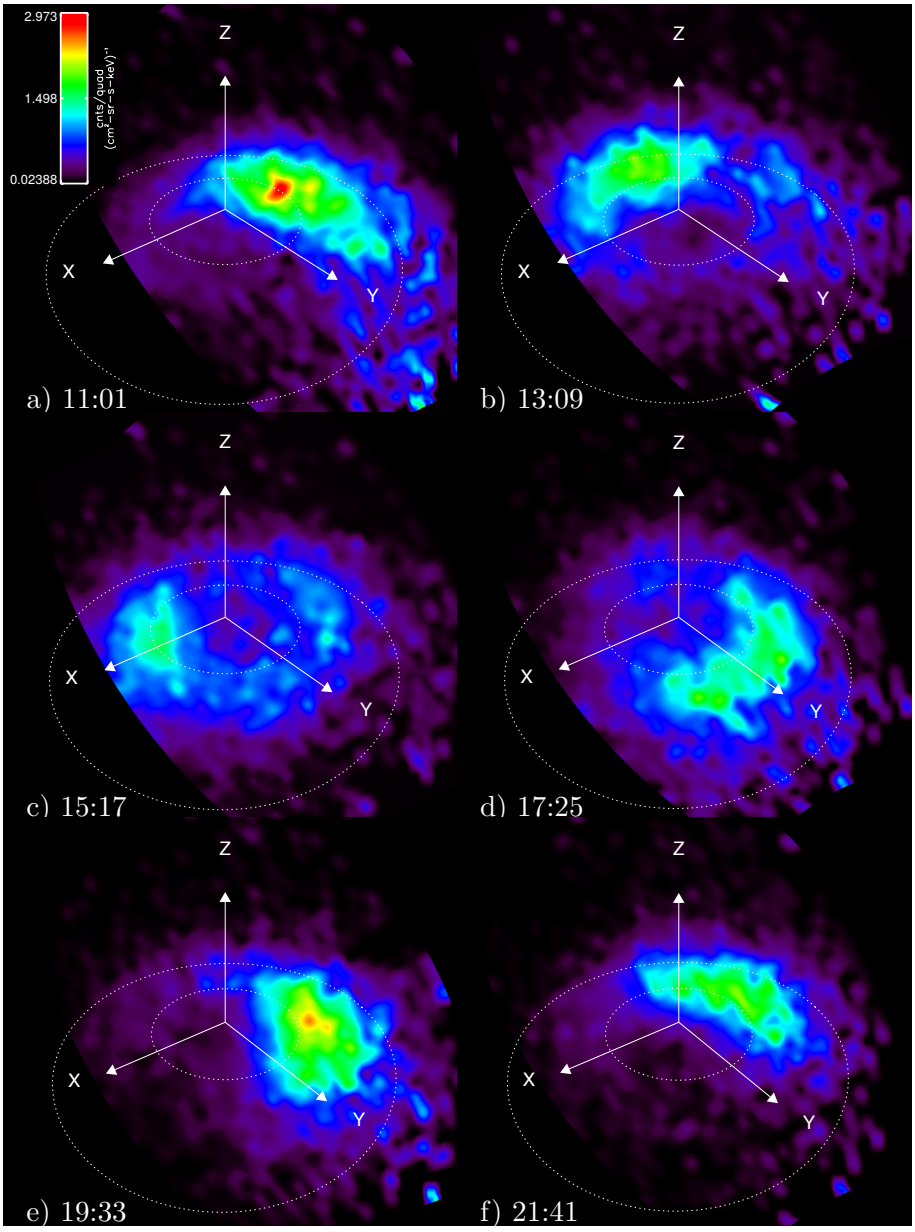

Figure 1.15. A sequence of ENA images of Saturn's ring current taken on 24 February 2007 by the Ion and Neutral Camera (INCA) showing the time evolution of a corotating 'bubble' of hot plasma over a full rotation of the planet. The ENA intensity is averaged over one hour, centered on the times stated in each panel. The Saturn Equatorial coordinate system (SZS) is indicated: Saturn is at the centre of this coordinate system with X pointing in the general direction of the Sun, Z aligned with the planet's axis of rotation and Y pointed towards the dusk side of the planet. The dashed lines show the orbits of Rhea ($\sim$8.7 R_S) and Titan ($\sim$20.2 R_S). The sharp edges seen in the first four panels on the dayside of the magnetosphere (positive X direction) are the edges of the INCA field of view. Credit: MIMI/APL.

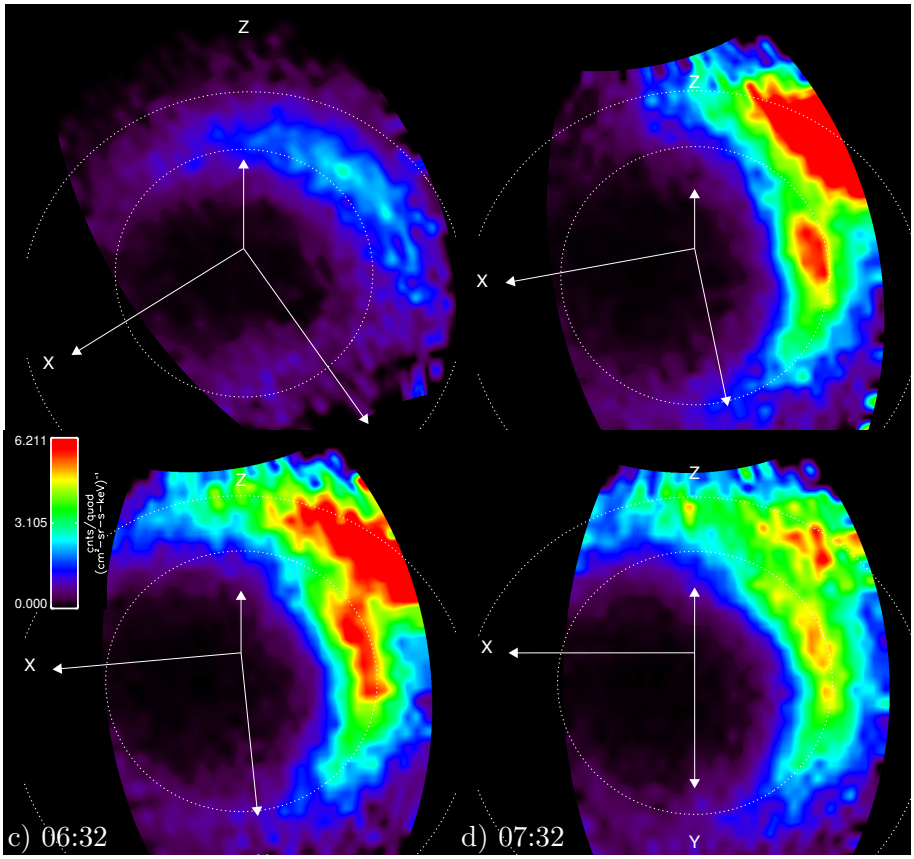

Figure 1.16. A sequence of ENA images of Saturn's magnetosphere taken by INCA, showing a large amount of energetic plasma flowing planetward from the magnetotail. a) ENA activity just prior to the arrival of the event. b) Just after the energetic plasma moves into the INCA field of view. c) Energetic plasma continues to move planetward, entering the dayside and filling much of the magnetosphere. d) Energetic plasma now spans the width of the INCA field of view. This event is much more intense than that shown in Figure 1.15 (note the difference in colour scale). The axes shown are in the SZS system. Credit: MIMI/APL.

At Saturn's magnetopause, the pressure associated with the suprathermal plasma is of the same order as the magnetic pressure and acts to inflate the magnetosphere, significantly increasing its size beyond what would be expected of the magnetic pressure alone. *Sergis et al.* (2007) found that the plasma sheet extends all the way out to the dayside magnetopause boundary and *Sergis et al.* (2009) found that the plasma β at Saturn for ions with energies greater than 3 keV varies between $\sim 10^{-2} - 10^{1}$ at radial distances concurrent with the magnetopause. The plasma beta is a dimensionless quantity. It is a convenient quantity to use when studying the dynamics that are taking place at the magnetopause (or, indeed, anywhere in the magnetosphere) since it describes which pressure source is dominant. β will be discussed in more in detail in Chapter 4. Most of the plasma pressure is contributed by energetic oxygen ions since they are relatively massive. After

protons, they are the most common ion species within Saturn's magnetosphere as they are constantly added to the system by the moons and the rings. As such, a short interaction by Cassini with a stream of water-group ions can cause a sharp increase in the measured plasma pressure, by an order of magnitude or more.

However, suprathermal plasma (particularly that composed of massive species) does not strictly obey the frozen-in condition in the way that thermal plasma does. These ions have very large gyroradii of the order of several planetary radii such that they cross many magnetic field lines during a single gyration. They are not constrained to follow a particular flux tube as even relatively small gradients in the magnetic field can cause them to drift significantly since the magnetic field varies significantly at the extremes of their gyration closest to and furthest away from the planet. In addition, they are able to pass straight through the magnetopause since their gyroradii are very large compared to the width of the magnetopause. *Berchem and Russell* (1982) found that Earth's magnetopause current layer typically has a width of between 400 km and 1000 km – small compared to the gyroradius of suprathermal water-group ions. Indeed, *Sergis et al.* (2013) detected 'islands' of water group ions within Saturn's magnetosheath, that then convect downtail with the solar wind. *Sergis et al.* (2013) even detected water group ions upstream of Saturn's bow shock. It is thus unclear what role water groups ions play on pressure balance at the magnetopause and what impact they have on the location of the magnetopause boundary. This will ultimately depend on whether they are part of organised structures, such as those detected using ENA imaging, and the fraction that tend to remain within the magnetosphere.

The magnetopause is the site at which energy, momentum and mass are transferred into the magnetosphere, ultimately from the Sun, but it may also be subject to internal drivers which likely complicate its geometry. One of the primary aims of this thesis is to accurately describe and better understand the effect of the solar wind and internal plasma processes on Saturn's magnetosphere, in terms of its extent and shape as defined by the magnetopause. This study has implications for other systems with significant quantities of internal plasma, such as Jupiter's magnetosphere for which there are limited data available.

1.4 Previous Empirical Studies of the Magnetopause

The Earth's magnetopause has been studied empirically ever since it was discovered in the early 1960s. The first empirical fit for the purposes of prediction was made by *Fairfield* (1971), who fitted a conic section to 474 crossings made by the *Imp 1-4* and *Explorer 33* and *Explorer 35* spacecraft. Variability in the solar wind dynamic pressure was not directly implemented into the fitting procedure, but *Fairfield* (1971) did note that this was the primary controlling factor behind orbit-to-orbit changes in the magnetopause location. *Fairfield* (1971) also noted that the orientation of the IMF affects the magnetopause location, shifting it earthward under southward IMF conditions, as found by *Aubry et al.* (1970). This is consistent with magnetic reconnection taking place along the dayside magnetopause boundary as described by *Dungey* (1961). The terrestrial dayside magnetic field points northwards (the magnetic and geographic poles are reversed) which means that magnetic reconnection is most efficient under conditions of southward IMF. When this is the case, magnetic flux is opened on the dayside of the planet most efficiently. Newly opened magnetic flux is then convected over the poles to the nightside of the planet due to the momentum of the solar wind to which it is now connected, eroding the magnetopause boundary.

A similar analysis was performed for Saturn's magnetopause by *Slavin et al.* (1983), who used magnetic field and particle data to identify crossings made by Pioneer 11, Voyager 1 and Voyager 2 during their flybys of the planet. Crossings separated by a time smaller than 10 hours were averaged together to remove crossings caused by boundary waves or multiple crossings resulting from spacecraft trajectories that graze the magnetopause surface. Such additional crossings could potentially lead to artificial weighting of the fit. *Slavin et al.* (1983) estimated the solar wind dynamic pressure for each crossing by assuming it is balanced by the interior magnetic pressure. So, from Equation 1.35, and using a Newtonian approximation to pressure balance in a supersonic flow (*Spreiter and Alksne*, 1970),

$$kD_P \cos^2 \Psi = \frac{B^2}{2\mu_0}, \tag{1.37}$$

where B is the magnetic field strength just inside the magnetopause boundary and Ψ is the angle between the flow direction and the normal to the magnetopause surface. The

dynamic pressure exerted on the magnetic field is reduced by a factor of k since the upstream solar wind is deflected around the magnetosphere, reducing the mass flux. For a highly supersonic, monatomic, ideal gas, $k = 0.88$ is appropriate (e.g. *Spreiter and Alksne*, 1970; *Walker and Russell*, 1995; *Petrinec and Russell*, 1995).

Slavin et al. (1983) used minimum variance analysis (MVA) to estimate the normal direction to the magnetopause surface (*Sonnerup and Cahill*, 1967) and, thus, calculate Ψ. Since magnetic fields are divergenceless, across an infinitesimally thin boundary the magnetic field is constant. Hence, if one assumes that the magnetopause is an infinitesimally thin interface, the direction in which the magnetic field varies by the least amount should coincide with the direction normal to the magnetopause surface. MVA is essentially a variant of principal component analysis, which is ultimately a technique used to perform dimensionality reduction by determining which linear combination of variables explains most of the variance in the data. It involves eigendecomposition of the data covariance matrix, the eigenvectors of which (the 'principal components') provide a linear mapping to the mean-subtracted data. By definition, the transformation does not change the directions of the eigenvectors so, under the above assumption, the eigenvector that explains the minimum amount of variance in the magnetic field coincides with the normal to the magnetopause. The eigenvectors are typically ordered by the amount of variance that each one describes. Hence, defined in this way, minimum variance analysis follows the same procedure but selects the last principal component only, i.e. the eigenvector that describes the least amount of variance. Mapped back onto the 'data manifold', this eigenvector points in the direction in which the magnetic field varies the least.

Using this technique, *Slavin et al.* (1983) were able to calculate Ψ assuming that the solar wind is flowing along the planet-Sun line. This is a reasonable assumption, but strictly speaking the orbital motion of the planet is expected to cause the incoming solar wind to be rotated by $\sim 1.4^\circ$ away from the planet-Sun line such that the solar wind is preferentially flowing into the morning side of the planet. This effect is likely to be negligible compared to other sources of uncertainty, such as the uncertainty in the dynamic pressure as a result of the pressure balance assumption. *Slavin et al.* (1983) accounted for fluctuations in the magnetopause position as a result of variability in the solar wind

dynamic pressure by scaling the magnetopause crossings to a fixed dynamic pressure,

$$r_{<D_P>} = r_{\mathrm{OBS}} \left(\frac{D_P}{<D_P>} \right)^{\frac{1}{\alpha}}, \tag{1.38}$$

where r_{OBS} and $r_{<D_P>}$ are observed and scaled distances from the planet to the magnetopause respectively, and $<D_P>$ is the dynamic pressure to which the crossings are scaled. α describes the 'compressibility' of the magnetosphere, its response to changes in the solar wind dynamic pressure. Smaller values of α indicate that the magnetosphere is more compressible or responsive to changes in D_P, whereas larger values of α indicate that the magnetosphere is more rigid or less responsive to changes in D_P. *Slavin et al.* (1983) normalised all of their crossings to the mean solar wind dynamic pressure assuming a dipolar pressure dependence on the magnetopause standoff distance, i.e. $\alpha = 6$. A three-parameter conic section was then fitted to the normalised crossings as done by *Slavin and Holzer* (1981) for the terrestrial planets.

Note that Equation 1.38 can also be applied to the Cartesian coordinates of the magnetopause crossing. Scaling crossings in this way helps to remove some of the scatter in the boundary crossings as a result of fluctuations in the solar wind dynamic pressure and is equivalent to collapsing the crossings onto a surface of constant pressure. This is a good assumption only if the compressibility of the magnetosphere is well known, and if the magnetopause scales self-similarly with dynamic pressure. Neither of these assumptions are well-founded, but this is nonetheless an improvement over previous studies in which the magnetopause position was essentially assumed to be independent of solar wind dynamic pressure by fitting a model to the actual crossing locations (e.g. *Aubry et al.*, 1970).

A new empirical magnetopause model was proposed by *Shue et al.* (1997) to describe the terrestrial magnetopause, which improves significantly upon the form used by previous authors. The *Shue et al.* (1997) empirical shape model contains a built-in dependence on the solar wind dynamic pressure and negates the need to scale magnetopause crossings as done by *Slavin et al.* (1983). The functional form of this model is,

$$r = r_0 \left(\frac{2}{1 + \cos\theta} \right)^K, \tag{1.39}$$

$$r_0 = a_1 D_P^{-a_2}, \tag{1.40}$$

$$K = a_3 + a_4 D_P, \tag{1.41}$$

where r is the distance from the planet centre to the point on the magnetopause surface described by the angle θ, the angle between the position vector of this point and the planet-Sun line as illustrated in Figure 1.17. The surface is parameterised in terms of the standoff distance, r_0, which controls the size of the magnetosphere, and the 'flaring' parameter, K, which controls the downstream shape as shown in Figure 1.18. Coefficients a_{1-4} control, respectively, 1) the size scale of the magnetosphere; 2) its response to changes in solar wind dynamic pressure; 3) the nominal downstream flaring of the magnetosphere; and finally, 4) the effect of dynamic pressure on magnetopause flaring. One of the advantages of the *Shue et al.* (1997) empirical form is that these coefficients are more physically meaningful than those of the conic section used in previous studies. It is also very flexible, in that it can model both open and closed magnetospheric configurations depending on the value of K. If $K = 0.5$, the magnetosphere is open with a constant tail radius. Above this value, the model shape expands with distance from the planet, and below this value the magnetosphere is closed as shown in Figure 1.18. As well as the solar wind dynamic pressure, D_P, *Shue et al.* (1997) also presented forms of the the magnetospheric standoff distance and the flaring parameter that depend on the orientation of the IMF, consistent with the observations of *Aubry et al.* (1970) and *Fairfield* (1971).

This model was applied to Saturn's magnetopause by *Arridge et al.* (2006) using observations from the first six orbits of the Cassini spacecraft, along with the flybys of Voyager 1 and Voyager 2. Consecutive crossings within $1\,\mathrm{R_S}$ of each other were averaged together to avoid the fit becoming biassed to regions more favourable for boundary wave formation, as was done by *Slavin et al.* (1983). A spatial averaging was used in order to account for the different spacecraft velocities. The coefficients a_i were determined using an interior-reflective Newton-Raphson fitting routine applied to the 26 averaged crossings that remained. The IMF dependency was omitted because it could not be measured in the

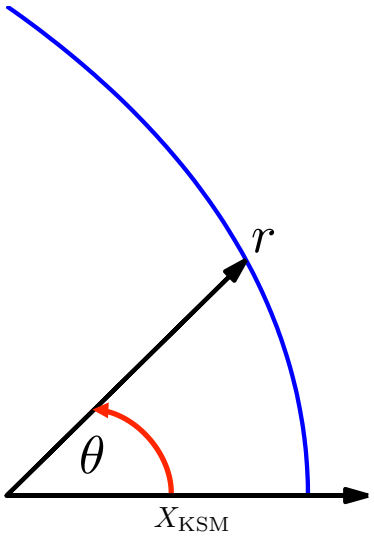

Figure 1.17. Illustration r and θ in the *Shue et al.* (1997) magnetopause model, the blue line shows the magnetopause.

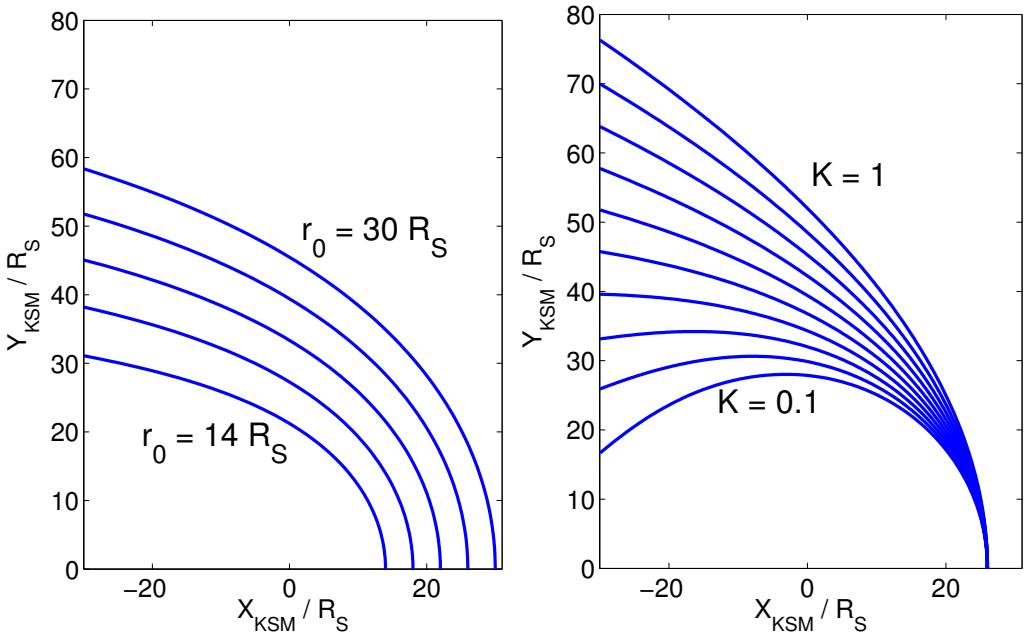

(a) Varying r_0 (b) Varing K

Figure 1.18. Demonstrates how varying the a) the standoff distance, r_0, and b) flaring parameter, K, changes the magnetopause geometry. r_0 is varied between $14\,\mathrm{R_S}$ (innermost line) and $32\,\mathrm{R_S}$ (outermost line), and K is varied between 0.1 (innermost line) and 1.0 (outermost line) in this figure. $K = 0.5$ is the constant tail radius solution, above (below) this, the magnetosphere is 'open' ('closed').

absence of a dedicated upstream monitor close to Saturn. More recently, MHD simulations by *Jia et al.* (2012) have found that the magnetopause location is relatively insensitive to changes in the IMF when compared to the influence of the solar wind dynamic pressure.

However, since magnetic reconnection occurs adjacent to the magnetopause boundary, it is the orientation of the magnetosheath magnetic field rather than the upstream IMF orientation that should be important for magnetic reconnection considerations. The magnetosheath field is highly variable in general (see the discussion in Chapter 2) so may depart significantly from the upstream IMF orientation. In principle, the magnetosheath magnetic field orientation is known for every magnetopause crossing making such an assessment possible, and this should be the focus of a future study. However, the amount by which the magnetopause has been eroded depends on the length of time over which magnetic field conditions favourable for magnetic reconnection have persisted, which may be difficult to ascertain. One way of measuring this may be to limit the study to inbound portions of the spacecraft trajectory where the spacecraft first crosses through the magnetosheath and then crosses the magnetopause since the conditions within the magnetosheath can then be measured over an extended period of time prior to the magnetopause crossing.

Arridge et al. (2006) made a more accurate assessment of the solar wind dynamic pressure by introducing an additional term to the pressure balance equation. In addition to the solar wind dynamic pressure, the high-density magnetosheath plasma imparts an additional 'static' pressure to the magnetopause surface. This acts to confine the downtail magnetosphere and is required since the dynamic pressure term vanishes as $\Psi \rightarrow 90°$. Without this pressure term, the magnetopause would extend indefinitely without closure. As such, Equation 1.37 is modified in order to include this term,

$$D_P \cos^2 \Psi + P_0 = \frac{B^2}{2\mu_0}, \tag{1.42}$$

where P_0 is the magnetosheath static pressure. This was further modified by *Petrinec and Russell* (1997) to,

$$kD_P \cos^2 \Psi + P_0 \sin^2 \Psi = \frac{B^2}{2\mu_0}, \tag{1.43}$$

who found that a constant static pressure introduces imaginary flow velocities close to the 'nose' of the magnetopause for a supersonic flow. From earlier aerodynamic studies considering supersonic flow about a body, it was found that multiplying the static pressure by $\sin^2 \Psi$ removes this problem by forcing the static pressure term to vanish in the vicinity of the sub-solar point. From Equation 1.43, it is clear that the dynamic pressure dominates close to the sub-solar point whereas the static pressure dominates in the regions of the magnetopause far downtail. For Saturn, *Arridge et al.* (2006) set P_0 to a constant pressure of 10^{-4} nPa based on average solar wind values determined using the results of gas dynamic modelling around Saturn's bow shock by *Slavin et al.* (1985).

Also, rather than using minimum variance analysis to calculate Ψ as was done by *Slavin et al.* (1983), *Arridge et al.* (2006) calculated the geometrical normal to the magnetopause model surface at the location of each magnetopause crossing. Since the analytical form of the surface is known (Equations 1.39–1.41) the normal to this surface at any given point described by polar coordinates (r, θ, ϕ) can be calculated as,

$$\mathbf{n} = \frac{\partial \mathbf{r}}{\partial \theta} \times \frac{\partial \mathbf{r}}{\partial \phi}, \tag{1.44}$$

where $\mathbf{r}$ is the radial vector from the planet to the point (r, θ, ϕ). The components of $\mathbf{r}$ are given by,

$$r_x = r \cos \theta, \tag{1.45}$$

$$r_y = r \sin \theta \cos \phi, \tag{1.46}$$

$$r_z = r \sin \theta \sin \phi, \tag{1.47}$$

where r is given by Equation 1.39. Hence, as presented by *Arridge et al.* (2006), one can calculate the components of the normal to the magnetopause surface using Equation 1.44

and the following relations,

$$\left.\frac{\partial r}{\partial \theta}\right|_x = r\sin\theta\left(\frac{K\cos\theta}{1+\cos\theta}-1\right), \tag{1.48}$$

$$\left.\frac{\partial r}{\partial \theta}\right|_y = r\cos\phi\left(\cos\theta+\frac{K\sin^2\theta}{1+\cos\theta}\right), \tag{1.49}$$

$$\left.\frac{\partial r}{\partial \theta}\right|_z = r\sin\phi\left(\cos\theta+\frac{K\sin^2\theta}{1+\cos\theta}\right), \tag{1.50}$$

$$\frac{\partial r}{\partial \phi} = r\sin\theta(0,-\sin\phi,\cos\phi). \tag{1.51}$$

There are several advantages to using this method over MVA. First of all, it makes the analysis self-consistent with the magnetopause surface assumed. Secondly, it is less susceptible to transient phenomena that could affect the true normal to the magnetopause surface, such as boundary waves due to Kelvin-Helmholtz instabilities (*Masters et al.*, 2012b). Events like these can drastically change the normal to the surface and can even cause the normal to point back towards the planet, violating the pressure balance equations above. The geometrical normal is not susceptible to these events and is relatively stable. It does depend on the coefficients a_i that define the surface though, which means that the normal to the surface changes as the fitting routine iterates. Hence, Ψ and the dynamic pressure also change on an iteration-by-iteration basis and need to be continually recalculated. The surface defined by the current set of coefficients must be fitted through the precise location of the magnetopause crossing, solving for the dynamic pressure that allows this. *Arridge et al.* (2006) used a Newton-Raphson root-finding method in order to achieve this. The normal to the surface at this point is then calculated and, from that, Ψ and D_P are calculated. As a result, fitting using this method is more computationally intensive than using MVA, but this is outweighed by the third and most compelling reason to use this method.

Without automating the procedure, performing MVA on a large set of magnetopause crossings is unfeasible. The largest barrier to complete automation is the accurate identification of the precise transition across the magnetopause current layer, which, thus far, has only been achieved by analysing the data manually, and even then can still be challenging. As such, MVA would have to be performed individually on each magnetopause crossing, which would be very time consuming for large datasets. Finally, MVA is only accurate for high magnetic shear crossings where a clear rotation in the magnetic field across the boundary can be seen, but *Arridge et al.* (2006) found that low-shear crossings were prevalent at Saturn.

Upon fitting the surface to their set of magnetopause crossings, *Arridge et al.* (2006) found a magnetospheric compressibility very different to that expected of a vacuum dipole. For a vacuum dipole, the exponent of Equation 1.40, a_2, is expected to be -1/6 whereas a value of $-1/4.3 \pm 0.4$ was found. This implies that the magnetosphere is more compressible or sensitive to changes in the dynamic pressure than the Earth's magnetosphere for example, where a value of -1/6.6 had been previously found by *Shue et al.* (1997). *Slavin et al.* (1983) previously found a rather dipolar compressibility of -1/6.1 for Saturn, though this may have been affected by assuming a dipolar compressibility when normalising the crossings to the average solar wind dynamic pressure. The magnetospheric compressibility is related to stress balance within the magnetosphere and is likely related to the influence of plasma on the global dynamics that take place there. It may also be linked to the presence of a magnetodisc and the currents that flow through it, which themselves generate a magnetic field. This likely changes the scaling of the total magnetospheric magnetic field from a dipolar scaling, contributing to the compressibility determined by *Arridge et al.* (2006). *Bunce et al.* (2007) found that the compressibility changes with system size but is relatively stable over a wide range of magnetospheric sizes. *Arridge et al.* (2006) also found that $a_4 = -1.5 \pm 0.3$. This indicates that as the dynamic pressure increases, the magnetopause becomes less flared and, hence, more streamlined. On the other hand, *Shue et al.* (1997) found that a_4 was small but positive for the terrestrial magnetosphere indicating that more open magnetic flux is presumably added to the magnetotail under high dynamic pressure conditions.

Achilleos et al. (2008) used the empirical magnetopause model presented by *Arridge et al.* (2006) to investigate the long-term statistical behaviour of Saturn's magnetopause.

They used 430 days of Cassini observations in addition to the Voyager magnetopause crossings used previously. *Achilleos et al.* (2008) found that the distribution of magnetopause standoff distances extrapolated from the magnetopause crossings observed during this time followed a 'bimodal' distribution (the sum of two normal distributions) with peaks at $\sim$22 R_S and $\sim$27 R_S. A similar result was obtained earlier by *Joy et al.* (2002) for the Jovian magnetosphere with modal distances of $\sim$63 R_J (Jovian radii) and $\sim$92 R_J. Both authors also analysed solar wind data in order to identify a possible external cause for this behaviour. *Joy et al.* (2002) used observations made by all of the spacecraft to venture upstream of Jupiter prior to the arrival of Cassini, with the exception of *Galileo* which suffered from data downlink constraints as a result of the failure of its high-gain antenna. They found some evidence of a bimodal solar wind dynamic pressure distribution, but also found that the dynamic pressure would need to increase by a factor of 7.8 between the 'quiet' and 'disturbed' dynamic pressure configurations in order to explain the observed distribution of magnetopause stand-off distances. However, an increase by a factor of just 4.3 was observed implying an additional source of pressure variability is necessary. Compressions are likely to be accompanied by significant changes in the combination of internal pressure sources.

Similarly, *Achilleos et al.* (2008) used measurements taken by the Cassini Plasma Spectrometer (CAPS) during the time that the spacecraft was upstream of Saturn on its way to rendezvous with the planet, in addition to measurements made by Pioneer 11. They compared the probability density function (PDF) of the magnetopause standoff distance to that of the solar wind dynamic pressure and found coincident peaks corresponding to the expanded magnetosphere. However, there was no peak corresponding to the compressed magnetospheric configuration with the pressure PDF tending towards a tailed distribution where a second peak was expected. This led those authors to conclude that an internal mechanism was likely to be responsible, leaving two possible candidates – the rotational anomaly and the Vasyliũnas cycle as discussed in Section 1.3.1. *Clarke et al.* (2006, 2010) observed that the magnetopause oscillates with an amplitude of $\sim$1.2 R_S as a result of the rotational anomaly. This meant that the rotational anomaly could be eliminated as the primary cause since an amplitude of $\sim$5 R_S would be required to explain the observations, though the rotational anomaly should still be present as 'scatter' in the data. It follows then that global reconfigurations of the magnetosphere as a result of the Vasyliũnas cycle

are the most promising explanation for the observed bimodailty.

Kanani et al. (2010) built upon the work of *Arridge et al.* (2006) by improving the treatment of pressure balance, modifying the canonical pressure balance equation to include the internal plasma pressure in addition to the magnetic pressure. They estimated this quantity using measurements taken by instruments on board Cassini: the Electron Spectrometer (CAPS-ELS), and the Magnetospheric Imaging Instrument (MIMI). These instruments are described in detail in Chapter 2. Specifically, *Kanani et al.* (2010) included the contribution from the suprathermal plasma population with energies in the range 27-4000 keV and thermal electrons with energies betwen 0.8 eV-27 keV. They also accounted for the pressure associated with low-energy protons by assuming that their number density is 20% of the low-energy electron density and, hence, that thermal protons have a pressure contribution equivalent to 20% of the electron pressure assuming equal temperatures. However, the pressure associated with the water-group ions within the thermal energy range was not included. In general, the pressure balance equation including the total plasma pressure can be written as,

$$kD_P \cos^2 \Psi + P_0 \sin^2 \Psi = \frac{B^2}{2\mu_0}(1+\beta), \tag{1.52}$$

where β is the ratio of total plasma pressure to the magnetic pressure adjacent to the magnetopause.

Kanani et al. (2010) modified the form of the static pressure further in response to finding that the dynamic pressure from Equation 1.43 was inconsistent with the results of MHD simulations. It was found to be consistently smaller than that predicted by *Hansen et al.* (2005), and arbitrarily increasing the value of P_0 resulted in negative dynamic pressures for some observations. *Kanani et al.* (2010) solved this by expressing P_0 in terms of D_P using the ideal gas law,

$$P_0 = nk_{\mathrm{B}}T, \tag{1.53}$$

where n and T are the number density and temperature of the solar wind and k_{B} is the Boltzmann constant. Equation 1.36 can then be solved for n and substituted into

Equation 1.53, which can, in turn, be substituted into Equation 1.52 to yield,

$$kD_P \cos^2\Psi + \frac{k_B T_{SW}}{1.16 m_p u_{SW}^2} D_P \sin^2\Psi = \frac{B^2}{2\mu_0}(1+\beta). \tag{1.54}$$

Kanani et al. (2010) also used many more data than previous studies, comprising approximately a year and a half of Cassini observations. These observations were averaged spatially in a similar way to *Arridge et al.* (2006). Fitting the empirical model described by Equations 1.39–1.41 to these observations yielded results mostly in agreement with those of *Arridge et al.* (2006) within the estimated fitting uncertainties. The only discrepancy between the results of *Kanani et al.* (2010) with those of *Arridge et al.* (2006) was in their determination of $a_4 = 0.4 \pm 0.5$. Instead of a magnetosphere that becomes less flared as the dynamic pressure increases, *Kanani et al.* (2010) found a magnetosphere that flares more with increasing dynamic pressure, similar to the behaviour found for Earth's magnetosphere by *Shue et al.* (1997). It should be noted though that the uncertainty in this coefficient means that the downstream shape of the magnetopause may be insensitive to changes in dynamic pressure. Also of note is that *Kanani et al.* (2010) found that Saturn's magnetosphere is substantially less compressible than was found by *Arridge et al.* (2006), but this difference is not statistically significant due to the large uncertainties associated with the former study. *Kanani et al.* (2010) found a compressibility of $1/(5.0 \pm 0.8)$, also indicating a magnetosphere significantly more compressible than a vacuum dipole.

The empirical studies mentioned thus far have assumed that the magnetopause is rotationally symmetrical about the planet-Sun line (axisymmetric). A later study by *Lin et al.* (2010) found that this assumption is appropriate for Earth's magnetosphere in most respects. *Lin et al.* (2010) resolved significant cusp-indentation regions but were unable to resolve a significant dawn-dusk asymmetry or a persistent north-south asymmetry at equinox. However, at Saturn, centrifugal confinement of cold plasma and the resulting inflation of the low-latitude magnetosphere due to enhanced plasma pressure causes the obstacle presented to the solar wind to be disc-like in nature. The solar wind flows more easily over the polar regions of a disc-like magnetosphere and thus some degree of 'polar flattening' of the magnetopause is expected. This is explored in Chapter 3 and built upon in the chapters that follow. The impact of variability in the interior thermal and suprathermal plasma pressures has also been neglected thus far, and is explored in Chapter 4.

In addition, *Lin et al.* (2010) found that a significant north-south asymmetry was introduced during the passage of the planet from equinox towards solstice in terms of the location of the cusp-indentation regions as well as the mean location of the high-latitude magnetopause. This is because the incoming solar wind flow direction is orthogonal to the magnetic dipole at equinox, but away from equinox a significant tilt is introduced between these vectors. Such behaviour was also predicted to occur for Saturn's magnetopause by *Maurice et al.* (1996) using a semi-empirical model of the Kronian magnetic field assuming a constant solar wind pressure, and by *Hansen et al.* (2005) using global MHD simulations. Thus far, observational studies of Saturn's magnetopause have been restricted to the low-latitude regions making an empirical study of this effect impossible. In addition, previous studies have been confined to one side of the planet such that other asymmetries in the geometry of Saturn's magnetopause have not yet been explored. Within this thesis, I aim to address and explore these unresolved issues in detail in Chapter 5.

This page was intentionally left blank

Chapter 2

The Cassini-Huygens Mission to Saturn

Any sufficiently advanced technology is indistinguishable from magic.

Arthur C. Clarke

For millennia Saturn has been the subject of human study and fascination. The earliest records began over two thousand years ago with the ancient Babylonians, who recorded observations and predictions of planetary phenomena on clay tablets (*Sachs*, 1974). Centuries later, the planets were studied by the ancient Greeks and Romans, and Saturn became well established into their belief systems as *Kronos* and *Saturnus* respectively. Around two thousand years later, the invention of the telescope revolutionised our knowledge of Saturn, providing the ability to view the planet in greater detail than ever before. Galileo was baffled by the appearance of large protrusions to either side of the planet that periodically disappeared (Figure 2.1a). Later, Christiaan Huygens was able to resolve these into a ring using a more powerful telescope (Figure 2.1b), and in the process discovered *Titan*, the largest moon in the Kronian system. These observations were fur-

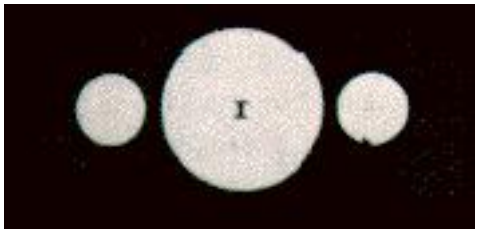

(a) Sketch by Galileo

(b) Sketch by Huygens

Figure 2.1. Early sketches of Saturn published in Huygens' *Systema Saturnium*, 1659.

ther refined by Giovanni Cassini, who observed a gap within the rings, now known as the *Cassini Division*, which indicated that the ring discovered by Huygens was not a single, solid ring, but is composed of many rings. From these very early telescopic observations, ground-based observations have continued to improve but the advent of the space age opened up a whole new realm of possibilities, allowing detailed measurements to be made from directly within Saturn's space environment.

Saturn has been visited by four spacecraft to date. The first of these was Pioneer 11 in 1979, followed by Voyager 1 in 1980 and Voyager 2 shortly after in 1981. All three of these spacecraft made flybys of the planet and provided snapshots of the system spaced several years apart. *Cassini-Huygens* was the first spacecraft to be captured into a stable orbit around Saturn in July 2004, and has provided sustained, long-term measurements ever since. Already one of the most successful planetary missions in history, it is clear that Cassini still has much to contribute to our understanding of Saturn and its environment, and this is epitomised by the exciting 'Grand Finale' end-of-mission sequence of orbits scheduled for 2017. The rest of this chapter will introduce the Cassini orbiter and will discuss the instrumentation on board which has been essential to this thesis.

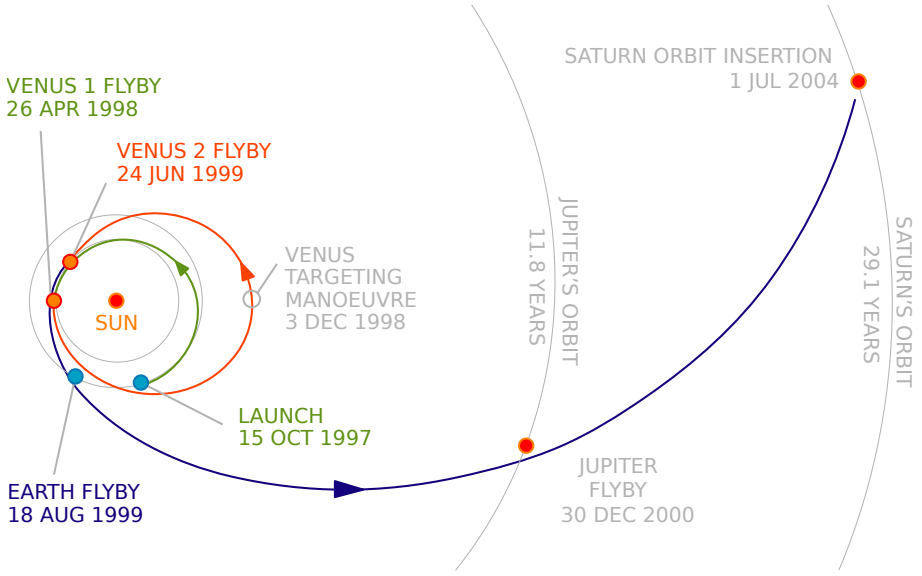

Figure 2.2. Cassini interplanetary trajectory. Accessed at `http://en.academic.ru/pictures/enwiki/67/Cassini_interplanet_trajectory.svg` on 19 July 2015.

2.1 The Cassini Orbiter

On October 15, 1997, Cassini-Huygens was launched from Cape Canaveral Air Force Station on a *Titan IV* rocket. This was the beginning of Cassini's seven year journey to Saturn shown in Figure 2.2, including two gravity assists from Venus, one from Earth and a final assist from Jupiter in order to reach the orbital distance of Saturn at approximately 9.5 AU. The *Huygens* probe was released on 25 December 2005 and entered Titan's atmosphere on 14 January 2005, and Cassini completed its original four-year mission after arriving at the planet close to northern winter solstice. This was followed by a two-year extended 'Equinox' mission, whereby the spacecraft sampled Saturn's environment during the planet's spring equinox. Cassini continues to surpass all expectations and is now nearing the end of its second extended mission termed 'Solstice', during which the spacecraft will sample Saturn's environment close to northern summer solstice. Cassini will have operated at Saturn for almost half of a Kronian year by the mission's end in 2017. The Cassini orbits used for each part of this thesis are discussed in their respective chapters, and Figures 3.1 and 4.1 show the spatial sampling of the spacecraft during the periods of time in which the measurements used within this thesis were made.

Dwindling propellant supplies have proven to be the ultimate limiting factor on the

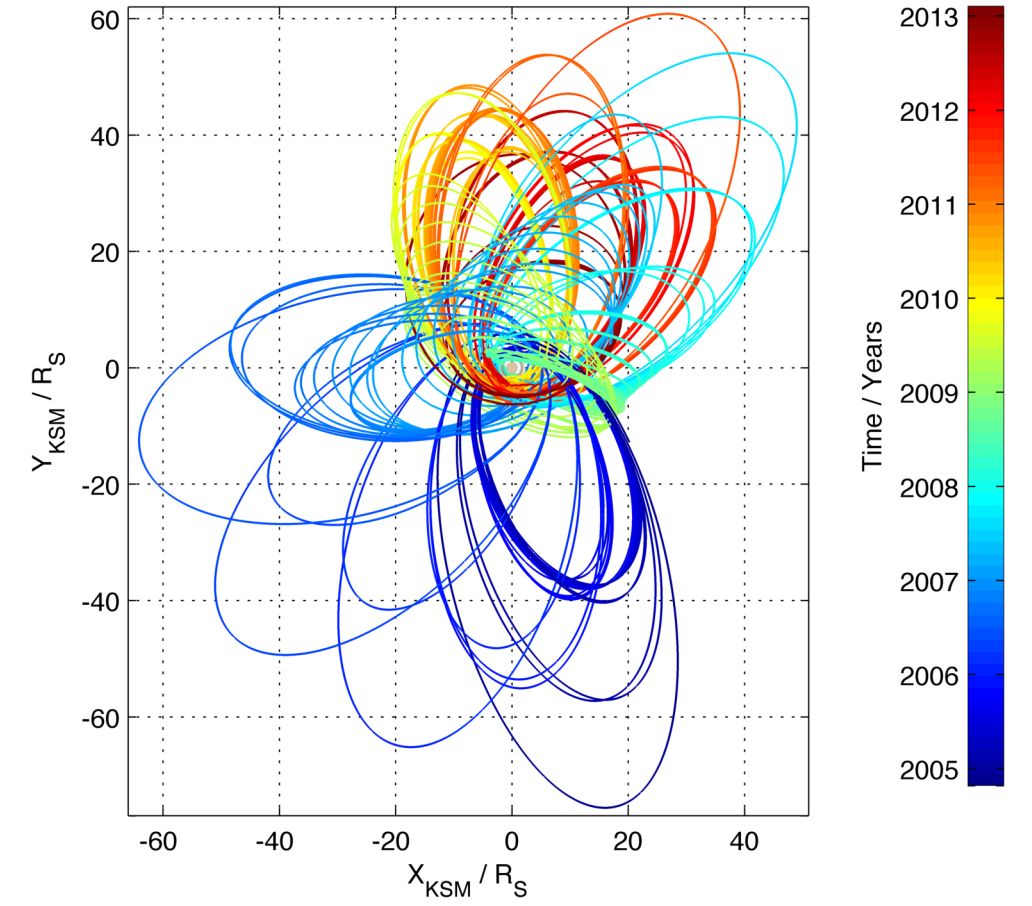

(a)

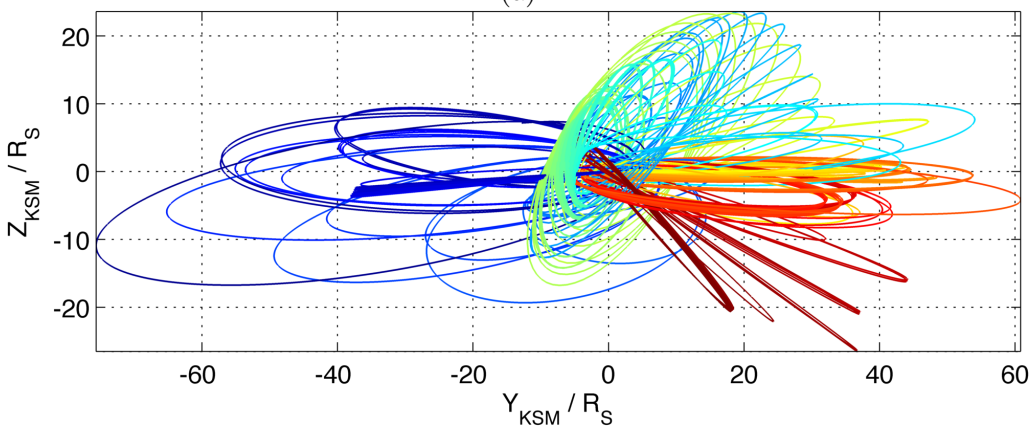

(b)

Figure 2.3. The trajectory of Cassini between SOI and early 2013, the period over which data has been used within this thesis.

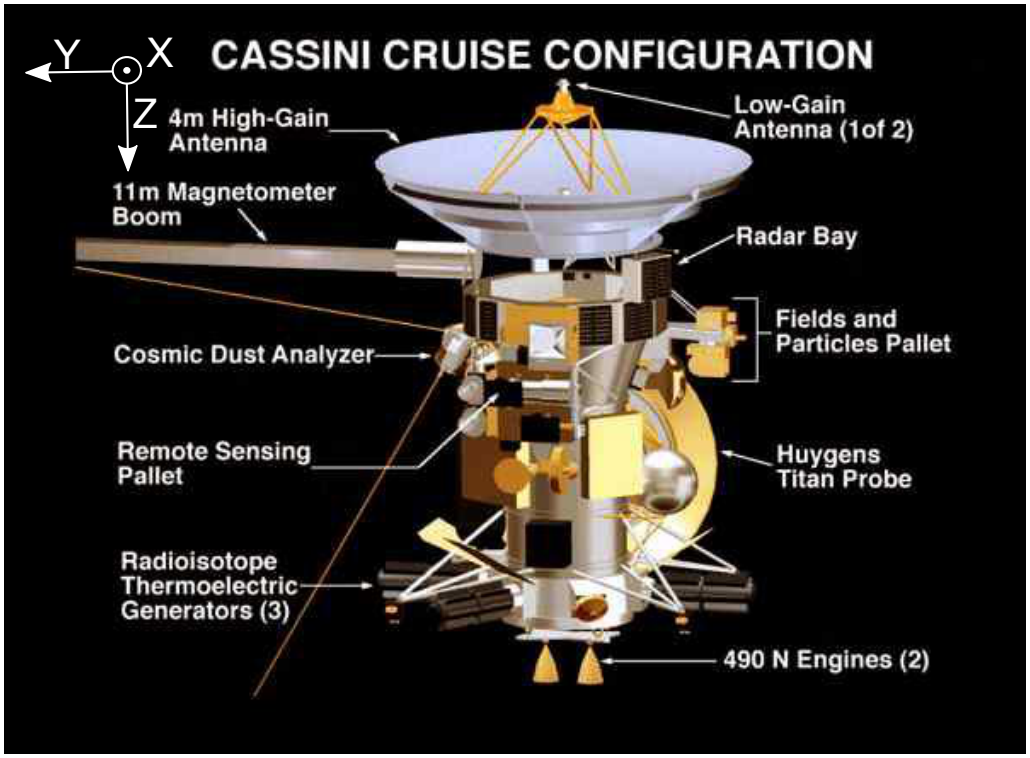

Figure 2.4. Schematic of Cassini including the spacecraft coordinate system. Accessed at `http://en.academic.ru/pictures/enwiki/67/Cassini_interplanet_trajectory.svg` on 19 July 2015.

spacecraft's life span. Without sufficient propellant, the spacecraft's end of life cannot be controlled and that is a problem because there is a remote possibility that, if an impact with one of the moons occurred, any life forms carried with the spacecraft from Earth could potentially contaminate that environment. For this reason, the spacecraft will be guided into a series of 22 decaying polar orbits known as the 'proximal' orbits, which will place the spacecraft's periapsis between the planet and the rings. This will allow exquisite mapping of the planet's magnetic and gravitational fields, in addition to high-resolution optical remote sensing of the rings and the planet. This option also has a relatively quick execution time and a relatively small impulse requirement in order to perform the manoeuvre, with a Δv requirement of $5 - 30\,\mathrm{m/s}$.

Attitude stabilisation is of the utmost importance for all spacecraft in order to, for example, facilitate communication with Earth and take images of fixed targets with long exposure times without 'smearing' the image across the relevant sensor. The Cassini orbiter is a three-axis-stabilised spacecraft – reaction wheels are mounted to three orthogonal spacecraft axes and are used to very accurately control the attitude of the spacecraft by

transferring angular momentum between themselves and the spacecraft chassis. Such a configuration is ideal for remote observations using 'point-and-stare' instruments, but compromises in situ field and particle observations for which a spinning spacecraft is preferable in order to calibrate magnetometers and observe particle fluxes from many directions (both of which will be discussed further in the following sections). In its original incarnation, Cassini was intended to be a spin-stabilised spacecraft with a de-spun scan platform from which optical instruments would operate, but this plan was changed due to budgetary constraints.

Cassini carries a payload of 12 instruments in total. These are powered by three radioisotope thermoelectric generators (RTGs), which generate heat through the radioactive decay of Pu-238, which is then converted into electricity using 572 thermocouples within each RTG. RTGs provide a stable DC power supply over long time periods due to the 87.7-year half-life of Pu-238 and are the power source of choice for spacecraft missions in the outer solar system where solar panels are unsuitable. Communications with Earth are achieved using the high-gain antenna and are relayed to the Space Flight Operations Facility at JPL via NASA's Deep Space Network (DSN). The DSN consists of three facilities located in California, Spain and Australia which are separated by approximately 120° longitude such that any spacecraft should be able to make contact with at least one of these facilities at any time. Commands and data are encoded into radio signals which are then sent back and forth between the spacecraft and the relevant operations facility via the DSN. Scientific data collected by Cassini is buffered onto solid state recorders for later transmission back to Earth such that the spacecraft is not limited by instantaneous data transfer rates. In the remainder of this chapter, the instruments used to collect the data used in this thesis will be discussed in more detail.

2.2 Fluxgate Magnetometer

Magnetic fields are fundamental to space plasma physics as, to a large extent, they dictate the flow of plasma due to the Lorentz force they impose upon charged particles as discussed in Chapter 1. Clearly then, magnetometers are essential in order to understand the complex interactions between the magnetic fields and plasma populations of the solar wind and those originating in the vicinity of the planets. Magnetometers are incredibly

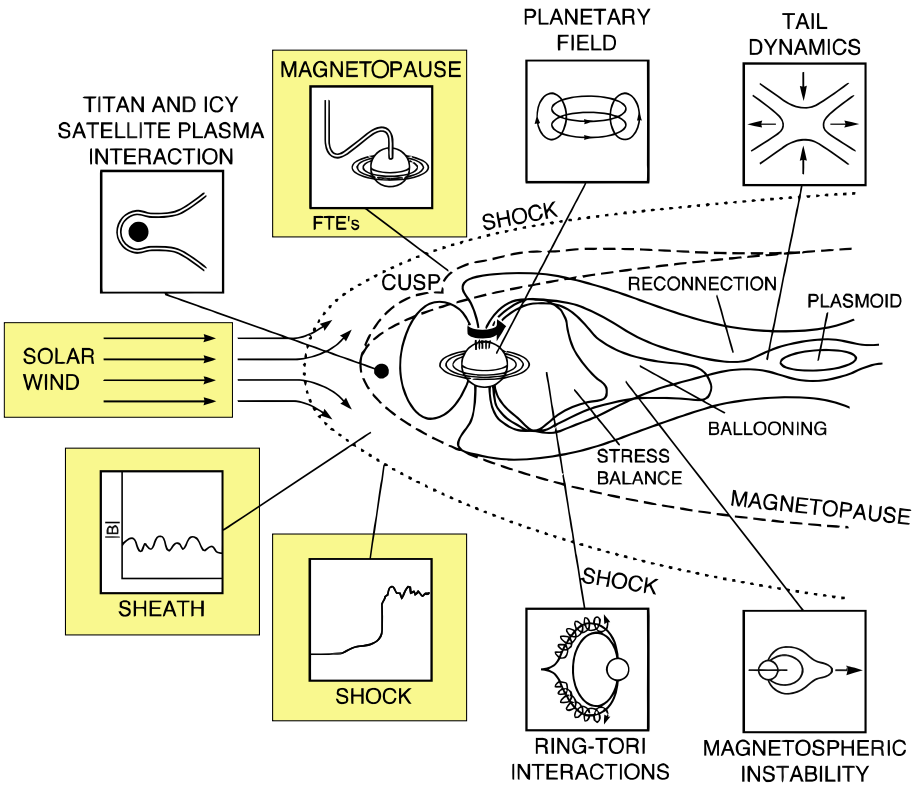

Figure 2.5. Summary of the objectives of the Cassini magnetic field investigation. Modified from *Dougherty et al.* (2004) to highlight the parts of the investigation to which this thesis contributes.

versatile instruments and have been responsible for a number of significant discoveries in this field, including the first detection of Earth's bow shock (*Holzer et al.*, 1966) and magnetopause (*Cahill and Amazeen*, 1963), the subsurface oceans of Galilean moons (e.g. *Khurana et al.*, 1998; *Kivelson et al.*, 2000; *Zimmer et al.*, 2000) and Enceladus' plumes (*Dougherty et al.*, 2006), among many others. They are incredibly versatile instruments as evidenced by the diverse range of phenomena that can be studied using magnetic data – these characterise the key scientific goals of the Cassini magnetic field investigation as illustrated in Figure 2.5, half of which are contributed to by this thesis.

The fluxgate magnetometer (FGM) is used to measure the strength and direction of the ambient magnetic field. A single fluxgate sensor is capable of measuring the magnetic field strength along the axis of its sensor coil, so Cassini's fluxgate magnetometer consists of three such sensors positioned orthogonally in order to measure the three-dimensional magnetic field vector (Cassini's FGM is shown in Figure 2.6). Each sensor consists of a highly magnetically susceptible core surrounded by a drive coil or solenoid, which is then

Figure 2.6. The fluxgate magnetometer with its cover off, alongside its electronics board. One of the three fluxgate sensors is visible as a dark disc-like object mounted onto the side of the white glass ceramic block that makes up the body of the FGM. This material was chosen because it has a low thermal expansion coefficient, which minimises misalignment of the individual sensors as a result of thermal fluctuations. From *Dougherty et al.* (2004).

surrounded by a sensor coil as shown in Figure 2.7. An alternating current flows through the solenoid which generates a magnetic field and magnetises the core until it becomes saturated. As shown in Figure 2.7, it is useful to consider the two halves of the FGM separately. The presence of an external magnetic field along the axis of the sensor causes one half of the core to become saturated before the other half. This causes a net change in magnetic flux passing through the sensor coil since the magnetic field generated by both halves of the core do not cancel exactly as they do in the case where there is no external magnetic field. In the presence of an external magnetic field, a voltage is induced in the sensing coil in accordance with Faraday's law. This voltage can be measured and is proportional to the external field after correcting for alignment errors.

The drive coil of Cassini's FGM is driven by a crystal-controlled 15.625 kHz square wave which drives the core into saturation in a stable and predictable, continually repeat-

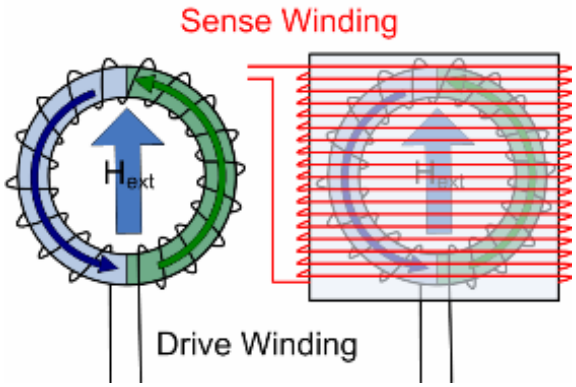

Figure 2.7. Schematic of a fluxgate magnetometer. The drive coil is shown in black and the sensor coil is shown in red and the core is represented by the blue and green ring. It is convenient to separate the core into two halves along the axis of the sensing coil since, in the presence of an external field along this axis, both halves generate a field along this axis but in opposite directions. Accessed at `http://www3.imperial.ac.uk/spat/research/areas/space_magnetometer_laboratory/spaceinstrumentationresearch/magnetometers/fluxgatemagnetometers/howafluxgateworks` on 20 July 2015.

ing cycle (*Dougherty et al.*, 2004). Furthermore, it is situated half way along the 11 m magnetometer boom (oriented along the +Y direction in spacecraft coordinates) in order to reduce contamination from magnetic fields generated by the spacecraft electronics. At the end of the boom is the vector helium magnetometer, which has not been used in this thesis. Cassini is capable of measuring the background magnetic field with a resolution of approximately one part in ten thousand using the FGM, but the background field strength varies by a few orders of magnitude depending primarily on the proximity of the spacecraft to Saturn. As such, Cassini's FGM can be operated within one of four ranges by changing the output amplification: $\pm 40\,\mathrm{nT}$, $\pm 400\,\mathrm{nT}$, $\pm 10,000\,\mathrm{nT}$ or $\pm 44,000\,\mathrm{nT}$. Switching between these is achieved automatically by the data processing unit. The magnetic field strength is typically a few and up to 10 nT in the vicinity of the magnetopause boundary, so the instrument operated in the lowest range for all of the measurements utilised in this thesis.

2.3 Electron Plasma Spectrometer

To a large extent, the solar wind and magnetospheric thermal plasma populations are separated by the magnetopause current sheet since the thermal electron gyroradius ($\sim$11 km

for a 10 eV electron in a 1 nT magnetic field) is small compared to the typical width of the magnetopause current layer (e.g. *Kaufmann and Konradi*, 1973; *Neugebauer et al.*, 1974; *Sonnerup and Ledley*, 1979; *Berchem and Russell*, 1982). This gives rise to two distinctly different electron populations across the boundary, making electron observations ideal for identifying the boundary itself. The Cassini Plasma Spectrometer (CAPS) (*Young et al.*, 2004) on board Cassini consists of three instruments. One of these is an electron spectrometer (CAPS-ELS).

CAPS-ELS is a 'top-hat' electrostatic analyser capable of measuring incident electrons with energies between 0.6 eV and 28.25 keV. The instrument itself is shown in Figure 2.8 and schematics are shown in Figures 2.9 and 2.10. Electrons enter a narrow 5° aperture and must follow a curved path between a pair of nested hemispherical plates in order to reach a microchannel plate (MCP), which they must strike in order to be detected. The inner plate is charged such that an electric field is formed between it and the grounded outer plate, deflecting the electrons entering the detector. Hence, for a given applied voltage, only electrons within a relatively narrow energy range are deflected by the right amount in order to be detected. To build up a full electron spectrogram, the instrument sweeps through a predefined set of voltages with an accumulation time of 31.25 ms each, a quarter of which is allocated to detector readout and voltage switching. Under normal operation, the instrument steps down through 63 logarithmically-spaced voltages in a time of ∼2 s.

The detector consists of eight individual microchannel plates (commonly referred to as anodes), each of which have a field of view (FOV) of $5^\circ \times 20^\circ$ and provide a total instrument FOV of $5^\circ \times 160^\circ$ around an axis parallel to the spacecraft X axis, as shown in Figure 2.10. Hence, information regarding the angular distribution of the incoming electrons is given based on which anode electrons are detected by. Typically, anode 5 is used since its FOV is the least obscured by other spacecraft components. CAPS is mounted onto an actuator that sweeps through an angle of 208° around an axis parallel to the Z axis in 200 s, giving the ELS a total effective field of view of $160^\circ \times 208^\circ$.

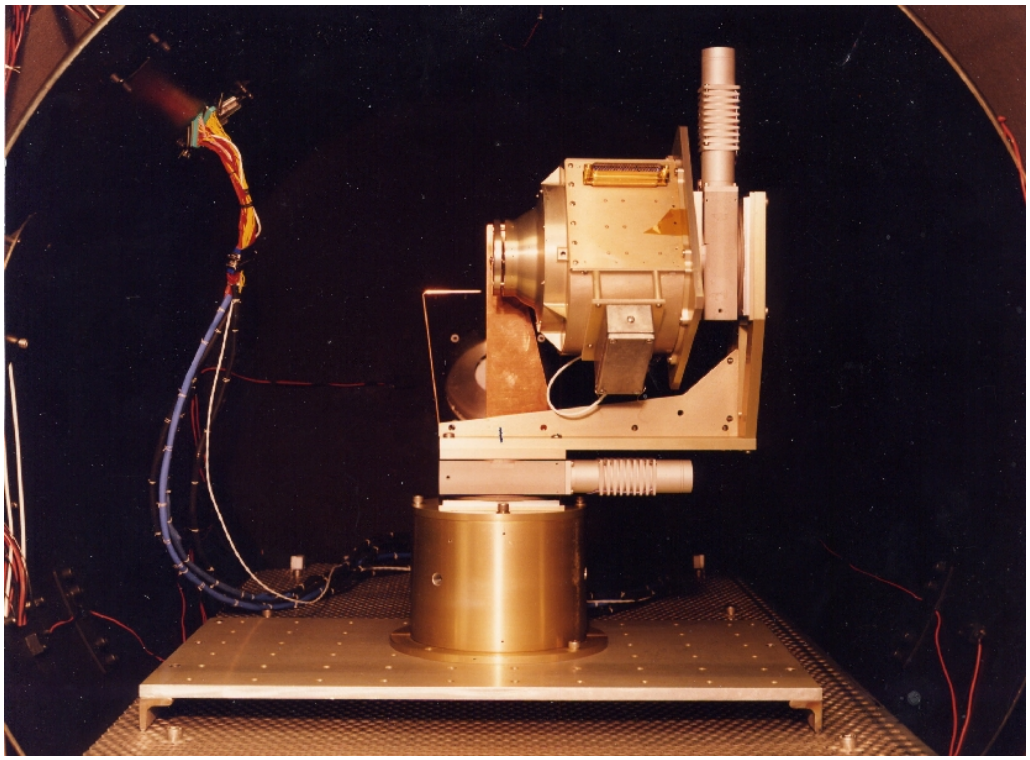

Figure 2.8. An image of the Cassini electron spectrometer taken during pre-flight testing in the Leybold vacuum chamber at the Mullard Space Science Laboratory.

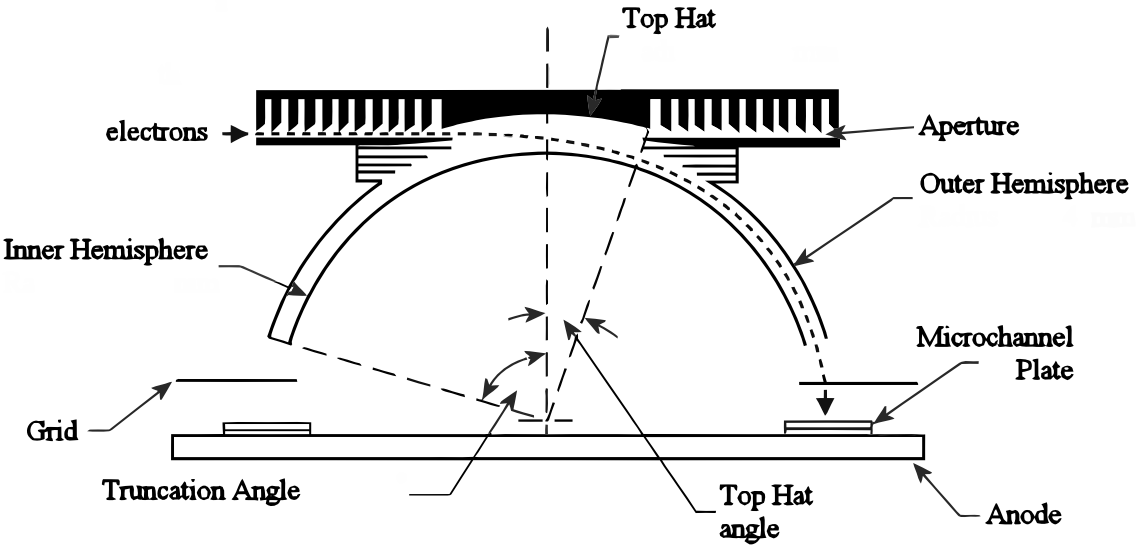

Figure 2.9. Schematic of a top-hat electrostatic analyser. From *Collinson and Kataria* (2010).

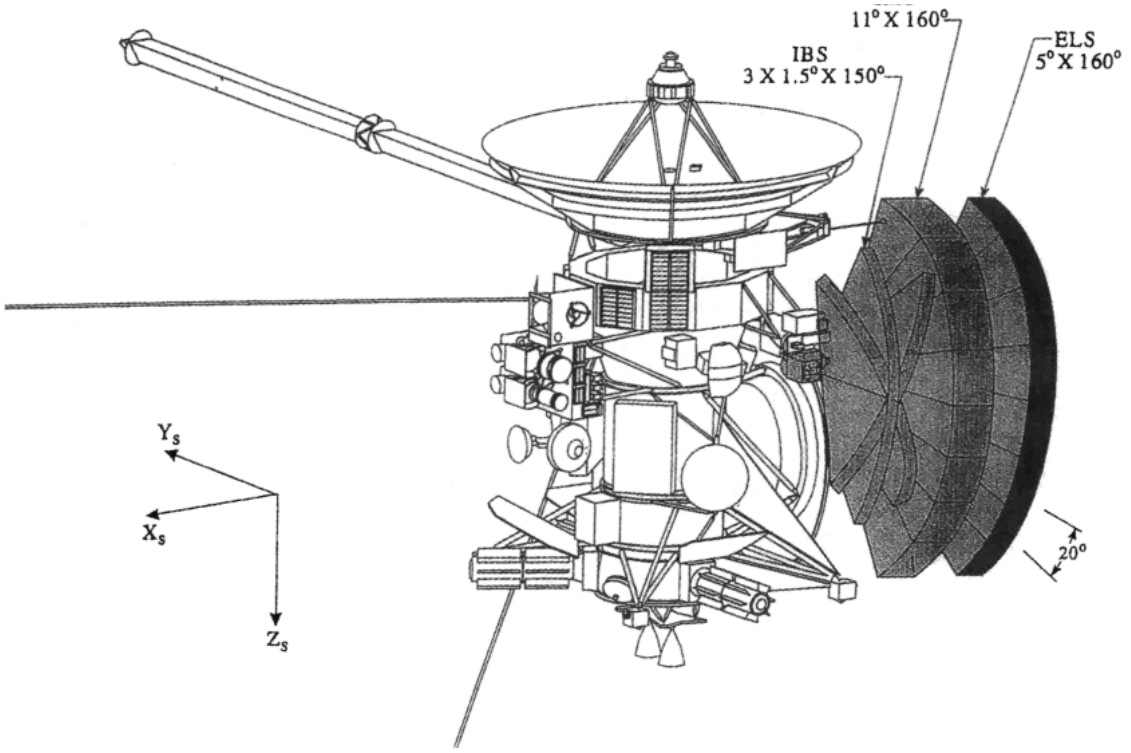

Figure 2.10. Schematic of the Cassini orbiter with the CAPS instrument enlarged. CAPS is oriented along the spacecraft's $-Y$ axis such that the ELS has an instantaneous coverage of $5° \times 160°$. However, it is also fixed to an actuator which sweeps through an angle of 208° around an axis parallel to the Z axis in 200 s. From *Rymer et al.* (2001).

2.4 Magnetospheric Imaging Instrument

Suprathermal plasma (usually defined to be > 27 keV for convenience) is an important source of pressure within Saturn's magnetosphere. At the magnetopause boundary, it has been found to be as important as the magnetic field pressure in holding off the flow of the solar wind (*Kanani et al.*, 2010). Saturn's magnetosphere contains an abundance of water-group elements originating from the rings and the plumes of water vapour ejected by Enceladus. Since oxygen is much more massive than protons and electrons, it is these ions that represent the most significant source of plasma pressure. Between 10 R_S and 19 R_S where the ring current resides, *Sergis et al.* (2007) found that the oxygen ions with energies > 10 keV contribute over 50% of the total particle pressure. These ions can be measured using the Magnetospheric Imaging Instrument (MIMI) (*Krimigis et al.*, 2004) on board Cassini, which is itself composed of three instruments to be discussed in turn.

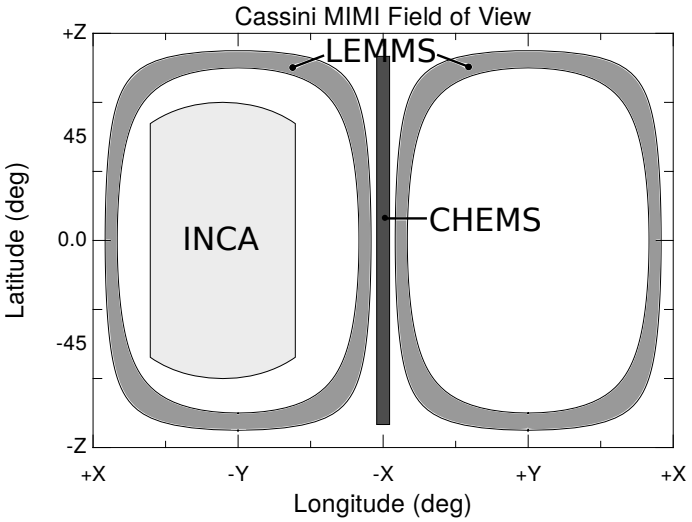

Figure 2.11. The field of view of the three instruments that make up MIMI. Note that the FOV depicted for LEMMS is that before the turntable was permanently parked in early 2005. Since then it has remained nearly aligned with CHEMS telescope 2, oriented such that the high and low energy telescopes are pointed 23° from the $\pm X$ axes respectively in the spacecraft coordinate system. Generated using The Cassini/MIMI Science Planning and Visualization Tool (JCSN).

2.4.1 Ion and Neutral Camera (INCA)

INCA can be used to remotely detect suprathermal plasma populations when operated in 'neutral' mode via ENA imaging as discussed in Section 1.3.4, or can be used to make very sensitive ion measurements when operating in 'ion' mode. Typically, the instrument is operated in neutral mode when the spacecraft is situated in the outer magnetosphere and the instrument viewing geometry is conducive to imaging the inner magnetosphere. The sensor operates in the energy range $7\,\text{keV} \leq E \leq 3\,\text{MeV}$ and its FOV is centred on the spacecraft's $-Y$ axis, covering a broad $90° \times 120°$ region as shown in Figure 2.11.

A schematic of INCA is shown in Figure 2.12. Particles must enter a fan-like arrangement of collimator plates which are alternately charged with $\pm 6\,\text{kV}$ when operating in neutral mode, causing ions with energies $\leq 500\,\text{keV}$ to be deflected into the plate walls and away from a series of microchannel plates. Neutral particles that are not deflected proceed into the instrument and come into contact with a thin foil, generating secondary electrons upon striking it. These secondary electrons are steered onto the 'start' MCP which records the strike time as well as the entrance location of the particle. The particle incurs a small amount of scattering but continues to the back of the sensor where it passes

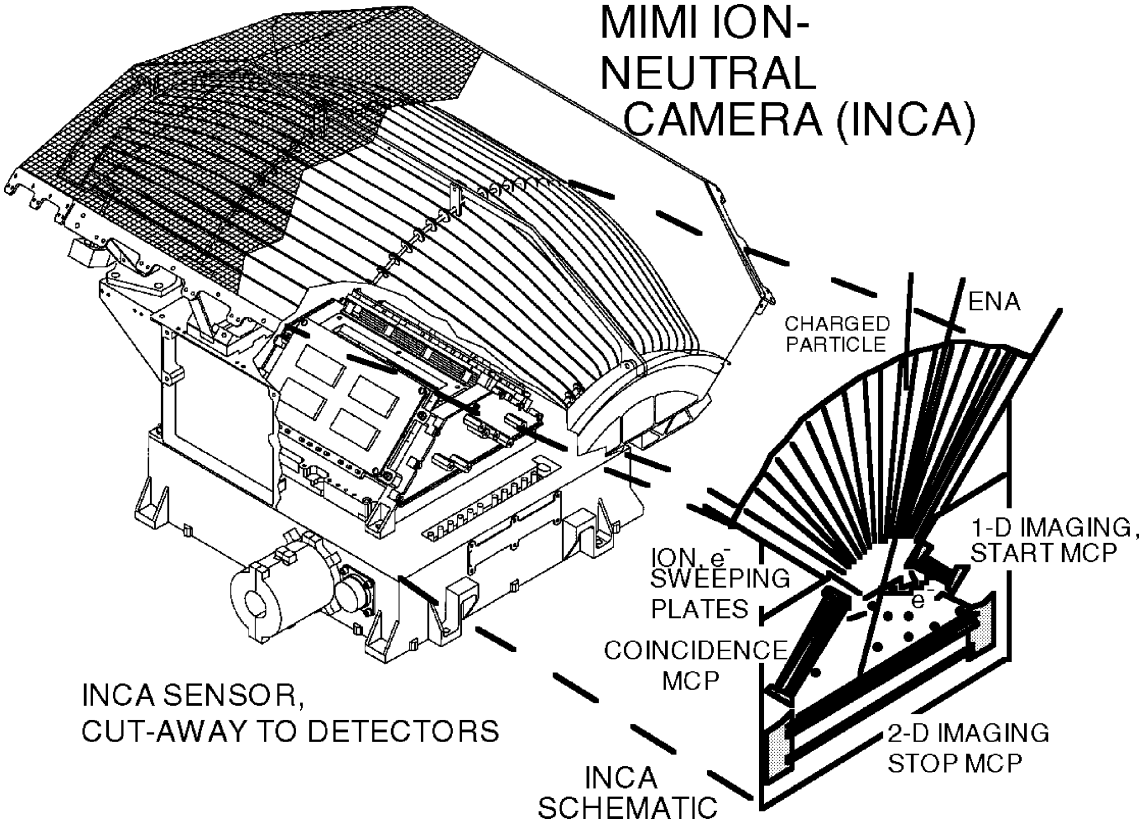

Figure 2.12. Schematic of INCA with an accompanying cut-away of the instrument, demonstrating its operation in neutral mode. A charged particle enters the fan-like arrangement of charged plates and is deflected into one of the plate walls. An ENA passes straight through the plates and hits a thin foil, generating secondary electrons which are deflected onto the start MCP. The ENA continues along its trajectory towards the stop MCP. From *Krimigis et al.* (2004).

through a second 'imaging' foil, generating a second set of secondary electrons. These are accelerated onto a 2-D 'stop' MCP which records the stop time and the 2-D striking position. Some of the secondary electrons produced at the imaging foil are also steered towards a third 'coincidence' MCP, the signal of which helps to reduce the measurement noise.

From these measurements, the mass, energy and arrival direction of the incoming particle can be found. Hydrogen and oxygen are the most common ion species within Saturn's magnetosphere, making them the most common ENA species too. The number of secondary electrons produced is highly dependent on the mass of the particle – it has been found that oxygen produces several times more secondary electrons than hydrogen, making mass determination relatively straightforward from the MCP pulse-height (*Krimigis et al.*,

2004). The trajectory of the particle can also be determined from the entrance location recorded by the start MCP and the striking position recorded by the stop MCP. Hence, a path length can be calculated and this information can be combined with the knowledge of the particle's mass to determine its energy.

2.4.2 Charge-Energy-Mass Spectrometer (CHEMS)

CHEMS is capable of detecting ions in the range $3 \leq E \leq 220\,\text{keV}$. It consists of three telescopes aligned along the spacecraft's $-X$ axis, providing a total FOV of 159° along the Z axis with a width of 8°. However, when the spacecraft spins about the Z axis, CHEMS is capable of measuring a near-complete three-dimensional plasma distribution.

A schematic of a CHEMS telescope is shown in Figure 2.13. The instrument consists of two concentric spherical plates that are oppositely charged at a maximum of $\pm 9.2\,\text{kV}$. In a similar way to CAPS-ELS, the plates are stepped through a series of 16 logarithmically spaced voltages, allowing the detection of only those ions within a small band of energy per charge. Ions that satisfy this criterion and pass through the deflection system must then pass through a thin carbon foil, upon which secondary electrons are emitted. These electrons are deflected by an electric field onto a start MCP which records the start of flight time. The ion continues to travel to the back of the telescope where a solid state detector (SSD) is located. Upon striking the SSD, secondary electrons are generated which are deflected towards a stop MCP. This allows the time of flight, and hence the ion's velocity and energy, to be calculated. The SSD also allows the residual energy of the ion to be measured, after losses due to scattering. The energy per charge is also known since this is limited by the voltage applied to the plates, and this allows the mass and charge state of the ion to be calculated (*Krimigis et al.*, 2004).

2.4.3 Low Energy Magnetospheric Measurements System (LEMMS)

LEMMS consists of two oppositely directed telescopes. Energetic electrons and ions within the ranges $0.015 \leq E \leq 0.884\,\text{MeV}$ and $0.03 \leq E \leq 18\,\text{MeV}$ respectively are detected by the low energy telescope with a FOV of 15°. Electrons and ions within $0.1 \leq E \leq 5\,\text{MeV}$ and $1.6 \leq E \leq 160\,\text{MeV}$ respectively are detected by the high energy telescope with a

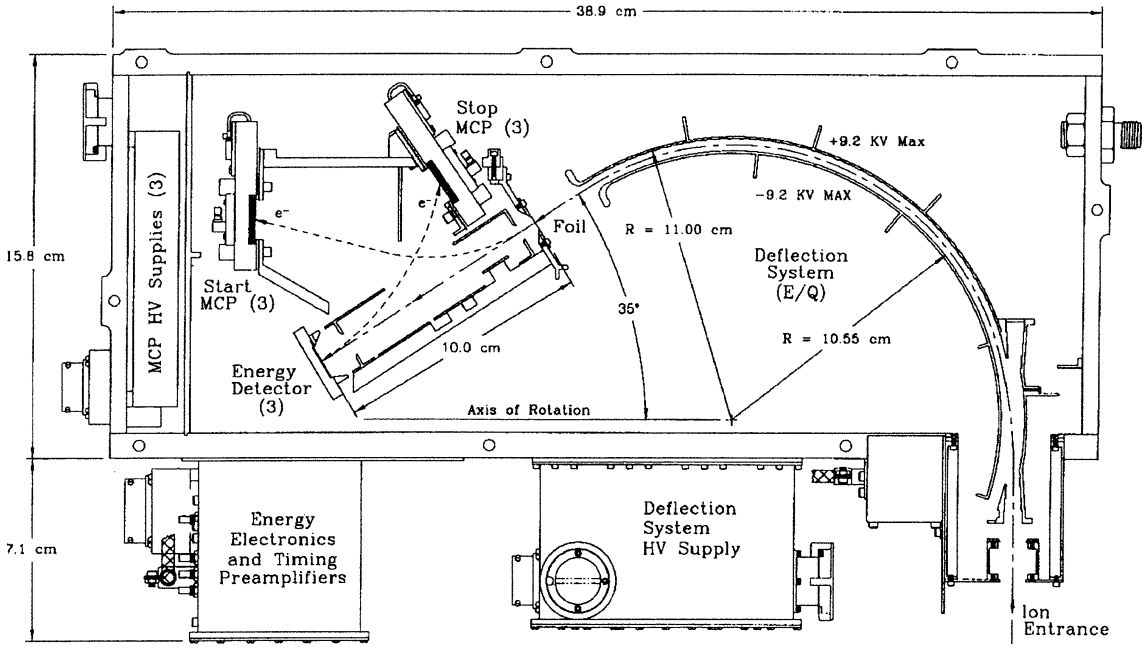

Figure 2.13. Schematic of one of the telescopes that make up the CHEMS instrument. From *Krimigis et al.* (2004).

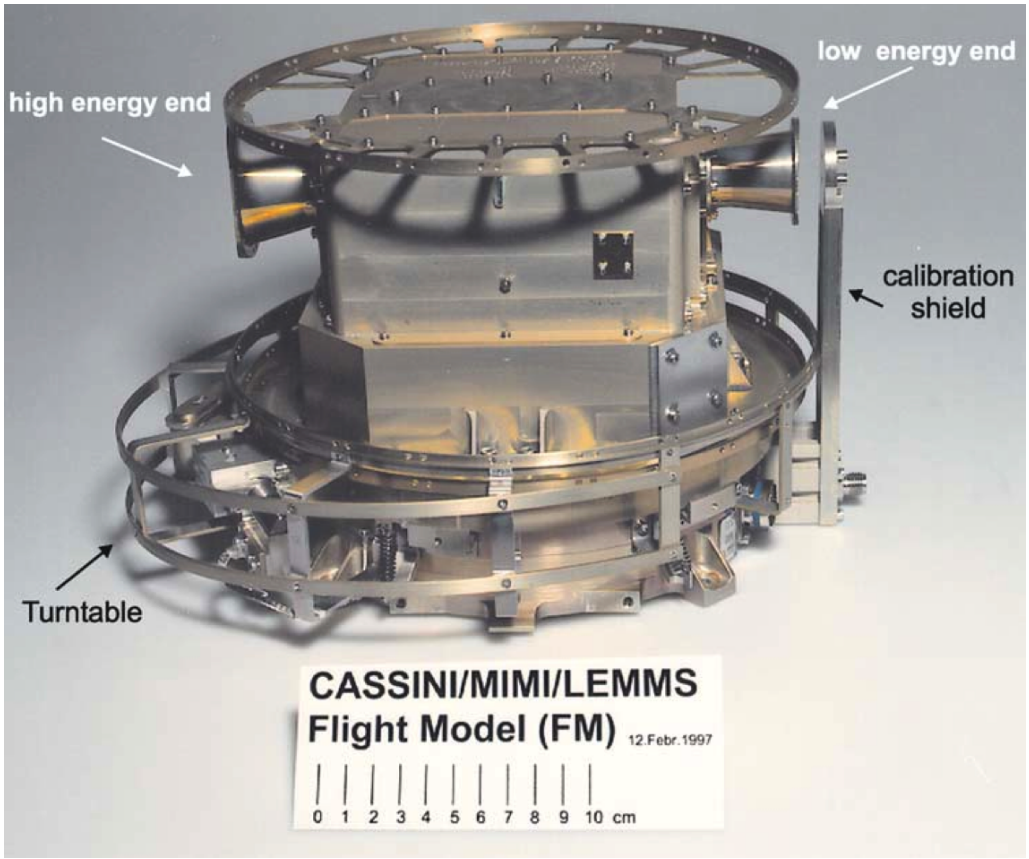

Figure 2.14. Image of LEMMS mounted on its turntable. From *Krimigis et al.* (2004).

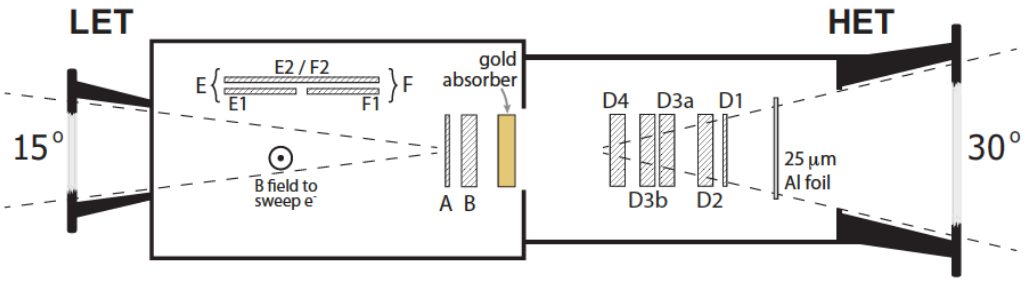

Figure 2.15. Schematic of LEMMS showing both the low energy telescope (LET) and the high energy telescope (HET). From *Krimigis et al.* (2004).

FOV of 30°. A platinum cover is used to shield the entire instrument from particles with energies below 30 MeV from penetrating it, and a calibration shield allows the background count rate to be characterised. The instrument is also mounted on a rotating platform that allowed it to make three-dimensional measurements of its surroundings and determine the incidence direction of energetic ions and electrons. However, in early 2005 anomalous voltage measurements caused the instrument team to question the reliability of the rotating platform. As such, the platform was permanently parked such that the instrument is not obscured by the spacecraft structure and is now nearly aligned with CHEMS telescope 2.

A schematic of LEMMS is shown in Figure 2.15. Upon entering the low energy telescope, the magnetic field of a permanent magnet deflects ions and electrons towards different detectors. Electrons strike detectors E or F depending on their incident energy, whilst ions strike detectors A or B. A gold absorber resides between the ion detectors and the detectors of the high energy telescope in order to prevent particles from penetrating through. The high energy telescope consists of a stack of five detectors, the front of which is covered by an aluminium foil to suppress sunlight and low energy ion contamination. These detectors distinguish ions and electrons through the use of logic conditions between several electronic thresholds of the detectors.

2.5 Magnetopause Observations

When the spacecraft traverses the magnetopause, it typically samples distinctly different plasma populations and magnetic fields on either side. A series of magnetopause crossings is shown in Figure 2.16. The electron density (and hence differential energy flux) tends to

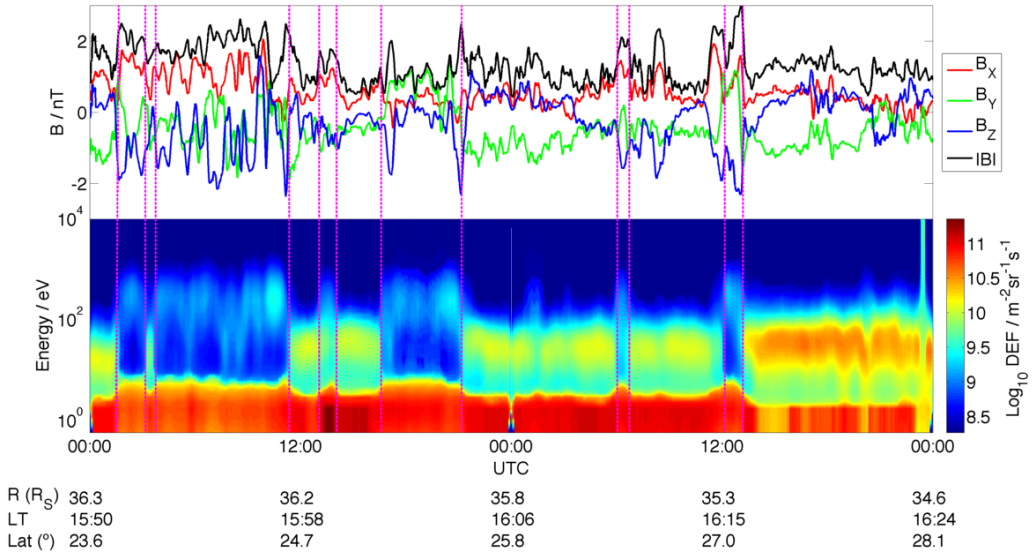

Figure 2.16. In situ data taken by the Cassini spacecraft over 48h starting at midnight on day 123 of 2007 (3 May). (top) The components of the magnetic field and its magnitude with a 1 min time resolution smoothed using a moving average filter with a span of 11 min. (bottom) An electron spectrogram from the CAPS-ELS instrument. The energy and differential energy flux (essentially a count rate calibrated for detector efficiency and geometry which is proportional to density) of the electrons are represented logarithmically. The vertical magenta lines indicate magnetopause crossings, 12 such crossings can be seen during this period characterised by sudden changes in electron energy and count rate and magnetic field strength, as well as rotations in the magnetic field. The persistent population of low energy ($<\sim$10 eV) electrons are the photoelectrons.

be elevated in the magnetosheath compared to within the magnetosphere with an order of magnitude difference typical. However, electrons in the magnetosheath are typically of lower energy than those found within the magnetosphere. The modal electron energy is typically an order of magnitude greater just inside the magnetosphere than in the magnetosheath. As such, it is often much easier to detect magnetopause crossings in the CAPS-ELS data than the FGM data.

It is not uncommon to sample regions containing an electron population with properties typical of both the magnetosheath and the magnetosphere, such as the region between the crossings located just after noon during the first 24-hour period displayed in Figure 2.16. These are often characteristic of 'low-latitude boundary layers' (LLBLs) and occur because the magnetopause is unstable and processes like localised reconnection and the Kelvin-Helmholtz instability can mix the two plasma populations together (e.g. *Masters et al.*, 2011).

A significant photoelectron population is present in Figure 2.16 and is a common feature of electron spectrograms constructed using CAPS-ELS measurements. These electrons are typically of energies below ∼10 eV and there is usually a clean cut-off between the photoelectrons and the electrons of the ambient plasma, making the photoelectrons easily identifiable. This cut-off is at the spacecraft potential, which is usually positive. The spacecraft potential depends on the ambient plasma conditions. It is determined by balancing the electrons leaving the spacecraft (e.g. through photoionisation, secondary electron production and electron backscattering) with the flux of electrons and ions incident upon the spacecraft (*Szita et al.*, 2001). The electron and ion flux is smaller within the magnetosphere so a larger spacecraft potential is required to balance the electrons that are liberated from the spacecraft. Hence, electrons require a larger amount of energy to escape the spacecraft potential within the magnetosphere than they do in the magnetosheath, causing the photoelectron population to extend to higher energies inside the magnetosphere.

In addition, the magnetic field strength is typically much stronger and less variable inside the magnetosphere compared to the magnetosheath. Transitions across the magnetopause are also often characterised by a sharp rotation in the magnetic field direction. The magnetic field often has a considerable southward component inside the magnetosphere, whereas the north-south component of the magnetosheath magnetic field is typically close to zero and highly variable. However, this is not always the case and a positive identification of a magnetopause crossing is not always possible using FGM data alone. In this situation, plasma data can provide complementary information.

For each magnetopause crossing identified, the average interior magnetic field strength and suprathermal plasma pressure are calculated over an interval of time as close as possible to the crossing, and preferably during which the magnetic field was fairly steady. In order to improve the statistics as far as was possible, this 'statistics interval' was selected such that it covered as large a period of time as was possible whilst keeping the standard deviation of the magnetic field strength less than 10% of its magnitude. Magnetic field data with a resolution of one minute was used, whilst the suprathermal plasma pressure moments had a resolution of 10 minutes – the minimum window usually required in order to have reliable statistics for the computation of the moment.

The suprathermal plasma pressure is highly variable and an increase in pressure by an order of magnitude from one 10 minute-average to the next is not uncommon. The population contributing this pressure consists mainly of protons and ions of oxygen (dominated by O^+). As oxygen ions are much more massive than protons, they contribute about four times more to the total pressure than a proton of similar velocity. As a result, it only takes a short interaction with a stream of these ions to increase the total pressure by an order of magnitude

The statistics intervals were typically no shorter than 20 minutes in duration such that they contained at least three suprathermal plasma pressure measurements. The median magnetic field strength and suprathermal plasma pressure were then calculated and used to calculate the final magnetic and suprathermal plasma pressure for each magnetopause crossing in order to reduce the probability that the pressures are subject to spurious measurements. For some of the crossings, reliable suprathermal pressure moments were unavailable so were discarded from the subsequent analyses.

Further statistical tests were also experimented with in order to be absolutely certain that the high variability of the suprathermal plasma pressure was not influencing the results of this work. For each crossing, the relative differences between the median and the upper and lower quartiles of the suprathermal plasma pressure were calculated. If either of these differences were greater than 0.6, the crossing was rejected, though the results presented in the following chapters were insensitive to this reduction so results have been presented using the full data set. Furthermore, outliers in terms of the 'plasma β' (the ratio of plasma to magnetic pressure) were removed by calculating the 'robust z-score' (*Rousseeuw and Hubert*, 2011) for each crossing and rejecting those outside of a standard deviation of two or three. Though, again, the results presented herein were insensitive to reducing the data in this way.

In the next four chapters, observations of Saturn's magnetopause have been extensively utilised in order to study the structure and geometry of Saturn's magnetopause in greater detail than has before been possible. In the first instance, such observations were used to study the high-latitude structure of Saturn's magnetopause.

Chapter 3

Polar Confinement of Saturn's Magnetopause Boundary

The diversity of the phenomena of nature is so great, and the treasures hidden in the heavens so rich, precisely in order that the human mind shall never be lacking in fresh nourishment.

Johannes Kepler

The research presented within this chapter represents the first advances towards a better understanding of the interaction between the solar wind and Saturn's magnetic field and plasma environment within this thesis. In order to characterise the typical size and shape of the magnetosphere, previous empirical studies of Saturn's magnetopause have necessarily utilised data obtained via spacecraft orbits that have predominantly sampled the near-equatorial magnetosphere as discussed in Section 1.4. As a result, the extent to which Saturn's polar magnetosphere is 'flattened' relative to the equatorial magnetosphere has not yet been assessed, and this has remained a major gap in our knowledge of the system. In this context, the term 'polar flattening' is referred to mean the departure of the mag-

netopause from axisymmetry about the planet-Sun line. One way this feature may arise of relevence to the Saturn system is the disc-like nature of the magnetospheric obstacle to solar wind flow. Polar flattening, or equivalently equatorial inflation, is directly related to the amount of plasma contained with the magnetosphere and its spatial and energy distributions, so is a fundamental aspect of fast-rotating systems with significant internal plasma sources. As such, the work presented herein presents a more complete picture of Saturn's magnetosphere than before.

A set of magnetopause crossings that occurred during the first set of highly-inclined orbits of Cassini have been identified and used to quantify the degree to which Saturn's magnetosphere is flattened. The possibility of a dynamic pressure dependence has also been investigated. Two dynamic pressure estimates were compared in order to down-select the data so as to increase the probability that the magnetopause was close to equilibrium when the spacecraft crossed it. This measure considerably reduced the degree of scatter in the location of the magnetopause. The spacecraft trajectory was then analysed to ensure that the sampling of the high-latitude magnetopause was adequate to infer polar flattening from the observations. Finally, the phase of the global magnetic oscillation has been determined for each of the magnetopause crossings in order to ascertain whether the apparent flattening observed could be a result of the global magnetic oscillations known to occur throughout the magnetosphere as discussed in Sections 1.3 and 3.4.

3.1 Magnetopause Observations

To evaluate the degree of polar flattening, in the first instance, spacecraft orbits from the beginning of 2007 up until the end of 2008 were examined. Cassini executed its first family of highly inclined orbits during this period. These orbits passed through the magnetopause in the northern hemisphere on the dusk side of the planet. Magnetopause crossing identifications were made by eye in both the MAG and the CAPS-ELS datasets as discussed in Section 2.5. Through careful analysis of the field and plasma data, 626 crossings were identified. Suprathermal plasma pressure moments were available for 610 of these crossings. Crossings within three hours of each other were averaged together, as it is likely that such closely-spaced crossings were caused by boundary waves on the magnetopause surface. *Masters et al.* (2012b) found that boundary waves have a period

of approximately three hours on the dusk side of the planet. Hence, it has been verified that the results of this study are insensitive to the presence of these waves by averaging together crossings that may be caused by such boundary dynamics.

The forthcoming analysis has been performed using the averaged data set containing 316 crossings. In addition, the analysis has been performed after reducing the data further through stringent statistical analysis of the suprathermal plasma pressure moments, as discussed in Section 2.5. This reduction was performed in order to ensure that the high degree of variability in the suprathermal plasma pressure does not significantly affect the results presented herein. Within the estimated uncertainties, the results obtained by repeating the analysis on the 196 crossings that satisfied these criteria yielded the same results as those found by analysing the averaged data set. Therefore, the results presented herein are derived from the averaged data set as opposed to the averaged and reduced data set, in order to boost the number of data and reduce the uncertainties as much as possible.

The crossing locations are shown in Figure 3.1. The Kronocentric Solar Magnetospheric (KSM) coordinate system has been used, in which the X-axis is directed from the planet to the Sun and the Z-axis is such that the magnetic dipole axis of the planet lies within the X-Z plane. The Y-axis completes the right-handed set and is thus pointed towards dusk local time. Much scatter can be seen in the crossing positions. This is because the observations were made over a period of 650 days, thus the magnetopause will have experienced large variations in shape and size in response to variations in the interior and exterior pressures adjacent to the magnetopause.

3.2 Pressure Balance

The techniques employed by *Kanani et al.* (2010) are used in order to estimate the solar wind dynamic pressure for each magnetopause crossing in the absence of a dedicated upstream solar wind monitor, as discussed in Section 1.4. In addition to the magnetic and suprathermal plasma pressures that *Kanani et al.* (2010) considered, the pressure contribution associated with the centrifugal force at the magnetopause has been considered

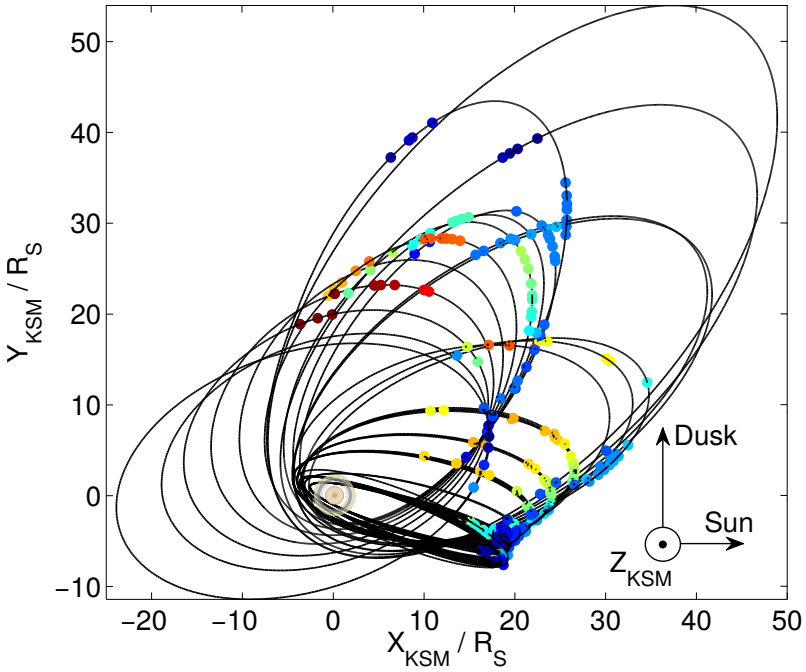

(a) Slice through the X-Y plane

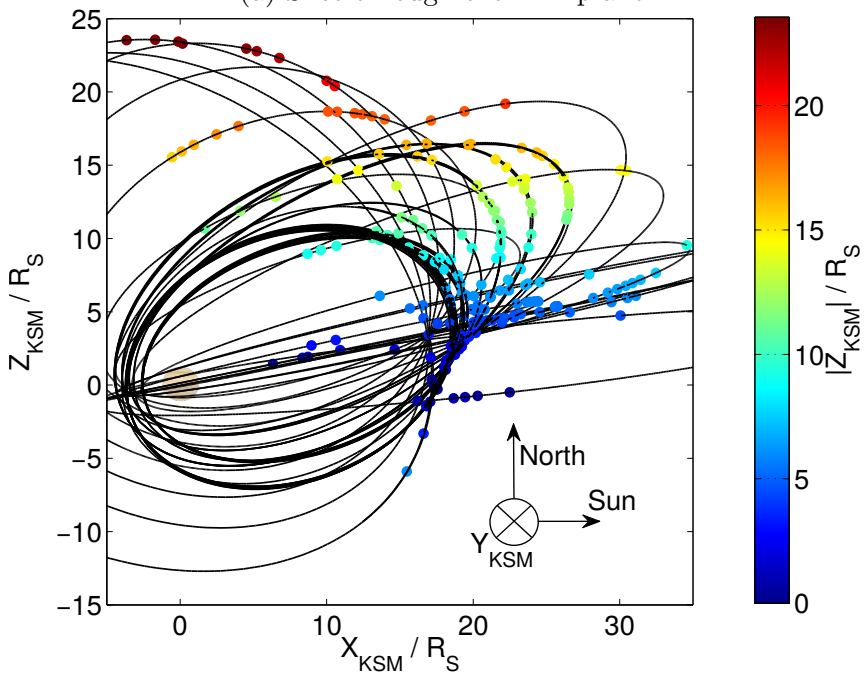

(b) Slice through the X-Z plane

Figure 3.1. The lines show consecutive orbits of the Cassini spacecraft around Saturn and the points are locations where a magnetopause crossing has been identified. Saturn and its rings are also displayed and are centred on the origin of each plot. Each crossing is coloured according to the absolute value of its Z_{KSM} coordinate. (a) Looking down on the the northern hemisphere, it shows that the majority of the crossings are confined to the noon-dusk sector. (b) Looking from dawn to dusk, it shows the high-latitude coverage of the spacecraft during this time.

as follows. A unit cross-section of the magnetopause layer has centrifugal force,

$$F_{\mathrm{CF}} = mR\omega^2 V, \tag{3.1}$$

where m is the mass per unit volume, V, ω is the angular velocity of the layer and R is the planet-layer distance. Assuming, generously, that the magnetopause layer has similar density and rotation rate to the plasma just inside the magnetopause, the net force acting on this layer per unit area must supply the centrifugal force in order to keep the plasma within the layer rotating, hence,

$$\frac{B^2}{2\mu_0} + P_{\mathrm{MIMI}} - P_{SW} = -F_{\mathrm{CF}}, \tag{3.2}$$

where B is the magnetic field strength just inside the magnetopause, P_{MIMI} is the suprathermal plasma pressure measured by MIMI and P_{SW} is the total solar wind pressure. From *Achilleos et al.* (2010a) Figure 10 (lower panel), the centrifugal force per unit volume just inside the magnetopause is,

$$F_{\mathrm{CF}} \sim 3 \cdot 10^{-9} \left(\frac{{B_0}^2}{\mu_0 R_S} \right), \tag{3.3}$$

where B_0 is the equatorial surface magnetic field strength with a typical value of $\sim$20000 nT and R_S is the equatorial radius of Saturn with a value of 60268 km. Considering the volume of the layer to be the unit area multiplied by the width of the layer then, by definition,

$$wF_{\mathrm{CF}} \leq 3 \cdot 10^{-9} \left(\frac{{B_0}^2}{\mu_0} \right) \left(\frac{w}{R_S} \right), \tag{3.4}$$

as, in reality, the density and rotation rate of the layer will be intermediate between the density and rotation rate either side of the magnetopause, and where w is the width of the layer. Also from *Achilleos et al.* (2010a) Figure 10 (middle panel),

$$\frac{B^2}{2\mu_0} + P_{\mathrm{MIMI}} \sim 0.02 \left(\frac{{B_0}^2}{\mu_0} \right), \tag{3.5}$$

thus,

$$\begin{aligned}\frac{wF_{\mathrm{CF}}}{\frac{B^2}{2\mu_0}+P_{\mathrm{MIMI}}} &\leq \left(\frac{3\cdot 10^{-9}}{0.02}\right)\left(\frac{w}{R_S}\right) \\ &\lesssim 10^{-7}\left(\frac{w}{R_S}\right),\end{aligned} \tag{3.6}$$

and w is of the order $1\,\mathrm{R_S}$ (*Masters et al.*, 2011). Thus,

$$\frac{wF_{\mathrm{CF}}}{\frac{B^2}{2\mu_0}+P_{\mathrm{MIMI}}} \leq 10^{-7}, \tag{3.7}$$

and hence, the centrifugal force is very small compared to the magnetic and suprathermal plasma pressure gradients and can be safely neglected.

In addition to the magnetic and suprathermal plasma pressures, *Kanani et al.* (2010) also included the pressure contribution from thermal electrons and protons derived from the CAPS-ELS instrument. However, they found that the partial pressures of this population were on average 1-2 orders of magnitude smaller than those associated with the magnetic field and the suprathermal ions. As such, the thermal electron and ion pressures are neglected for the purposes of this study, but in Chapter 4 the partial pressure associated with the thermal water-group ions is also considered.

3.3 Magnetopause Modelling

3.3.1 Initial Results

For present purposes, it is firstly necessary to normalise the crossing locations to predict where the magnetopause boundary would be located at a fixed value of solar wind dynamic pressure. When crossings are normalised in this way, one is essentially assuming that variations in the dynamic pressure cause the magnetopause to expand or contract self-similarly. The dynamic pressure may vary substantially from one crossing to the next, so removing this additional degree of freedom reduces the scatter in the crossing locations. This is achieved using Equation 1.38. Although the crossing locations are normalised to a common dynamic pressure in this study, in reality internal variability and the global planetary-period oscillations observed throughout the Kronian system are also expected

to affect the position of the magnetopause. In the first instance, the dynamic pressure is assumed to be the dominant driver and the effect of the magnetic oscillation is neglected. In Section 3.4, evidence to support this assumption is presented. The impact of internally driven variability in the magnetopause location is also addressed in Chapter 4.

Although normalising crossings to a common D_P is perhaps more visually intuitive, it would be more accurate to construct a separate surface for each crossing at the estimated dynamic pressure. The distances between those surfaces and the crossings that correspond to them could then be calculated and used as a 'goodness of fit' measure. *Arridge et al.* (2006) and *Kanani et al.* (2010) found that the magnetopause flaring is also dynamic-pressure-dependent, which violates the normalisation assumption. However, these authors found conflicting results – *Arridge et al.* (2006) found that the degree of tail flaring decreases with dynamic pressure but *Kanani et al.* (2010) found the opposite behaviour. This may indicate that the effect is poorly constrained or is small enough to be neglected. Furthermore, in Section 3.3.5 it is found that taking this variability into account using the *Kanani et al.* (2010) model does not change the tail flaring significantly when crossings observed under high and low dynamic pressure conditions are considered separately. In Chapter 4, a more accurate method of calculating the crossing-surface distance near-exactly is presented and used instead of calculating the distance between the X-Y projections as done in this chapter.

The normalised crossings projected onto the X-Y plane are shown in the upper left panel of Figure 3.2. In addition, X-Y slices of the axisymmetric model derived by *Kanani et al.* (2010) are also plotted to form a contour map of the magnetosphere looking down onto the northern hemisphere. The distance between each crossing and the corresponding slice through the model surface at the same Z_{KSM} coordinate has been calculated, and the crossings are coloured by this distance. The distance along the cylindrical radial direction is used here, as shown in Figure 3.3. Although there is a degree of scatter (which will be discussed in Section 3.3.2), the low-latitude crossings ($Z_{\mathrm{KSM}} \lesssim 10\,\mathrm{R_S}$) tend to fit the axisymmetric model well. However, the crossings seem to be systematically shifted away from the slices between $\sim 12 - 25\,\mathrm{R_S}$ Z_{KSM}. A simple mathematical dilation of the magnetopause boundary along the Z_{KSM} direction has been used to construct a flattened magnetopause whereby Z_{KSM} in the axisymmetric boundary model is replaced by $\mathcal{E}Z_{\mathrm{KSM}}$. Hence, the axisymmetric surface described by Equations 1.39-1.41 can be transformed into

a 'flattened' surface as:

$$\begin{pmatrix} x' \\ y' \\ z' \end{pmatrix} = \begin{pmatrix} 1 & 0 & 0 \\ 0 & 1 & 0 \\ 0 & 0 & \mathcal{E} \end{pmatrix} \begin{pmatrix} x \\ y \\ z \end{pmatrix}, \tag{3.8}$$

where $x = r\cos\theta$, $y = r\sin\theta\cos\phi$ and $z = r\sin\theta\sin\phi$; r is given by Equation 1.39 and ϕ is the angle between the projection of r onto the Y-Z plane and the Y_{KSM} axis as illustrated in Figure 3.4.

The factor $\mathcal{E}$ governs the degree of flattening; a value smaller (greater) than 1 represents a flattened (inflated) polar magnetosphere. In the top-right panel of Figure 3.2, a flattening of 20% (i.e. $\mathcal{E}$ is equal to 0.80) has been applied to the model magnetopause surface. The high-latitude crossings ($Z_{\mathrm{KSM}} \gtrsim 15\,\mathrm{R_S}$) and their corresponding X-Y slices are much closer together when the surface is flattened. This indicates that a surface flattened in the north-south direction is a better description of Saturn's magnetopause than an axisymmetric model, at least during the period of time in which these crossings were observed. The degree of polar flattening is evaluated over a longer period of time in Chapter 4. It is important to note that it is difficult to determine if the observed confinement arose as a result of the disk-like nature of the obstacle to the solar wind flow, or if it was caused by seasonal effects related to the hinging of the magnetosphere. Saturn was approaching vernal (spring) equinox at the time that these observations were made, and in the northern hemisphere its magnetic dipole was tilted away from the Sun by an angle ranging from $\sim$10° - 14°. Here, a dipole tilt angle of 0° indicates that Saturn's magnetic dipole is orthogonal to the upstream solar wind direction. As a result, seasonal effects may play some role in confining the magnetosphere, particularly for the crossings near the start of the observation period when the absolute dipole tilt was largest. This aspect will be investigated in Chapter 5.

The keen-eyed reader may also notice that flattening the surface changes the positions of the normalised crossings somewhat. The dynamic pressure is a function of the angle between the incoming solar wind direction and the normal to the magnetopause surface, Ψ, in accordance with Equation 1.54. This means that Equations 1.44–1.51, which were previously used to calculate the normal to the magnetopause surface, must be updated to account for the change in geometry introduced by flattening the surface. Since the flat-

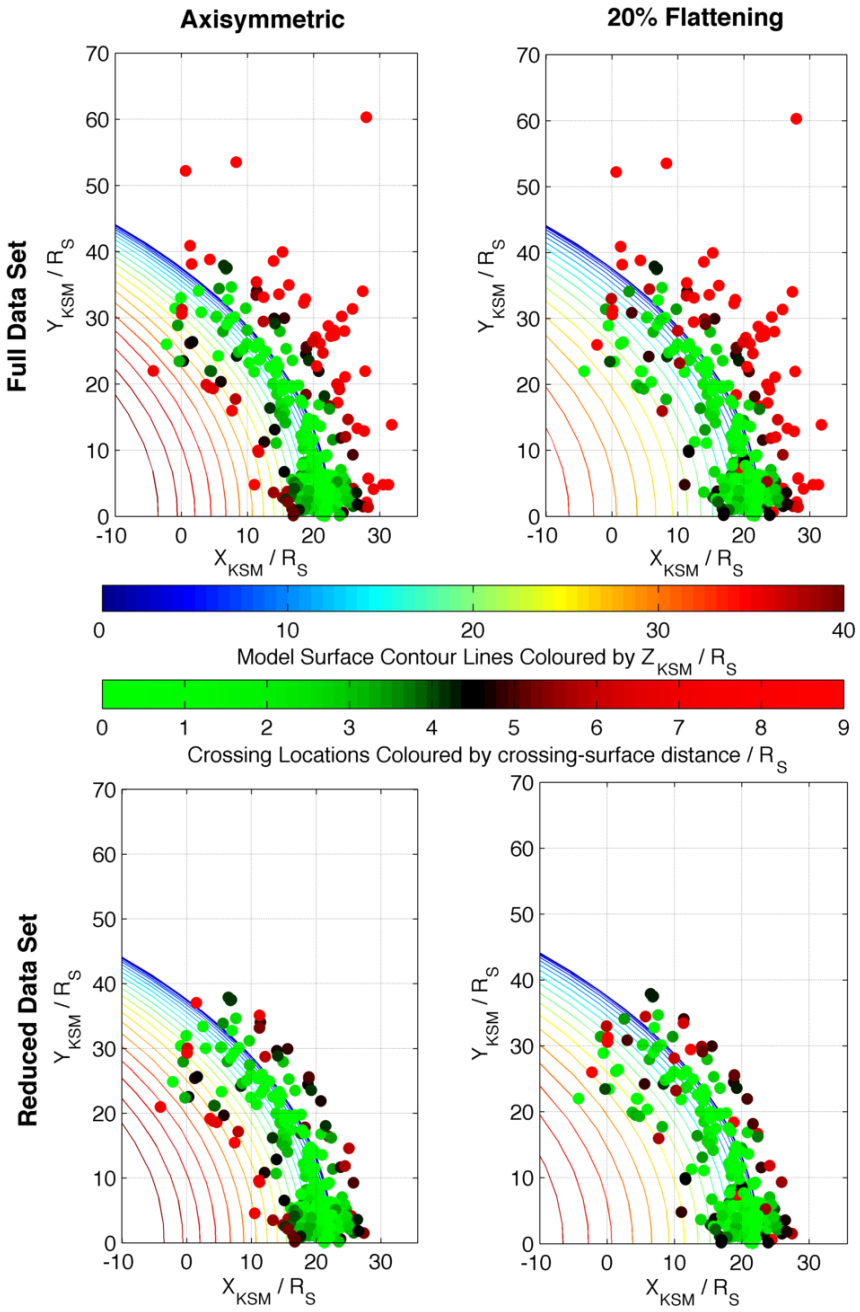

Figure 3.2. Magnetopause crossing locations are scaled to the average solar wind dynamic pressure and are coloured by the distance between them and the empirical surface of *Kanani et al.* (2010). Hence, the 'greener' the points are, the better the agreement between the observed locations of the crossings and the locations predicted by the model magnetopause. Note that crossings at a cylindrical radial distance of 9 R_S or greater from the surface at the same Z_{KSM} coordinate have been allocated the same colour in order to allow differences in distances smaller than this to be distinguished easily. Slices through the X-Y plane of the model surface are plotted as lines coloured by their Z_{KSM} coordinate, increasing in units of 2 R_S. The panels on the left use the original axisymmetric model but the model has been flattened by 20% along the Z_{KSM} axis in the panels on the right. The upper panels use the averaged data set whereas in the lower panels the data has been reduced using the criterion outlined in Section 3.3.2.

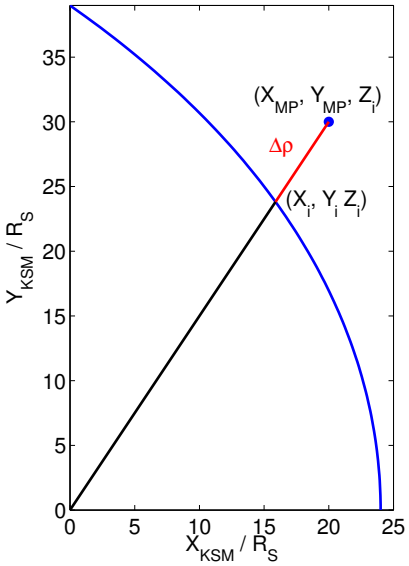

Figure 3.3. Illustrated is the distance $\Delta\rho$, the distance between a normalised magnetopause crossing and an X-Y slice (at the Z_{KSM} coordinate of the crossing) from a magnetopause surface constructed at $\langle D_P \rangle$. $\langle D_P \rangle$ is the pressure to which the crossings are normalised.

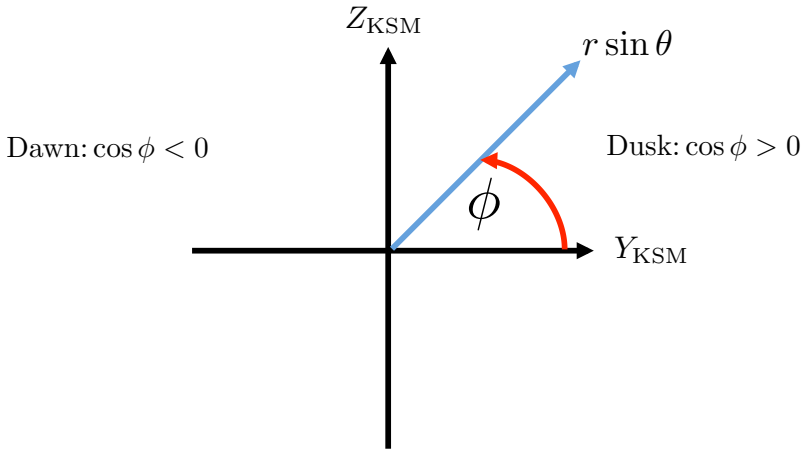

Figure 3.4. Illustration of the angle ϕ viewed from the Sun with the planet at the origin. ϕ is the angle between the projection of the radial vector onto the Y-Z plane (blue arrowed line) and the Y_{KSM} axis.

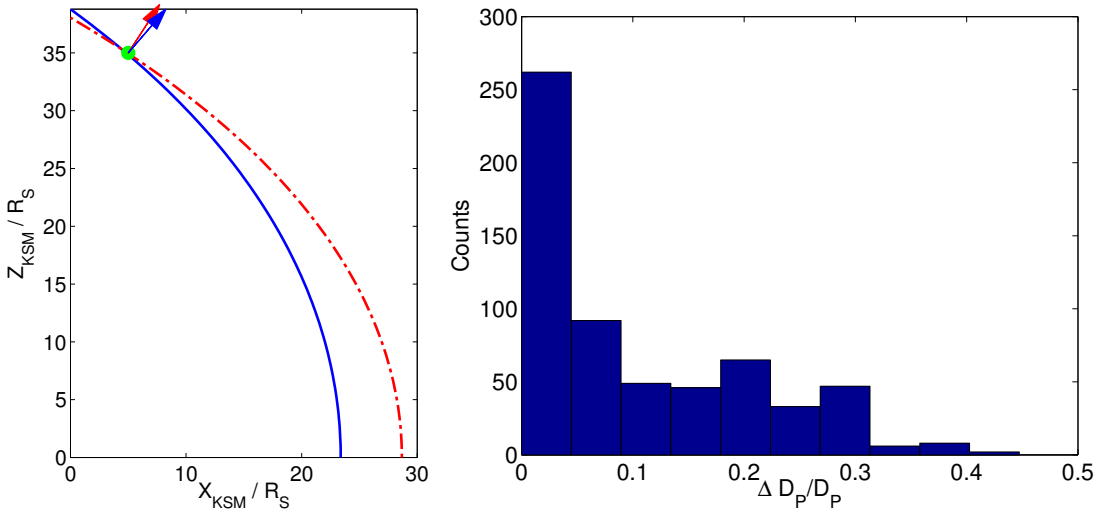

(a) (b)

Figure 3.5. (a) Shows two magnetopause surfaces with different geometries fitted through the exact location of a magnetopause crossing (green point). The blue, solid line is the axisymmetric surface of *Kanani et al.* (2010), whilst the red dot-dashed line is a version of that surface flattened by 20% (i.e. $\mathcal{E} = 0.80$). The flattened surface requires a much larger stand-off distance in order to pass through the crossing. Also plotted are the normals to each surface in their respective colours. The normal is required in order to estimate the solar wind dynamic pressure, so changing the surface geometry also changes the estimated dynamic pressure. (b) Shows the fractional difference between calculating D_P for all of the crossings used in this study using an axisymmetric model and a model flattened by 20%. Typically this is <0.001 nPa but is highly correlated with $Z_{\rm KSM}$ with a correlation coefficient of ∼0.87.

tening is applied in the Cartesian coordinate system by reducing the extent of the surface along the $Z_{\rm KSM}$ axis, it is now more convenient to calculate the normal to the magnetopause surface in Cartesian coordinates instead of the polar representation presented in Equation 1.44. If the surface can be expressed as $S(x, y, z) = 0$ then the normal to that surface can be calculated as,

$$\mathbf{n} = \left(\frac{\partial S}{\partial x}, \frac{\partial S}{\partial y}, \frac{\partial S}{\partial z} \right), \tag{3.9}$$

and one can translate between polar coordinates and Cartesian coordinates using the following relations,

$$x = r' \cos\theta, \tag{3.10}$$

$$y = r' \sin\theta \cos\phi, \tag{3.11}$$

$$z = r' \sin\theta \sin\phi, \tag{3.12}$$

where $r' = \sqrt{x^2 + y^2 + (z/\mathcal{E})^2}$ is the distance between the planet and the point on the magnetopause surface described by $(x, y, z/\mathcal{E})$. The surface to which these equations are applied is the flattened *Shue et al.* (1997) empirical shape model, which can be expressed as:

$$S(x, y, z) = r_0 \left(\frac{2}{1 + \frac{x}{r'}} \right)^K - r'. \tag{3.13}$$

Applying Equation 3.13 to Equation 3.9 yields,

$$n_x = 1 + \frac{1}{K}\frac{x}{r'} + \left(\frac{1}{K} - 1\right)\frac{x}{r'}^2, \tag{3.14}$$

$$n_y = \frac{1}{K}\frac{y}{r'} + \left(\frac{1}{K} - 1\right)\frac{xy}{r'^2}, \tag{3.15}$$

$$n_z = \frac{1}{\mathcal{E}^2}\left(\frac{1}{K}\frac{z}{r'} + \left(\frac{1}{K} - 1\right)\frac{xz}{r'^2}\right). \tag{3.16}$$

Since the surface has been flattened, the surface geometry has changed and the angular separation between the incoming solar wind direction (assumed to be along the X_{KSM} axis) and the normal to the magnetopause calculated at the exact location of the crossing has become larger. Therefore Ψ will be larger as shown in Figure 3.5. This will result in a different dynamic pressure estimate for each crossing and this difference will be more pronounced for crossings at larger values of Z_{KSM} where the geometry of the magnetopause varies by the largest amount when it is flattened. However, no significant changes in

the normalised locations of the magnetopause crossings can be seen in Figure 3.2 when the flattening is applied, which implies that this is a fairly minor effect. Figure 3.5b shows the fractional change in D_P (ΔD_P) for all of the crossings used in this study as a result of flattening an axisymmetric surface by 20%. Typically $\Delta D_P < 0.001\,\mathrm{nPa}$ but ΔD_P is highly correlated with Z_{KSM} with a correlation coefficient of $\sim$0.87 such that the estimated dynamic pressure can change by up to 50% for high-latitude crossings. This is outside of the $\sim$30% uncertainty associated with the suprathermal plasma pressure. In addition, some crossings present in the unflattened case may no longer be present when the magnetopause geometry is modified. This is because the iterative Newton-Raphson method used to fit the surface to each individual crossing cannot converge in these cases because the algorithm becomes stuck in an inescapable loop, which is a known issue (e.g. *Kim*, 2014). The further the magnetopause is perturbed from the axisymmetric case by varying $\mathcal{E}$ away from unity, the more difficult convergence seems to become.

A group of crossings at $Z_{\mathrm{KSM}} > 20\,\mathrm{R_S}$ are of great interest to this study. These unusual crossings are very far from the X-Y slices of the model at the same Z_{KSM} coordinate and do not fit either model well. The plasma β measured by the spacecraft for these crossings ranged between $\sim$15 and $\sim$25 and was exceptionally high compared to previous studies by *Sergis et al.* (2007, 2009) and *Masters et al.* (2012a), who found that the plasma β just inside the magnetopause can be of the order 10. For comparison, the median β for all of the crossings used in this study was 1.5. It is possible that some form of transient event occurred during this time and was responsible for energising the plasma or contributing more suprathermal plasma to the system at the time that these crossings were observed.

In order to determine if a solar event may have caused this energisation, the solar wind dynamic pressure estimated using the procedure outlined above was compared to estimates from the Michigan Solar Wind Model (mSWiM) of *Zieger and Hansen* (2008). This model uses data taken from many near-Earth spacecraft as an input and uses a one-dimensional MHD model to propagate this throughout the solar system as far as 10 AU. Its predictions are most accurate within 75 days of near-apparent opposition between the Earth and the object of interest when the Earth and the object are aligned accounting for the travel time. For Saturn, apparent opposition was at day 70 (11 March) 2007 which coincides with the beginning of the data set analysed here and the crossings of interest are within the 75 day period during which the model is most accurate. However, the solar wind dynamic

pressure estimated assuming pressure balance is approximately 60 times larger on average than that predicted by mSWiM, which implies that the high plasma β observed for these crossings was not caused by a solar event. Shifts in the predicted dynamic pressure time series by several hours are not enough to account for these differences, and such shifts introduce further discrepancies between both dynamic pressure estimates.

The elevated plasma pressures observed for these crossings may be the result of ion conics as described by *Mitchell et al.* (2009b); such ion flows of ionospheric origin can remain relatively steady over a period of an hour or more. Alternatively, the magnetopause boundary may have simply been far from equilibrium at the time that the spacecraft crossed it, which may mean the dynamic pressure estimated assuming pressure balance could be very different to the true dynamic pressure. Nonetheless, whatever the cause, it is clear that neither the empirical model constructed by *Kanani et al.* (2010) nor the modification made to that model here can account for the behaviour exhibited by the magnetopause during these observations. In Chapter 4, the impact of variability in the interior suprathermal plasma pressure is explored and the empirical model is modified in order to reconcile the model with observations made when the plasma β is elevated.

It is also worth noting that there is a strong correlation between β and Z_{KSM}. A correlation coefficient of $\sim$0.34 was calculated and the probability of such a strong correlation occurring by chance for a dataset of this size was calculated to be almost zero. In lieu of a physical mechanism responsible for this observation, it is likely to be the result of observational bias and may be additional evidence in favour of polar flattening. It appears that the expanded magnetosphere (corresponding to high-β conditions, as discussed in Chapter 4) is preferentially captured at high-latitudes. This may indicate that the high-latitude magnetosphere expands at a slower rate than the low-latitude magnetosphere in response to a plasma energisation, allowing the spacecraft to sample the expanded magnetosphere more often at high-latitudes. This implies that the degree of polar flattening may have a dependence on the interior plasma β.

3.3.2 Monitoring Pressure Equilibrium at the Magnetopause

In accordance with the statistical law of large numbers, if the magnetopause is observed many times, it is likely to be captured and depicted in an average state that is close to

equilibrium. Multi-spacecraft observations of the Earth's magnetopause by *Dunlop et al.* (2001) using the four *Cluster* spacecraft found that strong and sudden accelerations of the magnetopause boundary can occur. They found that the magnetopause can reach speeds of up to 300 km/s in response to the arrival of an interplanetary shock. If similar behaviour is common at Saturn, scatter may exist in the magnetopause observations where static equilibrium is not a good approximation. Although the magnetopause was assumed to be in equilibrium at the outset of this study, the departure from equilibrium can be quantified as follows.

A 'global' pressure estimate is made for each magnetopause crossing by calculating the dynamic pressure required for the axisymmetric model magnetopause surface to pass directly through each crossing. By calculating the stand-off distance required to achieve this, the expected dynamic pressure can be calculated using Equation 1.40. The ratio between D_P and this new pressure estimate, referred to as P_{GLOB}, can then be calculated. For a crossing observed at a time when the magnetopause is close to equilibrium, this ratio is expected to be close to unity. Large discrepancies between these pressure estimates, and hence a crossing for which this ratio is far from unity, may indicate that the magnetopause was far from equilibrium at the time that the measurements were made. Such observations will add additional scatter to the data when the crossings are normalised to the average dynamic pressure since the dynamic pressure estimates for the crossings rely on the assumption of pressure balance. This ratio was computed for each crossing and a histogram of the results is plotted in Figure 3.6a.

For an axisymmetric magnetopause observed in equilibrium, the ratio $\frac{D_P}{P_{\mathrm{GLOB}}}$ is expected to be unity at all points on the surface. However, when the surface departs from axisymmetry, the stand-off distance for an axisymmetric model fitted through any point on a flattened surface where $Z_{\mathrm{KSM}} \neq 0$ will be consistently underestimated as illustrated in Figure 3.5. Hence, P_{GLOB} will be consistently overestimated and the ratio will drop below unity as shown in Figure 3.6b. As a result, shifts in the ratio for a set of high-latitude magnetopause crossings may either indicate that the magnetopause was not close to equilibrium at the time of the measurement, or may indicate that the surface departs significantly from that of the model. The double-arrowed line in Figure 3.6a shows the range of ratios expected based on using an axisymmetric model to estimate P_{GLOB} for a surface which is actually flattened by 20% ($\mathcal{E} = 0.80$).

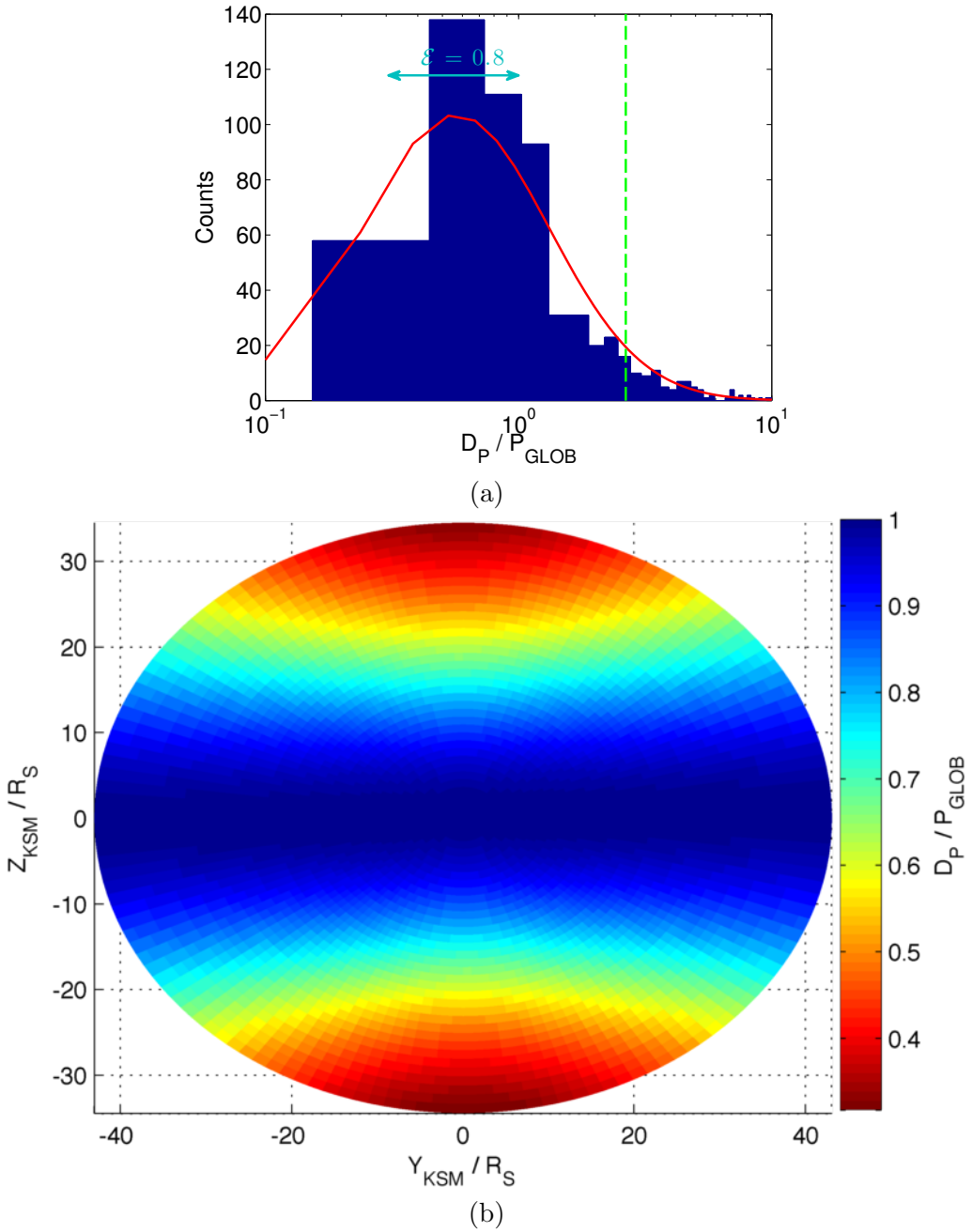

Figure 3.6. (a) The ratio between the dynamic pressure estimated assuming pressure balance and that estimated by fitting the *Kanani et al.* (2010) model through each crossing location has been calculated. This histogram shows the distribution of these ratios on a logarithmic axis and on top of this is plotted a log-normal curve (red line). (b) A flattened magnetopause viewed from the Sun and coloured by the ratio determined by fitting an axisymmetric model through each point on the flattened surface. The arrowed line on (a) indicates the range of ratios determined from (b), and the green dashed line indicates the range within which the magnetopause is judged to be close to equilibrium (the lower bound is off the scale of the graph).

The ratios are similarly distributed to a log-normal distribution and largely enclosed by this interval, but the ratio for some crossings significantly departs from the expected range. These cannot be explained by the departure of the surface from axisymmetry and, thus, it is suggested that they likely arise due to the departure of the surface from equilibrium. Hence, ratios that depart greatly from this range imply that the magnetopause was subject to strong accelerations at the time the observation was made. As a result, this ratio can be used as a diagnostic to determine if the magnetopause was likely to be close to equilibrium when the spacecraft encountered it. Furthermore, if the magnetosphere is just as likely to be expanding as it is to be contracting, a modest departure in the average ratio from unity indicates a systematic departure between the real magnetopause and the geometry assumed by the model – an axisymmetric surface in this case. Such a departure can clearly be seen in Figure 3.6a.

In the lower panels of Figure 3.2, a new criterion has been included to filter the data set. Crossings for which the ratio $\frac{D_P}{P_{\mathrm{GLOB}}}$ lies beyond one interquartile range from the median are discarded (corresponding to an acceptance level of $\sim$95%). This reduces the number of magnetopause crossings to 272, down from the 316 temporally averaged crossings. It can be seen by comparing the upper and lower panels of Figure 3.2 that the amount of scatter in the normalised positions of the crossings has been reduced considerably through the application of this criterion. This criterion removes outliers in a non-biased and non-selective way – more low-latitude crossings have been discarded than high-latitude crossings, as expected, given that the data set contains a larger number of low-latitude crossings.

3.3.3 Statistical Tests

It was noted in Section 3.3.1 that flattening the model magnetopause surface seems to improve its agreement with the observed location of the high-latitude magnetopause after accounting for variations in the solar wind dynamic pressure. Here, this will be demonstrated more rigorously using statistical measures.

Let us consider the Wilcoxon signed rank test (*Wilcoxon*, 1945). This test is used to test the hypothesis that a sample is drawn from a population with a median of zero, and is discussed in more detail in Appendix A.1. It is applied to the magnetopause crossings

that lie in a given range $\{Z_0, Z_f\}$ of the Z_{KSM} coordinate. This range will be referred to as the 'Z_{KSM} band' of the sample. It is necessary to separate crossings into bands of Z_{KSM} as uneven sampling of the high-latitude magnetopause may lead to observational bias if the test is applied to all crossing simultaneously. The quantity to which the rank sum test is applied, $\Delta\rho_i$, is the same distance measure used in Section 3.3.1 and illustrated in Figure 3.3, and is defined as follows:

$$\Delta\rho_i = [(X_{\mathrm{MP}}(Z_i, \mathcal{E}) - X_i)^2 + (Y_{\mathrm{MP}}(Z_i, \mathcal{E}) - Y_i)^2]^{\frac{1}{2}}, \tag{3.17}$$

where the symbols here have the following meanings. There are N normalised crossings in the given Z_{KSM} band, and the i^{th} crossing is located at (X_i, Y_i, Z_i) in KSM coordinates. The magnetopause surface is then constructed at $\langle D_P \rangle$, the pressure to which the crossings have been normalised. The point on the surface with $Z_{\mathrm{KSM}} = Z_i$ that is collinear to the normalised crossing location and (0, 0, Z_i) as illustrated in Figure 3.3 has coordinates $[X_{\mathrm{MP}}(Z_i, \mathcal{E}), Y_{\mathrm{MP}}(Z_i, \mathcal{E}), Z_i]$. Hence, $\Delta\rho_i$ represents a distance between each normalised crossing and the X-Y slice (at the same value of Z_{KSM}) of a magnetopause model with a particular flattening parameter. The two sets of such distances to be compared are simply the $\Delta\rho_i$ evaluated for $\mathcal{E} = 1.00$ (the axisymmetric case) and $\mathcal{E} < 1$ (a flattened magnetopause model). Let us represent these two sets of distances as $\Delta\rho_i(\mathcal{E} = 1.00)$ and $\Delta\rho_i(\mathcal{E} = 0.80)$ with $i = 1 \ldots N$. As shall be seen in the following analysis, $\mathcal{E} = 0.80$ appears to give values of $\Delta\rho_i$ significantly closer to 0 (i.e. a better agreement between the modelled and observed magnetopause location) at high latitudes. This procedure was then generalised by iterating through many values of $\mathcal{E}$ to find the value that, statistically speaking, is the most likely to represent the true magnetopause.

The signed rank test can be used to test the null hypothesis (the hypothesis accepted in the absence of conflicting information) that the median of a distribution is zero. In the case of this experiment, one may expect that if the magnetopause truly exhibits polar flattening, then the distances $\Delta\rho_i$ should, in general, be much closer to zero for the flattened model compared to the axisymmetric model. Hence, the probability $\Delta\rho_i$ is drawn from a population with a median close to zero should be much larger in the flattened case. This test is powerful as it does not rely on the population being normally distributed unlike similar tests, for example the Student's t-test. However, it does assume that the population is symmetric. The adjusted Fisher-Pearson standardised moment

coefficient (*Doane and Seward*, 2011) provides a measure of sample symmetry. This has been calculated for each Z_{KSM} band to determine if each band is, indeed, symmetric and, hence, if the Wilcoxon signed rank test applies. A coefficient of zero indicates that the data are perfectly symmetric, however this is very unlikely for real-world data. For a perfectly symmetric population, as $N \to \infty$ one would expect the sample skewness to tend towards zero as formalised by the Glivenko-Cantelli theorem (*Tucker*, 1959). However, if the sample size is finite, if sample points are drawn randomly from this population then fluctuations will tend to lead to a finite measured skewness. *Doane and Seward* (2010) compiled a table of sample skewness coefficients corrected for sample size. The Fisher-Pearson standardised moment coefficient has been calculated for each Z_{KSM} band. Each Z_{KSM} band was found to be approximately symmetric as the calculated coefficients are well within the limits proposed by *Doane and Seward* (2010). As such, the Wilcoxon signed rank test has been deemed to be appropriate for these data.

Table 3.1 indicates the p-value obtained by applying the Wilcoxon signed rank test to each Z_{KSM} band and for different values of $\mathcal{E}$. This tabulated value may be thought of as the probability of observing results at least as extreme ($\Delta\rho_i$ at least as large) as those that make up the sample, given that the null hypothesis is true. A p-value$\to 1$ thus indicates that there is a high probability of observing the sample under the null hypothesis, and hence, that the null hypothesis is likely to be true. In this case, that means that $\Delta\rho_i$ are likely to be drawn from a population with a median close to zero, which indicates agreement between the model and the observations. In practice, the values determined for each Z_{KSM} band were averaged to determine which value of $\mathcal{E}$ is most likely to match the observations. For each group of crossings, the p-value when a flattening of 19% is applied to the model magnetopause is much larger than that of the axisymmetric model. This indicates that, on average, flattening the magnetopause surface causes it to move closer to the crossing locations and improves the agreement between the data and the model prediction. For the sake of comparison, the results of this test with a flattening of 10% ($\mathcal{E}$ = 0.90) and 30% ($\mathcal{E}$ = 0.70) are also indicated.

$\mathcal{E}$	$P(Z_{KSM} < 7\,R_S)$	$P(7 < Z_{KSM} < 14\,R_S)$	$P(14 < Z_{KSM} < 21\,R_S)$
1.00	0.35 (131)	0.08 (98)	0.02 (33)
0.90	0.55 (131)	0.57 (97)	0.40 (31)
0.81	0.82 (129)	0.47 (94)	0.51 (31)
0.70	0.57 (128)	0.00 (92)	0.00 (28)

Table 3.1. The results of the Wilcoxon signed rank test. The number of crossings within each group is indicated in brackets. There were insufficient magnetopause crossings above $21\,R_S$ for the results to be considered reliable.

3.3.4 Uncertainty in $\mathcal{E}$

The value of $\mathcal{E}$ that provides the best fit between the model and the data is dependent on the distribution of the magnetopause crossings within the bands of Z_{KSM}. Hence it is also dependent on the width of the Z_{KSM} bands, ΔZ_{KSM}. This fact has been used to estimate the uncertainty in the value of $\mathcal{E}$ estimated here for Saturn's magnetosphere. This has been achieved by changing ΔZ_{KSM} and applying the Wilcoxon signed rank test multiple times, iteratively varying $\mathcal{E}$ between 0.70 and 0.90 with a resolution of 0.01. To ensure that a significant number of crossings lie within each band, the minimum value chosen for ΔZ_{KSM} was $5\,R_S$ and this was increased in steps of $1\,R_S$ up to a maximum value of $10\,R_S$. As there are many more crossings at smaller values of Z_{KSM}, it was found that bands at values of Z_{KSM} between $20-35\,R_S$ were sparsely populated. Crossings within these bands were moved down to the band below until a minimum of 25 crossings occupied each band as it is difficult to determine if a sample smaller than 25 is symmetric. This ensures that, statistically speaking, there are enough crossings within each band to enable us to draw conclusions from the data. Future studies could make use of a clustering algorithm, such as *k-means* as discussed in Appendix A.3 and used in Chapter 4, to identify the bands of Z_{KSM} that the crossings tend to naturally fall into.

This procedure yielded a mean, modal and median value of $\mathcal{E} = 0.82 \pm 0.03$, all of which were in agreement within the estimated uncertainties, indicating a polar confinement of $18 \pm 3\%$. A second uncertainty estimate has been made using the Monte Carlo BC_a Bootstrap method (*Efron*, 1987) as discussed in Appendix A.2. The same procedure used to determine $\mathcal{E}$ in Section 3.3.3 is used, but the crossings are iteratively resampled. The same number of data points as exist in the data set are randomly drawn with replacement, meaning that duplicate crossings will exist within each sample that is drawn. As the

crossings are drawn randomly, a different set of crossings are drawn for each resampling. This affects the results of the statistical tests and a confidence region at a given significance level can then be determined. The data were resampled 200 times and $\mathcal{E}$ was found to be 0.81 within a confidence interval of 0.75-0.84 at the 68.3% ($1\,\sigma$) confidence level.

3.3.5 Flattening Pressure Dependence

The reduced set of magnetopause crossings has been separated into two groups in Figure 3.7, one where the estimated dynamic pressure is above average and one where it is below. There seems to be a better distribution of crossings with lower than average dynamic pressure whereas the higher dynamic pressure crossings seem to be clustered around two regions of local time. The same techniques as previously discussed have been used to determine the value of $\mathcal{E}$ that provides the best fit between the model and each data sample.

For the low dynamic pressure crossings, a value of $\mathcal{E}$ of 0.75 within a confidence interval of 0.71 - 0.82 provides the best fit whereas for the high dynamic pressure crossings a value of 0.79 within a confidence interval of 0.78 - 0.93 was found. Hence, within the given uncertainties and for the range of dynamic pressures considered here, the polar confinement of the magnetosphere is insensitive to changes in dynamic pressure. However, the confidence intervals are offset which may indicate that the degree of polar flattening may change with dynamic pressure. These results indicate that the magnetosphere may be flatter under low dynamic pressure conditions. A compression may cause adiabatic heating of the plasma, which would allow more of the thermal plasma population to reach high latitudes and reduce flattening somewhat. Also, if the system is physically smaller, the small scale height of the thermal plasma population becomes less important. However, there is currently insufficient data to resolve this difference outside of the estimated uncertainties so this remains speculation. Future studies comprised of large datasets should endeavour to revisit this.

The flaring parameter, K, is dynamic pressure-dependent but is the same in both cases within the uncertainty limits of the nominal flaring determined by *Kanani et al.* (2010). Average values of $\sim$0.75 and $\sim$0.73 were found for the high and low dynamic pressure crossings respectively, which are both within the $\pm$0.07 uncertainty in a_3 determined by

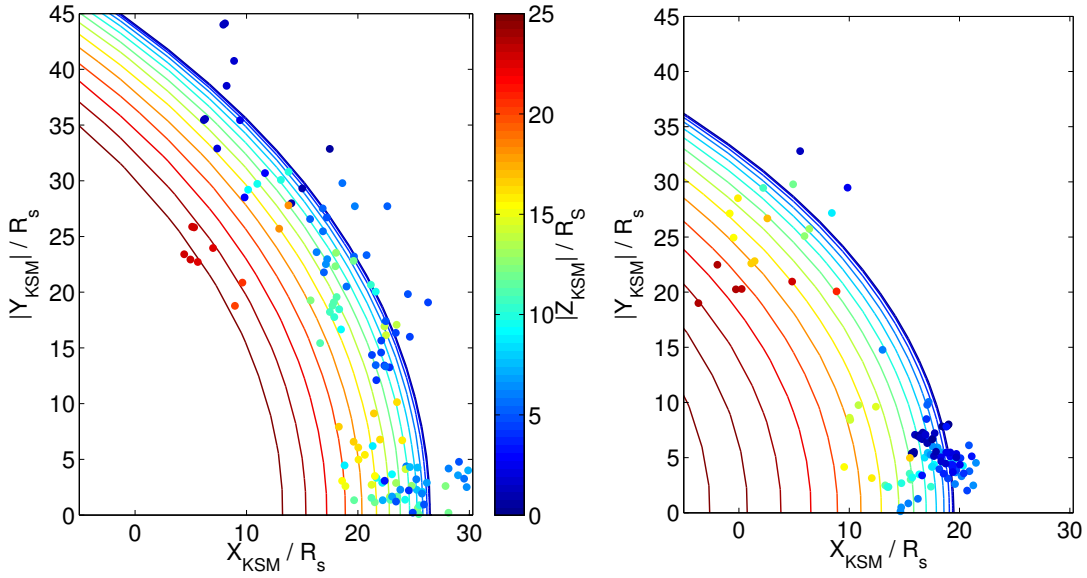

(a) Low Pressure Crossings (b) High Pressure Crossings

Figure 3.7. The crossings have been split into two populations, (a) one of lower than average dynamic pressure and (b) one of higher than average dynamic pressure. X-Y slices of a model flattened using a value of $\mathcal{E}$ of 0.81 have then been plotted over the crossing positions after normalising them to the average dynamic pressure in each group, both of which are coloured by their Z_{KSM} coordinate. The average dynamic pressure in the low pressure group is 0.009 nPa whereas the average dynamic pressure in the high pressure group is 0.045 nPa

Kanani et al. (2010).

3.3.6 Trajectory Analysis

The high-latitude observations discussed earlier in this chapter indicate that Saturn's magnetosphere is significantly flattened in the polar regions. However, it is not clear if this is a permanent feature of Saturn's magnetosphere or if there may be a more transient cause for this effect that is being highlighted as a result of insufficient sampling of the high-latitude magnetosphere. Since the spacecraft is restricted to sampling within a finite radial distance from the planet, if the actual mean position of the boundary is located beyond this maximum distance then the boundary can only be observed under atypical conditions in which the magnetopause is pushed closer to the planet. This could occur as a result of a solar wind compression or could occur as a result of a very low interior plasma pressure. In this context, Figure 3.7 indicates that the high-latitude magnetopause is observed independently of the dynamic pressure since approximately the same number

of crossings occurred under high and low dynamic pressure conditions. This implies that the mean location of the magnetopause boundary is well within the maximum planet-spacecraft distance.

Nonetheless, in order to ensure that the mean position of the boundary was well sampled, the spacecraft trajectory was analysed. Specifically one hopes to identify a clear transition between where the spacecraft spends 50% of the time inside and 50% of the time outside the magnetosphere, even for the high-latitude passes. A similar method to that employed by *Joy et al.* (2002) in the case of Jupiter and subsequently employed by *Achilleos et al.* (2008) in the case of Saturn is used here. The procedure is as follows:

1. Magnetopause crossings are located and the spacecraft trajectory is split into small time intervals. It is important that the list of crossings is as complete as possible to obtain accurate results. It is also important that the resolution with which the trajectory is sampled is small compared to the typical time between crossings. An interval of 10 minutes is used here, much smaller than the three hour period over which crossings were averaged in the preceding analyses.

2. At each point along the spacecraft trajectory, the full set of magnetopause crossings are used to determine if the spacecraft is inside or outside of the magnetosphere and $\rho_{\mathrm{KSM}} = \sqrt{Y_{\mathrm{KSM}}^2 + Z_{\mathrm{KSM}}^2}$ and $\phi_{\mathrm{KSM}} = \tan^{-1}\left(\frac{Z_{\mathrm{KSM}}}{Y_{\mathrm{KSM}}}\right)$ are calculated at each point in time. Occasionally, there may have been some doubt as to whether the spacecraft was inside or outside of the magnetosphere due to a data gap or other such anomaly, in which case the interval in question is discarded. Figure 3.8 shows the portions of the spacecraft orbit inside and outside the magnetosphere.

3. Separate the crossings into bins of X_{KSM} of width ΔX_{KSM} such that there are N_X 'bins' with centres X_{KSM}^i for $i = 1 \ldots N_X$. Further subdivide bins X_{KSM}^i into bins of ρ_{KSM} of width $\Delta\rho_{\mathrm{KSM}}$ with centres ρ_{KSM}^j for $j = 1 \ldots N_\rho$ such that there are now $N_X N_\rho$ bins each containing $M_{I_{ij}}$ data points inside the magnetosphere and $M_{O_{ij}}$ data points outside the magnetosphere.

4. For each X_{KSM}^i bin, calculate the probability distribution of ρ_{KSM}. The probability that the magnetopause's ρ_{KSM} coordinate exceeds that of ρ_{KSM}^j whilst it occupies a particular X_{KSM}^i bin can be estimated as $P(\rho_{\mathrm{KSM}} > \rho_{\mathrm{KSM}}^j) = M_{I_{ij}}/(M_{I_{ij}} + M_{O_{ij}})$.

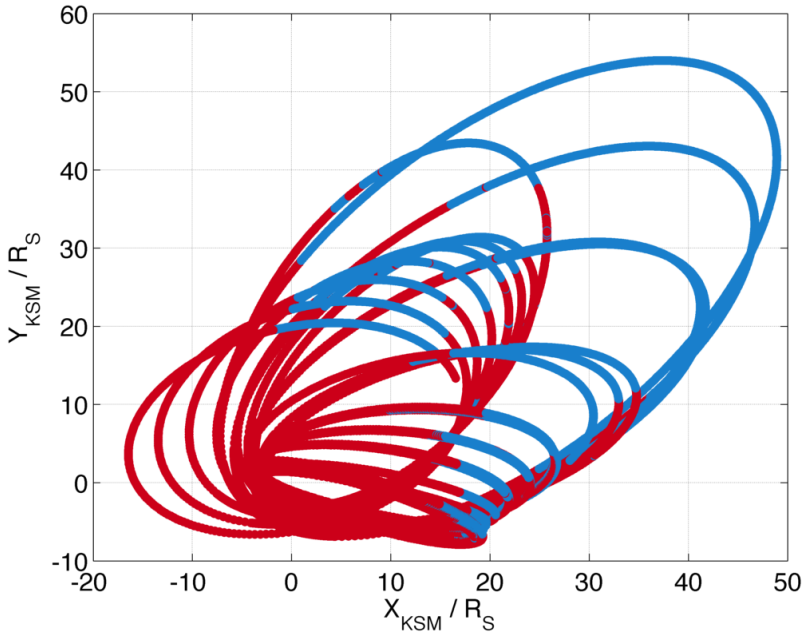

Figure 3.8. The portions of the Cassini trajectory within which the spacecraft was inside (red) and outside (blue) of the magnetosphere are indicated.

5. For each X^i_{KSM} bin, identify if there is a clear 'transition distance', ρ^T_{KSM}, between where the spacecraft spends 50% of the time inside and 50% of the time outside the magnetosphere. If this is the case, the magnetopause is being adequately sampled by the trajectories along which the magnetopause crossings are identified for that particular X_{KSM} bin.

The procedure outlined above was executed after separating the data into two groups based on their ϕ_{KSM} angles into equatorial ($\phi_{\mathrm{KSM}} \leq 50°$) and high-latitude ($\phi_{\mathrm{KSM}} > 50°$) parts of the trajectory. Since ϕ_{KSM} has been defined to range from $0° - 360°$, these data limits are valid only for magnetopause crossings in the northern hemisphere/near-equatorial southern magnetopause crossings. Figure 3.9 shows the results of following this procedure. Included are error bars at the 3σ level determined using a Monte Carlo Bootstrap method, run 1000 times for each X^i_{KSM} bin, such that 99.7% of the results are contained within them. Figure 3.9 shows that in most cases, the transition distance is well captured and hence the magnetopause is being adequately sampled. Figure 3.9b shows the results for the high-latitude parts of the trajectory. Most of the high-latitude crossings used to constrain the degree of polar flattening reside in the range $X_{\mathrm{KSM}} = 0 - 25\,\mathrm{R_S}$ as can be seen in Figure 3.1b. The transition distance is captured in all but one of the X^i_{KSM}

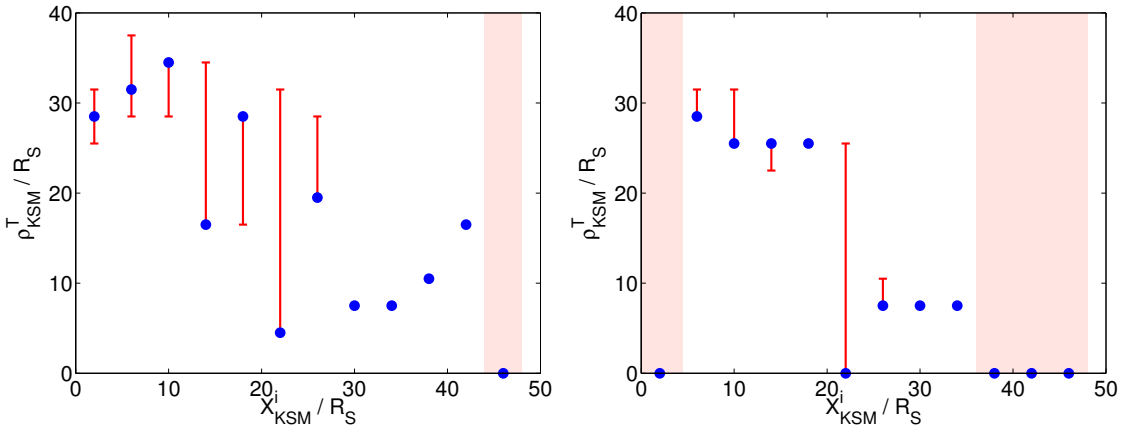

(a) Equatorial Regions (b) Polar Regions

Figure 3.9. The 'transition distance', ρ^T_{KSM}, has been determined through analysis of the spacecraft trajectories over which the magnetopause crossings used in this study were found, and is plotted for each X^i_{KSM} bin as blue points. Regions where a transition distance could not be identified are shaded red. Confidence intervals are also included and were determined using Monte Carlo Bootstrap simulations, resampling 1000 times for each X^i_{KSM} bin.

bins in this range. In addition to this, on average the transition distance is a few planetary radii smaller in the polar dataset than in the equatorial dataset, consistent with a polar confinement.

3.4 Phase of the Global Magnetic Oscillation

Clarke et al. (2006, 2010) found that the planetary-period magnetic oscillation that has been observed at Saturn affects the location of the magnetopause, causing periodic oscillation of the boundary itself with a typical amplitude of $\sim$1.2 $\mathrm{R_S}$. It follows that, these oscillations are likely to impact upon the locations of the magnetopause crossings used in this study. For the current study, this oscillation is not taken into account and is thus likely to contribute to the scatter in the crossing locations. However, a small investigation has been undertaken to determine if the apparent flattening of the magnetosphere discussed thus far may be caused by this oscillation. In order to investigate this, the Saturn Longitude System (SLS3) of *Kurth et al.* (2008) has been used. The SLS3 longitude of the spacecraft at each crossing has been calculated and plotted in Figure 3.10a. The longitude of the peak phase front (defined as 100 ° longitude in the 'core region' in the SLS3 system)

has also been plotted after taking into account the 'bend-back' of the phase front due to the time it takes for the perturbation to propagate through the magnetosphere. Parameters determined by *Arridge et al.* (2011) have been used to accomplish this. Specifically, the distance at which the plasma sheet becomes tilted is taken as $12\,\mathrm{R_S}$ and the phase delay is taken as $6.7^\circ\,\mathrm{R_S^{-1}}$. The difference in phase between the crossings and the peak phase front have been plotted in Figure 3.10b against the Z_{KSM} coordinate of the crossing.

The key result displayed in Figure 3.10 is that there is no evidence of a pattern between the distribution of the crossings in the SLS3 system and the Z_{KSM} coordinate. The crossings at large Z_{KSM} relevant to this study are distributed fairly evenly in SLS3 longitude. If the magnetopause flattening was highly dependent on the magnetic oscillation, one may expect that the crossings at larger Z_{KSM} would be clustered together at a similar longitude in the SLS3 system, but this is not the case. In addition to this, if the magnetic oscillation was the dominant influence on the high-latitude boundary location, the normalised boundary locations at large Z_{KSM} would be scattered evenly around the axisymmetric model boundary. This is not the case as most of these crossings lie inside the axisymmetric surface, as can be seen in Figure 3.2.

3.5 Discussion

The structure of Saturn's magnetosphere has been investigated using in-situ data from the Cassini spacecraft, paying particular attention to the high-latitude regions of the magnetopause which have not before been studied in detail. Magnetometer and electron plasma spectrometer data have been used to identify magnetopause crossings from a set of highly inclined orbits and estimate the solar wind dynamic pressure at the time of each crossing. The spatial locations of these crossings were then normalised to the average dynamic pressure and were compared to models of the magnetopause to determine if the magnetosphere of Saturn exhibits polar flattening as has been observed at Jupiter by *Huddleston et al.* (1998). Even so, a considerable amount of scatter is present in the data and further measures were taken to reduce this by comparing two different pressure estimates for each crossing and removing those where these estimates deviate by more than a factor of three.

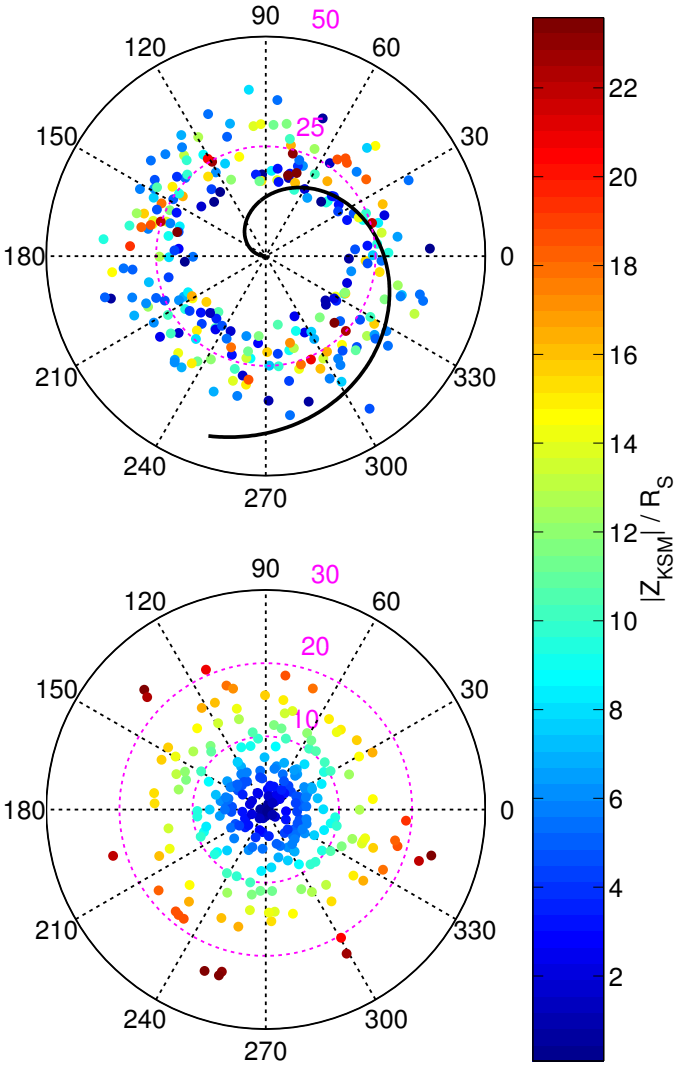

Figure 3.10. The reduced set of magnetopause crossings have been transformed into the SLS3 longitude system of *Kurth et al.* (2008). In (a) the crossings are plotted in this system, the radial distance indicated by the magenta labels corresponds to the extrapolated magnetopause stand-off distance and the crossings are coloured by the absolute value of their normalised Z_{KSM} coordinates. The equatorial peak phase front is plotted as a dark line and is assumed to be invariant of latitude, only radial distance. In (b) the phase difference between each magnetopause crossing and the peak phase front is plotted in order to account for the bend back of the phase front due to the finite wave speed. The black markers surrounding the outermost circle denote the phase difference and the inner magenta markers denote the absolute value of the Z_{KSM} coordinate of each crossing. There is good coverage of crossings at large Z_{KSM} (coloured green-red) with no obvious clustering in terms of phase difference.

By applying a simple dilation to the axisymmetric model magnetopause along the Z_{KSM} direction, a north-south flattening of 19% within a 1σ confidence interval of 13-22% has been found when compared to the *Kanani et al.* (2010) model. This model was derived from equatorial observations of the magnetopause that were not included in this study. Hence, it is expected that more accurate results may be determined by iteratively fitting the model to the observations, including polar flattening as a free parameter. Such a fitting procedure will be explored further in Chapter 4.

The magnetopause crossings identified in this investigation are limited almost exclusively to the dusk sector of the magnetopause and all of those in the dawn sector are located at equatorial latitudes. Future studies should include crossings from the dawn sector so that longitudinal asymmetries in the structure of the magnetopause can be identified. This aspect will be explored further in Chapter 5. Furthermore, these observations are also limited to the northern hemisphere of the planet. This means that the observed flattening could plausibly be related to the passage of the seasons. Seasonal variations are expected due to the angular separation between the magnetic dipole and the solar wind direction, and the corresponding hinging of the magnetodisc and north-south asymmetry that this introduces to the magnetic field structure of the magnetosphere (e.g. *Maurice et al.*, 1996; *Hansen et al.*, 2005). The magnetopause crossings used in this study were located when the planet was approaching the vernal equinox with a dipole tilt angle of $\sim 10^{\circ} - 14^{\circ}$. As such, an angle of $80^{\circ} - 76^{\circ}$ existed between the planetary dipole moment and the upstream solar wind direction. A similar study performed at a different planetary season may reveal what effects the hinging of the magnetodisc has on the structure of the magnetopause, and this will also be further discussed in Chapter 5.

Additional layers of complexity could be added to the model in future studies to improve its fit to the data. The phase of the magnetic oscillation has been briefly touched upon in this study to determine if it could explain the apparent polar flattening that was observed. No evidence was found that the crossings at high Z_{KSM} occured at a similar oscillation phase, as would be expected if the oscillations were the primary cause. However, the oscillations should have some degree of an influence on the location of the magnetopause as found by *Clarke et al.* (2006, 2010). It is likely that if this effect were to be properly taken into account in future studies, there would be a better overall fit between the observations and the model predictions of the magnetopause location.

Chapter 4

Towards A More Realistic Model of Saturn's Magnetopause

There is nothing like looking, if you want to find something. You certainly usually find something, if you look, but it is not always quite the something you were after.

J.R.R. Tolkien, *The Hobbit*

Opportunities multiply as they are seized.

Sun Tzu

In Chapter 3, it was demonstrated that Saturn's magnetosphere exhibits polar flattening. This was characterised by comparing the observed location of the high-latitude magnetopause with the location predicted by the axisymmetric *Kanani et al.* (2010) model, which was derived using equatorial magnetopause measurments. Also discussed in the previous chapter were several magnetopause crossings that did not fit either the axisymmetric model nor the flattened version of that model particularly well. These observations occurred during conditions in which the plasma β just inside the magnetopause exceeded 15, well in excess of the typical values found previously by *Sergis et al.* (2009) and *Masters*

et al. (2012a), for example. In this chapter, a more accurate empirical model of Saturn's magnetopause is presented within which these features are incorporated. This model is also derived from a much richer data set than that used in previous studies, comprising the largest set of crossings of the Kronian magnetopause to date. This list is available in Appendix B.

The most recent empirical models of Saturn's magnetopause are based on the model devised by *Shue et al.* (1997) to describe the Earth's magnetopause. However, the physical properties of Saturn and Jupiter and their magnetospheres relative to that of Earth (e.g. high rotation speeds, internal plasma sources, magnetospheric size scales) imply that the internal dynamics taking place at these systems are significantly different to those within Earth's magnetosphere. Previous empirical studies have also treated the solar wind dynamic pressure as the primary source of variability in the location of the magnetopause. However, magnetohydrodynamic (MHD) studies of the Kronian magnetosphere (e.g. *Zieger et al.*, 2010) found that internal plasma dynamics can change the geometry of Saturn's magnetopause significantly, particularly under low solar wind dynamic pressure conditions. Here, it will be shown that internal plasma dynamics imparts a similar degree of variability to the location of Saturn's magnetopause as does variability in the solar wind pressure. However, in contrast to to MHD studies, strong internally-driven variability in the magnetopause location occurs across the full range of solar wind conditions sampled. In addition to this aspect, previous studies are expanded upon by including high-latitude observations of Saturn's magnetopause in both hemispheres and near-equatorial observations of both the morning and evening sectors, providing much greater coverage of the dayside magnetopause.

4.1 An expanded set of Magnetopause Crossings

The study undertaken by *Kanani et al.* (2010) covered magnetopause crossings of the Cassini spacecraft from before Saturn Orbit Insertion (SOI, July 2004) until January 2006. During this time the spacecraft sampled the low-latitude magnetopause up to $\sim$40 R_S beyond the terminator on the dawn side of the planet. In Chapter 3, magnetopause observations made by Cassini between early 2007 and the end of 2008 were identified, during which the spacecraft sampled the high-latitude magnetopause in the northern hemisphere

on the dusk side of the planet. However, the spacecraft had far poorer coverage of the equatorial magnetopause during this period. Hence, for the purposes of the current study, the interval analysed by *Kanani et al.* (2010) has been reanalysed in order to fill in this 'gap' in the spatial sampling of the study performed in Chapter 3. In general, very good agreement with the original analysis performed by *Kanani et al.* (2010) was found in terms of the times at which crossings are observed.

The present study utilises the data covered by *Kanani et al.* (2010) and those employed in the previous chapter. They are also extended such that crossings from 28 June 2004 (just prior to Saturn orbit insertion) through to 29 October 2010, and from 13 May 2012 until 8 February 2013, are included. The latter period was added because the high-latitude magnetopause in the southern hemisphere was sampled during this time. Coverage was extended from the conclusion of the period used in the previous chapter to late 2010 in order to attain better coverage of the equatorial magnetopause on the dawn side of the planet. The orbits between 29 October 2010 and 13 May 2012 sampled a very similar region to that sampled in the preceding year: the equatorial region on the dusk side of the planet. As a result, they would not have contributed significantly to this study except to reduce the uncertainties in the model parameters derived. Owing to the time-consuming nature of the analysis, the orbits that took place after 13 May 2012 were prioritised, during which the high-latitude southern hemisphere was sampled. The spacecraft trajectories used in this study are shown in Figure 4.1. In the previous chapter, the trajectory of the spacecraft was analysed to ensure that the sampling of the high-latitude magnetopause was adequate, such that the results were not biased by observations of extreme magnetopause configurations. That exercise is not repeated here, but those results are used in order to reduce the data to avoid bias where necessary, i.e. crossings with $X_{\mathrm{KSM}} \leq 2.5\,\mathrm{R_S}$ were discarded because the transition distance was not clear for these crossings.

It should also be noted that, since this study spans a sizeable fraction of a Kronian year, seasonal variability in the magnetopause geometry is now an issue of which to be aware. Specifically, *Maurice et al.* (1996) and *Hansen et al.* (2005) predicted a significant north-south asymmetry in the magnetopause geometry under conditions where the magnetic dipole is not orthogonal to the direction of solar wind flow. Such a situation occurs over the majority of the Kronian year as those vectors are only truly orthogonal at equinox. Seasonal variability is thus expected to affect the location of the high-latitude

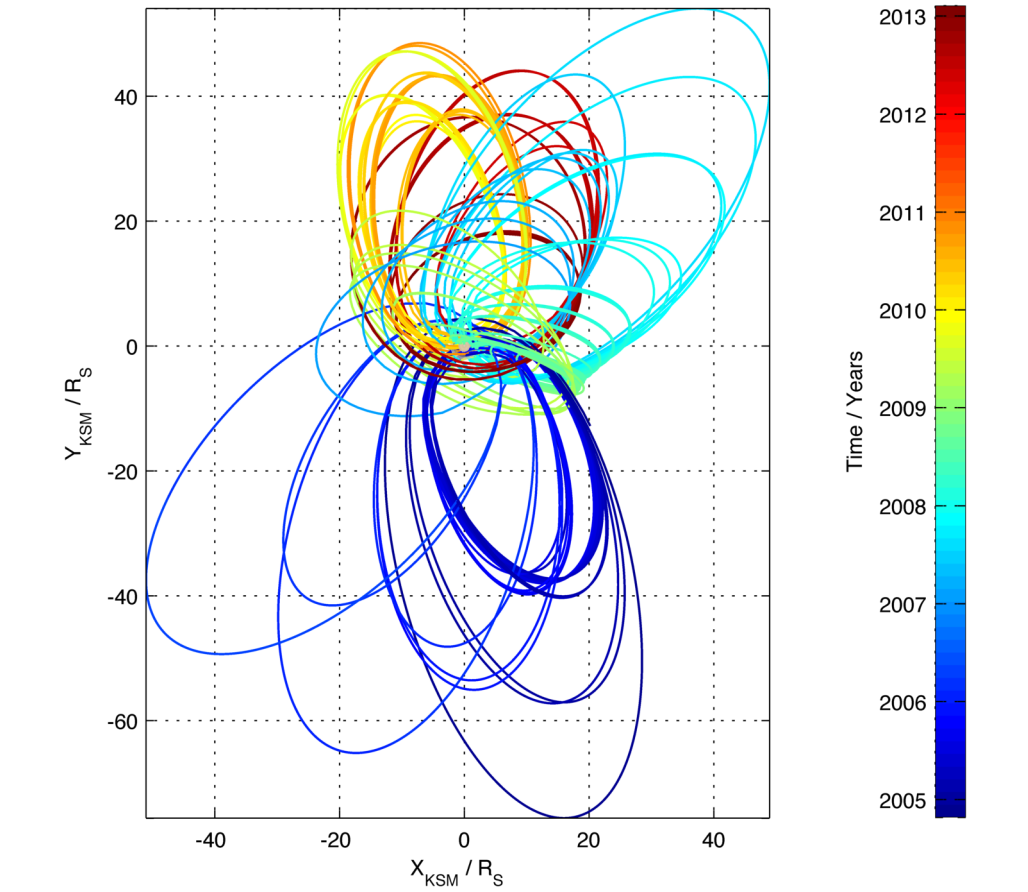

(a)

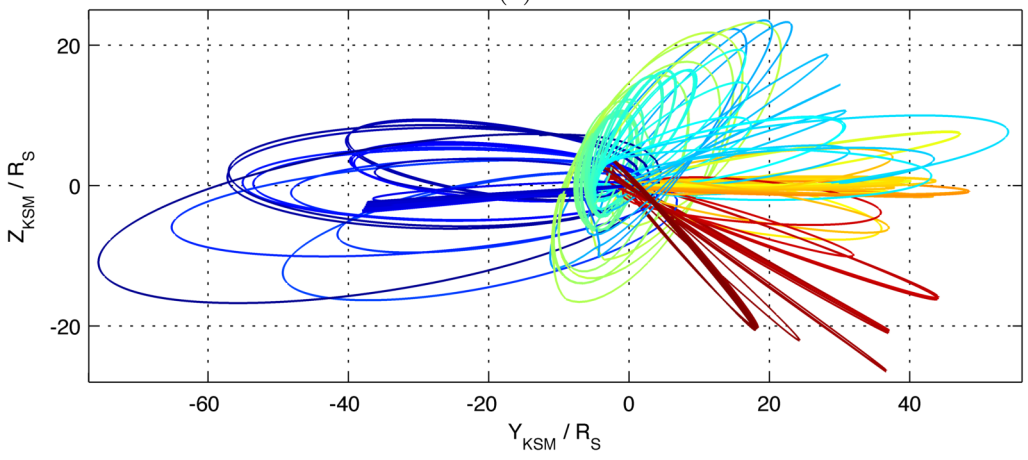

(b)

Figure 4.1. Spacecraft trajectories containing at least one crossing of the magnetopause from just prior to SOI in 2004 to late 2010, and from mid-2012 to early 2013. Orbits along which no crossings were found were discarded and the 'gaps' which arise from discarding orbits are smoothed over using a moving average filter with a span of 11 hours to avoid the appearance of sudden jumps in the location of the spacecraft. For comparison, Figure 2.3 shows the complete set of orbits between SOI in 2004 and early 2013.

magnetopause crossings. However, in the current study, all high-latitude observations were made at similar hemispheric season since the crossings in the northern and southern hemispheres were separated by roughly six years. The magnetic dipole was titled away from the Sun by $\sim 10 - 14^{\circ}$ in the northern hemisphere in 2007 when the high-latitude observations were made in that region. Similarly, in the southern hemisphere the southern magnetic pole was tilted away from the Sun by $\sim 14 - 17^{\circ}$ in 2012–2013 when the high-latitude observations took place there. As such, one may expect the degree of polar flattening to be similar in both hemispheres. Indeed, if the empirical model outlined in Section 4.3 is fitted to crossings in each hemisphere separately, the same degree of polar flattening is retrieved within the fitting uncertainties with a polar flattening of $19 \pm 1\%$ ($21 \pm 1\%$) found in the northern (southern) hemisphere. It is thus assumed for this particular dataset that it is appropriate to fit a single empirical model describing polar flattening using a single free parameter. However, the effect of seasonal variability on the high-latitude magnetopause will be quantified in Chapter 5.

As before, data from the Cassini fluxgate magnetometer and electron plasma spectrometer were used to identify magnetopause crossings. In total, 1607 magnetopause crossings were identified. Of these, suprathermal pressure moments derived from observations made by the MIMI instrument (*Sergis et al.*, 2009) were unavailable for 93 crossings, leaving 1514 crossings. In previous studies and in the previous chapter, crossings closely separated spatially and in time were averaged together to prevent artificial weighting due to boundary motions (e.g. *Slavin et al.*, 1983; *Arridge et al.*, 2006; *Kanani et al.*, 2010). Here, it is pointed out that, due to the underlying assumption of pressure balance across the magnetopause, this practice could, in fact, be detrimental and could reduce the accuracy of the empirical model. This is because the magnetopause moves much faster than the spacecraft (to zeroth order, it can be assumed that the spacecraft is stationary with respect to the magnetopause). As a result, if the magnetopause is observed on multiple occasions within a short period of time, it is likely to be close to equilibrium because, otherwise, it would be observed just once as it moves rapidly past the spacecraft. So, in that sense, the absence of averaging could improve the study as, essentially, measurements where pressure equilibrium is a good assumption would be slightly more highly weighted. Furthermore, *Jia et al.* (2012) found using MHD simulations that even under steady solar wind conditions the magnetopause experiences periodic movements. Temporal variability

of the magnetopause under such conditions will be preserved by using the full set of data without averaging.

For completeness, the effect of averaging on the results of this study was investigated. Crossings on the dawn and dusk sides within 5 and 3 hours of each other respectively were averaged together, in accordance with the study of Saturn's boundary motions by *Masters et al.* (2012b). In practice, if two crossings were observed within this period the one with the poorer statistics was discarded, judged by calculating the standard deviation in the magnetic field and suprathermal plasma pressure. In some cases, the estimated dynamic pressure between the two observations was significantly different, which added additional scatter to the data when the quantities were averaged. Since such crossings are close together both temporally and spatially, averaging their positions makes very little difference to their locations. After averaging, 737 crossings remained with which to fit the model. It was found that averaging had no significant effect on the fitting results presented in later sections within the estimated model parameter uncertainties, so the results fitted to the entire data set without averaging (i.e. using 1514 crossings) are presented. The only difference between made to the results is that the magnitude of the uncertainties in the fitted model parameters are smaller when the full data set is used.

The full set of magnetopause crossings is displayed in Figure 4.2 in the Kronocentric Solar Magnetospheric (KSM) system. The spacecraft positions were calculated using the reconstructed trajectory kernels of NASA's Navigation and Ancillary Information Facility 'SPICE' software library.

4.2 Estimating the Solar Wind Dynamic Pressure

The first stage of the fitting procedure involves estimating the dynamic pressure at the time of each magnetopause crossing, at which the model surface will be constructed. The same method is employed here to estimate the dynamic pressure as in the studies described in Chaper 1 and used in the previous chapter. *Kanani et al.* (2010) accounted for the pressure associated with low-energy protons by assuming that their number density is 20% of the low-energy electron density and, hence, that they have a pressure contribution equivalent to 20% of the electron pressure assuming equal temperatures. However, the

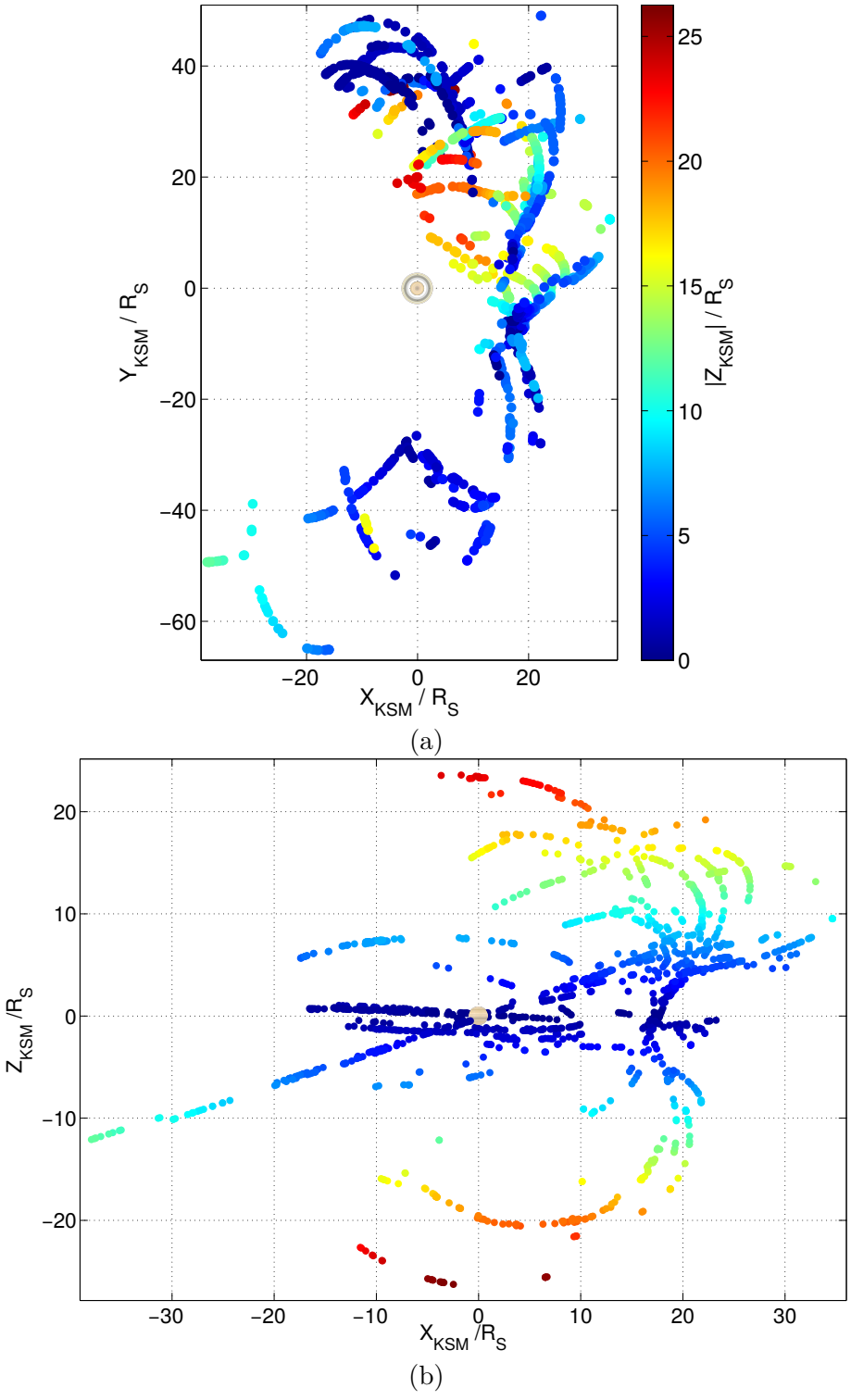

Figure 4.2. Shows the distribution of the magnetopause crossings between SOI in 2004 to late 2010, and from mid-2012 to early 2013 in the KSM system coloured by their Z_{KSM} coordinates with the planet at the origin. (a) shows that there is good coverage of the equatorial magnetopause on both flanks but high-latitude coverage is restricted to the dusk flank. (b) shows that there is high-latitude coverage of both hemispheres.

pressure associated with the water-group ions within this energy range was not considered by *Kanani et al.* (2010). In the present study, the pressure contribution made by the water group ion population with energies <45 keV (defined here as 'low-energy') is estimated using the results of a survey of such measurements made by *Thomsen et al.* (2010), who used Cassini plasma spectrometer (CAPS) measurements in order to accomplish this. The energy ranges of the CAPS and MIMI instruments overlap between 3−45 keV, and pressure moments derived from the latter are also used in this study, meaning that the pressure contribution for ions in the overlap region may be counted twice. However, *Sergis et al.* (2010) found that the overestimation of the total pressure due to this overlap is generally less than 25% as the sensitivity of the CAPS instrument drops as it approaches its upper limit detection threshold. This is of the same order as the uncertainty in the suprathermal plasma pressure.

Thomsen et al. (2010) surveyed the properties of the low-energy ion population using the CAPS ion mass spectrometer. They found that beyond $L{\sim}11\,\mathrm{R_S}$, where L is the intersection of a dipole field line with the magnetic equator, the pressure associated with the thermal water-group ion population at the rotational equator is comparable to the suprathermal contribution. This is in agreement with the results of *Sergis et al.* (2010). To obtain an upper limit estimate of the additional contribution made to the magnetospheric pressure by the thermal ions, the same data as was used by *Thomsen et al.* (2010) is used here with equatorial pressures binned by L. But instead of the bin averages (c.f., *Thomsen et al.* (2010), Figure 12), the maximum pressures found in each bin are fitted to in order to determine how sensitive the results are to the inclusion of this pressure source in the first instance. The resulting upper-limit profile is given by,

$$P_e(\mathrm{n\,Pa}) = 287L^{-3.14}, \tag{4.1}$$

where P_e is the equatorial pressure measured in nanopascal at the centre of the plasma sheet and L is measured in planetary radii. To account for the strong centrifugal confinement of the thermal plasma near the current sheet, the equatorial pressure (Equation 4.1) is scaled with height above the plasma sheet, z, in the same way as *Hill and Michel* (1976),

$$P_{\mathrm{COLD}}(z) = P_e \exp\left(-\frac{z^2}{H^2}\right), \tag{4.2}$$

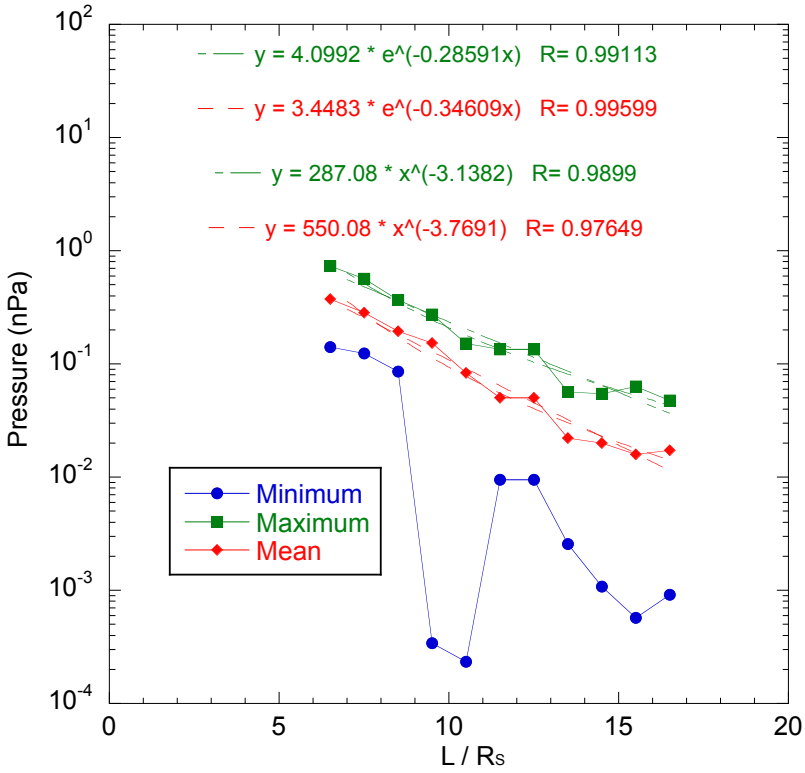

Figure 4.3. Power law fits to the mean, minimum and maximum thermal water-group ion pressures measured in the corotation direction.

where P_{COLD} is the thermal ion pressure contribution estimated for a given magnetopause crossing and H is the ion scale height at Saturn's magnetopause, which was found to be $\sim 5\,\mathrm{R_S}$ for low energy W^+ ions at $\mathrm{L}\sim 17\,\mathrm{R_S}$ by *Thomsen et al.* (2010).

Arridge et al. (2008) found that the plasma sheet is deflected out of the spin equator as a function of planetary season due to solar wind forcing on the magnetospheric field. This result appears intuitive when the system is viewed in the KSMAG frame of reference as shown in Figure 4.4. The KSMAG frame is equivalent to the KSM frame rotated about the Y_{KSM} axis. The Z_{KSMAG} axis is aligned with the magnetic dipole (and thus very nearly aligned with the spin axis of the planet) and the X_{KSMAG} axis points in the general direction of the Sun but is rotated away from the planet-Sun line by an angle equivalent to the dipole tilt angle in the KSM frame. As shown in Figure 4.4, in the KSMAG frame the solar wind is incident upon the magnetosphere at an angle λ to the dipole equator, so the naïve explanation is that the plasma sheet is deflected out of the plane of the magnetic equator by solar wind forcing.

However, in reality the interaction is more subtle than this as the solar wind cannot gain

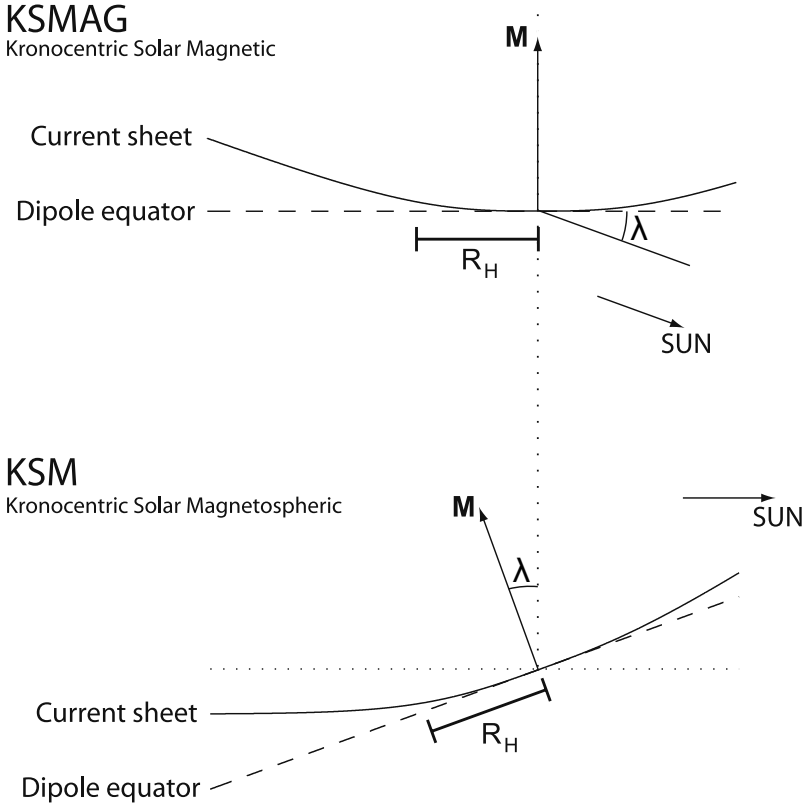

Figure 4.4. Shows the relationship between the KSM and KSMAG frames of reference. **M** is the magnetic dipole axis along which the Z_{KSMAG} axis is oriented. The KSMAG frame is equivalent to the KSM frame rotated about the Y_{KSM} axis by the dipole tilt angle, λ. Hence, the Y_{KSM} and Y_{KSMAG} axes are equivalent. Modified from *Arridge et al.* (2008).

direct access to the plasma sheet in order to deflect it out of the magnetic equator. Instead, the magnetospheric field becomes north-south asymmetric about the planet-Sun line away from equinox, partly by virtue of the tilted dipole with respect to the flow of the solar wind. Via the presence of magnetopause currents, solar wind forcing on this asymmetric magnetospheric field changes the structure of the magnetopause and this results in a large-scale change in the magnetospheric field. This ultimately causes the deflection of the plasma sheet out of the magnetic equator at a characteristic distance known as the 'hinging' distance. Presumably, at radial distances below the hinging distance the magnetic field is strong enough to resist the modification imparted upon the magnetospheric field by the solar wind. Or perhaps closer to the planet than the hinging distance, the modification is simply too small to be resolved using current methods.

Furthermore, *Arridge et al.* (2011) found that the plasma sheet also oscillates about

its mean deflected position in phase with the magnetic oscillation (e.g. *Andrews et al.*, 2008). To determine the effective value of z in Equation 4.2 for each of the magnetopause crossings used in this study, the spacecraft position is referenced with respect to the expected location of the current sheet, given by *Arridge et al.* (2011):

$$z_{\mathrm{CS}} = \left[\rho - r_{\mathrm{H}} \tanh\left(\frac{\rho}{r_{\mathrm{H}}}\right)\right] \tan\lambda + (\rho - \rho_0) \tan\theta_{\mathrm{TILT}} \cos\Psi_{\mathrm{PS}}, \tag{4.3}$$

where z_{CS} is the displacement of the current sheet away from the spin equator, ρ is the cylindrical distance from Saturn measured in the equatorial plane, r_{H} is the hinging distance and λ is the dipole tilt angle, which is equivalent to the subsolar latitude. ρ_0 is the distance at which the plasma sheet becomes tilted, θ_{TILT} is the tilt angle of the plasma sheet and, finally, Ψ_{PS} is the phase of the plasma sheet oscillation. The hinging distance has been taken to equal the standoff distance of the magnetopause surface that passes directly through each crossing location as suggested by *Arridge et al.* (2008). Values for θ_{TILT} ($7.0°$) and ρ_0 ($10\,R_{\mathrm{S}}$) were chosen in order to maximise the displacement of the oscillating current sheet whilst remaining consistent with the results of *Arridge et al.* (2011). The current sheet was chosen to be centred on any magnetopause crossing where its combined hinging and oscillation could cause it to move to such a position, thus maximising P_{COLD} in the first instance in order to ascertain how important this pressure contribution may be. If an upper limit estimate does not affect the results considerably, then it is unlikely to be an important contribution and a more detailed analysis would be unnecessary. Hence, Equation 1.54 then becomes:

$$kD_{\mathrm{P}} \cos^2(\Psi) + \frac{k_b T_{\mathrm{SW}}}{1.16 m_p u_{sw}^2} D_{\mathrm{P}} \sin^2(\Psi) = \frac{B^2}{2\mu_0} + P_{\mathrm{MIMI}} + P_{\mathrm{COLD}}. \tag{4.4}$$

The upper limit P_{COLD} that is used here is comparable to but smaller than P_{MIMI} in general but $P_{\mathrm{cold}}/P_{\mathrm{MIMI}} \ll 1$ for the high-latitude crossings as anticipated. Including the P_{COLD} term provides a small improvement to the fitting RMS residual discussed in the next section. However, the parameters derived from fitting the empirical model to the dataset described in Section 4.1 are insensitive to its inclusion within the fitting uncertainties at the 2σ level.

4.3 Fitting Procedure

The observations outlined in Section 4.1 will be used in order to construct a more accurate and flexible empirical model of the Kronian magnetopause. The empirical model presented by *Shue et al.* (1997) to describe the terrestrial magnetosphere and used by *Arridge et al.* (2006) and *Kanani et al.* (2010) in relation to the Kronian magnetosphere is used to facilitate this, but here it is modified to incorporate the polar flattening observed in Chapter 3. As a reminder to the reader, the *Shue et al.* (1997) empirical shape model is described by the following equations,

$$r = r_0 \left(\frac{2}{1 + \cos\theta} \right)^K, \tag{1.39 revisited}$$

$$r_0 = a_1 D_P^{-a_2}, \tag{1.40 revisited}$$

$$K = a_3 + a_4 D_P, \tag{1.41 revisited}$$

where r is the distance from the planet centre to the point on the magnetopause surface described by the angle θ, the angle between the position vector of this point and the planet-Sun line as shown in Figure 1.17. The surface is parameterised in terms of the standoff distance, r_0, which controls the size of the magnetosphere, and the 'flaring' parameter, K, which controls the downstream shape. Visual representations of these quantities are shown in Figure 1.18.

An iterative method is used to fit the model surface to the magnetopause observations, starting from an initial set of parameters a_i and iterating until these coefficients converge. The fitting routines used by *Arridge et al.* (2006) and*Kanani et al.* (2010) are implementations of the gradient-based family of Newton-like solvers which start at a given set of coefficients and iterate until convergence is achieved. These fitting routines are guided by

the RMS residual,

$$RMS = \sqrt{\frac{\sum_{i=1}^{N}(x_i - y(x_i))^2}{N}} \tag{4.5}$$

where $x_i - y(x_i)$ is the distance between the observed location of the magnetopause and the location predicted by the model for the i^{th} magnetopause crossing, and N is the number of observations. One of the major drawbacks of the fitting routines used in previous studies is that they can only achieve convergence within the basin of attraction within which the starting parameters fall, and this may not be the solution that minimised the RMS residual globally. Often, this is mitigated by repeating the fitting at different starting values to have a better chance of finding the global minimum. Here, a more sophisticated algorithm described by *Ugray et al.* (2006) is used which aims to locate the global minimum efficiently by generating a set of trial points which are then ordered based on their feasibility in terms of the fitting constraints. The only constraints used in this study are bounds on the coefficients; this is necessary as it is infeasible to sample all of parameter space in order to identify the best solution. In most cases, these bounds were chosen at the physical limit for each coefficient. Where there was no physical reason to restrict a parameter, very large bounds were chosen such that the solutions from past studies are contained by at least three times the estimated uncertainty. The best-fitting coefficients obtained in this study were all also more than 3σ away from the bounds prescribed.

A local solver is initiated at each trial point in the sequence and a list is compiled containing the starting points, the solutions that the solver ultimately converged to and the distance between the start and end points. Several different local solvers of varying complexity were experimented with by applying them to a synthetic set of magnetopause crossings randomly generated from a known model with the aim of reproducing that model. Dynamic pressures were also randomly generated for each synthetic crossing from the empirically determined pressure distribution and Gaussian noise was then added to the crossing locations. Each solver was then trialled on the synthetic data to evaluate which solver was able to most closely replicate the known model. Ultimately, the implementation of the interior-point algorithm of *Waltz et al.* (2005) in the *MATLAB Optimization Toolbox* provided the most accurate results. Between each call, the maximum distance between the trial solutions that successfully converged and the solutions they ultimately converged

to is used to estimate the radius of the basin of attraction for subsequent trial solutions by multiplying it by an empirically chosen scale factor. This scale factor is used to balance the compromise between efficiency and accuracy and was determined by *Ugray et al.* (2006) by running the global solver on many different problems of varying complexity.

Figure 4.5 illustrates the sequence of operations performed by the local solver for each trial solution. At each iteration, the dynamic pressure for each magnetopause crossing is estimated using Equation 4.4. The model described by parameters a_i is then constructed at the estimated dynamic pressure for each magnetopause crossing. The distance between the observed location of the magnetopause and that predicted by the model is then calculated. This is achieved as follows.

At each iteration, the model described by parameters a_i was fitted precisely through the location of each observed magnetopause crossing to within a tolerance of $10^{-6}\,\mathrm{R_S}$ in order to calculate Ψ and hence D_P. Initially, a simple Newton-Raphson solver was used to do this efficiently but it was found that successful convergence for many crossings was sensitive to the choice of a_i. Now, more sophisticated solvers from the MATLAB Optimization Toolbox are used. A Levenberg-Marquardt solver is used in the first instance as convergence can be achieved for the vast majority of crossings relatively efficiently using this solver. For crossings where this was not possible, the trust region reflective solver is used, which was more computationally expensive but has yet to fail to converge for this purpose. Complete convergence is necessary because the top-level local solver requires a smooth objective function and gradient thereof to operate correctly, an assumption which is violated if convergence is not achieved for every single crossing fed into the solver. On the boundary in coefficient space that defines the contour along which a particular crossing will only just converge using one of the simpler solvers, if one were to take an infinitesimally small step onto the other side of this boundary that crossings will no longer converge. The information provided by this crossing is lost on the 'non-converging' side of the boundary. One might imagine that this would cause an artificial 'jump' in the merit function across this boundary because, along the boundary, the information provided by that crossing is included but is lost immediately adjacent to it.

The model is then constructed using the resulting solar wind dynamic pressure estimate, and the distance between each observed magnetopause location and the locations

predicted by the model described by a_i is calculated as discussed in the next section. This set of distances is used to inform the top level solver as to how well the model described by a_i fits the observations. The current set of coefficients and the numerically computed derivative of the distance function are used to inform the search direction and, hence, the next set of coefficients. This procedure is repeated until the RMS distance converges to within $10^{-6}\,\mathrm{R_S}$.

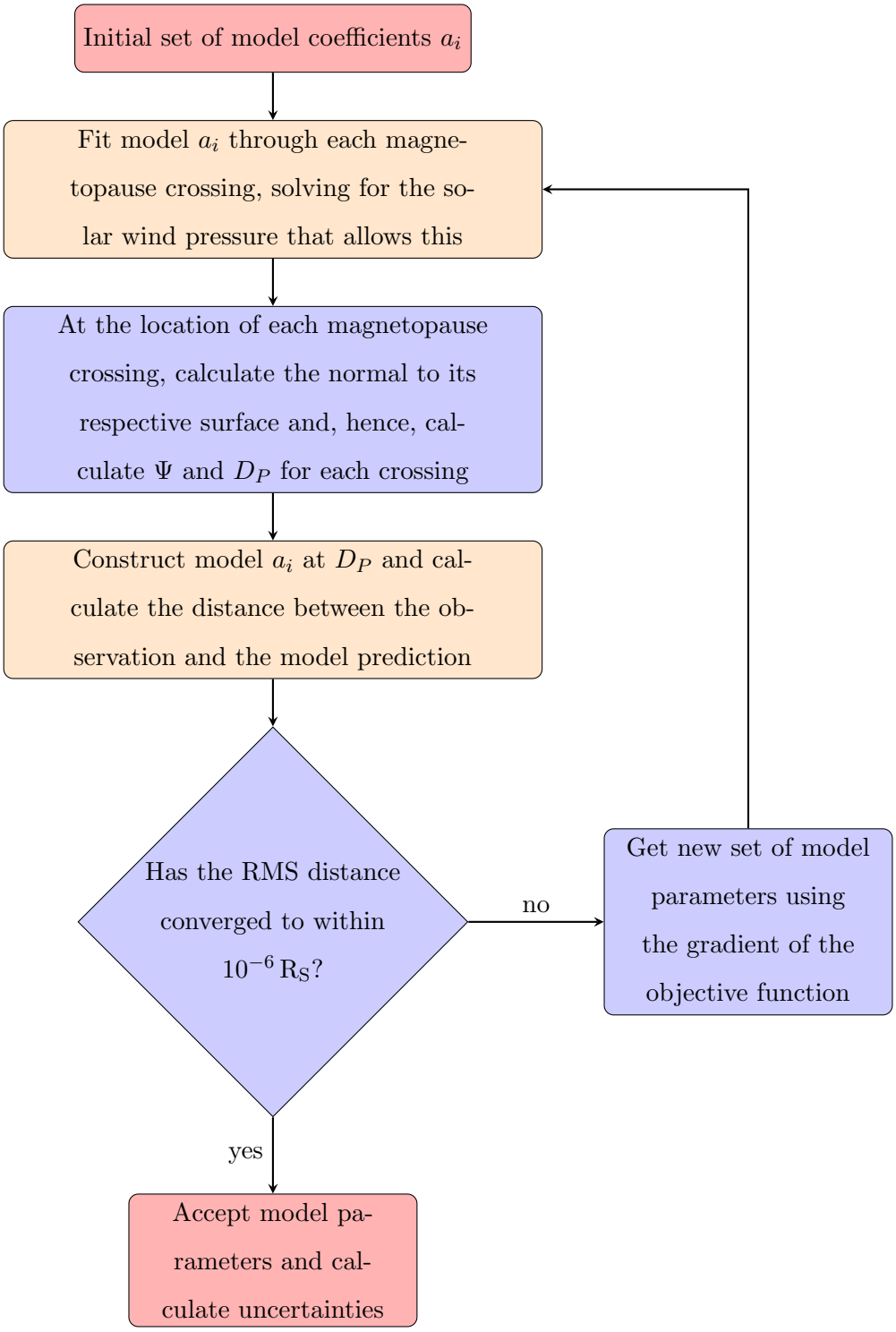

Figure 4.5. Flowchart illustrating the iterative fitting sequence described in Section 4.3. The processes shaded orange are themselves iterative processes, and the whole sequence is performed iteratively on a series of trial solutions in order to efficiently search for the solution that provides the minimum distance between the observed magnetopause and the location predicted by the model.

.

4.4 A Better 'Fitness' Criterion

In order for the solver to know in which direction to move in parameter space, a goodness-of-fit estimator must be calculated at each iteration. A good choice is the distance between each crossing location and the surface described by a_i and D_P. Previous studies used the distance between the crossing and the point where the model surface intersects the crossing radial vector (the blue and red points in Figure 4.6 respectively) as an approximation for the crossing-surface distance. Here, a near-exact solution to the minimum crossing-surface distance is found by solving a system of nonlinear equations numerically, using the fact that the shortest distance between a point and a surface is along the normal to the surface that passes through that point,

$$S(x_0, y_0, z_0) = r_0 \left(\frac{2}{1 + \frac{x}{r(x,y,z)}} \right)^K - r(x_0, y_0, z_0) = 0, \tag{4.6}$$

$$x_0 - x - Rn_x = 0, \tag{4.7}$$

where x and x_0 are the X_{KSM} coordinates of the crossing location and the point on the surface closest to the crossing respectively, n_x is the X_{KSM} component of the outward-directed normal to the surface computed at the closest point to the crossing and R scales the normal vector to the crossing location and is equal to the crossing-surface distance if the unit normal is used. Hence, R is zero if the model surface passes directly through the crossing location and positive (negative) if the crossing lies outside (inside) the surface. Equation 4.6 constrains the solution to lie on the surface. Analogous equations to Equation 4.7 can be constructed for the other two spatial coordinates, Y_{KSM} and Z_{KSM}, and these three equations ensure that the closest point to the crossing is found. An initial guess is required for (x_0, y_0, z_0, R), but the ultimate solution does not depend on this guess as there is only one solution that can satisfy these equations for any given magnetopause crossing and D_P. The radial approximation used in previous studies is a good first guess that can be used to minimise computation time.

These equations can be solved for (x_0, y_0, z_0, R) for each magnetopause crossing to an arbitrary degree of accuracy and so, effectively, represent an exact solution. The distance

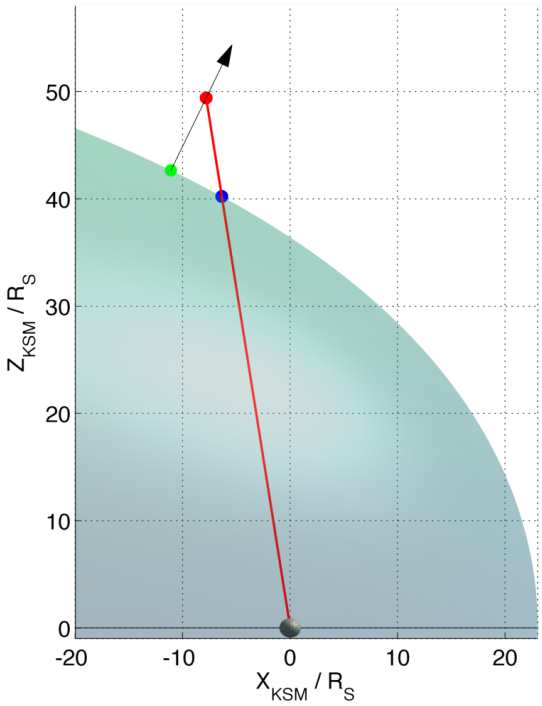

Figure 4.6. Illustrates how the distance between a magnetopause crossing and the empirical surface described by a_i is calculated. The red point is the observed magnetopause crossing, the shaded region is the empirical surface constructed at D_P and the planet is shown at the origin. The blue point is where the crossing radial vector (red line) intersects the surface and the green point is the closest point on the surface to the crossing, which is found iteratively. A view of the plane containing all three points of interest is displayed. The arrow indicates the normal to the surface at the closest point to the crossing and shows that it passes directly through the crossing location, meaning that the green point is, indeed, the closest point.

between each magnetopause crossing and the model surface, constructed at the dynamic pressure estimated assuming pressure balance from Equation 4.4, was calculated along with the RMS residual. The fitting routine was then iterated until the RMS residual converged to within a tolerance of $10^{-6}\,\mathrm{R_S}$. Fitting using the radial approximation method applied in previous studies and the exact method presented here yield the same results for all but one of the model coefficients within the estimated uncertainties. The coefficient a_3, which chiefly controls how much the magnetopause 'flares' by in Equation 1.41, was significantly different between the two methods. This is because the approximate method breaks down as an estimate of the shortest distance between the crossing and the model surface the further into the magnetotail the model is projected. The crossings in this region of space that best define the degree of magnetopause flaring so it stands to reason that a_3 would

be the most affected by such a change in the calculation of the crossing-surface distance. The results obtained using both methods were compared and it was found that the new method reduced the RMS residual by $\sim 0.6\,\mathrm{R_S}$, indicating a substantial increase in the model accuracy.

4.5 Coefficient Uncertainty Estimation

The most efficient method of estimating the standard error for each of the model coefficients is to approximate the coefficient covariance matrix. This can be done using the variance in the distance between observed magnetopause crossings and the locations predicted by the model, known as the residual. This distance, R, can be calculated using the procedure outlined in Section 4.4. The sample variance, σ^2, can then be calculated as,

$$\sigma^2 = \frac{1}{N-1}\sum_{j=1}^{N}(R_j - \mu)^2, \tag{4.8}$$

where N is the number of observations, R_j is the model-crossing distance for the j^{th} crossing and μ is the sample mean.

The coefficient covariance matrix can then be calculated from the variance and the Jacobian matrix, a matrix of dimensions $i \times j$ of the first order derivatives of the R quantities with respect to coefficient i:

$$J = \begin{pmatrix} \frac{\partial R_1}{\partial a_1} & \cdots & \frac{\partial R_1}{\partial a_i} \\ \vdots & \ddots & \vdots \\ \frac{\partial R_j}{\partial a_1} & \cdots & \frac{\partial R_j}{\partial a_i} \end{pmatrix}. \tag{4.9}$$

The coefficient covariance matrix, C, is then given by,

$$C = (J^T J)^{-1}\sigma^2, \tag{4.10}$$

where J and σ^2 are evaluated at the best-fitting set of coefficients. A first order approximation to the standard error of each coefficient can then be determined by taking the square root of the diagonal elements of C.

Note, though, that this approach neglects second order covariances between the coefficients, which are important if the magnitude of the off-diagonal elements are comparable to the magnitude of the diagonal elements of C. Figure 4.7 (which will be discussed in more detail in Section 4.6.1) shows that this is, indeed, the case for some of the coefficients used in this study. In particular, the upper left panel shows that the uncertainty ellipses are significantly inclined, which indicates a strong correlation between coefficients a_1 and a_2. The standard error calculated for a particular coefficient using the above procedure can be interpreted as the standard error of one coefficient assuming that the other coefficients remain fixed (the vertical or horizontal extent of the ellipse at the 'fixed' value of the other coefficient, depending on the coefficient being considered). However, if two coefficients are strongly correlated, changing one coefficient tends to cause a change in the other. Such a correlation indicates redundancy in the model and implies that the model can be simplified by expressing one coefficient in terms of the other coefficient. In this case, it indicates that system size (indicated by a_1) is strongly linked to the compressibility of the system (indicated by a_2).

In cases in which a strong correlation is identified, more robust methods can be used to estimate the uncertainties instead. For the purposes of the current discussion, the Monte Carlo Bootstrap method discussed in Appendix A.2 is used. This is a powerful technique that can be used to calculate the distribution of the coefficients, and contains few underlying assumptions: only that the data sample is a good representation of the underlying population and that data samples are independent of each other. This method involves running the fitting routine many times (400 samplings were used here), fitting the model to a different set of randomly drawn crossings each time. As such, it is computationally expensive. In this case, N magnetopause crossings are selected at random from the full set of N crossings, but, crucially, these crossings are selected with replacement. This means that, for a given random sample, some crossings are selected multiple times whereas some are discarded. As a result, the best-fitting coefficients are different for each random sample drawn. These coefficients are recorded and confidence intervals for each coefficient can be evaluated. These confidence intervals can then be corrected for bias and skewness (*Efron*, 1987).

In this case, the uncertainties estimated using both methods are comparable, and the maximum of these has been reported for each coefficient in Table 4.1.

Table 4.1. The fitting results of the present study are displayed, along with the results of previous studies. The RMS residual found between each model and the new dataset is shown to indicate the goodness of each fit.

Parameter	A06	K10	P14	Old r_0 law	New r_0 law
a_1	9.7 ± 1.0	10.3 ± 1.7		14.7 ± 0.3	10.5 ± 0.2
$\alpha = 1/a_2$	4.3 ± 0.3	5.0 ± 0.8		7.6 ± 0.4	5.7 ± 0.1
a_3	0.77 ± 0.03	0.73 ± 0.07		0.66 ± 0.01	0.67 ± 0.01
a_4	-1.5 ± 0.3	0.4 ± 0.5		0.18 ± 0.05	0.17 ± 0.03
Flattening %			19 ± 3	17 ± 1	19 ± 1
RMS[a]	7.35	4.70 (4.98)[b]	4.60 (3.51)[b]	4.42 (3.38)[b]	3.54 (3.13)[b]
No. of data	64 (26)[c]	191 (68)[c]	626 (196)[c]	1514	

[a]When applied to new set of crossings
[b]For high-latitude crossings ($\geq 30°$)
[c]After averaging
A06, K10 and P14 are the empirical models of *Arridge et al.* (2006); *Kanani et al.* (2010); *Pilkington et al.* (2014) respectively

4.6 Impact of Suprathermal Plasma on Magnetospheric Size

4.6.1 Initial Results

The initial results obtained by fitting the model to all crossings simultaneously are shown in Figure 4.7 as the black confidence ellipses, along with the results of previous studies, all at the 2σ level. Most coefficients are in agreement with previous studies within the fitting uncertainties, but for coefficients a_1 and a_2 there is a significant disagreement. Coefficient a_1 defines the scale size of the system and a_2 defines the compressibility of the magnetosphere – how strongly it reacts to variations in the solar wind dynamic pressure. Here, it was found that $a_2 = 1/(7.6 \pm 0.4)$, which apparently indicates that the magnetosphere is very 'stiff' and relatively unresponsive to changes in dynamic pressure. A value of 1/6 is expected for a dipole magnetic field (in the absence of plasma pressure) and is usually considered appropriate in the case of the Earth (e.g. *Shue et al.*, 1997). A value larger than this is expected for plasma-laden systems such as those of Saturn and Jupiter. For example, *Kanani et al.* (2010) found $a_2 = 1/(5.0 \pm 0.8)$ for Saturn and *Huddleston et al.* (1998) found $a_2 = 1/(4.5 \pm 0.8)$ for Jupiter. In this context, the value determined here does not seem physically feasible, at least when predicting the nominal response of the magnetosphere to changes in dynamic pressure.

A slightly different approach to obtaining both a_1 and a_2 is to take the logarithm of

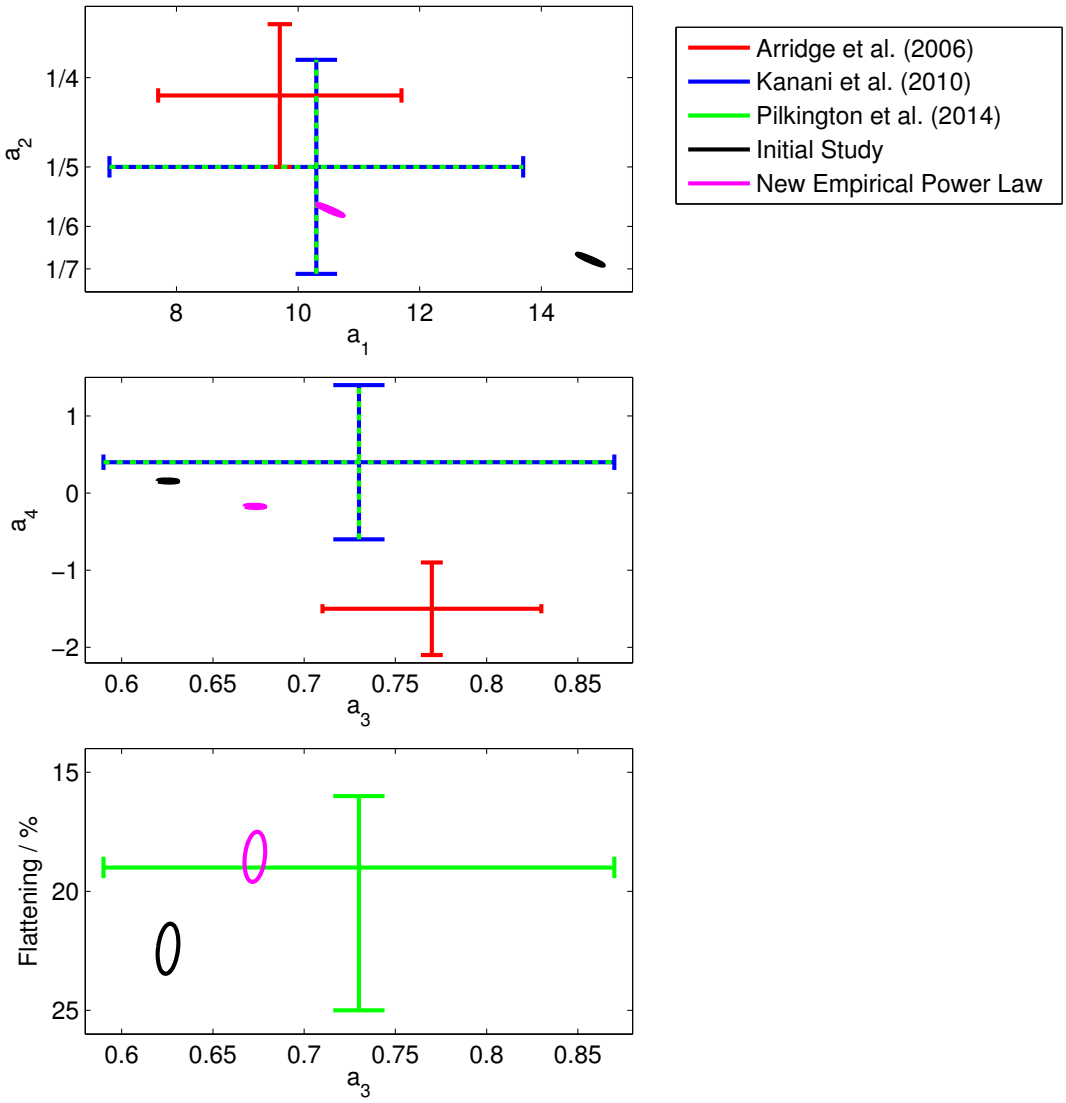

Figure 4.7. Shows the coefficients obtained by fitting the empirical model to magnetopause crossing data. All results are displayed at the 2σ (90%) confidence level. The coloured bars are the results of previous studies (*Pilkington et al.* (2014) used the *Kanani et al.* (2010) model, so dashed green lines have been added to indicate this) while the confidence ellipses indicate the result of this study using the usual stand-off distance power law (black) and the new β-dependent power law (magenta). See Table 4.1 for precise values of the coefficients. Note that the uncertainties are much smaller in this study due to the improvements made in the fitting procedure and the large amount of data used.

Equation 1.40 and rearrange to form a linear relationship,

$$\log r_0 = -a_2 \log D_P + \log a_1, \tag{4.11}$$

where D_P is estimated assuming pressure balance, as usual, and r_0 can be found for each crossing by fitting the surface directly through each crossing. Coefficients a_1 and a_2 can then be obtained from the resulting line of best fit when these quantities are plotted against each other. The subtle difference between this method and the global fitting method presented previously is that, in this case, the surface passes directly through each magnetopause crossing. Before, the surface was constructed at D_P, and did not necessarily pass directly through each magnetopause crossing. In fact, it is the distance between the surface constructed at D_P and the crossing location that is used to assess how well the model fits the data as described in Section 4.4.

The results of these two methods of estimating a_1 and a_2 are shown in Figure 4.8a. Reassuringly, both methods give the same results within the uncertainties. Interestingly though, there appears to be substantial scatter above the red lines of best-fit whereas there is relatively little below, as demonstrated in Figure 4.8c. Figure 4.8b shows the same data coloured by $\log \beta$, where β is the ratio of the total plasma pressure to the magnetic pressure. This parameter shows a remarkable trend with system size. It shows that the location of the magnetopause is affected dramatically by the plasma conditions adjacent to it, such that the extrapolated standoff location can vary by up to $10 - 15\,\mathrm{R_S}$ between low and high β conditions at constant D_P. Evidently, the usual standoff distance power law used to model the size of the magnetosphere, Equation 1.40, cannot adequately describe the Kronian system since a single one-dimensional power law cannot account for the variability in the size of the system as a result of the highly variable interior plasma conditions. Here, the system is observed to vary in size by a much larger amount than can be explained by the magnetopause oscillations observed by *Clarke et al.* (2010), typically of amplitude $\sim 1.2\,\mathrm{R_S}$ but occasionally as large as $\sim 4 - 5\,\mathrm{R_S}$. A similar degree of variability in standoff location has been identified under low ($< 0.005\,\mathrm{nPa}$) solar wind dynamic pressure conditions by *Jia et al.* (2012) using MHD simulations, but Figure 4.8b shows that the size of this variability is fairly insensitive to the solar wind dynamic pressure, peaking between $\sim 0.01\,\mathrm{nPa}$ and $\sim 0.1\,\mathrm{nPa}$.

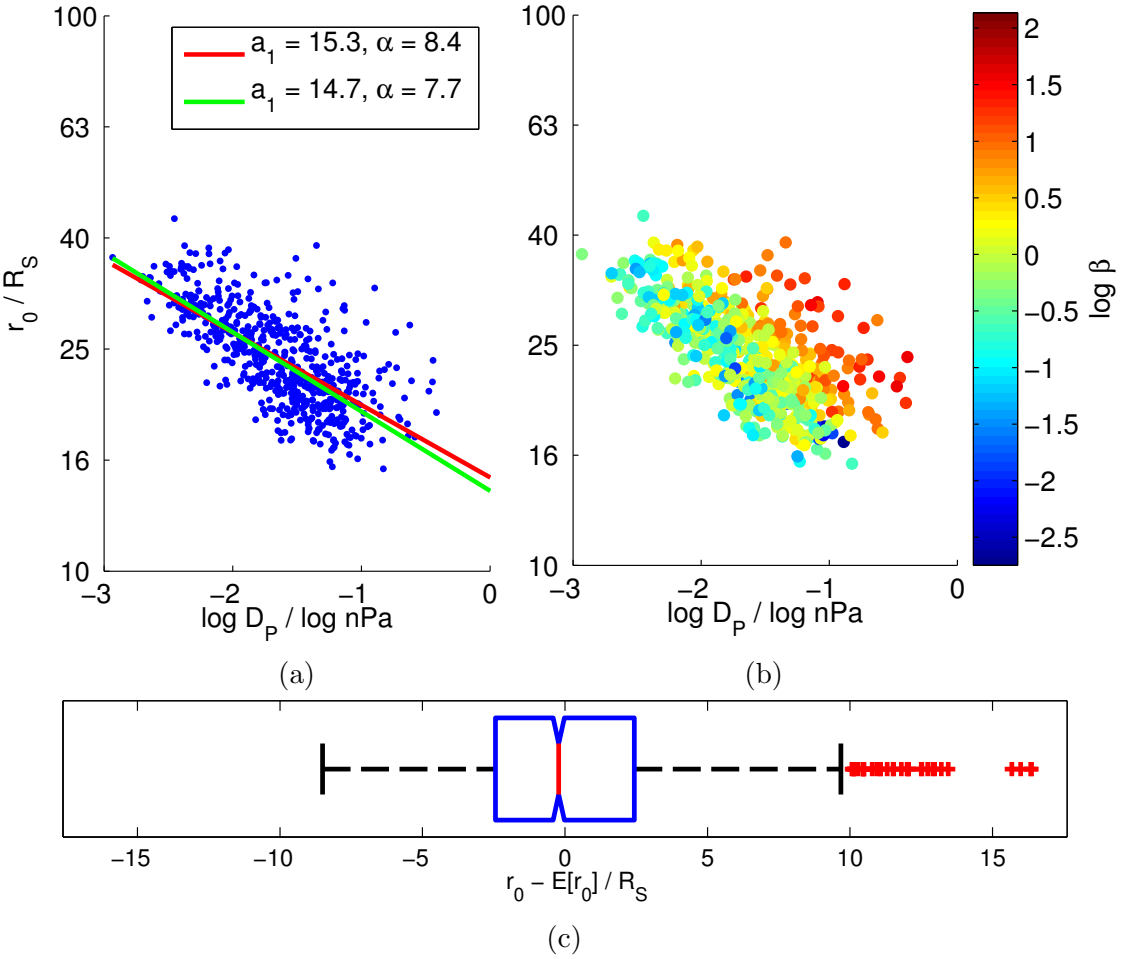

Figure 4.8. Shows Equation 4.11 plotted for the crossings used in this study. a) Two different methods are used to find coefficients a_1 and a_2 $(1/\alpha)$ as described in the text. Within the uncertainties, both methods give the same results and find that a_2 is much smaller than expected for Saturn. b) Shows the same data with a $\log \beta$ colour scale and shows that the plasma conditions inside the magnetosphere strongly affect the location of the magnetopause. c) Shows a 'box and whisker' diagram of r_0 minus the value predicted by the red model in (a). The vertical red line indicates the median value and the 'notch' indicates the 95% confidence interval in the median. The box indicates the region contained by the 25^{th} (q_1) and 75^{th} (q_3) percentiles and the whiskers indicate the maximum and minimum values within 1.5 times the interquartile range $(q_3$ - $q_1)$ from each quartile. This range corresponds to $\pm 2.7\sigma$, or 99.3% coverage, if the data are normally distributed. Red crosses are outliers that lie outside of this range. It shows that there is clearly much more scatter above the red line in (a) than there is below it.

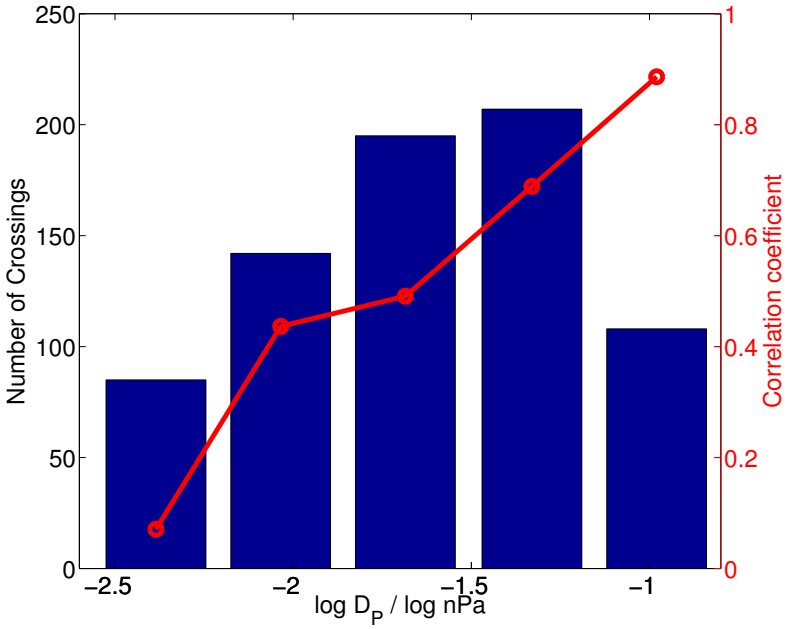

Figure 4.9. The crossings have been separated into groups of $\log D_P$ and the correlation between β and r_0 has been calculated. In all cases, these quantities are positively correlated and the correlation increases with D_P. Besides the smallest D_P bin, the p-value (the probability of such a correlation occurring by chance) is negligible. The correlation coefficients obtained here should be taken as lower limits as the D_P bins are fairly coarse to ensure that a representative number of crossings fall within each one.

Furthermore, Figure 4.9 shows that β and r_0 are strongly correlated, and that this correlation becomes more significant with increasing D_P. There is only a very weak correlation between these quantities within the smallest dynamic pressure group as there are very few high β crossings within this group (Figure 4.8b). A possible explanation for this is that Cassini's orbit usually lies inside the magnetopause when it is greatly expanded, so crossings under conditions of high interior β and low dynamic pressure cannot be measured frequently. Hence, the correlation between β and r_0 is low in these situations. This is supported by the data shown in Figure 4.8 – essentially, a detection threshold is reached whereby the magnetopause can only be sampled when it has a stand-off distance smaller than $40\,\mathrm{R_S}$ as such a magnetosphere could easily extend to $90\,\mathrm{R_S}$ on either side of the planet in the terminator plane. This may explain in part why *Jia et al.* (2012) predict that the variability in the size of the magnetosphere peaks at lower dynamic pressures than are observed here. Another explanation is that *Jia et al.* (2012) do not include a suprathermal plasma population in their simulations. To a large extent, suprathermal ions do not obey the frozen-in condition since even very small gradients

in the magnetic field can cause them to drift by virtue of their large gyroradii. So, by definition, suprathermal physics cannot be captured by MHD simulations.

However, observationally, it appears that the suprathermal plasma is the most important factor that controls β at the magnetopause, which, in turn, is highly indicative of how expanded the magnetosphere is at that time that a measurement is made. A very strong correlation has been found between the suprathermal plasma pressure and β with a correlation coefficient of 0.79, whereas the correlation coefficient between β and the magnetic pressure is just -0.12. But, by definition, β is controlled by both of these quantities. The fact that the correlation coefficient is much larger between β and the surpathermal plasma pressure than it is between β and the magnetic pressure indicates that, just inside the magnetopause, the suprathermal plasma pressure is much more variable than the magnetic pressure. Indeed, the magnetic pressure at the magnetopause typically varies by up to an order of magnitude, whereas the suprathermal plasma pressure can vary by a few orders of magnitude. Furthermore, although β describes both the magnetic field and plasma pressure, to a large extent the magnetic field at any point on the magnetopause surface only changes in response to magnetopause motion as a result of fluctuations in the solar wind pressure or interior plasma pressure.

A similar trend to that shown in Figure 4.9 is evident between r_0 and the total plasma pressure, though it is weaker than the aforementioned trend between r_0 and β. A possible explanation for this is that if the magnetic field is strong enough, it can suppress the expansion of the system since the plasma pressure must be strong enough to change the magnetic field configuration. The β parameter, on the other hand, describes which pressure source is controlling the system – is the magnetic field sufficient to confine the plasma or is the plasma pressure strong enough that it can reshape the system and significantly perturb the magnetic field?

In the first instance, one could repeat the analysis over small intervals of β to identify how the system scales under different interior plasma conditions. There are many different methods one could use to split the data. Here, a k-means clustering algorithm (as described in Appendix A.3) is used to separate the data as naturally as possible but in reality β is continuous and any small interval of β could be chosen provided that it contains enough crossings. This algorithm has been used to separate the data into three

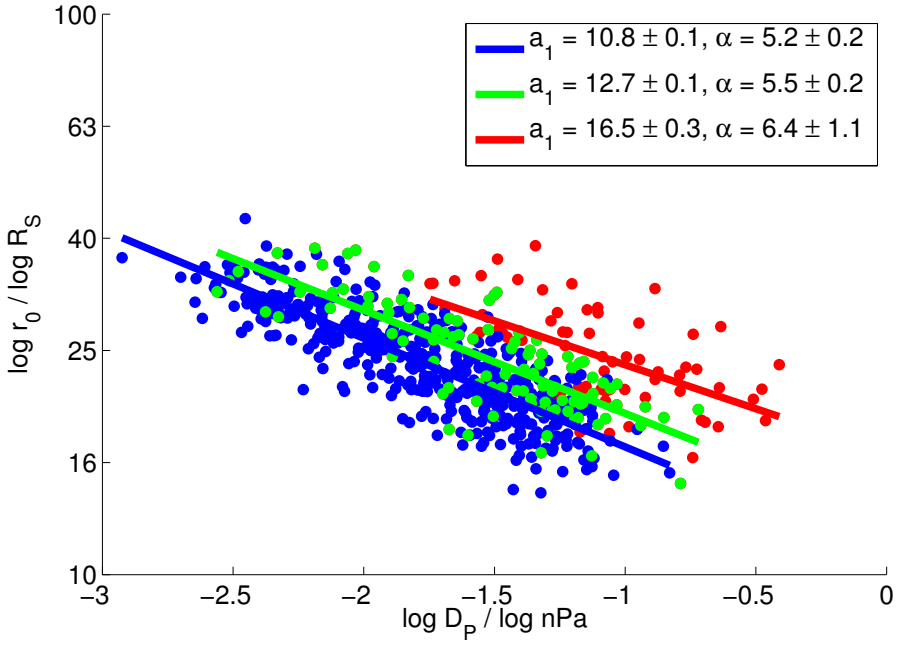

Figure 4.10. A k-means clustering algorithm has been used to separate crossings into three clusters based on β. They have been split into groups based upon the interior plasma conditions prevalent at the time of the crossing. The median β for the blue, green and red groups respectively is ∼0.6, ∼1.5 and ∼8.1 Lines of best fit have been fitted through these groups separately. Of particular note is that the factor that governs the size scale of the magnetosphere (a_1) increases with β well outside of the uncertainties. It appears that a_2 also changes systematically with β, but this change is within the fitting uncertainties. This result is insensitive to the number of clusters into which the data are separated (the analysis has been attempted with up to seven).

intervals of β and separate best-fit lines have been fitted through each cluster as shown in Figure 4.10. The median β for the crossings residing within each cluster is ∼0.6, ∼1.5 and ∼8.1 with no overlap between clusters. In each case, the magnetospheric compressibility remained the same within the estimated uncertainties and was $1/(5.5 \pm 0.2)$ on average, in agreement with *Kanani et al.* (2010). There does appear to be a systematic change in the magnetospheric compressibility with β, but this difference cannot be resolved outside of the uncertainties. However, a_1, which scales the size of the magnetosphere, changed between clusters well outside of the uncertainties and in the same sense as the average value of β for each cluster. This indicates that the magnetosphere can exist in a relatively 'plasma-depleted' or 'plasma-loaded' state as indicated schematically in Figure 4.11.

Conceptually this makes sense. Consider the simplified situation where the magnetosphere is initially in steady-state such that the internal and external pressures are equal. If

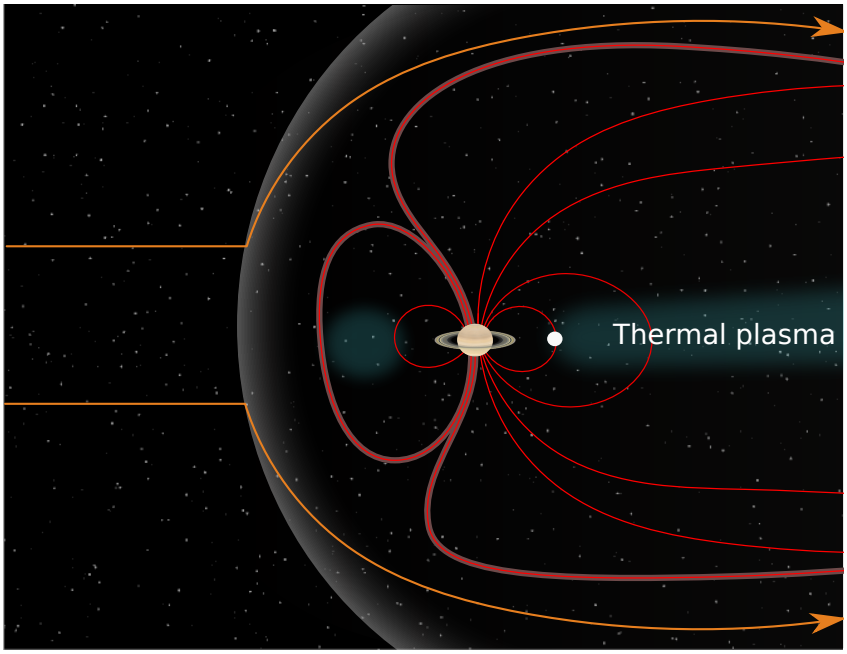

(a) Plasma Depleted

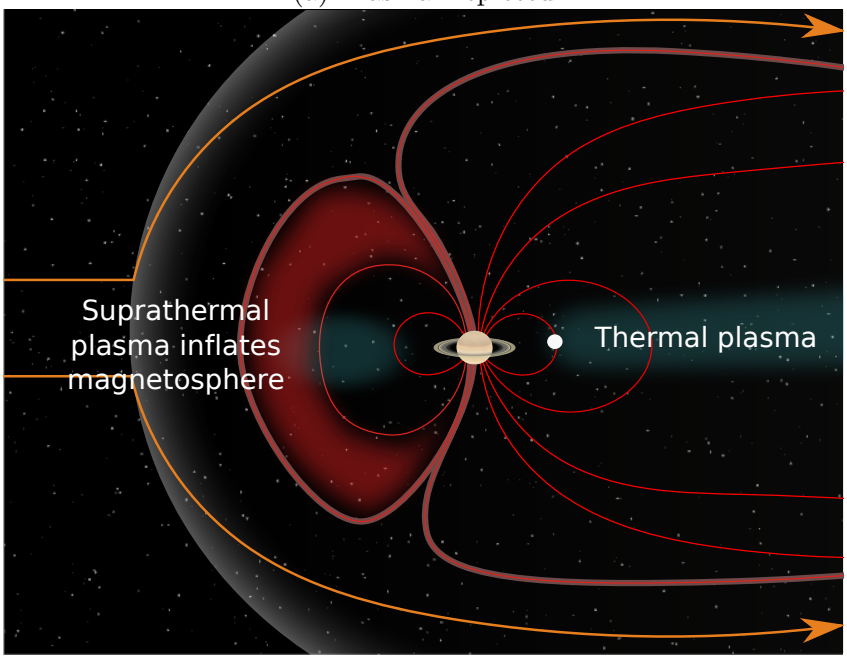

(b) Plasma Loaded

Figure 4.11. A schematic depicting two snapshots of the system under conditions in which the interior plasma pressure adjacent to the magnetopause is a) low and b) high, and the corresponding effects these conditions have on the magnetopause location. The white point represents Enceladus, a large plasma source within the system. When β is high, the plasma pressure dominates over the magnetic pressure and can change the magnetic field structure and push out the boundary. The magnetic field lines are distended radially outwards when the hot plasma pressure is increased in the corresponding force balance within the magnetosphere (*Achilleos et al.*, 2010b).

the interior plasma pressure then increases, the instantaneous β will also increase and the magnetosphere will expand in order to re-establish equilibrium. Hence, even for a steady dynamic pressure there is a range of plausible standoff distances depending on the internal conditions as a result of gradual mass loading. The large fluctuations in the observed interior plasma conditions may be caused by plasmoid loss as a result of Vasyliũnas-style reconnection in the magnetotail and the resulting planetward flow of energised plasma (*Vasyliunas*, 1983). Such a mechanism was predicted by *Zieger et al.* (2010) using MHD simulations. Alternatively, these observations could be explained by interchange/injection events as observed via energetic neutral atom imaging by the Ion and Neutral Camera on board Cassini (e.g. *Krimigis et al.*, 2007; *Brandt et al.*, 2010; *Mitchell et al.*, 2015) as shown in Figures 1.15 and 1.16. Both plasma interchange and the Vasyliũnas cycle lead to rapid changes in the interior plasma pressure, and are expected to affect pressure balance at the magnetopause boundary as a result. Future studies should aim to cross-correlate magnetopause crossings with ENA images of the magnetosphere to determine if they can provide some insight into the dominant mechanism.

The usual standoff distance power law cannot account for such internally-driven variability as the scaling factor, a_1, must change in response to variability in the interior plasma pressure even while the solar wind pressure remains steady. What is unclear, however, is how far-reaching this effect is. Is the magnetopause reacting to localised perturbations in the internal plasma pressure, or is it responding to large-scale, global fluctuations in the interior conditions? It is also unclear how β changes as the system expands. Ultimately it depends on the rate of change of the magnetic field strength and the plasma pressure with respect to system size. A theoretical treatment of this process could be the subject of future work.

4.6.2 Incorporating β into the Empirical Magnetopause Model

The original stand-off distance power law was derived in the context of Earth's magnetosphere, which is relatively devoid of plasma at the magnetopause. As such, at Earth, it is a good approximation to assume that the solar wind dynamic pressure is balanced by the magnetic pressure alone. Of course, this is far from true of the magnetospheres of Saturn and Jupiter and this aspect will be addressed here. The dynamic pressure at the stand-off

point can be estimated as:

$$D_P \propto \frac{B^2}{2\mu_0}(1+\beta), \tag{4.12}$$

assuming that the magnetopause is in static equilibrium. At this location, the magnetic field at the stand-off point can be expressed as $B = B_0 r_0^{-1/2a_2}$, where B_0 is the equatorial magnetic field at the surface of the planet. This power law is valid over a wide range of stand-off distances as found by *Bunce et al.* (2007) and *Achilleos et al.* (2014), but is affected by the magnetospheric plasma content, which causes a_2 to change. Hence r_0 can be expressed as:

$$r_0 = a_1 \left(\frac{D_\mathrm{P}}{1+\beta} \right)^{-a_2}. \tag{4.13}$$

Note that, strictly speaking, β in Equation 4.13 should be the plasma β measured just inside the standoff point. In the absence of this information, the locally measured β will be used in the first instance. The results of repeating the fitting procedure outlined in Section 4.3 with the new stand-off distance power-law expressed in Equation 4.13 are shown at the 2σ level in Figure 4.7 as the magenta confidence ellipses. Now, all coefficients are in agreement with previous studies and incorporating β into the empirical model results in a decrease in the RMS residual by $\sim$0.9 $\mathrm{R_S}$, indicating a large increase in the accuracy of the model without the use of additional free parameters. At first, this may appear puzzling because the earlier analyses by *Arridge et al.* (2006) and *Kanani et al.* (2010) did not include any dependence on β, so one may expect that they would agree better with the analysis performed without β? The explanation for this apparent paradox is that the data used in these earlier studies were confined to a region of the magnetosphere where β is, in general, relatively small as shown in Figure 4.12. The β dependence is still present within these data but has a much smaller influence.

The fact that using the local value leads to such a large increase in the predictive power of the model indicates that there may be a strong correlation between the local and 'nose' β. Indeed, adding an additional free parameter to 'scale' the local β to that expected at the stand-off point improves the accuracy of the model by $\sim$0.3 $\mathrm{R_S}$ with a scale factor of $\sim$0.4. This was achieved by simply multiplying β in Equation 4.13 by this constant scale factor. However, after performing a F-test on these models as described in Appendix A.4,

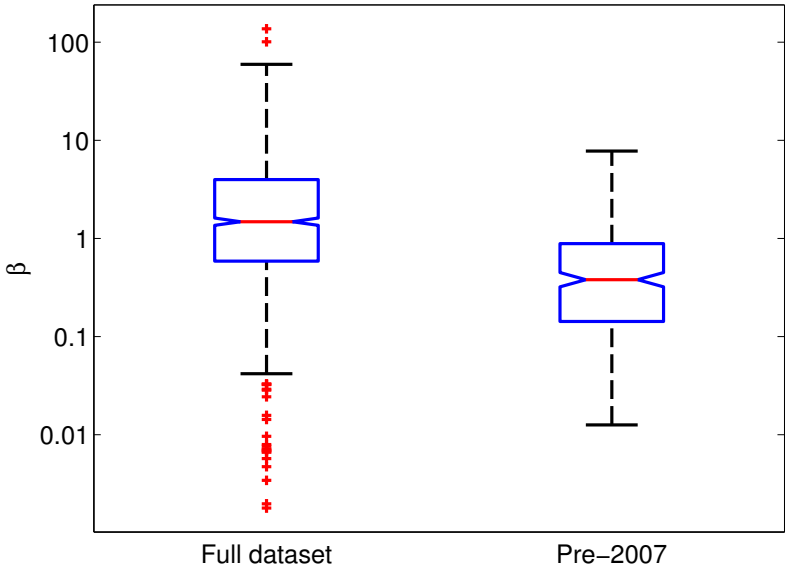

Figure 4.12. Shows 'box and whisker' diagrams describing the distribution of β adjacent to the magnetopause found during this study and found during the 'pre-2007' period over which data was used by *Kanani et al.* (2010). The red horizontal lines indicate the median values and the 'notches' indicate the 95% confidence interval of the median values. The boxes indicate the regions contained by the 25^{th} (q_1) and 75^{th} (q_3) percentiles and the whiskers indicate the maximum and minimum values within 1.5 times the interquartile range (q_3 - q_1) from each quartile. This range corresponds to $\pm 2.7\sigma$, or 99.3% coverage, if the data are normally distributed. Red crosses are outliers that lie outside of this range. It is clear that β was typically smaller in the pre-2007 period, probably because the spacecraft sampled a different part of the magnetopause (equatorial dawn) during this time than it did it did later in the mission. The spacecraft has almost exclusively sampled the dusk magnetopause from 2007–2013. Most of the outlying data points with very low β values within the full dataset are a series of high-latitude crossings that likely map to the cusp region in the northern hemisphere. The location of these can be seen in Figure 5.1b.

it was found that the additional free parameter does not provide a statistically significant improvement to the predictive power of the model. This may indicate that scaling β in this way may not represent the physical behaviour of the system, or is perhaps over-simplified. Since it was determined that β tends to be larger at dusk than dawn, it may make more sense for the scaling to be local time-dependent such that β is scaled up to the value expected at the standoff point for observations on the dawn side of the planet, and vice versa.

Fitting using Equation 4.13 in place of Equation 1.40, the magnetospheric compressibility agrees with previous studies though is more 'Earth-like' (more dipolar and nominally

closer to 1/6) than found in previous studies. In addition, it was found that the dynamic pressure has only a very small effect on the magnetospheric flaring, so can be safely neglected in future studies with minimal loss of model accuracy.

4.7 Revisiting Pressure Balance

Pressure balance has been used extensively in this and past studies to estimate the solar wind dynamic pressure in the absence of a dedicated upstream pressure monitor, though it remains unclear how appropriate this assumption is. In reality, the magnetopause is never truly in equilibrium due to the variable nature of the pressure sources on either side of the boundary. *Dunlop et al.* (2001) found that Earth's magnetopause can reach speeds of $\sim$300 km s^{-1} in response to interplanetary shocks. However, it can reach a state of quasi-equilibrium at times during which there are no sharp changes in the total pressure on either side of the boundary. It follows that, although the magnetopause can be subject to strong accelerations, pressure balance may still be a good assumption. In accordance with the law of large numbers, if the magnetopause is just as likely to be 'caught' moving towards the planet as it is to be moving away from the planet, the magnetopause will be depicted in a state close to equilibrium over long time scales. Though it is questionable how applicable even this assumption is! In order to ascertain if assuming pressure balance is a reasonable substitute for upstream pressure measurements, the distribution of these dynamic pressures has been compared to the distribution observed upstream of Saturn by spacecraft that have traversed this region. The 'balance' pressure is calculated using the model coefficients stated in Table 4.1.

Similarly to *Jackman and Arridge* (2011), data from Pioneer 11 and Voyager 2 have been used to complete this analysis. Measurements made between 1980 and 1982 are used during which the spacecraft were between 9.25 AU and 9.75 AU from the Sun. An interval symmetric in distance about Saturn's mean orbital distance ($\sim$9.5 AU) has been chosen since the dynamic pressure falls rapidly with distance from the Sun due to its r^{-2} dependence. This may cause the peak of the dynamic pressure distribution to be shifted to higher dynamic pressures otherwise, since, on average, measurements would be made closer to the Sun than Saturn is actually located.

The range of radial distances over which measurements are used must be balanced between using enough data to avoid potential biases, whilst remaining as close to Saturn's mean orbital distance as possible. It is important that the interval covers at least several solar rotation periods (∼24.5 days at the solar equator) to be sure that the spacecraft are sampling the average solar wind conditions instead of plasma originating from what may have been a particularly quiet or active region. Such activity can last for longer than a single solar rotation, potentially leading to periodic perturbations in the dynamic pressure. The data obtained by Voyager 1 at the time that the spacecraft were within this distance interval was of insufficient quality to incorporate into the analysis, and solar wind plasma moments from Cassini during its approach to Saturn were unavailable due to pointing constraints.

A histogram showing the distribution of the dynamic pressure estimated assuming pressure balance at the magnetopause is shown in Figure 4.13. The dynamic pressure was estimated as discussed in Section 4.2 neglecting the overestimated thermal ion pressure since it is unclear what effect including this contribution would have on the accuracy of the estimate. On top of this is plotted a Gaussian fit to the logarithmic distribution of dynamic pressures calculated using measurements made by Pioneer 11 and Voyager 2. Qualitatively, both distributions appear to be in close agreement, but there are notable differences between them. The median measured dynamic pressure is 0.020 nPa whereas the median dynamic pressure found assuming pressure balance is slightly larger at 0.025 nPa.

The observed dynamic pressures occurred between 1980 and 1982, close to solar maximum. The magnetopause observations occurred across approximately nine years and, hence, spanned the majority of a solar activity cycle. However, this particular solar cycle has been unusually quiet and included an extended minimum (e.g. *Russell et al.*, 2013). *Richardson and Kasper* (2008) found that the solar wind dynamic pressure can vary by a factor of two over a solar activity cycle and, perhaps counterintuitively, that the dynamic pressure tends to be a minimum near solar maximum in the outer heliosphere. As a result, dynamic pressure changes with solar cycle may be responsible for the departure between the peaks of the distributions shown in Figure 4.13.

The distribution estimated assuming pressure balance also appears to occupy a wider range of dynamic pressure values than the distribution that was measured by Pioneer

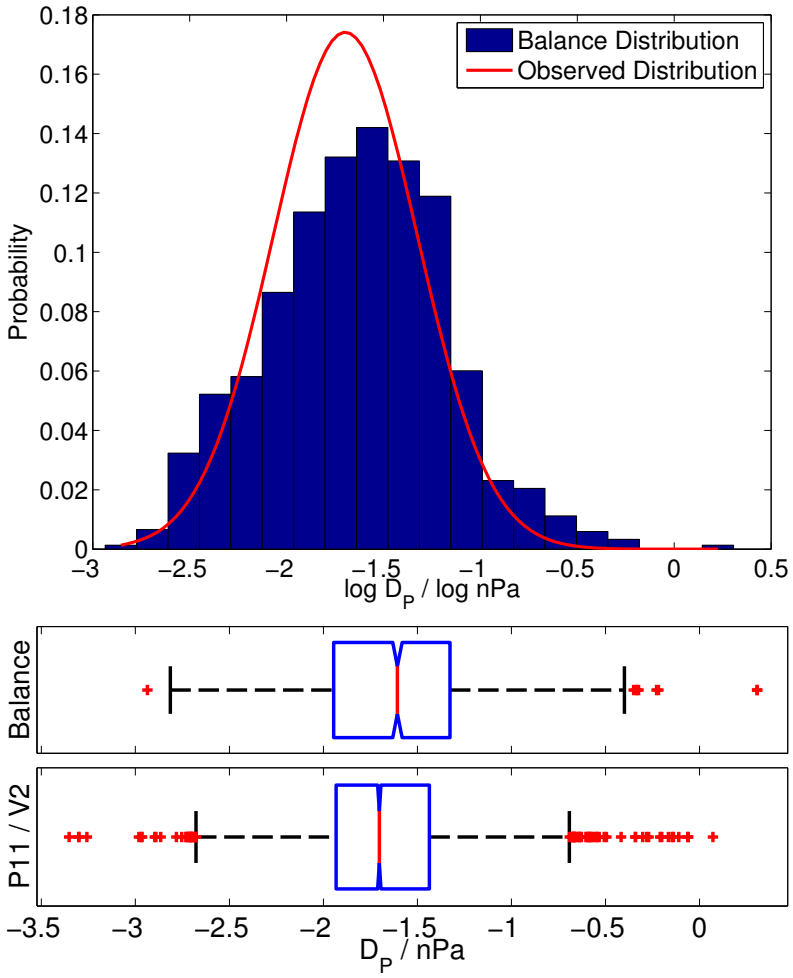

Figure 4.13. A comparison between the dynamic pressure distribution estimated assuming pressure balance at the magnetopause (blue histogram) and a fit to the distribution measured upstream of Saturn between 1980–1982 by Pioneer 11 and Voyager 2 (red line). 'Box and whisker' diagrams for each distribution are also displayed.

11 and Voyager 2. This may be related to the solar cycle, since the lower quartiles of both distributions are close together but the upper quartile of the balance distribution is larger than that of the measured distribution. It has already been discussed that a smaller average dynamic pressure may be expected for the measured distribution due to the influence of the solar cycle.

It is also possible that the difference between the distributions is the manifestation of measurements of the magnetopause that occurred when it was subject to strong accelerations. If the magnetopause is caught at a time at which it is moving towards the planet, the dynamic pressure estimated assuming pressure balance will be smaller than the dynamic

pressure estimated when the magnetopause actually reaches a quasi-equilibrium. This is because the magnetopause will be located closer to the planet when quasi-equilibrium is established. As a result, the initially measured magnetic field and, hence, the measured magnetic pressure will be smaller than when the magnetopause reaches its final equilibrium position. The plasma within the magnetosphere may also be heated adiabatically, resulting in a larger plasma pressure. Similar behaviour is expected when the magnetopause is caught at a time at which is it moving away from the planet. The instantaneous dynamic pressure estimated at this time will be larger than it would have been had the dynamic pressure been estimated after the magnetosphere had expanded until it had reached a quasi-equilibrium. This may result in a broadening of the dynamic pressure distribution.

In actual fact, one does not require particularly strong magnetopause accelerations to explain the observations – the inclusion of crossings with random, Gaussian, departures from equilibrium will cause broadening. This can be established using a simple numerical experiment. First, randomly generate a set of Gaussian measurements – synthetic dynamic pressures have been generated here using the distribution fitted to the dynamic pressures measured upstream of the planet shown in Figure 4.13. One can then add Gaussian noise to these measurements to represent overestimates and underestimates made as a result of estimating the dynamic pressure assuming pressure balance when, in fact, the magnetopause was not in equilibrium. It is established below that the key assumption associated with the law of large numbers is satisfied for Saturn's magnetopause, so it is appropriate to use Gaussian noise. The results of this experiment are shown in Figure 4.14. In the same way as was seen in Figure 4.13, random departures from equilibrium cause the distribution of dynamic pressures to broaden. This behaviour is expected as it can be demonstrated that the sum of two probability density functions (PDFs) is equivalent to the convolution of those PDFs. The solar activity cycle may be expected to broaden the distribution further.

In principle, one may be able to apply a correction to the dynamic pressures to account for this effect by scaling the estimates such that the standard deviation of the resulting distribution equals that of the measured distribution. This correction may be suitable when the average behaviour of the magnetopause is being considered, but there is no way of knowing how far the magnetopause departs from equilibrium for crossings on an individual basis. Nonetheless, taking into account the aforementioned systematic differences in the

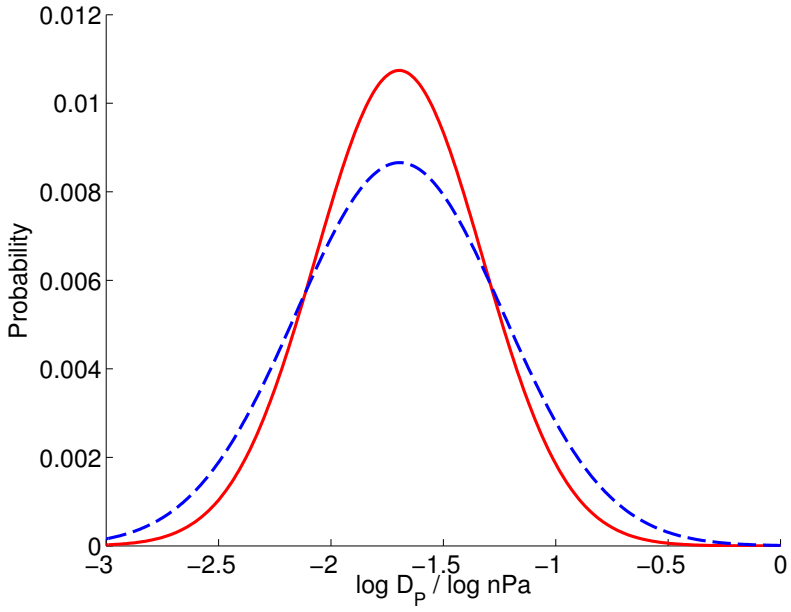

Figure 4.14. A numerical experiment exploring the influence of departures from equilibrium on the estimated solar wind dynamic pressure distribution. The red, solid, line shows the dynamic pressure distribution obtained from measurements made upstream of Saturn by Pioneer 11 and Voyager 2 as shown in Figure 4.13. The blue, dashed, line shows the effect of adding Gaussian noise to this distribution in order to simulate estimates made assuming pressure balance during a time when the magnetopause was not in equilibrium. The distribution becomes broader as a result, as observed in Figure 4.13.

measured and estimated dynamic pressure distributions, the pressure balance assumption appears to be a good substitute for direct solar wind measurements upstream of the planet.

The Kolmogorov-Smirnov test has been applied to test the null hypothesis that both dynamic pressure distributions displayed in Figure 4.13 were drawn from the same underlying population. The probability that this is the case was found to be very small (approximately one in one hundred thousand), and it is likely that this is a result of the differences in the distributions already highlighted. Possible explanations include the impact of the solar activity cycle on the average dynamic pressure and differences in solar activity between different epochs, in addition to measurements made when the magnetopause was far from equilibrium causing the distribution to broaden. Finally, an assessment of the skewness of the distribution has been made by calculating the adjusted Fisher-Pearson standardised moment coefficient (*Doane and Seward*, 2011), which was found to be ∼0.12, indicating a distribution slightly skewed to the right. A value of 0 indicates that the distribution is perfectly symmetric, but this is highly unlikely for real-world measurements. According

to a table of sample skewness coefficients that were adjusted for sample size and compiled by *Doane and Seward* (2010), one may consider this distribution approximately symmetric. This indicates that the spacecraft is just as likely to catch the magnetopause as it is expanding as when it is contracting. Hence, in accordance with the law of large numbers, it appears that the assumption of pressure balance at the magnetopause is appropriate to determine the long-term average behaviour of the magnetopause.

One may expect to observe a 'right-skewed' dynamic pressure distribution as a result of observational bias, whereby the tail is more fully developed at larger dynamic pressures. The spacecraft is more likely to observe the high-dynamic pressure tail of the distribution since, under these conditions, the magnetopause is pushed closer to the planet and thus the spacecraft is more likely to cross it. Conversely, the low-dynamic pressure tail is less likely to be observed since, under very low dynamic pressure conditions, the magnetopause is more likely to be further from the planet and may be located outside of the trajectory of an orbiting spacecraft. Such bias is apparent in Figure 4.13 as the high-dynamic pressure tail appears to be more developed than its counterpart – the low dynamic pressure tail appears to fall more rapidly. However, there is an excess of low dynamic pressure observations which may indicate the the magnetopause is more likely to be caught as it is moving towards the planet, and this appears to be balancing the effect of the aforementioned observational bias to produce a distribution that is approximately symmetric.

4.8 Revisiting Bimodality

Achilleos et al. (2008) used magnetopause crossings between 1 July 2004 and 3 September 2005 to assess the long-term statistical behaviour of Saturn's magnetosphere. They reported that the magnetospheric stand-off distance, which is a proxy for the global size of the magnetosphere, exhibits a bimodal structure, meaning that there are two most likely stand-off distances. It is plausible that these 'modes' correspond to measurements in which the magnetopause is caught in either a plasma-loaded or a plasma-depleted state with a relatively rapid transition between these states. The present study is an ideal opportunity to revisit bimodality in light of the much larger dataset that has been amassed. The stand-off distance has been calculated for each magnetopause crossing by passing the best-fitting model described in Table 4.1 directly through each magnetopause cross-

ing. This tends to be a more stable way of calculating the stand-off distance than using Equations 1.40 or 4.13 since information about all of the coefficients is used, and correlations between the coefficients mean that the stand-off distances do not change significantly within the coefficient uncertainties.

Figure 4.15 shows a histogram of stand-off distances extrapolated from the magnetopause observations using the model determined earlier in this chapter, with normal, lognormal (the best-fitting example of a skewed distribution in this case) and bimodal distributions fitted. Statistical tests have been used to determine which of these provides the best fit to the data. First of all, the Kolmogorov-Smirnov test (*Massey*, 1951) has been applied to test the null hypothesis that the data could have arisen from an underlying population that follows each distribution. Using this test, the normal distribution was overwhelmingly rejected with a negligible p-value, which can be interpreted as the probability of obtaining a distribution at least as 'extreme' as that observed provided that the null hypothesis is true. Since the probability is negligible, this test implies that the underlying stand-off distance population is very unlikely to be normally distributed. The p-value was much larger for the lognormal distribution, but was still negligible (approximately one in a million). On the other hand, the p-value for the bimodal distribution is $\sim$0.17. Whist this probability is still fairly low, it shows that the bimodal distribution is far more likely to describe the underlying population from which the data are drawn. Even so, the low probability indicates that the bimodal distribution is not able to capture the behaviour of the magnetopause entirely. It is possible that the degree of skewness evident in the distribution could be the reason why the p-value is still quite small for the bimodal distribution.

Higher order distributions can also be tested, such as a 'trimodal' distribution, which yields a p-value of 0.54. However, care must be taken not to overfit: the p-value will asymptotically approach 1 as more free parameters are added to the model. To ascertain whether this is the case, the Bayesian information criterion (BIC) (*Schwarz*, 1978) can be calculated. This is a measure of the information retained by the model whilst penalising additional free parameters. The model that minimises the BIC is the model that retains the most information about the distribution without introducing extraneous free parameters. In this case, the model that achieves this is a bimodal distribution with mean values of 20.7 R_S and 27.1 R_S with a mixing proportion of 43% and 57% respectively.

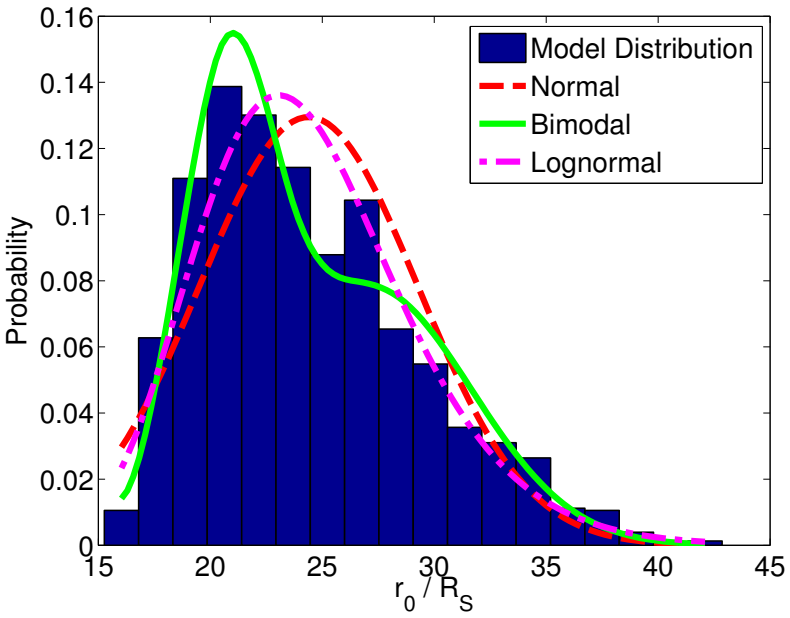

Figure 4.15. Shows the distribution of extrapolated stand-off distances found by fitting the best-fitting model specified in Table 4.1 through the precise location of each magnetopause crossing. On top of this are plotted normal (red, dashed line), bimodal (green, solid line) and lognormal (magenta, dot-dashed) distributions fitted to these data.

Previous analyses by *Joy et al.* (2002) and *Achilleos et al.* (2008) found that such bimodal behaviour could not be explained by variability in the solar wind dynamic pressure alone. This general conclusion is supported by *Jackman et al.* (2011) who analysed the solar wind conditions upstream of Saturn and Jupiter and found that the dynamic pressure distribution was best described by a single peak. This implies that the second peak in the distribution may plausibly be caused by internally driven plasma dynamics. Specifically, it may be symptomatic of the cycle of mass loading and unloading described by *Vasyliunas* (1983). If the transition between the loaded and unloaded states is rapid compared to the time that the system actually spends in each state, it stands to reason that the magnetosphere would be observed less often during this transition.

4.9 Discussion

Here, the largest and most complete set of Kronian magnetopause crossings to date has been assembled, covering approximately seven years of the Cassini mission and sampling far more of the global surface geometry than ever before. Assuming balance between

pressure sources internal and external to the magnetosphere, the solar wind dynamic pressure has been estimated and a pressure-dependent surface was fitted to the location of these crossings. Several key modifications were made to the fitting procedure over previous studies. Firstly, a more sophisticated solver was used to explore parameter space efficiently and ensure that the set of parameters that correspond to the global minimum are found. Secondly, the minimum distance between each magnetopause crossing and the empirical surface was calculated exactly. It was found that this made a significant difference to the degree of magnetopause flaring and smaller differences in the other parameters compared to the approximate method used in previous studies. It also led to an improvement in the RMS residual by $\sim 0.6\,\mathrm{R_S}$. Finally, the thermal ion pressure contribution was calculated more rigorously by exploiting the results of previous work and resulted in an additional increase in the model accuracy.

The dynamic pressure alone was not enough to account for the variability in the size of the magnetosphere. Furthermore, the extra variability could be attributed to dynamic plasma processes occurring inside the magnetosphere, which can cause the system to expand by $\sim 10 - 15\,\mathrm{R_S}$ at constant dynamic pressure. This is much larger than the periodic oscillation of the magnetopause location with amplitude $\sim 1.2\,\mathrm{R_S}$ as found by *Clarke et al.* (2010), but is consistent with MHD simulations which exhibit a similar degree of variability under low solar wind dynamic pressure conditions (e.g. *Jia et al.*, 2012). However, observationally, this variability does not appear to be limited to low dynamic pressures. This internal variability could be characterised in terms of the plasma β just inside the magnetopause. Subsequently, this effect was incorporated into the global fitting routine by adding a β dependency to the power law used in previous studies that relates the size of the magnetosphere to the dynamic pressure. Modifying the empirical model in this way results in a substantial increase in the accuracy of the model's predictions, reducing the RMS residual by $\sim 0.9\,\mathrm{R_S}$ (the model coefficients are displayed in Table 4.1). The internal variability described here may be associated with the build-up and subsequent loss of plasma from the system. It may also explain why the sizes of Jupiter's and Saturn's magnetospheres inferred from magnetopause observations exhibit bimodality as first found by *Joy et al.* (2002) and *Achilleos et al.* (2008) respectively.

In the next chapter, it will be discussed how the data employed in this chapter have been used to resolve significant asymmetries in the structure of Saturn's magnetopause.

Further studies should also look at more complex magnetopause structures, such as cusp-indentation regions. *Maurice et al.* (1996), for example, predict that Saturn's magnetopause has significant cusp-indentation regions that could be implemented into future empirical models as was done by *Lin et al.* (2010) to describe the terrestrial magnetopause. The main barrier to this exercise is a lack of cusp crossings to constrain such a model. During the course of this study, approximately 10 magnetopause crossings associated with the cusp region were identifed according to their high-latitude location and very low β values. Finally, *Clarke et al.* (2006, 2010) observed smaller-scale oscillations in the location of the boundary caused by oscillations in the magnetic field and plasma signatures that are known to occur throughout the Kronian system. Similarly, *Zieger et al.* (2010) found that the periodic release of plasmoids down into the magnetotail causes the magnetopause to oscillate as the resulting waves propagate through the system. For the present study these effects are neglected, but could, in principle, be added to the existing model as an extra layer of complexity on top of the internally driven variability already discussed.

This page was intentionally left blank

Chapter 5

Asymmetries in the Magnetopause Geometry

I keep the subject of my inquiry constantly before me, and wait 'til the first dawning opens gradually, by little and little, into a full and clear light.

Isaac Newton

In the previous chapter, a large set of magnetopause observations were identified and were used to construct a more precise model of Saturn's magnetopause by including the effect of variability in the interior plasma conditions on the location of the magnetopause. Here, that analysis will be extended to consider the effect of the subcorotational cold plasma population on the morphology of Saturn's magnetopause, in addition to seasonal variability in its typical location. The magnetopause crossings made by the Cassini spacecraft identified in the previous chapter are used here, which span almost a third of a Kronian year. Theoretical studies by *Maurice et al.* (1996) and *Hansen et al.* (2005) found that the geometry of the magnetopause changes significantly with planetary season. In particular, a north-south asymmetry in the distance between the planet and the magnetopause is

introduced when there is a significant tilt between the magnetic dipole and the incoming solar wind direction, which may be described using the KSM coordinate system. This asymmetry will be quantified in terms of the apparent polar flattening/inflation imposed by the orientation of the planetary dipole with respect to the solar wind flow direction, which changes with season.

In order to study asymmetries of this nature in the geometry of Saturn's magnetopause, modifications have been made to the empirical model and the fitting routine presented in Chapter 4. As a reminder to the reader, the empirical model used in Chapter 4 is based on the model presented by *Shue et al.* (1997) in reference to the terrestrial magnetopause. This model can be expressed by the following set of equations,

$$r = r_0 \left(\frac{2}{1 + \cos\theta} \right)^K, \qquad \text{(1.39 revisited)}$$

$$r_0 = a_1 D_P^{-a_2}, \qquad \text{(1.40 revisited)}$$

$$K = a_3 + a_4 D_P, \qquad \text{(1.41 revisited)}$$

where θ is the angle between the planet-Sun line and the position vector of a point on the magnetopause surface a distance r from the planet (as shown in Figure 1.17), r_0 is the magnetopause standoff distance which is a proxy for the global size of the magnetosphere, and K is the flaring parameter which controls the downstream shape of the magnetosphere. Parameters r_0 and K are illustrated in Figure 1.18 and are expressed in terms of a set of four fitting coefficients, a_i, which were determined in Chapter 4 and are noted in Table 4.1. In Chapter 4, it was found that the interior plasma conditions adjacent to the magnetopause boundary strongly affect the location of the magnetopause and this was incorporated into the model by updating Equation 1.40 to account for this,

$$r_0 = a_1 \left(\frac{D_\mathrm{P}}{1 + \beta} \right)^{-a_2}, \qquad \text{(4.13 revisted)}$$

where β is the ratio of the plasma pressure to the magnetic pressure just inside the magne-

topause. Strictly speaking, β in Equation 4.13 should be measured at the standoff point. In lieu of this information, the locally measured β was used in Chapter 4 and this greatly improved the accuracy of the model in terms of the RMS fitting residual, indicating a plausible global relationship between the locally measured β and that at the standoff point. I emphasise here that the use of a single spacecraft dataset, while being invaluable for constructing the magnetopause model described in the previous chapter, does not allow the distinction between local and global changes in the magnetopause geometry.

The model presented above has been modified further for the purposes of this part of the analysis. These modifications will be discussed in detail in the sections that follow in order to determine if a dawn-dusk asymmetry can be resolved, in addition to the seasonally induced change in the geometry of the magnetopause predicted by theoretical studies.

5.1 Dawn-Dusk Asymmetry

In the first instance, to determine if a dawn-dusk asymmetry could be present, the model was fitted to the crossings in the noon-dawn and noon-dusk sectors separately, between 3–12 hours and 12–20 hours local time respectively. All coefficients were set to the values found in Chapter 4 besides those that control the extent of tail flaring, used to define K. One could allow all parameters to vary but the degree of polar flattening on the dawn side of the planet is ill-constrained due to the lack of high-latitude pre-noon crossings. This could affect the other parameters as, away from the equator, a flatter, more flared surface and a less flattened but less flared surface can fit any given magnetopause crossing equally well as shown in Figure 3.5. The values of K determined in each case implied that there is a statistically significant difference in the tail flaring on the dawn and dusk flanks with the magnetopause extending further on the dawn flank. However, there are several problems with this methodology. Firstly, imposing a different degree of flaring in this way leads to a discontinuous surface at the poles. Also, as pointed out by *Petrinec and Russell* (1995) and *Joy et al.* (2002), empirical models can be biased by the simple fact that the magnetopause is only sampled along the spacecraft trajectory according to the solar wind conditions and magnetospheric configuration present at the time of the crossing.

To minimise the impact of observational bias, the data were down-sampled in order

to normalise the spacecraft sampling on either side of the planet. It can be seen in Figure 4.2 that observations of the magnetopause at dawn extend further in the X_{KSM} and Y_{KSM} directions than the observations of the magnetopause at dusk, and that the high-latitude observations lie on the dusk side of the planet only. As a result, the trajectory of the spacecraft has been considered and crossings that lie in a region that has not been adequately sampled on the opposite side of the planet have been removed. Specifically, crossings are accepted that satisfy the conditions $|Z_{\mathrm{KSM}}| \leq 10$ and $-18 \leq X_{\mathrm{KSM}} \leq 24$, the latter of which also accounts for potential biases in Y_{KSM} due to the trajectory of the spacecraft and correlations between the spacecraft X_{KSM} and Y_{KSM} coordinates. This left 989 magnetopause crossings with which to proceed with the analysis. The distribution of magnetopause standoff distances found in the previous chapter and found by *Achilleos et al.* (2008) is well-replicated and the mean positions of the boundary are still captured despite these restrictions.

Since the observations on the dawn and dusk sides of the planet are typically separated in time by years, long terms trends in the dynamic pressure, due to the solar cycle for example, could potentially affect the results of this study. For each magnetopause crossing, the dynamic pressure has been estimated assuming that it is exactly balanced by the total interior pressure just inside the magnetopause. Specifically, the locally measured magnetic and suprathermal plasma pressures were summed. As described in Chapter 4, these were then added to an upper limit estimate of the thermal ion pressure made using a thermal ion survey conducted by *Thomsen et al.* (2010), together with the empirical magnetodisc shape model presented by *Arridge et al.* (2011). The geometry of the model magnetopause was then used to scale the locally measured pressure (which is related to the component of the dynamic pressure acting normal to the surface as in Equation 4.4) up to the expected dynamic pressure upstream of the magnetosphere.

To ensure that the upstream conditions were similar when the observations on each side of the magnetopause were made, the Kolmogorov-Smirnov (K-S) test (*Massey*, 1951) as discussed in Appendix A.5 has been applied to the separate dynamic pressure distributions derived from the crossings on either side of the planet within the local time ranges described above. The K-S test tests the null hypothesis (the hypothesis accepted unless contradicted by the results of the test) that two independent random samples are drawn from the same underlying continuous population. Here, it is used to check that the dynamic pressure is

equally distributed for observations made on both sides of the planet. The null hypothesis could not be rejected at the 1σ significance level, indicating that the probability that the dynamic pressure distributions are significantly different is less than 69.1%, the lowest level of significance usually considered.

Throughout the period that this study encompasses, the spacecraft spent approximately three years sampling the dawn side of the planet, but one of these years was primarily spent traversing the magnetotail during which the magnetopause could not be observed. It spent approximately five years sampling the dusk side of the planet so, naturally, there are more observations of the magnetopause in that sector. If an empirical model were fitted to the reduced set of magnetopause crossings outlined above, the fit would be artificially weighted to the dusk magnetopause as a result. Such a weighting is removed by randomly sampling the data on the dusk side in order to balance the total number of crossings on either side. A technique known as 'stratified sampling' is used to mirror the local time distribution of crossings to prevent artificial weighting due to 'over-populated' local time sectors.

The procedure is as follows: the dawn crossings are separated into local time bins with a width of one hour and the percentage of crossings within each bin is calculated. The probability of a crossing occurring within each local time bin (LT) on the dawn side of the planet is then calculated and imposed on the random sample drawn from crossings on the dusk side. In practice, since the aim of this exercise is to equalise the number of crossings on both sides of the planet, one can just randomly draw the same number of crossings as exist within the corresponding local time bin on the dawn side of the planet. In any cases where there are fewer crossings on the dusk side in a particular mirrored local time bin (i.e. $24 - LT$), the dawn crossings in that particular bin are randomly sampled instead. The end result is an equivalent number of dawn and dusk crossings equally dispersed in terms of local time, to which the model is fitted. 716 magnetopause crossings remained in total.

The functional form of the flaring parameter has been modified to introduce a dawn-dusk asymmetry,

$$K = a_3 + a_4 D_P + a_5 \cos\phi, \tag{5.1}$$

where ϕ is the angle between the Y_{KSM} axis and the projection of the position vector of the magnetopause crossing onto the Y-Z plane as illustrated in Figure 3.4, and a_5 is a free parameter found by fitting the empirical surface to the data. The magnitude of a_5 hence controls the degree of the dawn-dusk asymmetry and $\cos\phi$ increases the tail flaring on one side of the planet and reduces it on the opposite side depending on the sign of a_5, with a smooth transition between both sides. As such, the asymmetry in terms of the flaring parameter will be of magnitude $2a_5$ at the equator in the X-Y plane.

Since the magnetopause geometry has been changed, the calculation of the normal to the surface must be updated to account for this. The form of the X-component of the normal remains the same as in Equation 3.14, and the updated Y- and Z-components of the normal can be expressed thusly,

$$n_y(a_5) = n_y + \frac{a_5 r' z \sec^2(z/y)}{y^3} \log\left(\frac{2}{1+\cos\theta}\right), \tag{5.2}$$

$$n_z(a_5) = n_z + \frac{a_5 r' \sec^2(z/y)}{y^2} \log\left(\frac{2}{1+\cos\theta}\right), \tag{5.3}$$

where $r' = \sqrt{x^2 + y^2 + (z/\mathcal{E})^2}$, $\cos\theta = x/r'$ and n_y and n_z are as defined in Equations 3.15 and 3.16.

Fitting the model to the reduced dataset outlined above using using Equation 5.1 confirms that the magnetopause extends further on the dawn flank as shown in Figure 5.1a. Since the crossings are sampled randomly, the Monte Carlo Bootstrap technique discussed in Appendix A.2 was used to repeat the procedure 100 times, fitting to a different set of crossings each time in order to ensure that, within the stated uncertainties, these results are insensitive to which crossings were randomly selected. This yields a median value of $a_5 = -0.024 \pm 0.007$ and reduced the RMS residual by $\sim$10% relative to a fit without the asymmetry term in Equation 5.1 (i.e. setting $a_5 = 0$). For the sake of comparison, $a_3 = 0.688 \pm 0.006$ and a_4 is close to zero within the uncertainties. The F-test, discussed in more detail in Appendix A.4, has been used to test the hypothesis that adding the extra free parameter significantly improves the predictive power of the model. This test simply relies on the improvement in the model prediction being large enough to outweigh the cost

of adding extra free parameters. Employing this test, it was found that the probability that this improvement was caused by random scatter in the data is negligible.

The physical cause of this asymmetry may be the intrinsic asymmetry in plasma flow around the planet with respect to the direction of solar wind flow. Plasma generally flows in the same direction as the planet rotates, so it flows against the direction of the solar wind at dawn and in the same direction as the solar wind at dusk. Hence, the magnetopause may plausibly be pushed further from the planet at dawn than at dusk. MHD simulations by *Kivelson and Jia* (2014) predict a mean asymmetry of $2.6\,\mathrm{R_S}$ at the near-equatorial terminator plane compared to the empirically derived asymmetry of $1.47 \pm 0.49\,\mathrm{R_S}$ found here when the surface is constructed at the same stand-off distance ($26.61\,\mathrm{R_S}$). The surfaces have been compared at the same standoff distance rather than the same dynamic pressure because it has been found that the asymmetry is insensitive to changes in the dynamic pressure within the limitations of the data used in this study by adding an additional, pressure-dependent, term to Equation 5.1. However, the absolute size of the asymmetry in terms of the distance between the planet and the magnetopause changes with system size. It should be noted though that the empirical model predicts that a dynamic pressure of $0.011 \pm 0.001\,\mathrm{nPa}$ is necessary for Saturn's magnetosphere to have a standoff distance of $26.61\,\mathrm{R_S}$, which is similar to the dynamic pressure used in the simulation of $0.013\,\mathrm{nPa}$.

A comparison between the MHD and the empirical surface is shown in Figure 5.1a. The largest discrepancy between these surfaces is at dusk, where the empirical surface lies further from the planet than the theoretical MHD surface. The discrepancy between these results can be explained by considering the effect that suprathermal plasma has on the magnetopause. In the previous chapter, it was found that the size of the magnetosphere is strongly correlated with β, the ratio of the plasma pressure to the magnetic pressure, just inside the magnetopause. The plasma β indicates the control that plasma has on the system. Plasma is confined by the magnetic field to varying degrees depending on the particle energy and the magnetic field strength. For the system to change in size as a result of a sudden influx of hot plasma for example (e.g. *Krimigis et al.*, 2007), the plasma pressure must be sufficient to overcome the constraining effect of the magnetic field and change the field structure across global scales.

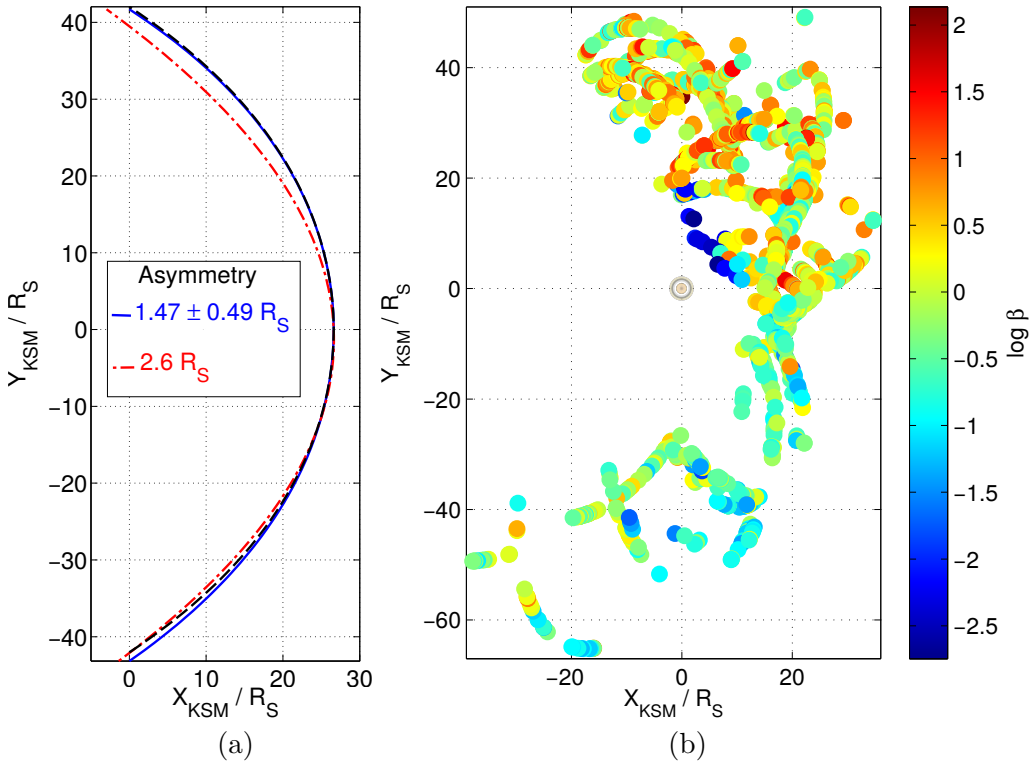

Figure 5.1. a) Comparison between the empirical dawn-dusk asymmetry from this work (blue solid line) to that derived from the MHD model of *Kivelson and Jia* (2014) (red dot-dashed line) and the dawn-dusk symmetric *Pilkington et al.* (2015) magnetopause model (black dashed line) constructed at the same stand-off distance. b) The spatial distribution of magnetopause crossings coloured by β, the ratio of the suprathermal plasma pressure to the magnetic pressure. In general, β is several times larger for crossings at dusk than at dawn and so reduces the extent of the empirical size asymmetry somewhat compared to the MHD results. The cluster of very low β crossings on the dusk side of the planet is likely to map to the cusp region.

An asymmetry in the suprathermal plasma pressure has been observed and is shown in Figure 5.1b in terms of the suprathermal plasma β. The asymmetry is displayed in terms of β since this parameter indicates which pressure source is controlling the dynamics within the system. However, it was determined in Section 4.6.1 that the suprathermal plasma pressure is the controlling factor as it is very highly correlated with β whereas the magnetic pressure is only weakly correlated with β. This is in the opposite sense to the aforementioned asymmetry in the distance from the planet to the magnetopause at dawn and dusk. Suprathermal plasma can, hence, perturb the magnetopause more at dusk, where β is relatively high, than it can at dawn, pushing the magnetopause further out at dusk than where it would otherwise be located. A similar asymmetry is seen in the ring

current (N. Sergis, private communication, 2015).

The cause of this asymmetry is unknown, but may be caused by the change in the flux tube configuration as flux tubes move around the planet. As expanded flux tubes in the dawn sector flow around the planet through noon, they are forced into a smaller volume because they move from the spacious magnetotail and into the dayside magnetosphere (e.g. *Kivelson and Southwood*, 2005; *Delamere and Bagenal*, 2013). Thus, one may expect the plasma within them to be heated adiabatically. However, magnetic field lines and, hence, flux tubes follow a lagging configuration in the sense of corotation as shown in Figure 5.2 (*Khurana and Schwarzl*, 2005). As flux tubes flow through noon and into the dusk sector, they expand again somewhat, but not to the same size as they were at dawn since, at dawn, they are free to drape all the way back into the magnetotail and can occupy a much larger volume. But at dusk the lack of magnetic field bendback is associated with a smaller-volume flux tube compared to the dawn side configuration. This may mean that the plasma within these flux tubes remains relatively compressed and energised and causes the flux tubes to expand and push the magnetopause further out than it would be located in the absence of this effect.

Such an effect is not present in the results of *Kivelson and Jia* (2014) as the suprathermal plasma population is not included in the MHD simulations. Suprathermal particles have such large gyroradii that the magnetic field gradients that exist within the magnetosphere cause them to drift significantly, such that the drift velocity is comparable to the subcorotational velocity of the plasma. Thus, they do not obey the frozen-in condition so, by definition, suprathermal physics cannot be captured by MHD simulations. As a result, the size asymmetry in the simulations appears larger than the empirically observed asymmetry since there is no suprathermal plasma pressure to counter it.

It is also possible that for a rapidly rotating magnetosphere like Saturn's, such an asymmetry may be caused by erosion of the dayside magnetopause via magnetic reconnection. If the rotation period of the planet is small compared to the timescale for the transport of newly-reconnected magnetic flux to the nightside of the planet, the dusk side of the magnetopause may be eroded preferentially. To make an assessment, we can assume that newly reconnected flux flows at the solar wind speed of $\sim$400 km/s and assume that reconnection occurs at the standoff point with a typical standoff distance of 27 R_S. If we

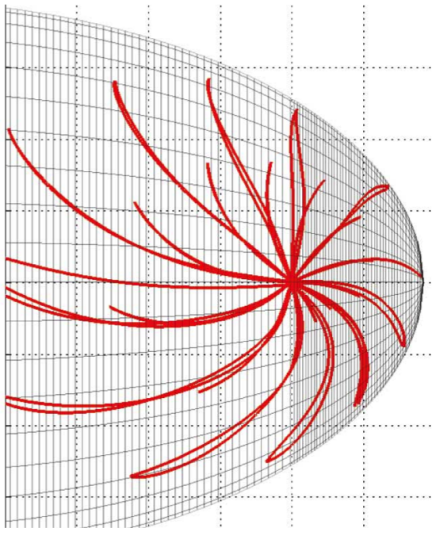

Figure 5.2. Illustration of the magnetosphere viewed from above with the Sun to the right, showing how the geometry of the magnetic field changes with local time. Based on the *Khurana and Schwarzl* (2005) magnetic field model. Credit: K. Khurana

assume the dayside magnetopause is circular then plasma at the reconnection site has to travel a distance $2\pi r_0/4$ to get to the night side of the planet. It would take just under 2 hours to travel this distance. To take the plasma to the edge of the region in which data are available, $40\,\mathrm{R_S}$ could be added to the distance the plasma must travel. In this case, the travel time is $\sim$3.5 hours or roughly one third of the planetary rotation period. Is this enough to cause the measured asymmetry? The asymmetry is fairly small so it is possible.

Also note that the orbital motion of the planet causes the incoming solar wind to be rotated by $\sim 1.4^\circ$ out of the X-Z plane such that the solar wind is preferentially flowing into the dawn side of the planet. This may also be expected to produce a small dawn-dusk asymmetry in the opposite sense to that detected here and may also reduce the asymmetry somewhat, but this is likely to be a comparatively small effect. *Kivelson and Jia* (2014) assume that the solar wind flows along the Saturn-Sun line, or the $-X_{\mathrm{KSM}}$ direction. If the aberration of flow does, indeed, cause a small asymmetry, then including it in the simulation would partially reduce the discrepancy between the observations and the MHD prediction.

5.2 Seasonal North-South Asymmetry

Maurice et al. (1996) constructed a semi-empirical magnetic field model for Saturn consisting of planetary dipole, current sheet and magnetopause contributions, partly based on data taken by Voyager 1 and Voyager 2. They were able to derive the shape of the magnetopause from this information assuming a fixed solar wind dynamic pressure. They found that the magnetopause geometry changed with planetary season due to variations in the angle λ between the magnetic dipole and the Z_{KSM} axis. When the *Maurice et al.* (1996) magnetopause surface is recast into the KSM coordinate system, there is a significant difference in its geometry in opposite hemispheres in the presence of a significant dipole tilt. The smallest dipole tilt tested by *Maurice et al.* (1996) was 15°, but the effect is probably present at smaller values than this as a gradual deflection, increasing with the magnitude of the dipole tilt. Specifically, their surface is flatter in the north and more elongated in the south under conditions similar to those when Cassini arrived at Saturn ($\lambda = -26.7°$). Similar results were obtained by *Hansen et al.* (2005) through MHD simulations of the Kronian magnetosphere. Observations of such seasonal changes can be used to separate this effect from intrinsic flattening arising from the disc-like nature of the obstacle to solar wind flow due to the presence of the magnetodisc, which preferentially inflates the low-latitude magnetosphere.

Such a study is hampered by the fact that the high-latitude observations utilised here were all observed at similar hemispheric season, i.e. the crossings in both hemispheres experience a similar 'effective' dipole tilt. The observations of the northern hemisphere took place when the dipole was tilted away from the Sun by $\sim 10 - 14°$ in the northern hemisphere. The observations in the southern hemisphere took place 5–6 years later when the southern magnetic pole was similarly tilted away from the Sun in the southern hemisphere by $\sim 14 - 17°$. As these observations are in opposite hemispheres, a similar effective dipole tilt is experienced and, hence, no north-south asymmetry would be expected. Indeed, when the fitting is repeated for crossings in the north and south separately allowing only $\mathcal{E}$ to vary, the same degree of flattening is found within the uncertainties. Hence, for this particular dataset, seasonal variability cannot be quantified through modification of the functional form of the empirical model as was done in Section 5.1.

However, seasonal variations may be taken into account using the 'general deformation

method' proposed by *Tsyganenko* (1998), who described how one can warp the current sheet and, indeed, the entire magnetopause surface in response to a dipole tilt. Such an effect has been observed in Saturn's current sheet by *Arridge et al.* (2008). The form that *Tsyganenko* (1998) employed satisfies the condition that the current sheet follows the magnetic equator close to the planet. At a distance known as the 'hinging distance', R_H, the current sheet is gradually deflected out of the magnetic equator, and is aligned parallel to solar wind flow at distances much larger than R_H. *Tsyganenko* (1998) described a procedure whereby one can warp a north-south symmetric surface in Cartesian coordinates using his Equations 7–11. Here, this operation is performed in reverse by assuming that the magnetopause was warped when Cassini made its observations. The coordinates of the magnetopause crossings are hence points situated on this warped surface. These can be transformed into the north-south symmetric 'dewarped', or equinoctial, frame of reference described by Equations 1.39–1.41 through simple algebraic manipulation to yield,

$$\begin{pmatrix} X \\ Y \\ Z \end{pmatrix} = \begin{pmatrix} \sin\lambda^* & 0 & \sin\lambda^* \\ 0 & 1 & 0 \\ -\tan\lambda^* & 0 & \sec\lambda^* \end{pmatrix} \begin{pmatrix} X^* \\ Y^* \\ Z^* \end{pmatrix}, \tag{5.4}$$

where * denotes coordinates in the warped frame (the crossing locations), coordinates without superscripts are in the dewarped frame and λ^* is the effective tilt angle, which is radially dependent and given by,

$$\sin\lambda^* = \frac{R_H \sin(-\lambda)}{(R_H^3 + r^3)^{1/3}}, \tag{5.5}$$

where r is the planet-crossing distance and λ is the dipole tilt as defined above. Note the change in notation from *Tsyganenko* (1998) to remain consistent with previous studies of the Kronian magnetopause. A first-order approximation for the hinging distance, R_H, is the standoff distance of the surface that passes directly through the crossing (*Arridge et al.*, 2008). Using Equation 5.4, the seasonal warping of the magnetopause can be removed from the observations, and then the empirical north-south symmetric surface can be fitted. Provided that this is a satisfactory correction for the seasonal distortion of the magnetopause surface, the best fitting value of $\mathcal{E}$ is then a good indication of the degree of polar flattening intrinsic to the shape of the magnetospheric obstacle.

Fitting with this transformation reduced the RMS residual by ∼5% and yielded a polar flattening of $14 \pm 1\%$, which is significantly different to the $19 \pm 1\%$ determined in Chapter 4. In Chapter 4, the empirical model was fitted in the KSM reference frame in which the magnetopause geometry is subject to seasonal variability. This then leads to the conclusion that the presence of the magnetodisc imparts a polar flattening of $14 \pm 1\%$. When the dipole is tilted $10 - 17^{\circ}$ away from the Sun in either hemisphere, the surface exhibits an effective polar flattening of a further $5 \pm 1\%$ (providing a total flattening of $19 \pm 1\%$) in that hemisphere. Presumably, the magnetopause is also inflated in the opposite hemisphere but there is currently no observational evidence to support this due to a lack of high-latitude magnetopause observations at a time when the magnetic pole is tilted towards the Sun. A representation of this modification is shown in Figure 5.3, though the magnetopause is likely to be warped even further under true solstice conditions. The warping of the surface probably varies monotonically with the degree of tilt and the asymmetries are likely to be present, though smaller, for dipole tilts less than those considered here. This is supported by the fact that repeating the fitting after removing the warping using the procedure outlined above provides a better fit to the data without the addition of free model parameters, though the improvement is relatively small.

5.3 Discussion

Magnetometer and plasma data have been analysed to construct an extended set of magnetopause crossings comprising coverage over most regions of Saturn's dayside magnetopause. These have been used to probe the structure of Saturn's magnetopause in greater detail than ever before. This analysis has revealed a significant dawn-dusk asymmetry in the size of the magnetosphere, with the magnetopause extending further from the planet on the dawn side. It is suggested that this is caused by the intrinsic asymmetry in plasma flow around the planet with respect to the direction of solar wind flow. *Kivelson and Jia* (2014) have derived a similar, though larger, average asymmetry from MHD simulations. However, an opposing asymmetry in the suprathermal plasma β was also observed adjacent to the magnetopause. This likely acts to reduce the extent of the size asymmetry as the magnetopause can be perturbed more by internal plasma pressure on the dusk side of the planet. This additional asymmetry may account for the discrepancy between the two

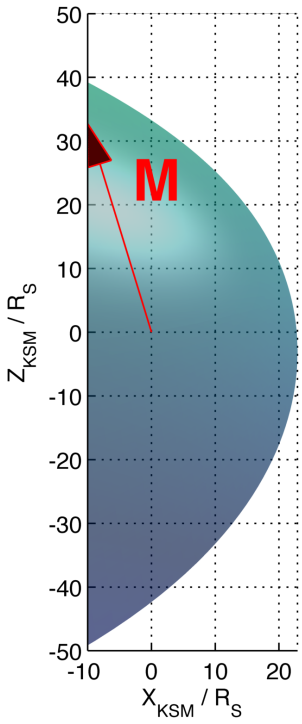

Figure 5.3. The warped magnetopause is shown with the dipole tilted 17° away from the Sun in the northern hemisphere. This introduces a clear north-south asymmetry in its extent.

results, since the MHD simulation does not include a suprathermal plasma population.

In addition, since these measurements span a wide range of planetary season, it has been ascertained that a north-south asymmetry is introduced during phases of the planetary season away from equinox, in agreement with theoretical work. This result can be interpreted as an additional component of polar flattening and inflation in opposite hemispheres, in addition to the intrinsic flattening due to the presence of the magnetodisc. These contributions have been separated using the general deformation method of *Tsyganenko* (1998) and a flattening intrinsic to the shape of the obstacle of $14 \pm 1\%$ has been found. This means that the remaining $5 \pm 1\%$ determined initially in Chapter 3, and verified in Chapter 4 using a more robust method, can be attributed to seasonal effects since the high-latitude observations of the magnetopause occurred under conditions where additional seasonal confinement of the polar region is expected. However, it is yet to be determined whether this is accompanied by a polar inflation of the magnetopause in the summer hemisphere as predicted theoretically as complementary high-latitude observations of the summer hemisphere have so far been unavailable. High-latitude observations

of the magnetopause under true solstice conditions, when the magnetic dipole is tilted by $\sim$26.7° relative to the orientation of the incoming solar wind, have been unavailable thus far. It is likely that the magnetopause will be warped even further under these conditions. Observations over a wider range of season than are currently available would be useful in order to verify this and may mean that this effect could be incorporated into more advanced empirical models.

This page was intentionally left blank

Chapter 6

Further Discussion and Conclusions

It is paradoxical, yet true, to say, that the more we know, the more ignorant we become in the absolute sense, for it is only through enlightenment that we become conscious of our limitations. Precisely one of the most gratifying results of intellectual evolution is the continuous opening up of new and greater prospects.

Nikola Tesla

The magnetospheric environments of the gas giants Saturn and Jupiter are significantly different to that of Earth, causing the dominant dynamics taking place within these magnetospheres to differ significantly. These differences manifest themselves as morphological differences in the geometry of the magnetopause, and the signatures of these have been explored in detail within this thesis in the context of Saturn's magnetopause.

Plasma sources exist within all planetary magnetospheres. Perhaps the most striking difference between the magnetospheres of the gas giants and the Earth's magnetosphere is the amount of plasma being continually added to the system. In the case of Saturn, the

primary source of plasma comes in the form of Enceladus, the satellite which orbits within Saturn's magnetosphere at a radial distance of $\sim$4.0 R_S. A heat source interior to the moon causes the ejection of vast plumes of ice and water-group molecules, in addition to traces of carbon dioxide, ammonia and hydrocarbons. These molecules are partially ionised and begin to gyrate in the presence of the magnetic field, which is primarily dipolar at the orbital distance of Enceladus. Mass loading estimates vary, but tend to be within the range $12 - 250\,\mathrm{kg\,s^{-1}}$ determined by *Bagenal and Delamere* (2011). Similarly, Io provides $260 - 1400\,\mathrm{kg\,s^{-1}}$ of plasma in the form of disassociated sulphureous gas that is ejected by the moon due to volcanic activity. In comparison, the plasma source rate within Earth's magnetosphere is just $\sim 5\,\mathrm{kg\,s^{-1}}$ (e.g. *Krupp*, 2015).

Though in the absence of their rapid rotation rates, it is questionable how large an effect the plasma within the giant planet magnetospheres would have on the dynamics taking place within the magnetosphere and, hence, on the geometry of the magnetopause. It is the combination of the presence of this plasma with the rapid planetary rotation rates of the outer planets that strongly influences the magnetospheric shape and size. It would be an interesting experiment in the context of exoplanet studies to determine what would happen if a volcanically active moon was placed within Earth's inner magnetosphere. Would the slower rotation rate of Earth be sufficient for the ensuing rotational and plasma dynamics to significantly impact upon the geometry of the magnetopause?

The rotation of the planet is partially imposed upon the magnetospheric plasma through the coupling of the magnetosphere and the ionosphere. The ionosphere is threaded by the planetary field and is thus magnetically conjugate to the magnetosphere. Ionised particles originating in the magnetosphere are accelerated from the Keplerian velocity of their source moon up to the angular velocity of the near-corotational flux tubes in the vicinity of the moon. This is mediated by ion-neutral collisions in the ionosphere. Saturn and Jupiter both rotate far more rapidly than Earth, with rotational periods of (presumably, for Saturn, as discussed in Section 1.3) $\sim$10.7 hours and $\sim$9.9 hours respectively compared to Earth's rotational period of $\sim$24 hours. Combined with the larger sizes of their magnetospheres, this leads to centrifugal confinement of the thermal component of the plasma and causes the formation of an extended magnetodisc structure, which resides near the magnetic equator. The subject of the first part of this thesis was to determine to what extent the presence of Saturn's magnetodisc affects the geometry of its magne-

topause.

6.1 The impact of the magnetodisc

The Cassini spacecraft was captured into a stable orbit around Saturn in July 2004 and has provided near-continuous measurements of Saturn's magnetospheric environment ever since. Prior to 2007, Cassini sampled the equatorial magnetopause on the dawn side of the planet in addition to traversing the near-planet magnetotail region. During 2007 and 2008, Cassini was able to make measurements of the magnetopause at high latitudes, which, for the first time, allowed an assessment of the impact of the magnetodisc upon the high-latitude geometry of Saturn's magnetopause.

In order to accomplish this, the fluxgate magnetometer and the electron plasma spectrometer on board Cassini were used to identify transitions across the magnetopause boundary, typically characterised by sharp changes in the measured electron populations and magnetic field signatures. At Saturn, the magnetic field is typically stronger inside the magnetosphere than it is in the magnetosheath. The magnetosphere also tends to have a larger southward-pointing component of the magnetic field than the magnetosheath due to the substantial contribution of the magnetic dipole and outer ring current to the total magnetic field. In the magnetosheath, the north-south component of the magnetic field is typically small since, at the orbit of Saturn, the IMF is rotated from its poloidal configuration close to the Sun to a toroidal configuration in the outer heliosphere. As such, there is typically an angle of close to 90° between the IMF and Saturn's planetary dipole. The Sun's magnetic field is tilted with respect to its axis of rotation, and this causes the heliospheric current sheet to cyclically pass over the planet. The planet will alternate between lying above and below the current sheet with an oppositely directed IMF on either side.

Magnetopause crossings are perhaps more obvious when viewed in the electron data than they are viewed in the magnetic field data. After disregarding the photoelectrons, the modal electron count rate (which is proportional to the electron density) is typically an order of magnitude greater in the magnetosheath than it is in the magnetosphere. Conversely, the modal electron energy is typically an order of magnitude greater in the magnetosphere than it is in the magnetosheath. In addition, the photoelectron population

tends to stretch to energies a few electronvolts higher within the magnetosphere than in the magnetosheath. As such, two very different electron populations with significantly different modal energies and densities are typically observed on either side of the magnetopause. In the author's opinion, this makes magnetopause crossings far easier, in general, to identify in the electron data than in the magnetic field data.

However, identifying crossings in both datasets provides a reliable method of cross-validating detections. In principle, one could use cross-validation as a method of estimating the uncertainty in the time and spatial location of magnetopause crossings by estimating the time of the transition using both sets of data. However, since such a discrepancy may be up to the order of minutes, and this is very small compared to the typical time between crossings, the uncertainty in the magnetopause location is very small relative to other sources of uncertainty.

Cross-validation can also be useful in order to eliminate false positive magnetopause detections. Similarly, cross-validation can be useful in order to accurately identify closely-separated boundary crossings as a result of magnetopause boundary waves and periodic oscillations. Such attention to detail is necessary in order to accurately determine whether the spacecraft was inside or outside the magnetosphere at any given time. This may be useful when one wishes to reduce the data to periods of time during which the spacecraft is inside or outside of the magnetosphere. Examples of where this would be important are if conducting studies on plasmoid release in the magnetotail or characterising the solar wind conditions in the magnetosheath.

For the purposes of this study, this identification was necessary in order to ensure that the spacecraft was sampling the typical location of the high-latitude magnetopause rather than extreme magnetospheric configurations. If the spacecraft typically encounters the magnetopause approximately the same number of times on highly inclined orbits as on equatorial orbits, it is likely that the high-latitude magnetopause is being adequately sampled. This is, of course, assuming that the equatorial orbits are themselves adequately sampling the mean equatorial location of the boundary. Also, approximately the same number of observations occurred under low and high dynamic pressure conditions, which also implies that the mean location of the high-latitude boundary is being observed.

To provide additional evidence, the magnetopause crossings were used to construct

empirical probability distributions of the likelihood of finding the spacecraft inside the magnetosphere over different ranges of the X_{KSM} coordinate. Equatorial and high-latitude portions of the trajectory were separated and if a clear transition occurred between the spacecraft spending half of its time inside and half of its time outside the magnetosphere for a particular X_{KSM} bin, then that particular bin was deemed to have been adequately sampled. This was found to be the case for all X_{KSM} bins in the equatorial regions of the magnetosphere. The high-latitude regions were adequately sampled for all but one X_{KSM} bin, so the few crossings within that bin were discarded for the purposes of the analysis.

The analysis then consisted of comparing the high-latitude locations of the magnetopause to the locations predicted by the axisymmetric *Kanani et al.* (2010) model. The crossing locations were normalised to the average dynamic pressure assuming that the solar wind dynamic pressure is exactly balanced by interior pressure sources at the magnetopause. Specifically, the interior magnetic and suprathermal plasma pressures were considered. The high-latitude magnetopause was observed systematically closer to the planet than the location predicted by the model, consistent with a flattened geometry. A thorough statistical analysis of this discrepancy was then undertaken and it was found that the boundary was best characterised by a polar flattening of $18 \pm 3\%$ relative to the equatorial magnetopause. No significant dependence of this parameter on dynamic pressure was found.

The last element to this part of the investigation was to determine how likely it is that the polar flattening measurement made here could have been affected by magnetopause oscillations at the presumed planetary period. It has been known since the Voyager era that periodic modulations of many magnetospheric parameters occur within Saturn's magnetosphere. These include the magnetic field strength, electron flux and radio emissions, among others. Several phase ephemerides have been constructed in order to model these oscillations. The one used here is the SLS3 system, which is tied to the phase of the Saturn Kilometric Radiation (SKR). The phase of the oscillation in terms of the SKR phase was determined for each crossing and was corrected for the wave propagation time. In order for these oscillations to have a significant impact upon the polar flattening measurement, one may expect that the high-latitude observations would have to occur at a similar phase. However, the high-latitude observations were approximately evenly dispersed in terms of the corrected oscillation phase, meaning that it is unlikely that the PPOs significantly

affected the degree of polar flattening obtained here.

Although it was clear that polar flattening had been detected, the cause was not clear at this stage of the analysis as there are thought to be two primary causes of polar flattening. The first, as mentioned, is the presence of the magnetodisc, which preferentially inflates the equatorial magnetosphere due to the enhanced thermal plasma pressure present in this region. A second potential cause is the passage of the planet through the seasons, defined in terms of the angle between the magnetic dipole and the direction of upstream solar wind flow.

Theoretical studies have found that the magnetopause becomes north-south asymmetric when the magnetic dipole is significantly tilted with respect to the planet-Sun line (e.g. *Maurice et al.*, 1996; *Hansen et al.*, 2005). In contrast, a north-south symmetric magnetosphere is expected at equinox since the magnetic dipole and the planet-Sun line are then orthogonal. In the presence of a significant dipole tilt, one hemisphere becomes further flattened with respect to the equinoctial magnetopause, whereas the magnetopause becomes 'inflated' in the opposite hemisphere. As such, it is difficult to separate the degree of polar flattening intrinsic to the shape of the disc-like obstacle from that due to the seasonally induced contribution.

During the period of time at which the high-latitude observations used in this study were made, the dipole was titled away from the Sun by between 10° and 14° in the northern hemisphere. With the dipole oriented in this way, one would expect to see polar flattening in the northern hemisphere before even considering the magnetopause being subject to an intrinsic flattening. Hence, at this stage in the investigation it could not be stated conclusively what effect the magnetodisc acting alone would have on the geometry of Saturn's magnetopause.

6.2 The impact of suprathermal plasma

The degree of polar flattening obtained in Chapter 3 inherently depends on the *Kanani et al.* (2010) model since it was derived by comparing the observed high-latitude magnetopause with the location predicted by that model. The *Kanani et al.* (2010) model is

based upon that devised by *Shue et al.* (1997) to describe the terrestrial magnetopause and was fitted to equatorial observations of the magnetopause. Here, this model was modified to incorporate polar flattening and was fitted to a new set of observations. These observations combined measurements taken during the time period used by *Kanani et al.* (2010) and the sequence of highly inclined spacecraft passes used in Chapter 3. In addition, coverage was extended to include equatorial measurements on the opposite side of the planet and high-latitude observations of the southern hemisphere to build up a much more complete picture of the Kronian magnetopause.

For the most part, the fitting results were in agreement with previous studies, with the exception of the parameters that control the size of the magnetosphere and its response to changes in the solar wind dynamic pressure. These parameters predicted a magnetosphere that was extremely 'stiff' and unresponsive to changes in the solar wind dynamic pressure, in contrast to previous investigations and theoretical predictions (e.g. *Hansen et al.*, 2005; *Arridge et al.*, 2006; *Kanani et al.*, 2010). Further investigation revealed that this apparent behaviour was artificial and was caused by the impact of the suprathermal plasma pressure on the size of the magnetosphere. It was found that variability in the suprathermal plasma pressure can cause the location of the magnetopause to change by $10-15\,\mathrm{R_S}$ at fixed solar wind pressure. This is a similar degree of variability to that imposed by the typical variability in the solar wind dynamic pressure itself, which was previously assumed to be the primary cause of changes in the location of the magnetopause (as has been found at Earth).

The power law used to model the standoff distance was modified in order to account for the additional degree of variability imposed by the suprathermal plasma pressure. Fitting using this new law resulted in a large reduction in the root-mean-squared residual distance between the observed location of the magnetopause and that predicted by the model by $\sim$20% without the addition of free parameters. The fitting coefficients obtained were also in agreement with those determined in previous studies within the estimated uncertainties, though the magnetosphere was found to be more somewhat 'Earth-like' in its response to variations in the dynamic pressure than had been previously found.

In addition, a smaller nominal degree of tail flaring was found than previous studies due to the improved crossing-surface distance criterion used in this work. The correlation

between the degree of tail flaring and the solar wind dynamic pressure was found to be very weak and within the uncertainty associated with the nominal tail flaring under typical solar wind conditions. A similar result was found by *Kanani et al.* (2010), who found that a dynamic pressure dependence on the tail flaring may not exist within the estimated model uncertainies. As such, the tail flaring can probably be assumed independent of solar wind dynamic pressure in future studies. Finally, using this fitting technique, the same degree of polar flattening was obtained as that found in Chapter 3 within the estimated measurement uncertainties.

This new magnetopause model was then used to estimate the dynamic pressure for each magnetopause crossing assuming pressure balance. This thesis has made extensive use of the pressure balance assumption so an assessment was made as to its applicability for Saturn's magnetosphere. The estimated dynamic pressure distribution was compared to that measured upstream of Saturn by Pioneer 11 and Voyager 2. The average dynamic pressures determined from both distributions are in close agreement, and the small discrepancy between them may be caused by the phase of the solar cycle and the epoch of observation.

One of the cornerstones of the pressure balance assumption is the law of large numbers. In accordance with the law of large numbers, a system will be observed in its average state if a sufficiently large number of observations are made. In this case, that means that the magnetosphere will be depicted in a state close to equilibrium assuming that the magnetopause is just as likely to be moving towards the planet as it is to be moving away from the planet. However, this assumption has not been tested. If this was not the case, one may expect the dynamic pressure distribution estimated assuming pressure balance to be skewed. After calculating the adjusted Fisher-Pearson standardised moment coefficient, it was found that the 'balance' distribution is approximately symmetric, indicating that the pressure balance assumption is reasonable.

However, it was found that it is unlikely that both distributions were drawn from the same underlying 'true' dynamic pressure distribution after applying the Wilcoxon Signed rank test to the distributions. This may be partly caused by a broadening of the balance distribution as a result of measurements made during periods when the magnetopause was not in equilibrium. The dynamic pressure would be underestimated or overestimated

with respect to the true value depending on whether the magnetopause is moving towards or away from the planet. The addition of such discrepancies to the real distribution can cause broadening, as demonstrated using a numerical experiment. Differences in the solar cycles/epochs observed may also cause systematic differences in the underlying distributions. Taking these factors into account, pressure balance appears to do a remarkable job of estimating the true dynamic pressure distribution at least over long time scales

The final aspect of this part of the study was to make use of the large number of observations accumulated throughout this work to assess the size distribution of Saturn's magnetosphere. It was found that a bimodal distribution explains the distribution far better than a normal or a skewed distribution, in agreement with a previous study by *Achilleos et al.* (2008). The locations of these 'modes' were comparable to those found by *Achilleos et al.* (2008), with peaks at $20.7\,R_S$ and $27.1\,R_S$ with roughly equal mixing proportions. It was also found that the improvement made to the fit by adding the additional mode was large enough to compensate for the additional free parameters involved in fitting a bimodal distribution. Additional modes used in addition to the bimodal model potentially led to overfitting. Hence, it has been demonstrated that even over very long time scales, Saturn's magnetosphere seems to favour one of two preferred sizes, though the reason that this is the case is unclear.

Previous authors found no evidence of a purely solar wind-related cause for this behaviour at both Saturn and Jupiter, which leads one to suspect that it may be driven internally. It has been suggested that the bimodal pattern may be caused by the Vasyliũnas cycle, recurring cycles of mass loading and unloading via magnetic reconnection in the magnetotail. This is plausible provided that the system spends more time in the 'loaded' and 'depleted' parts of the cycle than it does in the intermediate stages and that the transition between the two states is adequately rapid. It may be useful to explore this possibility further using MHD simulations of the Kronian magnetosphere. One could even fly the Cassini trajectory through the simulation in order to predict the standoff distance distribution that Cassini is likely to observe and to determine whether the observed bimodal behaviour may be caused artificially by sampling biases.

6.3 Saturn's asymmetric magnetopause

The magnetopause crossings identified in Chapter 4 sample most regions of the Kronian magnetopause so have been used to make a more detailed assessment of Saturn's magnetopause morphology. These observations include extensive coverage of the equatorial magnetopause on both sides of the planet, meaning that they could be used to explore the possibility of a dawn-dusk asymmetry in the extent of the magnetopause.

However, as with all observational studies, there are several potential biases which first needed to be accounted for. Although Cassini sampled the equatorial magnetopause on both sides of the planet, it did not necessarily do so equally in terms of both coverage and the time spent (and, hence, the number of observations made) on both sides of the planet. Ultimately, the spacecraft trajectory is determined by balancing the scientific objectives of the instrument teams against the operational concerns of the engineering teams. As such, it is not feasible to sample all regions of the magnetosphere equally as doing so would be more demanding on the propellant supplies and would, in turn, reduce the lifespan of the mission. For Cassini, to boost the efficiency of propellant usage, significant changes in the spacecraft trajectory often coincided with moon flybys by carefully controlling the incident trajectory of the spacecraft (using the moons as 'tour engines').

Nonetheless, equal sampling would be advantageous for a study of this nature. To account for differences in the spacecraft sampling on both sides of the planet (dawn and dusk), crossings identified within regions that were not traversed by the spacecraft in the mirrored region on the opposite side of the planet were discarded. This included all of the high-latitude crossings ($Z_{\mathrm{KSM}} > 15\,\mathrm{R_S}$), which occurred exclusively on the dusk side of the planet in the orbits considered. The spacecraft also spent far more time on the dusk side of the planet, so the magnetopause was observed many more times on that side. As a result, a model fitted to these data would be artificially weighted to the dusk side by sheer weight of numbers. To eliminate such a weighting, the crossings on the dusk side were randomly sampled, drawing the same number of crossings as were present on the dawn side of the planet in the mirrored local time sector. The crossings on the dusk side were sampled in such a way that the local time distribution of crossings on the dawn side of the planet was imposed. Of course, more crossings exist within local time sectors that were more frequently traversed by the spacecraft, and this comprises another form of

observational bias.

The functional form of the model used in Chapter 4 was modified to include a dawn-dusk asymmetry. The degree of polar flattening was fixed to that found in Chapter 4 since the high-latitude crossings, which constrain this parameter, have been discarded for the reasons outlined above. After fitting the model to the reduced set of observations, a significant dawn-dusk asymmetry was found whereby the magnetopause tends to extend further from the planet on the dawn side than it does on the dusk side of the planet. It is suggested that this asymmetry is caused by the flow of plasma around the planet in the sense of corotation. On the dawn side of the planet the plasma flows against the solar wind, which may push the boundary out somewhat relative to the dusk magnetopause.

The size of the empirically measured asymmetry was then compared to the prediction made by *Kivelson and Jia* (2014) using MHD simulations of the Kronian magnetosphere. *Kivelson and Jia* (2014) found that the location of the magnetopause was far more variable on the dawn side of the planet than on the dusk side, and found an asymmetry in the average location of the magnetopause after performing a quadratic fit to its location. The asymmetry found by *Kivelson and Jia* (2014) was in the same sense at that determined here, with the magnetosphere extending further at dawn than dusk. A quantitative assessment of the agreement between the empirical and theoretical results was then made. *Kivelson and Jia* (2014) ran their simulation with a dynamic pressure of 0.013 nPa and found that the standoff distance was 26.61 R_S on average with an average asymmetry of 2.6 R_S at the equator in the terminator plane. The empirical model was constructed at the same standoff distance found by *Kivelson and Jia* (2014) and yielded an asymmetry somewhat different in size of $1.47 \pm 0.49\,R_S$.

A dawn-dusk asymmetry in the typical suprathermal plasma pressure adjacent to the magnetopause was also detected, which could explain the discrepancy in the size of the aforementioned asymmetries. The suprathermal plasma pressure adjacent to the magnetopause has a tendency to be larger at dusk than at dawn. The median suprathermal plasma β was $\sim$0.6 and $\sim$1.7 in the dawn and dusk sectors respectively. It is likely that the more energetic plasma pushes the magnetopause further out at dusk and reduces the asymmetry somewhat relative to dawn. It was found in Chapter 4 that the size of the magnetosphere is strongly correlated with β, making this a plausible suggestion. How-

ever, MHD simulations cannot capture suprathermal physics so most such models, including that of *Kivelson and Jia* (2014), do not contain a suprathermal plasma population. Hence, the asymmetry in the extent of the magnetopause appears larger in the simulations without the β asymmetry to oppose it. Solar wind aberration due to the velocity of the planet relative to the solar wind may also help to reduce the asymmetry somewhat. Aberration causes the solar wind to be rotated out of the planet-Sun line and to flow more incident upon the dawn sector. *Kivelson and Jia* (2014) assume the solar wind flows along the planet-Sun line, so this may also partially explain the discrepancy. However, this is likely to be a much weaker effect than the asymmetry in β.

Earlier in the study, it was established that Saturn's magnetosphere is subject to significant polar flattening. There were two potential candidate causes for this. These were i) polar flattening cause by the presence of the magnetodisc, which preferentially inflates the equatorial magnetosphere; and ii) seasonally induced 'warping' of the magnetopause caused by the tilted magnetic dipole of the planet with respect to the solar wind direction. Using the measurements outlined in Chapter 3, there was no obvious way to distinguish between these potential causes because the observations were too close together in terms of the phase of the Kronian season at which they were measured. In this latter part of the study, with observations spanning a period of almost half of a Kronian year, the two contributions to the net polar flattening could be separated.

To accomplish this, the magnetopause was assumed to be warped at the time that the observations took place. The crossings were then recast into a 'dewarped' frame of reference using the 'general deformation method' of *Tsyganenko* (1998). *Tsyganenko* (1998) described how one could warp a north-south symmetric equinoctial surface based on the dipole tilt angle. This procedure was reversed in order to remove the warping from the observations. The degree of flattening obtained by fitting to the dewarped crossings is then, presumably, the approximate flattening intrinsic to the obstacle, and the difference between this and the flattening obtained by fitting in the KSM frame of reference corresponds to the seasonally induced part.

In this way, an intrinsic flattening of $14 \pm 1\%$ was determined, with a seasonally induced component of $5 \pm 1\%$ for a dipole tilt of $10° - 17°$. This indicates that the presence of the centrifugally-confined thermal component of the magnetospheric plasma

has a significant impact on the geometry of the magnetopause and is likely to affect the magnetospheres of other planets with significant internal sources of plasma. In particular, it would be interesting to explore the effect of thermal plasma on Jupiter's magnetosphere, which is known to have a much larger mass loading rate than is present within Saturn's magnetosphere. The effect could be extreme – larger amounts of thermal plasma in the Jovian system could potentially make the entire magnetosphere rather disc-like in nature and strongly asymmetric. Indeed, the results of a study undertaken by *Huddleston et al.* (1998) indicate that Jupiter's magnetosphere may be subject to a larger degree of polar flattening than Saturn's magnetosphere.

On the other hand, Jupiter's magnetosphere is much larger and Jupiter's internal dipole is ∼35 times stronger than that of Saturn. *Vasylinas* (2008) used a simple scaling analysis to show that, relatively speaking, plasma may have a more significant effect on Saturn's magnetosphere despite the larger plasma source rate within Jupiter's magnetosphere in absolute terms. The primary cause of this was attributed to the difference in the planetary magnetic field strength between Jupiter and Saturn. The thermal plasma within Jupiter's magnetosphere may have a more subtle effect on the magnetospheric geometry as a result. Upcoming missions to Jupiter's magnetosphere, such as NASA's *Juno* mission and ESA's *JUICE* mission, may be able to shed some light on this comparison.

6.4 Final remarks and directions for future research

Throughout this thesis, the impact of the thermal and suprathermal magnetospheric plasma populations on the size and shape of Saturn's magnetopause has been explored. The abundance of plasma within Saturn's magnetosphere, combined with its rapid rate of rotation, cause the geometry of the magnetopause to depart significantly from the axial symmetry found of Earth's magnetosphere at equinox. Thus, empirical models have been updated accordingly. It has been long known that equatorially confined plasma within the giant planet magnetospheres inflates them beyond the size expected based purely on the planetary magnetic dipole. Here, it has been demonstrated that this plasma preferentially inflates Saturn's equatorial magnetosphere and leads to polar confinement of the magnetopause boundary, in addition to an apparent flattening caused by the seasonally induced warping of the magnetosphere. The impact of warping on the high-latitude magnetopause

has been quantified in the winter hemisphere of the planet over a small range of dipole tilt angles. A lack of high-latitude measurements has thus far made this exercise impossible in the summer hemisphere, though it would be interesting to see if the summer hemisphere is relatively inflated in the polar regions under these conditions as theory predicts. An assessment over a wider range of dipole tilt angles would also be beneficial, particularly under true solstice conditions.

Furthermore, it has been demonstrated that a significant dawn-dusk asymmetry in the extent of the magnetosphere is present. It is likely that this is also caused by interior plasma and rotational dynamics. It has been demonstrated for the first time that the variability in the suprathermal plasma pressure adjacent to the magnetopause causes large changes in the location of the magnetosphere with a similar degree of variability to that caused by changes in the solar wind dynamic pressure. Thus, one cannot infer the size of the magnetosphere from solar wind measurements alone. It would be interesting to investigate how global or localised an effect this is. The measurements presented here use single spacecraft encounters with the magnetopause to infer the size of the magnetosphere. As such it is unclear if the change in the location of the magnetopause is very localised or if it corresponds to a more wide-spread global change in the size of the magnetosphere.

It would also be of interest to explore how the plasma β parameter adjacent to the magnetopause evolves as the system changes in size. If a sudden plasma energisation occurs adjacent to the magnetopause, elevating β and causing the magnetopause to move outwards, how does β change as the magnetosphere undergoes a reconfiguration in order to reach a new equilibrium with the solar wind? The magnetic field strength and, hence, the magnetic pressure would surely decrease, but the plasma pressure may also be expected to cool adiabatically as it expands to fill the larger magnetosphere. The evolution of β would depend on the rate of change of the magnetic pressure with respect to the rate of change of the plasma pressure, a factor that one expects would depend on the evolving flux tube geometry during the system expansion.

Finally, additional layers of complexity could be added to the empirical model to improve its accuracy. With additional high-latitude observations, a reliable seasonal dependance on the degree polar flattening could be added. Account of the periodic oscillations in the magnetic pressure could also be taken by modifying the functional form of the standoff

distance parameter. One would expect that such measures will improve the accuracy of the model, but one should also be wary of proceeding beyond the point of diminishing returns. That is, there should always be an appropriate balance between the number of model parameters, the number of individual measurements used to construct the model and the improvement made to the model by the addition of further free parameters.

This page was intentionally left blank

Appendix A

Appendix A: A Hitchhiker's Guide to Statistical Analysis

If a man will begin with certainties, he shall end in doubts;
but if he will be content to begin with doubts, he shall end in certainties.
Sir Francis Bacon, *The Advancement of Learning*

"Would it save you a lot of time if I just gave up and went mad now?"
Douglas Adams, *The Hitchhiker's Guide to the Galaxy*

A.1 Wilcoxon Signed Rank Test

The signed rank test is a statistical hypothesis test proposed by *Wilcoxon* (1945). It can be applied to two sets of observations to test the null hypothesis that both sets of observations are drawn from populations with the same median value. In addition it can be applied to a single set of observations to test the null hypothesis that the median of the population from which these observations are drawn is equal to a specific value.

In Section 3.3.3 the latter version of this test was applied to the distances between the observed set of magnetopause crossings and the locations predicted by an empirical model of the magnetopause, $\Delta\rho_i$. Two models were used: the axisymmetric *Kanani et al.* (2010) model and a version of that model flattened along the Z_{KSM} axis by a factor $\mathcal{E}$, where $\mathcal{E} < 1$. If the model predictions are in good agreement with the observations, one would expect a median distance close to zero. Here, the application of this test will be outlined.

1. The first and most important step is to state the null hypothesis: what is being tested? If the magnetopause crossings are, indeed, crossings of a flattened magnetosphere, one expects the distances $\Delta\rho_i$ will be closer to zero when the flattened model is used than when the axisymmetric model is used. Hence, we are testing the null hypothesis that both sets of distances $\Delta\rho_i$ are drawn from populations with median values of zero. These results may provide evidence in favour of polar flattening if the probability that this is the case is much larger for the flattened model than the axisymmetric model.

2. The difference between the distances $\Delta\rho_i$ and the hypothesised median, M, is calculated:

$$d_i = \Delta\rho_i - M. \tag{A.1}$$

3. To apply the signed rank test, we order the union of both sets $\Delta\rho_i(\mathcal{E} = 1)$ and $\Delta\rho_i(\mathcal{E} = 0.80)$ in ascending order ignoring the signs, assigning a rank of 1 to the lowest absolute value, 2 to the second lowest absolute value, and so on.

4. Each rank is then labelled with its sign according to the sign of d_i, which, in this case, is the same as the sign of $\Delta\rho_i$.

5. The sum of the ranks of positive and negative d_i can then be calculated, W^+ and W^- respectively. The test statistic, W, is the minimum of W^+ and W^- in the two-tailed test.

6. The p-value can be calculated from W and the number of observations in the sample, N. For large sample sizes (>20), the distribution of W approaches a normal

distribution and the p-value can be calculated using the z-statistic,

$$z = \frac{(W - N(N+1)/4)}{\sqrt{\frac{N(N+1)(2N+1) - tieadj}{24}}}, \tag{A.2}$$

where *tieadj* is an adjustment made in the case of any tie rankings or observations exactly equalling M. One can then approximate the p-value by evaluating the normal cumulative distribution function at z. This should be multiplied by two for the two-tailed test.

A.2 Monte Carlo Bootstrap

The Monte Carlo Bootstrap technique allows one to infer characteristics of a population without actual knowledge of the population distribution. Instead, a sample drawn from this population is used to infer characteristics of its parent population. It is thus a useful technique when the underlying population distribution is unknown or unobserved. As the size of the sample increases, its distribution asymptotically approaches that of the population from which it is drawn so the measured characteristics also asymptotically approach the 'true' characteristics of the population. This is a powerful technique with few underlying assumptions, only that the observations are a good representation of the underlying population and that the data are independent.

Essentially, the data are randomly resampled with replacement. This means that the same number of data points are drawn from the data as exist in the sample, but are drawn 'with replacement' such that data in the new sample are not necessarily unique. Duplicate points are very likely to exist in the new sample – theoretically one may expect N/e data points to be duplicates, where N is the sample size and e is the base of the natural logarithm. This sample is then operated upon in the same way as the original sample and this procedure is repeated a large number of times, drawing a different sample each time. Since a different combination of data are operated upon at each resampling, the estimated parameter (the degree of polar flattening for example) is likely to vary for each resample if it is a continuous quantity. The distribution of this parameter can then be derived and can be corrected for bias and skewness (*Efron*, 1987), and uncertainties and confidence intervals can be calculated from this at any given level of significance. If

the sample is a good representation of the population, then the distribution of parameter estimates is a good approximation to the true population parameter.

Increasing the number of times the original sample is resampled can reduce the possibility of artefacts associated with the random sampling method and will allow the distribution of the parameter to be better captured. Using more random samples, however, does not increase the accuracy with which the estimated distribution represents the true population distribution. The level of accuracy is ultimately limited by the original sample drawn from the population, which can only contain a finite amount of information about the underlying distribution. Hence, increasing the number of resamples essentially improves the resolution of the parameter distribution derived from the sample, but there are no guarantees that this is accurately representative of the underlying population. Thus, it is good practice to use other techniques to ascertain that the original sample is representative of the population, such as the trajectory analysis of Section 3.3.6.

A.3 K-means Clustering

K-means is a prototype based clustering method. Each data vector, $\mathbf{x}_i$ belongs to exactly one cluster, c, with a prototype μ_c. The precise definition of the prototype depends on the distance measure used to categorise the data, but in the Euclidean case it is simply the average location of the data within each cluster. The aim is to find good prototypes and good assignments of data vectors to prototypes. However, an exact solution to this is impossible as the problem is circular. Given a good set of prototypes, it would be trivial to assign data to each cluster by simply assigning them to the nearest prototype. Similarly, given a good set of assignments we could let the prototypes be the means of each cluster. However, one usually has neither of these requirements and must thus determine them both simultaneously. Iterative methods may be used to achieve this, and k-means is one such method.

The data are initially randomly allocated to clusters and μ_c is then calculated for each cluster. The aim is to minimise the average distance between the data and their prototypes. Taking the Euclidean distance as our distance measure, the distance between

each datum and each prototype is defined as,

$$d_{ic} = ||\mathbf{x}_i - \mu_c||^2, \tag{A.3}$$

from which clusters c_i can be assigned as,

$$c_i = \arg\min_c d_{ic}, \tag{A.4}$$

and one can define,

$$r_{ic} = \begin{cases} 1 & \text{if } c_i = c, \\ 0 & \text{otherwise.} \end{cases} \tag{A.5}$$

One can then repeat the above procedure iteratively in order to calculate,

$$\arg\min_{\mathbf{R},\boldsymbol{\mu}} J(\mathbf{R}, \boldsymbol{\mu}) = \sum_{i=1}^{N}\sum_{c=1}^{K} r_{ic} d_{ic} \tag{A.6}$$

where J is the objective function to minimise, $\mathbf{R}$ is the complete set of r_{ic}, $\boldsymbol{\mu}$ is the complete set of μ_c, N is the number of observations and K is the number of clusters. The problem of separating data into clusters then becomes an optimisation problem. An example showing k-means in operation is shown in Figure A.1.

As with other optimisation problems, there are potential pitfalls with this approach. Since the data are randomly assigned to a cluster in the first instance, it is possible that different initialisations can lead to different solutions as the algorithm may converge to a local minimum rather than the global minimum. The possibility of this occurring can be minimised by repeating the minimisation many times and using the result that corresponds to the minimum. Clustering also has its own unique set of issues. Firstly, one must select the number of clusters into which the data are separated. Increasing K always decreases J so it is not simply a case of choosing the number of clusters that minimises the objective function. For example, in the extreme case that one sets $K = N$, a cluster will be centred on each data point rendering $J = 0$, a result that is of no practical use. For the purposes of this work, clustering was applied to continuous data as discussed in Section 4.6.1 for illustrative purposes only, so the number of clusters is not of particular importance in this

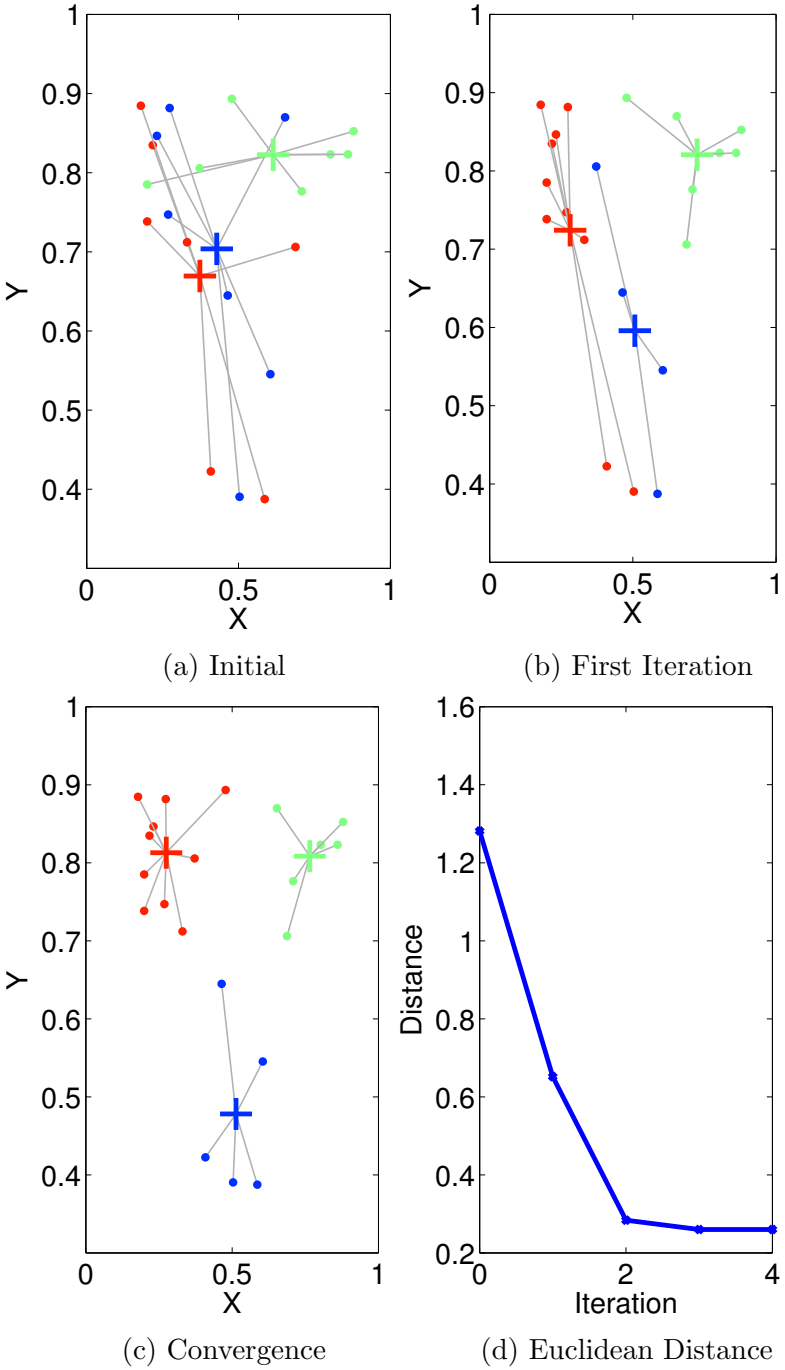

Figure A.1. Demonstrates the iterative k-means clustering method. (a) The data are randomly assigned to a cluster. The location of each prototype is calculated by calculating the mean of data within each cluster. (b) The average distance between the data and their prototypes is minimised iteratively until convergence is reached (c). (d) Shows the objective function as a function of iteration number, and shows that the algorithm is able to converge to a stable solution.

case. In addition, it is possible to initialise empty clusters. Those clusters could simply be dropped or could be reassigned.

A.4 F-Test

When fitting an empirical model to any type of data, the issue of overfitting is one that should be at the forefront of any good scientist's mind. Given N observations, one could fit these data perfectly with a model consisting of N free parameters, but, in doing so, how much does one really learn about the system being studied? The problem can be summarised in terms of what one is hoping to achieve with the model – explanation (a model as simple as possible, but no simpler) or prediction (all models are false, but some are useful). Typically, scientists hope to use models in conjunction with observations in order to explain the world around them so tend to lean towards explanation, invoking enough free parameters to explain the data but no more. Such models tend to be more robust and applicable to conditions that were not directly observed, and are often more useful, especially when the data are sparse and continuous. The F-test is a useful tool used to compare nested models in order to ascertain if adding extra free parameters significantly improves the predictive power of the model and helps to prevent departures into the realm of overfitting. Overfitting is the situation where adding additional parameters to the model do not significantly aid in the explanation of the data.

For a model with f degrees of freedom, where the degree of freedom is the number of observations minus the number of free parameters, a commonly used goodness of fit estimator between the model and the observations is the sum of squared residuals,

$$S = \sum_{i=1}^{N} R^2 \tag{A.7}$$

where N is the number of observations and R is the distance between the observed crossing and location predicted by the model for the i^{th} observation. The F-statistic between two models, F_{STAT} can then be computed as,

$$F_{STAT} = \frac{f_2}{S_2}\left(\frac{S_1 - S_2}{f_1 - f_2}\right) \tag{A.8}$$

where S_1 and S_2 and f_1 and f_2 are the sum of squared residuals and the degrees of freedom of models 1 and 2 respectively, and $f_1 > f_2$. Since model 2 has more free parameters, it is expected that $S_1 > S_2$. The probability that the additional free parameters introduced in model 2 are not warranted because the improvement in the sum of squared residuals is not significant, otherwise known as the p-value of the test, can be determined by integrating the F-distribution at F_{STAT}.

A.5 Kolmogorov-Smirnov Test

The Kolmogorov-Smirnov (K-S) test (*Massey*, 1951) is a useful tool to employ when one wishes to analyse the distribution of a series of measurements. One can use it to test how likely it is that a series of measurements follow a hypothesised distribution (the one-sample K-S test), or it can be used to test how likely it is that two independent sets of measurements were drawn from the same underlying population (the two-sample K-S test). One of its main advantages over other tests that serve a similar purpose, such as Student's T-test for example, is that it makes no assumptions whatsoever about the distribution of the data.

In both variations of the K-S test, the cumulative distribution function (CDF) is calculated for both distributions and these are then compared against each other. In the case of the one-sample test, the empirical distribution function is calculated from the measurements and is compared against the analytical CDF of the reference distribution. In the two-sample test the empirical distribution function is calculated for each sample and these are then compared against each other. The maximum absolute difference between these two distributions is quantified in terms of the D statistic; D_n in the case of the one-sample test and $D_{m,n}$ in the case of the two sample test for samples of size m and n. The D statistic is defined as the maximum absolute difference between the two distributions as shown in Figure A.2. Intuitively, as the number of data within the sample approaches infinity, the distribution of the sample asymptotically approaches that of its parent population. In that case, if the parent population follows the hypothesised distribution in the one-sample test, D_n will tend towards zero, and if the two samples are drawn from the same population in the two-sample test, $D_{m,n}$ will tend towards zero. This tendency is formalised by the Glivenko-Cantelli theorem (*Tucker*, 1959).

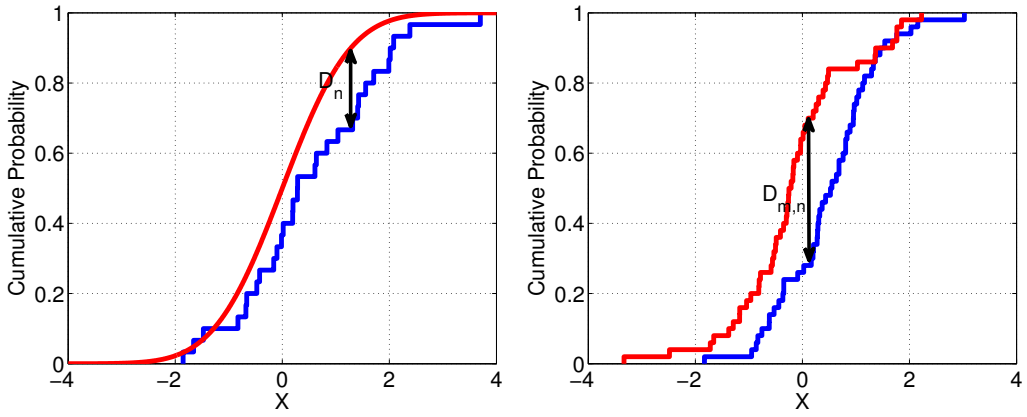

(a) One-sample K-S Test (b) Two-sample K-S Test

Figure A.2. Illustrating the Kolmogorov-Smirnov Test. a) A sample is tested against a hypothesised distribution by calculating its empirical cumulative distribution function and comparing that against the CDF of the hypothesised distribution. b) Two samples are tested against each other in order to determine the probability that they are drawn from the same underlying distribution by calculating their CDFs and comparing them.

The probability of observing a D-statistic at least as large as that observed provided that the null hypothesis is true (the p-value) can then be calculated from the D-statistic. In the one-sample test, the null hypothesis is that the data are, indeed, drawn from the hypothesised distribution and in the two-sample test, the null hypothesis is that the two data samples are drawn from the same underlying distribution. The p-value can then be evaluated by referencing the D-statistic to a table of critical values for different significance levels. Alternatively, it can be approximated by evaluating Kolmogorov's distribution in the limit that $n \to \infty$ as discussed by (*Marsaglia et al.*, 2003). The latter approach was employed in this work using the *MATLAB Statistic Toolbox*.

This page was intentionally left blank

Appendix B

Appendix B: Magnetopause Crossing Observations

This appendix lists all of the magnetopause crossings identified through the course of this study. When the spacecraft traverses the magnetopause, it typically samples distinctly different plasma populations and magnetic fields on either side. An example of some magnetopause crossings are shown in Figure 2.16, and Section 2.5 describes how these were determined. The spacecraft positions were calculated using the reconstructed trajectory kernels of NASA's Navigation and Ancillary Information Facility (NAIF) 'SPICE' geometry information system. Distances are quoted in units of Saturnian radii (R_S) with $1\,\mathrm{R_S} = 60268\,\mathrm{km}$. Note that the inbound/outbound determination was not recorded at the time that each crossing was identified, but was instead calculated by post-processing the crossing list. Most determinations appear to be correct, but they should not be relied upon for scientific purposes. Take care especially when there are inconsistencies in the list e.g. an outbound crossing followed by another outbound crossing. Such inconsistencies can occur as a result of e.g. data gaps or boundary waves, but may be the result of an incorrect inbound/outbound determination.

Year	DOY	Hour	Minute	(I)n/(O)utbound	X_{KSM}	Y_{KSM}	Z_{KSM}
2004	180	18	42	I	16.97	-29.85	-2.24
2004	180	18	51	O	16.95	-29.80	-2.23
2004	180	19	52	I	16.76	-29.35	-2.17
2004	180	20	21	O	16.68	-29.13	-2.13
2004	180	20	27	I	16.66	-29.09	-2.13
2004	180	20	44	O	16.61	-28.96	-2.11
2004	180	21	09	I	16.53	-28.78	-2.08
2004	180	21	32	O	16.47	-28.62	-2.06
2004	180	21	56	I	16.39	-28.44	-2.03
2004	180	23	07	O	16.18	-27.91	-1.95
2004	181	02	44	I	15.51	-26.29	-1.71
2004	300	07	32	I	18.82	-10.12	7.32
2004	300	08	21	O	18.66	-9.82	7.33
2004	300	10	42	I	18.19	-8.95	7.36
2004	308	14	31	O	-9.53	-41.44	-15.92
2004	308	18	18	I	-9.32	-42.20	-16.00
2004	308	20	00	O	-9.22	-42.55	-16.03
2004	309	01	16	I	-8.91	-43.58	-16.14
2004	309	18	50	O	-7.85	-46.85	-16.41
2004	348	02	33	I	18.75	-10.87	7.33
2004	348	03	48	O	18.53	-10.45	7.32
2004	348	05	26	I	18.23	-9.90	7.30
2004	356	20	16	O	0.47	-44.74	-4.03
2005	022	19	27	O	-1.23	-44.35	-4.69
2005	044	16	40	I	21.71	-19.81	8.06
2005	045	00	10	O	21.03	-17.77	7.94
2005	045	01	28	I	20.91	-17.41	7.92
2005	054	22	08	O	11.74	-39.12	4.90
2005	054	23	05	I	11.84	-39.16	4.94
2005	054	23	18	O	11.87	-39.18	4.95
2005	054	23	42	I	11.91	-39.19	4.97
2005	054	23	51	O	11.92	-39.20	4.97
2005	065	21	44	I	19.57	-14.11	7.99
2005	066	00	08	O	19.30	-13.47	7.88
2005	066	01	26	I	19.14	-13.13	7.82
2005	066	02	06	O	19.06	-12.95	7.78
2005	066	04	16	I	18.78	-12.36	7.67
2005	066	05	45	O	18.58	-11.95	7.59
2005	066	05	59	I	18.55	-11.89	7.57
2005	072	11	09	O	3.34	-32.22	1.38
2005	087	02	22	I	17.22	-9.68	6.94
2005	087	03	26	O	17.04	-9.36	6.87
2005	087	04	03	I	16.94	-9.17	6.83
2005	087	04	21	O	16.88	-9.08	6.81
2005	087	12	55	O	15.21	-6.40	6.13
2005	087	13	04	I	15.18	-6.35	6.11
2005	100	07	33	O	16.15	-29.11	3.59
2005	100	10	06	I	16.21	-28.72	3.61
2005	100	10	58	O	16.23	-28.58	3.62
2005	103	08	37	I	14.09	-12.44	3.39
2005	107	19	14	O	-0.20	-26.59	-1.75
2005	109	20	12	I	6.52	-34.10	-2.19
2005	109	22	24	O	6.81	-34.32	-2.20
2005	110	00	10	I	7.04	-34.49	-2.21
2005	110	00	57	O	7.14	-34.56	-2.22
2005	110	02	12	I	7.30	-34.68	-2.22
2005	110	09	51	O	8.27	-35.32	-2.26
2005	117	18	46	I	22.15	-27.99	-1.69
2005	117	19	09	O	22.16	-27.94	-1.69
2005	119	06	19	I	21.86	-21.62	-1.28
2005	119	06	23	O	21.86	-21.60	-1.28
2005	119	06	26	I	21.86	-21.59	-1.28
2005	119	06	37	O	21.85	-21.55	-1.27
2005	119	12	08	I	21.64	-20.38	-1.20
2005	119	12	21	O	21.63	-20.34	-1.20

Continued on next page

Table B.1 – *Continued from previous page*

Year	DOY	Hour	Minute	(I)n/(O)utbound	X_{KSM}	Y_{KSM}	Z_{KSM}
2005	119	19	43	I	21.26	-18.68	-1.10
2005	119	20	05	O	21.24	-18.60	-1.09
2005	120	07	41	I	20.40	-15.79	-0.92
2005	120	09	09	O	20.27	-15.41	-0.90
2005	120	12	33	I	19.95	-14.53	-0.84
2005	121	08	19	O	17.29	-8.84	-0.50
2005	121	11	07	I	16.77	-7.96	-0.44
2005	126	16	27	O	1.77	-29.84	-1.97
2005	126	18	36	I	2.07	-30.20	-2.00
2005	126	18	51	O	2.10	-30.25	-2.00
2005	126	19	14	I	2.15	-30.31	-2.00
2005	126	21	09	O	2.42	-30.62	-2.02
2005	126	23	48	I	2.78	-31.03	-2.05
2005	127	04	44	O	3.45	-31.76	-2.10
2005	128	00	46	I	6.11	-34.19	-2.26
2005	128	00	54	O	6.13	-34.20	-2.26
2005	128	01	08	I	6.16	-34.22	-2.26
2005	128	01	50	O	6.25	-34.30	-2.27
2005	137	19	54	I	21.30	-19.81	-1.33
2005	145	03	44	O	2.44	-30.98	-2.24
2005	145	07	26	I	2.93	-31.54	-2.28
2005	145	13	38	O	3.76	-32.41	-2.34
2005	157	13	29	I	17.73	-10.29	-0.78
2005	166	00	40	O	10.21	-37.09	-2.98
2005	166	05	37	I	10.77	-37.28	-3.00
2005	166	07	56	O	11.03	-37.36	-3.01
2005	166	13	29	I	11.64	-37.51	-3.02
2005	167	05	52	O	13.36	-37.73	-3.05
2005	167	10	32	I	13.83	-37.72	-3.05
2005	167	12	25	O	14.02	-37.71	-3.05
2005	175	00	48	I	19.73	-15.47	-1.30
2005	175	04	07	O	19.42	-14.58	-1.22
2005	182	03	23	O	3.65	-33.01	-2.84
2005	193	21	10	I	18.11	-11.72	-1.09
2005	194	05	50	O	16.80	-9.04	-0.85
2005	194	06	57	I	16.61	-8.68	-0.82
2005	199	14	44	O	0.83	-30.19	-2.75
2005	199	16	33	I	1.07	-30.50	-2.78
2005	199	16	48	O	1.10	-30.54	-2.79
2005	199	17	18	I	1.17	-30.62	-2.79
2005	199	17	44	O	1.23	-30.69	-2.80
2005	211	12	20	I	19.68	-16.45	-1.64
2005	218	09	26	O	2.02	-31.92	-3.10
2005	219	04	49	I	4.47	-34.38	-3.36
2005	219	05	23	O	4.55	-34.44	-3.36
2005	219	21	14	I	6.49	-35.92	-3.52
2005	219	21	49	O	6.56	-35.97	-3.53
2005	227	14	13	I	20.74	-27.51	-2.88
2005	227	15	56	O	20.76	-27.22	-2.85
2005	227	19	14	I	20.79	-26.65	-2.80
2005	229	08	35	I	20.04	-18.97	-2.05
2005	237	14	51	O	3.25	-34.27	-2.26
2005	237	16	01	I	3.38	-34.37	-2.25
2005	237	16	57	O	3.48	-34.46	-2.25
2005	240	11	02	I	9.89	-36.47	-1.79
2005	240	13	18	O	10.08	-36.42	-1.77
2005	246	12	08	I	14.74	-15.75	0.16
2005	246	17	48	O	14.29	-13.97	0.25
2005	246	19	48	I	14.10	-13.31	0.28
2005	246	21	55	O	13.87	-12.60	0.31
2005	246	23	27	I	13.70	-12.07	0.34
2005	251	20	09	O	-1.60	-29.22	-0.73
2005	251	22	54	I	-1.31	-29.77	-0.62
2005	263	06	47	I	17.21	-24.46	6.20
2005	263	07	23	O	17.20	-24.34	6.20

Continued on next page

Table B.1 – *Continued from previous page*

Year	DOY	Hour	Minute	(I)n/(O)utbound	X_{KSM}	Y_{KSM}	Z_{KSM}
2005	263	19	58	I	16.89	-21.48	6.09
2005	264	03	16	I	16.59	-19.68	5.99
2005	264	09	12	I	16.27	-18.11	5.88
2005	264	15	43	O	15.82	-16.28	5.72
2005	264	17	20	I	15.69	-15.81	5.68
2005	273	10	32	O	6.38	-38.46	2.15
2005	273	13	11	I	6.63	-38.60	2.24
2005	274	00	02	O	7.64	-39.08	2.60
2005	274	06	56	O	8.26	-39.30	2.83
2005	274	07	37	I	8.32	-39.32	2.85
2005	274	07	50	O	8.34	-39.32	2.86
2005	274	07	57	I	8.35	-39.33	2.86
2005	274	08	06	O	8.36	-39.33	2.87
2005	274	08	20	I	8.38	-39.34	2.88
2005	274	08	32	O	8.40	-39.34	2.88
2005	274	08	36	I	8.41	-39.34	2.88
2005	275	07	12	O	10.34	-39.57	3.58
2005	275	10	08	I	10.58	-39.55	3.67
2005	275	18	06	O	11.21	-39.44	3.90
2005	275	18	28	I	11.24	-39.44	3.91
2005	275	18	43	O	11.26	-39.43	3.92
2005	275	20	03	I	11.36	-39.40	3.96
2005	276	03	07	O	11.90	-39.23	4.15
2005	276	09	24	I	12.36	-39.01	4.32
2005	276	17	31	O	12.93	-38.67	4.53
2005	282	16	09	I	15.94	-17.41	5.70
2005	282	17	31	O	15.85	-17.03	5.67
2005	283	01	57	I	15.17	-14.53	5.44
2005	283	04	04	O	14.96	-13.87	5.36
2005	283	06	06	I	14.75	-13.22	5.29
2005	283	06	41	O	14.69	-13.03	5.27
2005	283	11	04	I	14.16	-11.58	5.08
2005	283	11	17	O	14.13	-11.50	5.07
2005	283	11	35	I	14.09	-11.40	5.06
2005	288	07	23	O	-1.84	-28.68	-0.84
2005	288	09	44	I	-1.60	-29.15	-0.76
2005	288	14	46	O	-1.08	-30.11	-0.58
2005	288	16	40	I	-0.88	-30.45	-0.51
2005	288	17	31	O	-0.80	-30.61	-0.48
2005	289	20	41	I	2.01	-34.64	0.51
2005	290	00	46	O	2.43	-35.12	0.66
2005	293	22	20	I	11.00	-39.04	3.72
2005	293	23	18	O	11.07	-39.02	3.74
2005	294	05	55	I	11.58	-38.83	3.93
2005	294	06	30	O	11.62	-38.81	3.94
2005	297	23	20	I	16.35	-30.64	5.68
2005	297	23	45	O	16.37	-30.58	5.69
2005	298	02	08	I	16.42	-30.20	5.71
2005	298	10	45	O	16.59	-28.77	5.78
2005	298	22	34	I	16.69	-26.59	5.83
2005	298	22	53	O	16.69	-26.53	5.83
2005	299	02	14	I	16.69	-25.87	5.83
2005	299	03	48	O	16.69	-25.55	5.83
2005	299	05	53	I	16.68	-25.12	5.83
2005	299	11	48	O	16.62	-23.86	5.82
2005	299	13	54	I	16.59	-23.39	5.81
2005	307	18	26	O	-13.04	-34.63	-4.67
2005	323	15	47	I	12.18	-45.52	4.17
2005	323	16	55	O	12.24	-45.38	4.20
2005	324	01	25	I	12.70	-44.25	4.36
2005	324	03	49	O	12.83	-43.93	4.40
2005	324	05	48	I	12.93	-43.65	4.44
2005	324	09	10	O	13.10	-43.17	4.50
2005	324	20	36	I	13.66	-41.45	4.70
2005	335	23	48	O	-13.22	-32.89	-4.68

Continued on next page

Table B.1 – *Continued from previous page*

Year	DOY	Hour	Minute	(I)n/(O)utbound	X_{KSM}	Y_{KSM}	Z_{KSM}
2005	336	02	21	I	-13.13	-33.43	-4.65
2005	336	06	04	O	-12.98	-34.21	-4.60
2005	336	18	50	I	-12.41	-36.72	-4.40
2005	338	11	45	I	-10.16	-43.33	-3.64
2005	338	14	11	O	-10.01	-43.66	-3.59
2005	338	20	10	I	-9.63	-44.45	-3.46
2005	338	22	23	O	-9.49	-44.73	-3.41
2005	338	23	39	I	-9.41	-44.89	-3.38
2005	339	01	50	O	-9.27	-45.16	-3.33
2005	339	03	26	I	-9.17	-45.35	-3.30
2005	339	08	57	O	-8.80	-46.01	-3.17
2005	339	20	36	I	-8.02	-47.29	-2.91
2005	340	05	24	O	-7.42	-48.17	-2.70
2005	342	04	16	O	-4.05	-51.69	-1.54
2005	349	12	20	I	8.90	-49.09	2.93
2005	349	13	05	O	8.95	-49.02	2.94
2005	349	14	10	I	9.02	-48.93	2.97
2005	350	07	43	O	10.17	-47.25	3.36
2005	350	17	47	I	10.80	-46.16	3.58
2005	350	20	34	O	10.97	-45.84	3.64
2005	350	21	56	I	11.05	-45.68	3.67
2005	351	09	29	O	11.73	-44.26	3.91
2005	351	10	50	I	11.81	-44.08	3.93
2005	351	11	53	O	11.87	-43.95	3.96
2005	351	13	02	I	11.94	-43.79	3.98
2005	351	15	25	O	12.07	-43.48	4.03
2005	351	21	25	I	12.40	-42.65	4.14
2005	365	08	59	O	-11.92	-39.71	-4.16
2005	365	09	36	I	-11.88	-39.79	-4.15
2005	365	14	50	O	-11.59	-40.47	-4.05
2005	365	19	10	I	-11.34	-41.02	-3.97
2006	001	14	50	O	-10.12	-43.22	-3.56
2006	008	11	17	I	2.31	-46.28	0.65
2006	008	15	54	O	2.67	-45.99	0.78
2006	008	22	15	I	3.17	-45.54	0.95
2006	024	22	42	O	-29.69	-38.86	-10.04
2006	026	03	32	I	-29.87	-43.47	-10.11
2006	026	05	54	O	-29.87	-43.82	-10.11
2006	029	19	02	I	-28.48	-54.38	-9.65
2006	030	09	10	O	-28.04	-55.76	-9.50
2006	030	09	40	I	-28.02	-55.81	-9.50
2006	030	13	06	O	-27.91	-56.13	-9.46
2006	031	01	02	I	-27.49	-57.19	-9.32
2006	031	08	13	O	-27.22	-57.80	-9.23
2006	031	15	55	I	-26.92	-58.42	-9.13
2006	032	12	47	O	-26.04	-59.97	-8.83
2006	032	13	09	I	-26.02	-59.99	-8.83
2006	033	09	42	O	-25.07	-61.31	-8.51
2006	033	10	15	I	-25.04	-61.34	-8.50
2006	034	00	36	O	-24.33	-62.15	-8.26
2006	037	05	20	O	-19.94	-64.86	-6.80
2006	037	08	17	I	-19.75	-64.91	-6.73
2006	037	22	56	O	-18.81	-65.10	-6.42
2006	038	08	27	I	-18.18	-65.18	-6.21
2006	038	13	29	O	-17.85	-65.20	-6.10
2006	039	05	34	I	-16.75	-65.19	-5.73
2006	039	08	54	O	-16.51	-65.17	-5.65
2006	039	12	07	I	-16.29	-65.15	-5.58
2006	039	16	19	O	-15.99	-65.12	-5.48
2006	039	16	24	I	-15.99	-65.12	-5.48
2006	039	16	38	O	-15.97	-65.12	-5.47
2006	053	23	35	I	10.85	-22.28	3.49
2006	054	04	59	O	11.04	-20.38	3.56
2006	054	06	22	I	11.07	-19.89	3.57
2006	054	08	40	O	11.13	-19.04	3.59

Continued on next page

Table B.1 – *Continued from previous page*

Year	DOY	Hour	Minute	(I)n/(O)utbound	X_{KSM}	Y_{KSM}	Z_{KSM}
2006	054	15	24	I	11.22	-16.43	3.63
2006	071	01	15	O	-19.72	-41.49	-6.51
2006	071	08	03	I	-19.05	-41.37	-6.29
2006	071	12	57	O	-18.56	-41.26	-6.13
2006	071	13	06	I	-18.54	-41.26	-6.12
2006	071	13	40	O	-18.48	-41.24	-6.10
2006	071	13	43	I	-18.48	-41.24	-6.10
2006	071	14	26	O	-18.40	-41.22	-6.08
2006	071	14	38	I	-18.38	-41.22	-6.07
2006	071	19	01	O	-17.93	-41.09	-5.92
2006	071	21	28	I	-17.67	-41.01	-5.84
2006	071	23	44	O	-17.43	-40.93	-5.76
2006	072	00	54	I	-17.30	-40.89	-5.72
2006	072	02	14	O	-17.16	-40.84	-5.67
2006	072	02	18	I	-17.15	-40.84	-5.67
2006	072	04	55	O	-16.86	-40.73	-5.58
2006	072	05	26	I	-16.81	-40.71	-5.56
2006	072	05	36	O	-16.79	-40.71	-5.55
2006	072	13	38	I	-15.89	-40.34	-5.26
2006	072	15	08	O	-15.72	-40.26	-5.20
2006	072	19	36	I	-15.21	-40.02	-5.04
2006	073	23	33	O	-11.81	-37.97	-3.93
2006	074	07	56	I	-10.73	-37.16	-3.57
2006	074	09	33	O	-10.51	-36.99	-3.51
2006	074	09	58	I	-10.46	-36.95	-3.49
2006	074	10	58	O	-10.33	-36.84	-3.44
2006	074	14	23	I	-9.87	-36.47	-3.30
2006	074	14	35	O	-9.84	-36.45	-3.29
2006	074	17	02	I	-9.52	-36.17	-3.18
2006	074	20	21	O	-9.07	-35.78	-3.03
2006	075	04	37	I	-7.92	-34.72	-2.66
2006	075	12	28	O	-6.82	-33.62	-2.30
2006	075	15	54	I	-6.32	-33.09	-2.14
2006	075	22	02	O	-5.44	-32.11	-1.85
2006	075	23	29	I	-5.22	-31.86	-1.78
2006	076	01	21	O	-4.95	-31.54	-1.69
2006	076	02	02	I	-4.85	-31.43	-1.66
2006	076	03	19	I	-4.66	-31.20	-1.59
2006	076	06	15	O	-4.22	-30.67	-1.45
2006	076	12	18	I	-3.31	-29.50	-1.16
2006	076	14	41	O	-2.95	-29.02	-1.04
2006	076	14	41	I	-2.95	-29.02	-1.04
2006	076	20	12	O	-2.11	-27.84	-0.76
2006	076	20	30	I	-2.07	-27.78	-0.75
2006	076	20	40	O	-2.04	-27.74	-0.74
2006	076	21	21	I	-1.93	-27.59	-0.71
2006	105	19	36	I	-37.89	-49.34	-12.09
2006	105	22	42	O	-37.60	-49.33	-12.00
2006	105	23	16	I	-37.55	-49.32	-11.98
2006	106	00	14	O	-37.45	-49.32	-11.95
2006	106	05	12	I	-36.98	-49.28	-11.80
2006	106	13	04	O	-36.20	-49.19	-11.55
2006	106	17	08	I	-35.79	-49.14	-11.42
2006	106	23	22	O	-35.15	-49.04	-11.21
2006	107	01	06	I	-34.97	-49.01	-11.16
2006	108	10	07	O	-31.35	-48.13	-10.00
2006	108	11	30	I	-31.19	-48.08	-9.95
2007	033	11	24	O	15.01	0.15	-6.64
2007	033	12	43	I	15.24	0.51	-6.29
2007	033	14	02	O	15.46	0.86	-5.95
2007	033	15	23	I	15.66	1.23	-5.59
2007	033	23	31	O	16.62	3.39	-3.32
2007	034	06	30	I	17.06	5.17	-1.29
2007	034	06	51	O	17.08	5.26	-1.19
2007	034	07	02	I	17.08	5.30	-1.14

Continued on next page

Table B.1 – *Continued from previous page*

Year	DOY	Hour	Minute	(I)n/(O)utbound	X_{KSM}	Y_{KSM}	Z_{KSM}
2007	034	12	08	O	17.18	6.54	0.37
2007	034	15	14	I	17.16	7.26	1.28
2007	034	16	15	O	17.14	7.49	1.57
2007	034	18	25	I	17.08	7.97	2.21
2007	035	02	29	O	16.64	9.66	4.53
2007	035	02	45	I	16.62	9.71	4.60
2007	070	08	54	O	15.92	14.79	11.29
2007	070	20	40	I	14.78	16.39	13.61
2007	070	23	00	O	14.52	16.68	14.04
2007	070	23	21	I	14.48	16.72	14.10
2007	070	23	46	O	14.43	16.77	14.18
2007	072	16	09	I	8.68	19.93	20.08
2007	072	22	58	O	7.55	20.18	20.79
2007	074	17	36	I	0.02	19.99	23.43
2007	074	17	58	O	-0.05	19.98	23.44
2007	074	19	12	I	-0.27	19.93	23.47
2007	075	03	08	O	-1.70	19.56	23.58
2007	075	14	03	I	-3.66	18.90	23.55
2007	089	04	49	O	10.71	22.44	20.33
2007	089	07	05	I	10.41	22.54	20.53
2007	089	10	02	O	10.00	22.67	20.79
2007	089	23	25	I	8.10	23.08	21.80
2007	090	01	00	O	7.87	23.11	21.90
2007	090	03	46	I	7.47	23.16	22.07
2007	090	07	20	O	6.94	23.20	22.28
2007	090	08	25	I	6.77	23.21	22.34
2007	090	13	19	O	6.04	23.23	22.58
2007	090	15	11	I	5.75	23.23	22.67
2007	090	17	34	O	5.39	23.22	22.77
2007	090	18	08	I	5.30	23.22	22.79
2007	090	19	54	O	5.03	23.21	22.86
2007	090	21	41	I	4.75	23.19	22.93
2007	090	22	46	O	4.58	23.17	22.96
2007	091	00	14	I	4.36	23.15	23.01
2007	092	02	09	O	0.27	22.27	23.33
2007	092	03	28	I	0.06	22.20	23.31
2007	102	03	29	O	18.71	14.86	9.27
2007	102	04	18	I	18.72	15.01	9.41
2007	102	04	38	O	18.72	15.07	9.47
2007	102	05	19	I	18.72	15.20	9.58
2007	102	06	24	O	18.72	15.40	9.76
2007	102	08	22	I	18.71	15.76	10.08
2007	102	12	55	O	18.67	16.56	10.81
2007	102	16	43	I	18.60	17.20	11.39
2007	104	09	30	O	16.36	22.52	16.63
2007	104	10	22	I	16.29	22.61	16.72
2007	104	10	58	O	16.24	22.67	16.78
2007	104	11	40	I	16.18	22.73	16.85
2007	104	12	01	O	16.15	22.77	16.89
2007	104	13	45	I	16.00	22.93	17.07
2007	104	21	19	O	15.33	23.59	17.80
2007	104	22	20	I	15.23	23.67	17.89
2007	104	23	06	O	15.16	23.73	17.96
2007	105	02	22	I	14.85	23.98	18.25
2007	116	22	46	O	17.54	8.70	4.13
2007	116	23	26	I	17.63	8.87	4.24
2007	117	02	47	O	18.05	9.72	4.80
2007	117	04	27	I	18.24	10.13	5.06
2007	117	04	49	O	18.28	10.22	5.12
2007	117	04	59	I	18.30	10.26	5.15
2007	117	05	31	O	18.36	10.39	5.23
2007	117	06	13	I	18.43	10.56	5.34
2007	117	07	23	O	18.55	10.84	5.53
2007	123	01	33	I	14.11	28.05	18.11
2007	123	03	14	O	13.94	28.10	18.16

Continued on next page

Table B.1 – *Continued from previous page*

Year	DOY	Hour	Minute	(I)n/(O)utbound	X_{KSM}	Y_{KSM}	Z_{KSM}
2007	123	03	35	I	13.90	28.11	18.17
2007	123	10	08	O	13.19	28.25	18.35
2007	123	11	04	I	13.08	28.26	18.37
2007	123	11	21	O	13.05	28.27	18.38
2007	123	16	51	I	12.43	28.33	18.50
2007	123	21	15	O	11.92	28.35	18.57
2007	124	05	57	I	10.88	28.32	18.67
2007	124	06	47	O	10.78	28.31	18.67
2007	124	08	07	I	10.61	28.29	18.68
2007	124	08	43	O	10.54	28.29	18.68
2007	124	11	26	I	10.20	28.24	18.69
2007	124	13	11	O	9.98	28.21	18.69
2007	126	08	36	I	4.09	25.88	17.73
2007	126	09	05	O	4.02	25.84	17.71
2007	126	09	16	I	3.99	25.82	17.70
2007	126	09	45	O	3.92	25.78	17.68
2007	126	17	43	I	2.76	24.99	17.25
2007	126	18	18	O	2.68	24.92	17.22
2007	126	20	16	I	2.39	24.71	17.10
2007	126	20	33	O	2.35	24.67	17.08
2007	127	02	22	I	1.49	23.98	16.70
2007	127	04	35	O	1.16	23.70	16.54
2007	127	05	53	I	0.97	23.53	16.44
2007	127	06	08	O	0.93	23.50	16.42
2007	127	06	46	I	0.84	23.41	16.37
2007	127	06	58	O	0.81	23.39	16.35
2007	127	07	30	I	0.73	23.31	16.31
2007	127	09	50	O	0.38	22.99	16.12
2007	127	10	38	I	0.26	22.88	16.06
2007	127	11	01	O	0.21	22.82	16.03
2007	127	12	58	I	-0.08	22.54	15.86
2007	127	15	23	O	-0.44	22.17	15.64
2007	127	17	01	I	-0.69	21.91	15.49
2007	133	20	46	O	20.45	14.11	6.71
2007	133	21	05	I	20.47	14.18	6.74
2007	133	23	23	O	20.65	14.67	6.97
2007	134	00	03	I	20.70	14.81	7.04
2007	134	06	21	O	21.10	16.10	7.66
2007	134	07	41	I	21.17	16.36	7.78
2007	134	15	15	O	21.52	17.80	8.47
2007	134	15	48	I	21.54	17.90	8.52
2007	134	17	13	O	21.59	18.16	8.64
2007	134	18	31	I	21.63	18.39	8.75
2007	135	01	57	O	21.82	19.68	9.36
2007	135	05	07	I	21.87	20.20	9.61
2007	135	05	54	O	21.88	20.33	9.67
2007	135	06	11	I	21.88	20.37	9.70
2007	135	12	45	O	21.93	21.40	10.19
2007	135	13	04	I	21.93	21.44	10.21
2007	135	15	27	O	21.93	21.80	10.38
2007	135	17	32	I	21.92	22.11	10.53
2007	135	22	38	O	21.88	22.82	10.87
2007	135	23	56	I	21.86	23.00	10.95
2007	136	00	27	O	21.86	23.07	10.99
2007	136	01	12	I	21.85	23.17	11.04
2007	136	02	42	O	21.82	23.37	11.13
2007	136	04	15	I	21.79	23.57	11.23
2007	136	12	33	O	21.60	24.61	11.72
2007	136	13	32	I	21.57	24.72	11.78
2007	136	13	53	O	21.56	24.76	11.80
2007	136	15	59	I	21.49	25.01	11.92
2007	136	19	34	O	21.37	25.41	12.11
2007	136	21	40	I	21.29	25.63	12.22
2007	137	00	21	O	21.18	25.92	12.35
2007	137	02	57	I	21.07	26.18	12.48

Continued on next page

Table B.1 – *Continued from previous page*

Year	DOY	Hour	Minute	(I)n/(O)utbound	X_{KSM}	Y_{KSM}	Z_{KSM}
2007	137	11	22	I	20.66	26.98	12.86
2007	137	12	36	O	20.60	27.09	12.92
2007	142	15	01	I	8.18	27.98	13.39
2007	142	17	22	O	7.84	27.77	13.29
2007	142	22	21	I	7.12	27.30	13.07
2007	142	23	04	O	7.02	27.23	13.04
2007	142	23	48	I	6.91	27.15	13.00
2007	143	01	20	O	6.68	26.99	12.93
2007	143	02	25	I	6.52	26.88	12.87
2007	143	02	36	O	6.50	26.86	12.86
2007	143	03	02	I	6.43	26.81	12.84
2007	143	03	48	O	6.32	26.72	12.80
2007	143	14	23	I	4.71	25.42	12.18
2007	143	18	27	O	4.08	24.85	11.91
2007	143	22	50	I	3.40	24.19	11.60
2007	144	04	22	O	2.52	23.28	11.16
2007	144	09	45	I	1.65	22.30	10.70
2007	149	07	40	O	19.61	11.30	4.99
2007	149	09	54	I	19.90	11.83	5.17
2007	149	13	27	O	20.32	12.66	5.45
2007	150	13	16	I	22.30	17.63	7.09
2007	150	15	03	O	22.40	17.96	7.20
2007	150	15	49	I	22.44	18.10	7.24
2007	150	17	12	O	22.51	18.36	7.33
2007	153	09	17	I	22.57	27.20	9.95
2007	153	09	52	O	22.54	27.26	9.97
2007	157	09	07	I	14.89	30.69	10.37
2007	157	10	43	O	14.70	30.64	10.34
2007	157	11	58	I	14.56	30.60	10.31
2007	157	13	56	O	14.32	30.54	10.28
2007	157	15	14	I	14.16	30.49	10.25
2007	157	15	55	O	14.07	30.46	10.24
2007	157	18	06	I	13.80	30.38	10.19
2007	157	18	27	O	13.76	30.36	10.18
2007	157	20	18	I	13.53	30.28	10.14
2007	157	23	40	O	13.10	30.12	10.06
2007	158	06	44	I	12.17	29.71	9.87
2007	158	09	37	O	11.78	29.52	9.78
2007	158	10	56	I	11.60	29.43	9.74
2007	158	14	04	O	11.17	29.20	9.64
2007	158	17	38	I	10.66	28.91	9.51
2007	158	23	10	O	9.87	28.42	9.30
2007	159	01	04	I	9.59	28.24	9.23
2007	159	01	55	O	9.47	28.16	9.19
2007	159	03	50	I	9.18	27.96	9.11
2007	159	04	04	O	9.15	27.94	9.10
2007	159	04	12	I	9.13	27.92	9.10
2007	159	04	32	O	9.08	27.89	9.08
2007	159	04	49	I	9.03	27.86	9.07
2007	159	04	55	O	9.02	27.85	9.07
2007	159	05	54	I	8.87	27.74	9.02
2007	159	08	19	O	8.51	27.47	8.92
2007	164	04	49	O	14.65	4.25	2.42
2007	164	14	31	I	16.98	7.05	3.44
2007	164	17	38	O	17.61	7.90	3.75
2007	168	09	34	I	24.51	24.77	5.69
2007	168	10	32	O	24.51	24.90	5.69
2007	168	10	38	I	24.51	24.91	5.69
2007	168	10	53	O	24.51	24.94	5.69
2007	168	18	28	I	24.46	25.86	5.71
2007	168	21	26	O	24.43	26.20	5.72
2007	168	22	55	I	24.40	26.37	5.72
2007	169	08	48	O	24.19	27.41	5.71
2007	169	09	05	I	24.18	27.44	5.71
2007	169	09	18	O	24.18	27.46	5.71

Continued on next page

Table B.1 – *Continued from previous page*

Year	DOY	Hour	Minute	(I)n/(O)utbound	X_{KSM}	Y_{KSM}	Z_{KSM}
2007	169	09	24	I	24.18	27.47	5.71
2007	169	09	50	O	24.16	27.51	5.71
2007	169	14	59	I	24.01	28.00	5.69
2007	169	15	12	O	24.00	28.02	5.69
2007	169	15	41	I	23.98	28.06	5.69
2007	169	18	12	O	23.89	28.29	5.68
2007	169	18	42	I	23.88	28.33	5.68
2007	169	22	23	O	23.73	28.65	5.66
2007	170	00	25	I	23.65	28.81	5.65
2007	170	01	19	O	23.61	28.88	5.64
2007	170	01	21	I	23.61	28.89	5.64
2007	170	01	54	O	23.58	28.93	5.64
2007	170	02	07	I	23.57	28.95	5.64
2007	170	02	22	O	23.56	28.97	5.64
2007	170	13	44	I	22.99	29.78	5.55
2007	172	02	17	O	20.37	31.30	5.08
2007	172	04	10	I	20.20	31.33	5.05
2007	173	09	10	O	17.25	31.23	4.47
2007	174	02	16	I	15.18	30.58	4.04
2007	174	02	51	O	15.10	30.55	4.03
2007	174	03	48	I	14.98	30.50	4.00
2007	174	04	17	O	14.92	30.47	3.99
2007	175	00	05	I	12.18	29.03	3.41
2007	175	01	37	O	11.96	28.88	3.36
2007	175	02	47	I	11.78	28.77	3.32
2007	175	03	19	O	11.70	28.72	3.31
2007	175	04	40	I	11.50	28.58	3.26
2007	175	04	56	O	11.46	28.56	3.25
2007	175	05	47	I	11.33	28.47	3.23
2007	175	06	09	O	11.27	28.43	3.21
2007	175	09	16	I	10.80	28.09	3.11
2007	175	10	20	O	10.63	27.97	3.07
2007	175	10	30	I	10.61	27.96	3.07
2007	175	18	46	O	9.28	26.93	2.78
2007	175	19	53	I	9.10	26.77	2.74
2007	175	20	25	O	9.01	26.70	2.72
2007	175	20	42	I	8.97	26.66	2.71
2007	175	21	35	O	8.82	26.54	2.67
2007	175	23	02	I	8.58	26.33	2.62
2007	175	23	24	O	8.52	26.27	2.61
2007	175	23	42	I	8.47	26.23	2.60
2007	181	03	28	O	19.62	10.96	4.06
2007	181	05	23	I	19.92	11.51	4.12
2007	181	05	55	O	20.01	11.66	4.14
2007	181	06	05	I	20.03	11.70	4.14
2007	181	07	22	O	20.23	12.06	4.19
2007	181	07	46	I	20.29	12.17	4.20
2007	181	12	51	O	21.00	13.56	4.35
2007	181	13	39	I	21.11	13.77	4.37
2007	181	14	37	O	21.23	14.02	4.40
2007	181	16	26	I	21.46	14.50	4.45
2007	181	19	10	O	21.79	15.20	4.52
2007	181	19	24	I	21.81	15.26	4.52
2007	181	20	26	O	21.93	15.52	4.55
2007	181	20	37	I	21.95	15.57	4.55
2007	181	21	41	O	22.07	15.84	4.58
2007	181	22	02	I	22.11	15.93	4.58
2007	181	22	30	O	22.16	16.04	4.59
2007	181	22	34	I	22.16	16.06	4.60
2007	181	23	02	O	22.21	16.18	4.61
2007	182	05	03	I	22.82	17.64	4.73
2007	182	07	41	O	23.06	18.27	4.79
2007	182	09	49	I	23.24	18.77	4.83
2007	182	10	26	O	23.29	18.91	4.84
2007	182	14	48	I	23.64	19.90	4.91

Continued on next page

Table B.1 – *Continued from previous page*

Year	DOY	Hour	Minute	(I)n/(O)utbound	X_{KSM}	Y_{KSM}	Z_{KSM}
2007	182	15	24	O	23.68	20.04	4.92
2007	182	15	43	I	23.71	20.10	4.92
2007	182	16	13	O	23.74	20.22	4.93
2007	183	04	27	I	24.52	22.83	5.10
2007	183	04	48	O	24.54	22.90	5.10
2007	184	12	28	I	25.62	28.76	5.34
2007	184	18	06	O	25.70	29.68	5.36
2007	184	22	40	I	25.74	30.40	5.37
2007	185	06	11	O	25.77	31.54	5.38
2007	185	06	47	I	25.77	31.63	5.38
2007	185	07	02	O	25.77	31.67	5.38
2007	185	08	27	I	25.77	31.88	5.38
2007	185	08	54	O	25.77	31.94	5.38
2007	185	10	02	I	25.77	32.11	5.38
2007	185	10	37	O	25.77	32.19	5.38
2007	185	16	52	I	25.74	33.07	5.38
2007	185	18	17	O	25.73	33.26	5.38
2007	185	22	19	I	25.69	33.80	5.37
2007	185	22	41	O	25.68	33.85	5.37
2007	186	00	38	I	25.66	34.10	5.36
2007	186	01	49	O	25.64	34.25	5.36
2007	186	03	32	I	25.62	34.48	5.36
2007	186	05	09	O	25.59	34.68	5.35
2007	186	14	47	I	25.40	35.84	5.32
2007	186	15	07	O	25.39	35.88	5.31
2007	187	07	37	I	24.93	37.67	5.22
2007	187	08	07	O	24.91	37.72	5.22
2007	187	08	32	I	24.90	37.76	5.22
2007	187	08	59	O	24.88	37.81	5.21
2007	194	23	01	I	11.05	41.16	2.41
2007	195	00	04	O	10.93	41.09	2.38
2007	195	15	28	I	9.18	39.83	2.02
2007	195	15	57	O	9.13	39.79	2.01
2007	195	18	09	I	8.87	39.58	1.96
2007	195	20	37	O	8.58	39.35	1.90
2007	195	22	33	I	8.35	39.15	1.85
2007	196	00	46	O	8.09	38.93	1.80
2007	196	08	03	I	7.22	38.14	1.62
2007	196	08	09	O	7.20	38.12	1.62
2007	196	08	54	I	7.12	38.04	1.60
2007	196	09	08	O	7.09	38.01	1.59
2007	196	09	51	I	7.00	37.93	1.58
2007	196	10	05	O	6.97	37.90	1.57
2007	196	10	29	I	6.92	37.85	1.56
2007	196	11	35	O	6.79	37.72	1.53
2007	196	12	45	I	6.65	37.59	1.50
2007	196	13	45	O	6.52	37.46	1.48
2007	196	14	46	I	6.40	37.34	1.45
2007	196	15	30	O	6.31	37.25	1.43
2007	196	15	49	I	6.27	37.21	1.43
2007	204	01	18	O	22.81	0.19	4.62
2007	204	06	15	I	24.22	1.21	4.91
2007	204	08	41	O	24.88	1.70	5.05
2007	232	16	11	I	22.30	49.11	4.61
2007	232	17	09	O	22.18	49.03	4.59
2007	238	14	26	I	0.89	28.31	0.32
2007	244	16	50	O	28.77	3.85	4.64
2007	244	22	54	O	30.08	4.95	4.74
2007	266	13	44	I	23.25	39.73	-0.41
2007	266	17	42	O	22.65	39.44	-0.48
2007	266	18	08	I	22.59	39.41	-0.49
2007	266	19	23	O	22.39	39.32	-0.51
2007	267	08	37	I	20.33	38.22	-0.74
2007	267	12	34	O	19.69	37.86	-0.80
2007	267	12	45	I	19.66	37.84	-0.81

Continued on next page

Table B.1 – *Continued from previous page*

Year	DOY	Hour	Minute	(I)n/(O)utbound	X_{KSM}	Y_{KSM}	Z_{KSM}
2007	267	15	16	O	19.25	37.60	-0.85
2007	267	18	42	I	18.68	37.27	-0.91
2007	275	04	37	O	19.21	-2.63	3.37
2007	275	04	46	I	19.26	-2.61	3.38
2007	292	01	37	O	23.31	29.63	6.92
2007	292	01	52	O	23.27	29.62	6.91
2007	292	16	57	I	20.61	28.73	6.34
2007	292	22	36	O	19.56	28.32	6.11
2007	293	04	28	I	18.43	27.85	5.86
2007	293	08	05	O	17.71	27.52	5.70
2007	293	11	46	I	16.97	27.18	5.53
2007	293	13	38	O	16.58	26.99	5.44
2007	293	14	37	I	16.38	26.89	5.39
2007	293	17	39	O	15.75	26.57	5.25
2007	293	18	13	I	15.63	26.50	5.22
2007	300	01	55	O	26.28	0.96	4.89
2007	300	04	41	I	26.92	1.39	5.04
2007	300	16	41	O	29.45	3.25	5.67
2007	300	22	29	I	30.55	4.14	5.94
2007	301	01	41	O	31.12	4.62	6.09
2007	314	13	14	I	29.27	30.45	7.94
2007	314	13	31	O	29.23	30.45	7.94
2007	315	19	31	I	24.70	29.67	7.05
2007	315	21	03	O	24.44	29.61	6.99
2007	315	21	31	I	24.37	29.59	6.98
2007	315	21	52	O	24.31	29.57	6.97
2007	315	22	04	I	24.27	29.56	6.96
2007	316	01	30	O	23.69	29.41	6.84
2007	316	01	58	I	23.62	29.38	6.82
2007	316	02	44	O	23.48	29.35	6.80
2007	316	10	08	I	22.19	28.95	6.53
2007	316	11	27	O	21.95	28.87	6.48
2007	316	13	32	I	21.58	28.74	6.40
2007	316	21	27	O	20.11	28.20	6.09
2007	316	22	02	I	20.00	28.16	6.06
2007	318	22	24	O	9.43	22.37	3.66
2007	318	23	05	I	9.26	22.25	3.61
2007	324	14	51	O	28.00	1.40	5.88
2007	324	16	09	I	28.22	1.56	5.95
2007	324	21	15	O	29.02	2.17	6.24
2007	324	22	54	I	29.27	2.37	6.33
2007	324	23	46	O	29.40	2.47	6.38
2007	325	02	04	I	29.72	2.74	6.50
2007	325	02	44	O	29.81	2.82	6.54
2007	325	03	20	I	29.90	2.89	6.57
2007	325	07	08	O	30.40	3.34	6.76
2007	325	07	41	I	30.47	3.40	6.79
2007	325	11	07	O	30.89	3.80	6.96
2007	325	14	34	I	31.29	4.20	7.13
2007	325	17	16	O	31.59	4.51	7.25
2007	325	23	28	I	32.21	5.21	7.52
2007	326	00	24	O	32.29	5.32	7.56
2007	326	01	32	I	32.40	5.44	7.61
2007	326	02	05	O	32.45	5.51	7.63
2007	326	03	41	I	32.59	5.68	7.70
2007	326	05	10	O	32.71	5.85	7.76
2007	328	23	43	I	34.65	12.33	9.52
2007	328	23	59	O	34.64	12.35	9.53
2007	329	00	10	I	34.64	12.37	9.53
2007	329	01	32	O	34.61	12.48	9.55
2007	335	08	54	I	13.63	15.47	6.09
2007	339	10	16	O	21.99	-1.97	4.28
2007	340	15	57	I	27.72	1.61	7.42
2007	340	16	35	O	27.81	1.68	7.48
2007	340	17	25	I	27.94	1.78	7.56

Continued on next page

Table B.1 – *Continued from previous page*

Year	DOY	Hour	Minute	(I)n/(O)utbound	X_{KSM}	Y_{KSM}	Z_{KSM}
2007	340	18	34	O	28.10	1.92	7.67
2007	344	04	01	I	32.99	10.64	13.16
2007	344	04	22	O	32.99	10.68	13.17
2007	346	10	13	I	30.55	14.80	14.63
2007	346	12	06	O	30.39	14.92	14.65
2007	346	12	16	I	30.38	14.93	14.65
2007	346	14	47	O	30.16	15.08	14.67
2007	346	15	18	I	30.11	15.11	14.68
2007	346	16	28	O	30.01	15.17	14.69
2007	348	16	12	I	24.09	16.98	14.19
2007	348	16	25	O	24.06	16.98	14.18
2007	348	16	40	I	24.02	16.98	14.17
2007	348	18	25	O	23.73	17.01	14.12
2007	348	19	04	I	23.63	17.02	14.10
2007	348	19	25	O	23.57	17.02	14.09
2007	348	20	23	I	23.41	17.03	14.05
2007	348	23	52	O	22.82	17.06	13.93
2007	349	01	25	I	22.56	17.07	13.87
2007	354	19	31	O	18.15	-3.63	2.51
2007	354	20	36	I	18.49	-3.52	2.65
2007	354	22	53	O	19.19	-3.27	2.94
2007	354	23	00	I	19.24	-3.26	2.96
2007	355	08	57	O	21.72	-2.12	4.60
2007	363	19	32	I	22.21	16.19	19.21
2007	364	13	06	O	19.42	16.56	18.69
2007	365	01	05	I	17.27	16.61	18.11
2007	365	02	43	O	16.97	16.60	18.02
2007	365	06	40	I	16.20	16.57	17.77
2008	010	03	27	O	25.54	5.69	15.09
2008	010	05	29	I	25.41	5.85	15.21
2008	010	17	51	O	24.39	6.78	15.86
2008	010	18	45	I	24.30	6.84	15.90
2008	030	19	02	O	23.57	-1.70	6.72
2008	030	21	52	I	23.94	-1.44	7.13
2008	032	06	17	O	26.38	1.58	11.29
2008	032	09	27	I	26.46	1.87	11.63
2008	032	16	17	O	26.57	2.49	12.35
2008	032	19	54	I	26.58	2.81	12.70
2008	033	01	01	O	26.54	3.27	13.18
2008	033	04	33	I	26.48	3.58	13.49
2008	033	05	55	O	26.45	3.69	13.61
2008	033	07	36	I	26.40	3.84	13.75
2008	033	08	53	O	26.37	3.95	13.86
2008	033	10	00	I	26.33	4.05	13.95
2008	033	10	56	O	26.30	4.13	14.02
2008	033	11	02	I	26.30	4.13	14.03
2008	033	12	32	O	26.24	4.26	14.15
2008	033	13	46	I	26.19	4.37	14.25
2008	033	14	12	O	26.18	4.40	14.28
2008	033	14	16	I	26.17	4.41	14.28
2008	033	14	57	O	26.14	4.46	14.33
2008	033	17	36	I	26.02	4.68	14.53
2008	034	00	02	O	25.66	5.21	14.96
2008	034	02	50	I	25.48	5.43	15.14
2008	034	09	44	O	24.96	5.96	15.53
2008	034	10	38	I	24.88	6.03	15.57
2008	034	12	04	O	24.76	6.14	15.64
2008	034	15	39	I	24.43	6.40	15.81
2008	035	01	28	O	23.40	7.09	16.17
2008	035	02	41	I	23.26	7.17	16.21
2008	036	01	45	O	19.97	8.50	16.46
2008	036	03	03	I	19.75	8.56	16.44
2008	037	14	36	O	12.18	9.43	14.66
2008	037	18	05	I	11.26	9.39	14.29
2008	037	19	21	O	10.91	9.37	14.15

Continued on next page

Table B.1 – *Continued from previous page*

Year	DOY	Hour	Minute	(I)n/(O)utbound	X_{KSM}	Y_{KSM}	Z_{KSM}
2008	037	21	20	I	10.37	9.34	13.92
2008	041	20	18	O	19.82	-3.64	3.10
2008	048	03	43	I	19.75	8.46	16.40
2008	048	04	10	O	19.67	8.48	16.39
2008	048	04	36	I	19.60	8.50	16.39
2008	056	15	00	O	23.53	1.50	13.23
2008	056	17	17	I	23.42	1.69	13.47
2008	057	00	05	O	23.00	2.24	14.13
2008	057	00	38	I	22.97	2.29	14.18
2008	057	04	30	O	22.67	2.60	14.53
2008	057	07	57	I	22.37	2.87	14.81
2008	057	10	18	O	22.15	3.05	14.99
2008	057	11	47	I	22.01	3.17	15.10
2008	057	15	56	O	21.57	3.49	15.39
2008	057	16	34	I	21.50	3.53	15.43
2008	064	01	40	O	17.87	-4.54	1.43
2008	064	01	55	I	17.93	-4.52	1.48
2008	064	02	07	O	17.98	-4.51	1.52
2008	064	02	40	I	18.11	-4.48	1.63
2008	064	04	23	O	18.50	-4.39	1.96
2008	064	04	27	I	18.51	-4.39	1.97
2008	064	04	50	O	18.60	-4.36	2.04
2008	064	07	59	I	19.26	-4.18	2.64
2008	064	10	56	O	19.84	-3.99	3.20
2008	064	13	01	I	20.21	-3.86	3.59
2008	064	16	25	O	20.79	-3.63	4.22
2008	064	18	51	I	21.16	-3.46	4.66
2008	065	02	00	O	22.11	-2.93	5.92
2008	065	03	30	I	22.28	-2.82	6.18
2008	065	05	32	O	22.51	-2.66	6.52
2008	065	06	29	I	22.60	-2.59	6.68
2008	065	13	06	O	23.19	-2.06	7.77
2008	065	15	21	I	23.35	-1.88	8.13
2008	065	18	30	O	23.55	-1.63	8.61
2008	069	14	41	I	17.02	5.47	16.49
2008	069	16	41	O	16.64	5.59	16.49
2008	069	22	32	I	15.45	5.90	16.40
2008	076	04	33	O	23.12	-2.27	7.66
2008	076	15	52	I	23.79	-1.35	9.40
2008	076	17	34	O	23.86	-1.21	9.65
2008	076	22	10	I	23.99	-0.83	10.30
2008	077	08	58	O	24.04	0.07	11.72
2008	077	10	09	I	24.03	0.17	11.87
2008	077	14	28	O	23.94	0.53	12.39
2008	077	15	00	I	23.93	0.58	12.45
2008	077	15	44	O	23.91	0.64	12.53
2008	078	01	01	I	23.52	1.41	13.54
2008	078	05	36	O	23.25	1.79	13.98
2008	078	09	20	I	22.98	2.09	14.33
2008	085	11	23	O	18.40	-4.67	1.87
2008	085	17	20	I	19.52	-4.38	3.06
2008	085	17	37	O	19.56	-4.36	3.12
2008	085	17	52	I	19.60	-4.35	3.17
2008	085	19	28	O	19.82	-4.26	3.49
2008	086	00	00	I	20.39	-4.00	4.40
2008	086	03	55	O	20.80	-3.75	5.16
2008	086	08	14	I	21.18	-3.47	5.99
2008	086	08	45	O	21.22	-3.43	6.08
2008	086	16	48	I	21.68	-2.86	7.55
2008	086	17	00	O	21.69	-2.85	7.59
2008	087	01	12	I	21.90	-2.24	8.99
2008	087	01	56	O	21.90	-2.18	9.10
2008	088	02	42	I	21.03	-0.20	12.65
2008	088	03	59	O	20.93	-0.10	12.81
2008	088	04	31	I	20.88	-0.06	12.87

Continued on next page

Table B.1 – *Continued from previous page*

Year	DOY	Hour	Minute	(I)n/(O)utbound	X_{KSM}	Y_{KSM}	Z_{KSM}
2008	088	05	04	O	20.84	-0.01	12.93
2008	088	11	18	I	20.26	0.50	13.62
2008	088	14	15	O	19.94	0.74	13.92
2008	088	23	22	I	18.78	1.47	14.72
2008	089	03	01	O	18.25	1.76	14.98
2008	089	05	41	I	17.83	1.97	15.16
2008	089	06	53	O	17.64	2.06	15.23
2008	089	08	26	I	17.38	2.18	15.31
2008	089	10	43	O	16.99	2.35	15.43
2008	089	15	01	I	16.20	2.67	15.61
2008	090	03	33	O	13.59	3.55	15.79
2008	090	17	36	I	10.05	4.37	15.28
2008	114	14	20	O	19.98	-4.55	3.71
2008	115	02	22	I	21.20	-3.81	6.04
2008	123	15	37	O	18.03	-5.24	1.24
2008	123	19	38	I	18.77	-5.08	2.07
2008	124	01	44	O	19.72	-4.78	3.30
2008	124	06	56	I	20.38	-4.50	4.33
2008	124	07	20	O	20.42	-4.47	4.41
2008	124	07	43	I	20.47	-4.45	4.49
2008	124	10	28	O	20.75	-4.28	5.02
2008	124	10	32	I	20.76	-4.28	5.03
2008	124	15	38	O	21.20	-3.96	5.99
2008	125	07	04	I	21.88	-2.86	8.71
2008	125	23	19	O	21.66	-1.58	11.19
2008	126	00	13	I	21.62	-1.51	11.31
2008	126	00	32	O	21.60	-1.48	11.36
2008	126	00	43	I	21.59	-1.46	11.38
2008	126	01	47	O	21.54	-1.38	11.53
2008	126	04	43	I	21.38	-1.14	11.92
2008	141	07	56	O	18.73	-5.34	1.97
2008	141	08	27	I	18.80	-5.33	2.06
2008	141	08	56	O	18.86	-5.32	2.15
2008	141	10	43	I	19.09	-5.28	2.48
2008	141	11	40	O	19.20	-5.25	2.65
2008	141	11	54	I	19.23	-5.25	2.69
2008	141	12	28	O	19.29	-5.23	2.80
2008	141	13	48	I	19.44	-5.19	3.04
2008	141	20	53	O	20.05	-4.95	4.30
2008	142	09	55	I	20.57	-4.34	6.47
2008	142	10	28	O	20.57	-4.31	6.56
2008	142	10	48	I	20.58	-4.30	6.61
2008	142	11	43	O	20.58	-4.25	6.76
2008	142	11	52	I	20.58	-4.24	6.78
2008	142	12	03	O	20.58	-4.23	6.81
2008	142	12	24	I	20.58	-4.21	6.86
2008	142	13	27	O	20.58	-4.15	7.02
2008	142	19	02	I	20.49	-3.83	7.86
2008	143	05	19	O	19.98	-3.17	9.26
2008	143	06	53	I	19.87	-3.06	9.46
2008	143	13	04	O	19.32	-2.63	10.19
2008	143	14	28	I	19.17	-2.52	10.34
2008	165	13	09	O	17.73	-3.72	8.68
2008	165	16	09	I	17.31	-3.50	8.98
2008	177	07	20	O	16.89	-5.87	-0.40
2008	177	07	36	I	16.93	-5.88	-0.36
2008	177	08	25	O	17.07	-5.89	-0.21
2008	177	09	16	I	17.21	-5.90	-0.06
2008	177	09	44	O	17.28	-5.91	0.02
2008	177	11	08	I	17.49	-5.92	0.26
2008	191	04	59	O	16.08	-5.98	-1.22
2008	191	05	46	I	16.23	-6.00	-1.09
2008	191	10	03	O	17.00	-6.09	-0.35
2008	192	16	21	I	19.37	-5.68	4.70
2008	193	12	08	O	18.42	-4.65	7.48

Continued on next page

Table B.1 – *Continued from previous page*

Year	DOY	Hour	Minute	(I)n/(O)utbound	X_{KSM}	Y_{KSM}	Z_{KSM}
2008	193	20	00	I	17.52	-4.11	8.39
2008	200	16	59	O	18.01	-4.50	7.89
2008	200	21	48	I	17.40	-4.15	8.42
2008	201	07	07	O	15.89	-3.39	9.28
2008	201	10	03	I	15.31	-3.13	9.50
2008	201	16	28	O	13.89	-2.53	9.87
2008	201	18	23	I	13.42	-2.34	9.95
2008	214	20	17	O	16.60	-3.94	8.86
2008	215	12	27	I	13.40	-2.32	10.51
2008	227	05	02	O	16.83	-6.83	-1.42
2008	227	05	56	I	16.96	-6.84	-1.24
2008	241	22	23	O	16.72	-7.01	-1.57
2008	241	23	00	I	16.81	-7.01	-1.45
2008	241	23	39	O	16.91	-7.02	-1.33
2008	241	23	51	I	16.94	-7.02	-1.29
2008	242	18	10	O	18.63	-6.77	2.28
2008	243	15	59	I	18.32	-5.63	6.23
2008	243	16	14	O	18.31	-5.61	6.28
2008	243	17	41	I	18.20	-5.51	6.52
2008	243	19	34	O	18.05	-5.37	6.82
2008	244	11	59	I	15.93	-3.93	9.14
2008	244	14	07	O	15.55	-3.72	9.39
2008	244	14	42	I	15.44	-3.66	9.46
2008	271	15	06	O	17.30	-7.38	-0.75
2008	271	17	52	I	17.62	-7.37	-0.22
2008	271	18	32	O	17.69	-7.37	-0.09
2008	271	18	41	I	17.71	-7.37	-0.06
2008	278	20	23	O	16.76	-7.43	-1.47
2008	278	20	31	I	16.78	-7.43	-1.45
2008	278	20	41	O	16.80	-7.43	-1.41
2008	278	20	59	I	16.84	-7.44	-1.36
2008	278	22	44	O	17.08	-7.45	-1.02
2008	279	00	41	I	17.32	-7.45	-0.64
2008	279	01	16	O	17.39	-7.45	-0.53
2008	279	02	32	I	17.54	-7.45	-0.28
2008	279	03	35	O	17.65	-7.44	-0.07
2008	279	05	14	I	17.81	-7.42	0.25
2008	279	05	54	O	17.87	-7.42	0.38
2008	279	06	36	I	17.93	-7.41	0.51
2008	279	07	54	O	18.04	-7.38	0.77
2008	279	10	51	I	18.25	-7.32	1.34
2008	279	17	03	O	18.54	-7.13	2.53
2008	279	18	03	I	18.57	-7.10	2.72
2008	302	01	29	O	18.43	-6.94	4.13
2008	302	01	48	I	18.43	-6.93	4.19
2008	316	23	25	O	18.76	-7.63	2.64
2008	317	00	10	I	18.82	-7.60	2.78
2008	317	00	44	O	18.85	-7.58	2.89
2008	317	02	38	I	18.97	-7.50	3.26
2008	317	10	52	O	19.26	-7.10	4.80
2008	317	19	20	I	19.24	-6.56	6.31
2008	317	23	04	O	19.13	-6.29	6.95
2008	318	02	22	I	18.98	-6.03	7.49
2008	318	08	33	O	18.57	-5.51	8.45
2008	318	10	21	I	18.42	-5.35	8.72
2008	318	21	32	O	17.17	-4.25	10.21
2008	319	01	53	I	16.53	-3.79	10.70
2008	319	09	20	O	15.22	-2.94	11.42
2008	319	10	29	I	15.00	-2.81	11.51
2009	036	15	30	O	12.14	-9.95	-8.98
2009	036	18	59	I	12.92	-10.08	-8.29
2009	041	02	27	O	10.88	1.62	15.06
2009	041	06	19	I	9.88	2.32	15.41
2009	041	13	55	O	7.77	3.66	15.86
2009	041	18	13	I	6.51	4.38	15.96

Continued on next page

Table B.1 – *Continued from previous page*

Year	DOY	Hour	Minute	(I)n/(O)utbound	X_{KSM}	Y_{KSM}	Z_{KSM}
2009	061	08	13	O	14.77	-10.71	-5.43
2009	061	09	27	I	14.99	-10.67	-5.10
2009	061	18	46	O	16.35	-10.15	-2.57
2009	061	20	07	I	16.51	-10.05	-2.20
2009	061	22	04	O	16.73	-9.90	-1.65
2009	061	22	31	I	16.77	-9.87	-1.53
2009	062	02	36	O	17.16	-9.51	-0.38
2009	062	03	55	I	17.26	-9.38	-0.01
2009	063	15	14	O	16.80	-4.51	9.32
2009	063	16	56	I	16.62	-4.22	9.70
2009	084	14	14	O	11.09	-10.97	-9.55
2009	084	14	58	I	11.27	-10.99	-9.39
2009	088	15	01	O	12.53	1.91	15.19
2009	088	16	06	I	12.30	2.14	15.36
2009	089	02	48	O	9.78	4.38	16.73
2009	089	07	31	I	8.56	5.32	17.16
2009	089	13	12	O	7.03	6.41	17.54
2009	089	14	36	I	6.63	6.67	17.61
2009	089	19	07	O	5.35	7.49	17.76
2009	090	00	49	I	3.69	8.45	17.81
2009	090	03	59	O	2.76	8.96	17.77
2009	090	05	17	I	2.38	9.16	17.74
2009	118	06	07	O	16.53	-1.84	12.85
2009	118	06	31	I	16.49	-1.76	12.94
2009	118	07	04	O	16.44	-1.65	13.07
2009	118	07	04	O	16.44	-1.65	13.07
2009	118	07	12	I	16.42	-1.62	13.10
2009	118	07	20	O	16.41	-1.60	13.13
2009	118	07	28	I	16.40	-1.57	13.16
2009	118	07	30	I	16.40	-1.57	13.17
2009	118	07	39	O	16.38	-1.54	13.20
2009	118	08	21	I	16.31	-1.40	13.36
2009	118	08	31	O	16.29	-1.36	13.40
2009	118	08	36	I	16.28	-1.35	13.42
2009	118	08	36	I	16.28	-1.35	13.42
2009	119	04	10	O	13.57	2.55	17.19
2009	119	17	53	I	11.00	5.19	19.02
2009	132	17	20	O	16.96	-4.21	9.33
2009	133	12	44	I	15.95	-0.45	14.30
2009	133	13	51	O	15.84	-0.23	14.55
2009	133	15	25	I	15.69	0.08	14.89
2009	133	17	37	O	15.46	0.52	15.36
2009	133	21	01	I	15.07	1.19	16.05
2009	134	16	02	O	12.30	4.87	19.21
2009	135	07	31	O	9.44	7.64	20.88
2009	135	13	52	O	8.16	8.70	21.33
2009	135	14	06	I	8.11	8.74	21.34
2009	135	15	35	I	7.81	8.98	21.43
2009	136	17	19	O	2.15	12.61	21.79
2009	136	21	18	I	1.25	13.07	21.66
2009	166	12	33	O	0.64	18.00	23.32
2009	166	13	41	I	0.45	18.12	23.32
2009	166	19	59	O	-0.64	18.76	23.27
2009	166	21	25	I	-0.88	18.90	23.24
2009	242	01	39	O	8.89	23.46	5.25
2009	242	02	36	I	8.83	23.74	5.29
2009	242	11	25	O	8.21	26.15	5.66
2009	242	16	44	I	7.81	27.51	5.85
2009	242	18	13	O	7.69	27.88	5.91
2009	242	19	34	I	7.58	28.21	5.95
2009	242	22	05	O	7.38	28.81	6.04
2009	244	17	59	O	3.43	37.26	7.10
2009	244	18	11	I	3.41	37.29	7.11
2009	244	18	32	O	3.38	37.34	7.11
2009	244	20	34	I	3.19	37.65	7.15

Continued on next page

Table B.1 – *Continued from previous page*

Year	DOY	Hour	Minute	(I)n/(O)utbound	X_{KSM}	Y_{KSM}	Z_{KSM}
2009	246	18	05	I	-1.22	43.13	7.62
2009	247	00	59	I	-1.89	43.74	7.66
2009	249	14	12	I	-7.64	46.94	7.58
2009	249	21	01	O	-8.25	47.07	7.54
2009	250	09	57	I	-9.39	47.20	7.44
2009	250	11	49	O	-9.55	47.21	7.42
2009	250	12	21	I	-9.59	47.21	7.41
2009	250	12	37	O	-9.62	47.21	7.41
2009	250	13	17	I	-9.67	47.21	7.41
2009	250	14	59	O	-9.82	47.21	7.39
2009	250	15	13	I	-9.84	47.21	7.39
2009	250	15	31	O	-9.87	47.21	7.38
2009	250	18	59	I	-10.16	47.20	7.35
2009	250	19	36	O	-10.22	47.20	7.34
2009	251	00	56	I	-10.67	47.16	7.29
2009	251	02	21	O	-10.78	47.14	7.27
2009	251	02	28	I	-10.79	47.14	7.27
2009	251	02	38	O	-10.81	47.14	7.27
2009	251	02	44	I	-10.82	47.14	7.27
2009	251	02	55	O	-10.83	47.14	7.26
2009	251	04	35	I	-10.97	47.12	7.25
2009	251	04	44	O	-10.98	47.11	7.24
2009	251	04	50	I	-10.99	47.11	7.24
2009	251	04	56	O	-11.00	47.11	7.24
2009	251	05	20	I	-11.03	47.11	7.24
2009	251	05	27	O	-11.04	47.10	7.24
2009	251	18	58	I	-12.14	46.84	7.07
2009	252	03	11	O	-12.79	46.59	6.95
2009	252	03	50	I	-12.84	46.57	6.94
2009	252	04	10	O	-12.87	46.56	6.94
2009	252	08	31	I	-13.21	46.40	6.87
2009	252	10	27	O	-13.36	46.33	6.84
2009	254	01	40	O	-16.13	44.07	6.13
2009	254	02	14	I	-16.16	44.03	6.12
2009	254	12	16	O	-16.79	43.22	5.91
2009	254	12	39	I	-16.81	43.18	5.90
2009	254	15	30	O	-16.99	42.93	5.83
2009	254	15	40	I	-17.00	42.92	5.83
2009	254	16	06	O	-17.02	42.88	5.82
2009	254	20	42	I	-17.29	42.46	5.72
2009	254	21	43	I	-17.35	42.36	5.69
2009	254	21	59	O	-17.36	42.34	5.69
2009	254	22	50	I	-17.41	42.26	5.67
2009	266	08	27	I	8.67	25.48	5.46
2009	266	11	09	I	8.48	26.20	5.57
2009	266	13	27	O	8.31	26.79	5.65
2009	268	21	14	I	3.48	37.81	7.06
2009	268	23	16	O	3.29	38.11	7.09
2009	269	09	24	I	2.33	39.52	7.24
2009	269	20	25	O	1.28	40.90	7.36
2009	270	22	19	I	-1.20	43.53	7.55
2009	271	01	57	I	-1.55	43.84	7.57
2009	273	18	30	I	-7.54	47.01	7.47
2009	274	10	34	O	-8.95	47.17	7.34
2009	274	11	11	I	-9.01	47.17	7.33
2009	274	11	46	O	-9.06	47.17	7.33
2009	274	12	24	I	-9.11	47.17	7.32
2009	274	13	10	O	-9.18	47.17	7.32
2009	274	14	04	I	-9.25	47.17	7.31
2009	274	14	15	O	-9.27	47.17	7.31
2009	274	15	38	I	-9.39	47.17	7.29
2009	274	16	15	O	-9.44	47.17	7.29
2009	274	18	48	I	-9.66	47.16	7.26
2009	275	03	42	O	-10.41	47.08	7.16
2009	275	05	09	I	-10.53	47.06	7.15

Continued on next page

Table B.1 – *Continued from previous page*

Year	DOY	Hour	Minute	(I)n/(O)utbound	X_{KSM}	Y_{KSM}	Z_{KSM}
2009	275	08	27	O	-10.80	47.01	7.11
2009	275	11	59	I	-11.09	46.94	7.06
2009	277	11	06	O	-14.66	44.97	6.33
2009	277	11	57	I	-14.71	44.91	6.31
2009	292	08	04	O	-4.16	35.88	0.39
2009	292	11	26	I	-4.55	36.25	0.40
2009	292	12	55	O	-4.71	36.41	0.40
2009	292	14	46	I	-4.92	36.60	0.40
2009	292	18	19	I	-5.32	36.94	0.41
2009	292	22	41	I	-5.81	37.34	0.42
2009	293	02	39	O	-6.24	37.68	0.44
2009	293	10	23	I	-7.08	38.27	0.45
2009	293	15	29	O	-7.63	38.61	0.47
2009	294	21	40	I	-10.70	39.90	0.53
2009	294	22	37	O	-10.79	39.92	0.54
2009	297	09	02	I	-15.77	39.13	0.63
2009	297	16	41	O	-16.32	38.72	0.64
2009	297	18	52	I	-16.47	38.60	0.64
2009	312	12	05	O	-7.05	38.51	0.50
2009	312	21	45	O	-8.07	39.11	0.53
2009	313	02	44	I	-8.58	39.36	0.54
2009	313	04	19	O	-8.75	39.44	0.55
2009	313	07	34	I	-9.08	39.58	0.56
2009	313	07	46	O	-9.10	39.59	0.56
2009	313	09	30	I	-9.27	39.66	0.56
2009	313	09	46	O	-9.30	39.67	0.56
2009	313	13	43	I	-9.69	39.81	0.57
2009	313	15	31	O	-9.87	39.87	0.58
2009	313	20	40	I	-10.37	40.01	0.59
2009	313	20	53	I	-10.40	40.02	0.59
2009	313	22	32	I	-10.56	40.06	0.60
2009	313	22	48	O	-10.58	40.06	0.60
2009	314	04	18	O	-11.11	40.17	0.61
2009	314	10	37	I	-11.70	40.24	0.63
2009	314	14	27	O	-12.05	40.26	0.64
2009	314	20	58	I	-12.63	40.25	0.65
2009	315	01	00	O	-12.98	40.22	0.66
2009	315	04	04	I	-13.25	40.18	0.66
2009	315	11	11	O	-13.85	40.05	0.68
2009	316	02	56	I	-15.10	39.56	0.71
2009	316	10	49	O	-15.68	39.20	0.72
2009	316	16	01	I	-16.05	38.93	0.73
2009	316	19	28	I	-16.29	38.73	0.73
2009	316	23	10	I	-16.54	38.50	0.74
2009	346	16	29	O	4.03	24.05	-0.13
2009	346	17	44	I	3.91	24.36	-0.14
2009	346	21	34	O	3.54	25.29	-0.18
2009	346	22	17	I	3.47	25.46	-0.18
2009	348	16	45	O	-0.85	32.85	-0.51
2009	348	18	01	I	-0.98	33.00	-0.52
2009	348	21	57	O	-1.39	33.46	-0.55
2009	348	22	13	I	-1.42	33.49	-0.55
2009	348	22	55	O	-1.49	33.57	-0.55
2009	348	23	23	I	-1.53	33.62	-0.56
2010	001	14	10	O	-5.73	35.71	-5.46
2010	001	14	57	I	-5.81	35.73	-5.49
2010	003	10	28	O	-9.77	35.57	-6.83
2010	003	14	04	I	-10.07	35.43	-6.92
2010	033	06	52	O	-5.17	37.48	0.25
2010	033	10	14	I	-5.51	37.70	0.27
2010	033	17	33	O	-6.24	38.10	0.31
2010	033	18	52	O	-6.37	38.16	0.32
2010	034	05	26	O	-7.39	38.58	0.37
2010	034	09	04	I	-7.74	38.69	0.39
2010	034	09	25	O	-7.77	38.70	0.39

Continued on next page

Table B.1 – *Continued from previous page*

Year	DOY	Hour	Minute	(I)n/(O)utbound	X_{KSM}	Y_{KSM}	Z_{KSM}
2010	034	10	25	I	-7.87	38.72	0.39
2010	034	11	01	O	-7.92	38.74	0.40
2010	034	13	04	I	-8.11	38.79	0.41
2010	034	14	26	O	-8.24	38.81	0.41
2010	034	15	18	I	-8.32	38.83	0.42
2010	034	18	39	O	-8.63	38.88	0.43
2010	034	19	12	I	-8.68	38.89	0.44
2010	034	19	46	O	-8.74	38.90	0.44
2010	035	17	35	I	-10.65	38.84	0.54
2010	035	18	55	O	-10.76	38.82	0.55
2010	035	19	14	I	-10.79	38.81	0.55
2010	035	19	25	O	-10.81	38.81	0.55
2010	036	00	43	O	-11.24	38.68	0.57
2010	036	02	59	I	-11.43	38.62	0.58
2010	036	03	29	O	-11.47	38.60	0.59
2010	036	05	46	I	-11.65	38.53	0.60
2010	036	19	44	O	-12.72	37.94	0.65
2010	036	20	47	O	-12.80	37.88	0.66
2010	049	19	41	O	-2.51	35.42	0.13
2010	049	19	52	I	-2.53	35.44	0.13
2010	049	19	59	O	-2.54	35.45	0.13
2010	049	20	11	I	-2.56	35.47	0.13
2010	049	20	27	O	-2.59	35.50	0.14
2010	049	20	54	I	-2.63	35.55	0.14
2010	050	00	13	O	-2.98	35.88	0.16
2010	050	00	50	I	-3.05	35.94	0.16
2010	050	11	24	O	-4.14	36.88	0.22
2010	050	15	02	I	-4.51	37.15	0.24
2010	050	16	25	O	-4.65	37.26	0.25
2010	050	21	57	I	-5.21	37.63	0.28
2010	050	22	35	O	-5.28	37.67	0.29
2010	051	01	55	I	-5.61	37.86	0.31
2010	051	18	52	O	-7.26	38.62	0.40
2010	051	20	00	I	-7.37	38.65	0.41
2010	052	00	23	O	-7.79	38.77	0.43
2010	052	01	53	I	-7.93	38.81	0.44
2010	052	04	43	O	-8.19	38.87	0.45
2010	052	05	15	I	-8.24	38.88	0.46
2010	053	06	25	O	-10.47	38.89	0.58
2010	054	16	46	I	-13.13	37.54	0.74
2010	054	18	29	O	-13.25	37.43	0.75
2010	054	23	05	I	-13.56	37.12	0.77
2010	055	01	46	O	-13.74	36.92	0.78
2010	055	02	58	I	-13.82	36.83	0.78
2010	055	05	24	O	-13.98	36.65	0.79
2010	055	07	24	I	-14.11	36.48	0.80
2010	055	08	05	O	-14.15	36.43	0.80
2010	055	08	24	I	-14.17	36.40	0.80
2010	068	04	02	O	-4.21	37.24	0.47
2010	068	06	04	I	-4.41	37.39	0.48
2010	069	14	28	O	-7.57	38.95	0.68
2010	069	15	34	I	-7.67	38.98	0.69
2010	069	23	31	I	-8.40	39.12	0.73
2010	070	06	08	I	-9.00	39.17	0.77
2010	070	17	06	O	-9.95	39.13	0.83
2010	072	06	48	I	-12.90	37.77	1.00
2010	072	12	07	O	-13.27	37.42	1.02
2010	072	18	01	I	-13.66	37.00	1.05
2010	083	06	56	O	2.22	29.38	0.03
2010	083	09	00	O	2.00	29.78	0.05
2010	084	13	58	O	-1.03	34.32	0.27
2010	084	14	55	I	-1.13	34.44	0.28
2010	084	15	23	O	-1.18	34.49	0.28
2010	084	16	17	I	-1.27	34.60	0.29
2010	084	17	49	O	-1.43	34.79	0.30

Continued on next page

Table B.1 – *Continued from previous page*

Year	DOY	Hour	Minute	(I)n/(O)utbound	X_{KSM}	Y_{KSM}	Z_{KSM}
2010	084	20	07	I	-1.67	35.06	0.31
2010	084	21	08	O	-1.78	35.17	0.32
2010	085	08	13	I	-2.93	36.32	0.40
2010	085	20	48	O	-4.21	37.38	0.49
2010	085	21	19	I	-4.26	37.41	0.49
2010	086	00	21	O	-4.56	37.63	0.51
2010	086	04	32	I	-4.98	37.90	0.54
2010	086	05	40	I	-5.09	37.97	0.55
2010	086	06	57	I	-5.22	38.05	0.56
2010	086	22	07	O	-6.69	38.76	0.65
2010	087	09	19	I	-7.74	39.07	0.72
2010	088	13	53	O	-10.25	39.10	0.89
2010	089	00	51	I	-11.15	38.82	0.94
2010	089	02	29	O	-11.28	38.77	0.95
2010	089	03	23	I	-11.35	38.74	0.95
2010	089	04	30	O	-11.44	38.69	0.96
2010	089	06	53	I	-11.62	38.60	0.97
2010	101	00	55	O	6.92	29.42	-0.28
2010	101	08	57	O	6.28	31.11	-0.23
2010	101	15	19	I	5.75	32.35	-0.19
2010	101	20	15	O	5.34	33.25	-0.16
2010	102	04	29	I	4.62	34.65	-0.11
2010	102	07	55	O	4.32	35.20	-0.09
2010	102	17	05	I	3.50	36.56	-0.03
2010	102	20	03	O	3.23	36.97	-0.01
2010	103	03	59	I	2.51	38.00	0.04
2010	103	06	08	O	2.31	38.26	0.05
2010	107	01	23	I	-6.02	43.65	0.61
2010	121	02	37	O	7.67	27.76	-0.37
2010	128	02	15	I	-7.07	43.75	0.72
2010	128	05	45	O	-7.36	43.70	0.74
2010	128	17	16	I	-8.31	43.43	0.81
2010	141	00	19	O	9.06	23.83	0.10
2010	141	01	19	I	9.02	24.08	0.14
2010	141	06	24	O	8.79	25.29	0.33
2010	141	07	44	I	8.72	25.60	0.38
2010	141	10	07	O	8.60	26.13	0.47
2010	141	16	32	I	8.25	27.48	0.70
2010	141	17	30	O	8.19	27.68	0.74
2010	141	18	33	I	8.13	27.89	0.78
2010	142	23	11	O	6.20	32.58	1.79
2010	144	12	26	I	3.24	36.25	2.97
2010	144	12	39	O	3.22	36.27	2.98
2010	144	17	20	I	2.83	36.56	3.11
2010	144	20	20	O	2.57	36.72	3.20
2010	144	22	13	I	2.41	36.82	3.25
2010	144	23	33	O	2.30	36.88	3.29
2010	145	12	58	I	1.16	37.38	3.65
2010	147	12	50	O	-2.93	36.85	4.70
2010	148	03	22	I	-4.14	35.97	4.93
2010	160	09	58	O	3.36	36.36	-0.46
2010	161	21	07	I	0.34	37.86	-0.33
2010	161	22	32	O	0.22	37.88	-0.33
2010	162	19	55	I	-1.63	37.79	-0.24
2010	162	22	24	O	-1.85	37.74	-0.23
2010	163	01	03	I	-2.07	37.67	-0.22
2010	173	19	10	O	7.81	28.19	-2.73
2010	173	20	27	I	7.72	28.44	-2.78
2010	177	03	24	O	1.11	36.69	-5.54
2010	177	13	02	I	0.23	36.96	-5.77
2010	177	18	41	O	-0.28	37.04	-5.90
2010	177	22	10	I	-0.60	37.07	-5.97
2010	177	22	34	O	-0.64	37.07	-5.98
2010	178	00	16	I	-0.79	37.08	-6.01
2010	178	01	26	O	-0.90	37.08	-6.04

Continued on next page

Table B.1 – *Continued from previous page*

Year	DOY	Hour	Minute	(I)n/(O)utbound	X_{KSM}	Y_{KSM}	Z_{KSM}
2010	180	21	03	I	-6.76	33.44	-6.74
2010	180	22	04	O	-6.84	33.33	-6.74
2010	180	22	35	I	-6.89	33.27	-6.74
2010	181	04	15	O	-7.32	32.61	-6.73
2010	189	19	39	O	7.59	29.61	-1.21
2010	189	23	07	I	7.33	30.33	-1.24
2010	191	05	35	O	4.88	35.68	-1.39
2010	197	05	38	I	-7.74	42.50	-1.40
2010	197	14	27	O	-8.45	42.10	-1.37
2010	198	05	59	I	-9.63	41.16	-1.31
2010	198	08	00	O	-9.78	41.02	-1.30
2010	198	11	19	I	-10.03	40.77	-1.29
2010	207	21	09	O	9.94	17.24	-0.81
2010	208	03	38	I	9.81	19.48	-0.89
2010	208	03	50	O	9.80	19.54	-0.90
2010	208	12	15	I	9.50	22.17	-0.99
2010	208	15	53	O	9.34	23.23	-1.02
2010	208	18	13	I	9.22	23.88	-1.04
2010	208	21	49	O	9.03	24.86	-1.08
2010	208	23	18	I	8.95	25.26	-1.09
2010	209	01	04	O	8.85	25.71	-1.10
2010	209	12	21	I	8.14	28.44	-1.19
2010	209	14	04	O	8.02	28.82	-1.20
2010	210	02	55	I	7.09	31.49	-1.28
2010	210	03	48	O	7.03	31.66	-1.29
2010	210	13	42	I	6.25	33.46	-1.34
2010	210	16	19	O	6.04	33.90	-1.35
2010	210	23	55	I	5.42	35.12	-1.38
2010	211	04	16	I	5.05	35.78	-1.40
2010	211	07	27	I	4.78	36.23	-1.41
2010	211	11	26	O	4.44	36.78	-1.42
2010	219	06	08	O	-11.22	38.99	-1.17
2010	220	06	39	I	-12.73	36.07	-1.03
2010	231	06	21	I	5.12	36.37	-1.51
2010	234	00	12	I	-0.66	42.47	-1.59
2010	235	08	58	I	-3.56	43.42	-1.55
2010	235	21	16	O	-4.63	43.45	-1.52
2010	235	22	42	I	-4.75	43.44	-1.51
2010	236	01	53	O	-5.02	43.41	-1.51
2010	236	11	16	I	-5.81	43.26	-1.48
2010	236	16	50	O	-6.28	43.13	-1.46
2010	236	18	48	I	-6.44	43.07	-1.45
2010	237	01	02	O	-6.95	42.86	-1.43
2010	237	03	15	I	-7.14	42.78	-1.42
2010	237	09	25	O	-7.63	42.51	-1.40
2010	237	12	03	I	-7.84	42.38	-1.39
2010	237	14	31	O	-8.04	42.25	-1.38
2010	237	15	16	I	-8.10	42.21	-1.37
2010	253	12	50	O	0.62	41.71	-1.64
2010	254	03	25	I	-0.68	42.50	-1.63
2010	254	08	04	O	-1.09	42.69	-1.62
2010	254	23	42	I	-2.48	43.16	-1.60
2010	255	04	59	O	-2.94	43.25	-1.58
2010	255	11	31	I	-3.51	43.32	-1.57
2010	255	14	37	O	-3.78	43.33	-1.56
2010	255	18	51	I	-4.15	43.34	-1.55
2010	256	05	48	O	-5.09	43.24	-1.51
2010	256	08	33	I	-5.32	43.20	-1.50
2010	256	15	41	O	-5.92	43.04	-1.48
2010	256	19	27	I	-6.24	42.93	-1.46
2010	257	20	40	O	-8.27	41.77	-1.35
2010	258	03	25	I	-8.79	41.33	-1.31
2010	258	08	39	I	-9.18	40.95	-1.28
2010	258	12	29	I	-9.46	40.65	-1.26
2010	258	12	38	O	-9.48	40.64	-1.26

Continued on next page

Table B.1 – *Continued from previous page*

Year	DOY	Hour	Minute	(I)n/(O)utbound	X_{KSM}	Y_{KSM}	Z_{KSM}
2010	258	14	47	I	-9.63	40.46	-1.25
2010	258	15	33	O	-9.69	40.40	-1.24
2010	259	00	09	I	-10.30	39.63	-1.19
2010	259	03	50	O	-10.56	39.27	-1.17
2010	260	05	16	I	-12.18	36.29	-0.99
2010	269	23	04	O	7.49	31.99	-1.27
2010	270	00	22	I	7.38	32.26	-1.27
2010	270	00	54	O	7.34	32.37	-1.27
2010	270	02	18	I	7.23	32.67	-1.27
2010	270	02	36	O	7.21	32.73	-1.27
2010	270	12	55	I	6.37	34.76	-1.27
2010	270	13	49	O	6.30	34.93	-1.27
2010	271	03	38	I	5.13	37.33	-1.26
2010	271	08	02	O	4.74	38.03	-1.25
2010	272	16	38	I	1.82	42.37	-1.18
2010	273	04	16	O	0.76	43.59	-1.15
2010	273	13	59	I	-0.12	44.48	-1.11
2010	273	16	14	O	-0.33	44.67	-1.10
2010	274	12	50	I	-2.21	46.17	-1.02
2010	275	08	42	I	-3.99	47.19	-0.94
2010	275	09	24	O	-4.05	47.22	-0.93
2010	275	23	23	I	-5.29	47.70	-0.87
2010	278	08	47	O	-10.10	47.70	-0.56
2010	279	05	54	I	-11.73	46.94	-0.43
2010	295	13	21	O	4.58	39.64	-1.43
2010	295	15	52	I	4.36	40.00	-1.42
2010	296	11	59	O	2.59	42.54	-1.37
2010	296	17	01	I	2.14	43.10	-1.35
2010	296	17	27	O	2.10	43.15	-1.35
2010	297	00	50	I	1.44	43.90	-1.33
2010	297	06	32	O	0.93	44.44	-1.31
2010	297	08	05	I	0.79	44.59	-1.30
2010	297	14	43	O	0.20	45.16	-1.27
2010	301	20	48	I	-8.67	48.38	-0.73
2010	302	04	42	O	-9.30	48.22	-0.68
2010	302	17	15	I	-10.29	47.85	-0.59
2012	134	08	39	I	14.90	35.84	-3.55
2012	136	07	20	O	9.42	33.53	-2.19
2012	136	07	24	I	9.41	33.52	-2.19
2012	136	11	45	O	8.84	33.13	-2.05
2012	136	19	52	I	7.76	32.30	-1.78
2012	136	21	08	O	7.59	32.16	-1.74
2012	138	18	44	I	0.94	24.55	-0.11
2012	143	12	34	O	19.09	11.86	-5.32
2012	143	15	12	I	19.39	12.52	-5.52
2012	143	20	35	I	19.93	13.82	-5.92
2012	144	03	56	O	20.52	15.50	-6.42
2012	144	07	54	I	20.79	16.37	-6.67
2012	144	13	42	O	21.11	17.58	-7.02
2012	144	18	49	I	21.34	18.61	-7.31
2012	144	23	17	O	21.50	19.46	-7.54
2012	145	00	01	I	21.52	19.60	-7.58
2012	145	13	41	I	21.77	22.01	-8.22
2012	145	16	17	I	21.79	22.44	-8.33
2012	145	16	37	O	21.79	22.49	-8.35
2012	145	16	52	I	21.79	22.53	-8.36
2012	145	19	02	I	21.79	22.88	-8.44
2012	145	19	57	O	21.79	23.02	-8.48
2012	151	21	16	I	11.34	31.36	-9.34
2012	152	05	30	I	10.28	30.92	-9.10
2012	152	05	30	I	10.28	30.92	-9.10
2012	175	08	29	I	-3.85	36.34	-12.14
2012	175	08	29	I	-3.85	36.34	-12.14
2012	182	18	54	I	17.22	7.63	-4.19
2012	182	18	54	I	17.22	7.63	-4.19

Continued on next page

Table B.1 – *Continued from previous page*

Year	DOY	Hour	Minute	(I)n/(O)utbound	X_{KSM}	Y_{KSM}	Z_{KSM}
2012	183	04	29	I	18.61	10.61	-5.35
2012	183	04	29	I	18.61	10.61	-5.35
2012	183	07	44	O	18.99	11.57	-5.72
2012	183	07	44	O	18.99	11.57	-5.72
2012	193	17	26	I	10.14	43.99	-16.20
2012	193	17	26	I	10.14	43.99	-16.20
2012	206	11	36	O	16.17	5.52	-3.55
2012	206	11	36	O	16.17	5.52	-3.55
2012	220	06	53	I	-4.07	32.06	-17.72
2012	220	06	53	I	-4.07	32.06	-17.72
2012	220	07	11	O	-4.10	32.02	-17.70
2012	220	07	11	O	-4.10	32.02	-17.70
2012	220	07	18	I	-4.11	32.01	-17.69
2012	220	07	18	I	-4.11	32.01	-17.69
2012	220	07	46	O	-4.17	31.96	-17.66
2012	220	07	46	O	-4.17	31.96	-17.66
2012	220	07	58	I	-4.19	31.93	-17.65
2012	220	07	58	I	-4.19	31.93	-17.65
2012	228	10	00	O	18.81	10.51	-6.17
2012	228	10	00	O	18.81	10.51	-6.17
2012	240	19	36	I	-1.78	33.79	-18.83
2012	240	19	36	I	-1.78	33.79	-18.83
2012	240	20	42	I	-1.91	33.69	-18.77
2012	240	20	42	I	-1.91	33.69	-18.77
2012	250	12	19	O	20.27	15.35	-9.20
2012	250	12	19	O	20.27	15.35	-9.20
2012	250	13	16	I	20.31	15.57	-9.33
2012	250	13	16	I	20.31	15.57	-9.33
2012	250	19	19	I	20.50	16.95	-10.11
2012	250	19	19	I	20.50	16.95	-10.11
2012	250	20	19	O	20.52	17.17	-10.24
2012	250	20	19	O	20.52	17.17	-10.24
2012	250	23	56	I	20.59	17.96	-10.69
2012	251	09	03	O	20.66	19.87	-11.76
2012	251	13	37	I	20.65	20.77	-12.27
2012	251	16	07	I	20.63	21.25	-12.54
2012	251	16	29	O	20.63	21.32	-12.58
2012	252	11	12	I	20.21	24.65	-14.44
2012	253	03	50	O	19.53	27.22	-15.87
2012	253	17	34	I	18.79	29.10	-16.91
2012	253	17	41	O	18.78	29.11	-16.92
2012	253	17	42	I	18.78	29.12	-16.92
2012	253	17	49	O	18.77	29.13	-16.93
2012	253	17	53	I	18.77	29.14	-16.93
2012	253	18	01	O	18.76	29.16	-16.94
2012	253	18	02	I	18.76	29.16	-16.94
2012	253	18	27	O	18.74	29.21	-16.97
2012	255	07	00	I	16.11	33.14	-19.11
2012	255	08	24	O	15.99	33.26	-19.18
2012	261	14	06	I	-0.01	34.78	-19.56
2012	261	14	21	O	-0.04	34.76	-19.54
2012	262	14	16	I	-2.88	32.70	-18.29
2012	263	02	38	I	-4.32	31.33	-17.47
2012	263	03	58	O	-4.48	31.17	-17.38
2012	263	10	01	I	-5.17	30.41	-16.92
2012	263	10	58	O	-5.28	30.28	-16.85
2012	264	03	57	O	-7.17	27.80	-15.38
2012	264	04	17	I	-7.20	27.74	-15.35
2012	271	06	32	O	19.07	11.92	-8.14
2012	271	09	30	I	19.18	12.68	-8.68
2012	271	10	13	O	19.20	12.86	-8.81
2012	271	10	23	O	19.21	12.90	-8.84
2012	271	17	47	I	19.35	14.71	-10.14
2012	271	18	29	O	19.36	14.87	-10.26
2012	271	18	33	I	19.36	14.89	-10.27

Continued on next page

Table B.1 – *Continued from previous page*

Year	DOY	Hour	Minute	(I)n/(O)utbound	X_{KSM}	Y_{KSM}	Z_{KSM}
2012	271	18	41	O	19.36	14.92	-10.29
2012	272	07	57	I	19.28	17.90	-12.44
2012	272	08	39	O	19.27	18.05	-12.54
2012	272	11	22	I	19.21	18.62	-12.95
2012	272	13	07	O	19.16	18.98	-13.22
2012	272	13	32	I	19.15	19.07	-13.28
2012	272	13	58	O	19.14	19.16	-13.34
2012	278	13	02	I	6.71	35.71	-25.53
2012	278	14	18	O	6.56	35.76	-25.57
2012	278	14	24	I	6.55	35.77	-25.57
2012	278	14	36	O	6.52	35.77	-25.58
2012	284	05	12	I	-9.40	33.13	-23.96
2012	284	05	42	O	-9.46	33.09	-23.93
2012	284	13	25	I	-10.30	32.42	-23.46
2012	284	14	21	O	-10.40	32.33	-23.40
2012	284	20	22	I	-11.04	31.76	-23.00
2012	285	00	24	O	-11.47	31.36	-22.72
2012	285	01	23	I	-11.57	31.26	-22.65
2012	305	18	06	I	-2.46	36.25	-26.26
2012	306	01	52	O	-3.39	36.01	-26.09
2012	306	02	17	I	-3.44	36.00	-26.08
2012	306	02	31	O	-3.47	35.99	-26.08
2012	306	03	08	I	-3.54	35.97	-26.06
2012	306	03	31	O	-3.59	35.96	-26.05
2012	306	03	41	I	-3.61	35.95	-26.05
2012	306	04	57	O	-3.76	35.90	-26.01
2012	306	10	47	I	-4.46	35.68	-25.85
2012	306	11	49	O	-4.58	35.63	-25.82
2012	306	12	07	I	-4.61	35.62	-25.81
2012	306	15	08	I	-4.97	35.49	-25.71
2012	323	18	07	I	10.04	23.87	-21.40
2012	323	19	07	O	9.90	23.91	-21.45
2012	323	19	38	I	9.82	23.92	-21.47
2012	323	21	19	O	9.59	23.98	-21.54
2012	323	21	29	I	9.56	23.99	-21.54
2012	323	22	01	I	9.49	24.00	-21.56
2012	323	23	06	O	9.33	24.04	-21.60
2012	339	19	53	I	3.74	18.16	-20.37
2012	347	01	18	O	16.83	3.57	-2.03
2012	347	04	20	I	17.23	4.26	-2.78
2012	347	04	47	O	17.28	4.36	-2.89
2012	347	06	08	I	17.43	4.66	-3.22
2012	347	09	25	I	17.76	5.38	-4.01
2012	347	12	17	O	17.99	5.99	-4.68
2012	349	05	26	I	17.54	13.09	-12.96
2012	349	06	14	O	17.48	13.20	-13.09
2012	349	12	54	I	16.92	14.05	-14.14
2012	349	15	48	I	16.64	14.40	-14.58
2012	349	17	11	O	16.50	14.56	-14.78
2012	350	17	04	I	13.60	16.79	-17.72
2012	351	20	46	I	9.24	18.14	-19.83
2012	351	21	17	O	9.15	18.16	-19.85
2012	352	02	11	I	8.29	18.25	-20.07
2012	352	02	41	O	8.20	18.26	-20.09
2012	352	13	12	I	6.30	18.31	-20.38
2012	353	03	26	O	3.61	18.05	-20.40
2012	353	06	47	I	2.97	17.93	-20.34
2012	353	19	19	O	0.52	17.29	-19.90
2012	353	19	44	I	0.44	17.26	-19.88
2012	365	13	52	I	7.46	18.22	-20.31
2013	007	13	42	O	16.81	3.16	-1.98
2013	007	16	54	I	17.25	3.88	-2.78
2013	009	12	08	O	18.12	11.87	-12.02
2013	009	16	43	I	17.83	12.52	-12.81
2013	009	18	06	O	17.74	12.71	-13.04

Continued on next page

Table B.1 – *Continued from previous page*

Year	DOY	Hour	Minute	(I)n/(O)utbound	X_{KSM}	Y_{KSM}	Z_{KSM}
2013	010	00	11	I	17.25	13.51	-14.02
2013	010	00	32	O	17.22	13.55	-14.07
2013	010	00	56	I	17.19	13.60	-14.14
2013	010	01	10	O	17.17	13.63	-14.17
2013	010	01	49	I	17.11	13.71	-14.27
2013	010	01	56	O	17.10	13.73	-14.29
2013	010	02	21	I	17.06	13.78	-14.35
2013	010	07	23	O	16.58	14.37	-15.09
2013	010	12	55	I	15.98	14.97	-15.86
2013	010	14	15	O	15.84	15.11	-16.03
2013	011	09	38	O	13.32	16.76	-18.22
2013	011	11	36	I	13.03	16.89	-18.40
2013	012	07	53	I	9.81	17.87	-19.87
2013	012	08	46	O	9.66	17.90	-19.92
2013	012	11	34	I	9.17	17.98	-20.05
2013	012	12	24	O	9.03	18.00	-20.09
2013	012	13	52	I	8.78	18.03	-20.15
2013	012	16	22	O	8.33	18.07	-20.25
2013	013	15	15	O	4.09	17.97	-20.55
2013	013	17	19	I	3.70	17.91	-20.52
2013	014	00	09	O	2.37	17.67	-20.36
2013	014	04	23	I	1.55	17.47	-20.21
2013	014	11	06	O	0.23	17.07	-19.88
2013	014	12	49	I	-0.11	16.96	-19.78
2013	021	11	25	O	18.33	6.14	-5.56
2013	021	14	07	I	18.47	6.68	-6.17
2013	021	14	40	O	18.50	6.79	-6.30
2013	021	14	43	I	18.50	6.80	-6.31
2013	021	14	48	O	18.50	6.81	-6.33
2013	021	14	51	I	18.51	6.82	-6.34
2013	021	14	59	O	18.51	6.85	-6.37
2013	021	15	14	I	18.52	6.90	-6.43
2013	023	15	18	O	16.58	14.29	-15.28
2013	023	18	24	I	16.26	14.63	-15.71
2013	023	20	56	O	15.98	14.90	-16.05
2013	024	23	02	I	12.49	17.02	-18.85
2013	025	01	04	O	12.18	17.13	-19.02
2013	027	15	32	I	0.87	17.20	-20.08
2013	038	03	59	I	12.94	16.73	-18.73
2013	038	15	14	O	11.19	17.35	-19.59
2013	038	15	24	I	11.16	17.35	-19.60
2013	038	16	07	O	11.04	17.38	-19.65
2013	038	16	26	I	10.99	17.40	-19.67
2013	038	19	26	O	10.50	17.52	-19.85
2013	038	20	05	I	10.39	17.55	-19.89
2013	039	00	34	O	9.63	17.70	-20.13
2013	039	02	02	I	9.38	17.74	-20.19

Bibliography

Achilleos, N., C. S. Arridge, C. Bertucci, C. M. Jackman, M. K. Dougherty, K. K. Khurana, and C. T. Russell (2008), Large-scale dynamics of Saturn's magnetopause: Observations by Cassini, *Journal of Geophysical Research*, *113*(A11), 1–14. 67, 68, 115, 157, 159, 160, 166, 187

Achilleos, N., P. Guio, and C. S. Arridge (2010a), A model of force balance in Saturn's magnetodisc, *Monthly Notices of the Royal Astronomical Society*, *401*(4), 2349–2371. 50, 97

Achilleos, N., P. Guio, C. S. Arridge, N. Sergis, R. J. Wilson, M. F. Thomsen, and A. J. Coates (2010b), Influence of hot plasma pressure on the global structure of Saturns magnetodisk, *Geophysical Research Letters*, *37*(20), 1–5. 148

Achilleos, N. A., C. S. Arridge, P. Guio, N. M. Pilkington, A. Masters, N. Sergis, A. Coates, and M. K. Dougherty (2014), Modelling the Compressibility of Saturn's Magnetosphere, *AGU Fall Meeting Abstracts*, p. 4296. 150

Acuna, M. H., J. E. P. Connerney, P. Wasilewski, R. P. Lin, K. A. Anderson, C. W. Carlson, J. McFadden, D. W. Curtis, D. Mitchell, H. Reme, C. Mazelle, J. A. Sauvaud, C. D'Uston, A. Cros, J. L. Medale, S. J. Bauer, P. Cloutier, M. Mayhew, D. Winterhalter, and N. F. Ness (1998), Magnetic Field and Plasma Observations at Mars: Initial Results of the Mars Global Surveyor Mission, *Science*, *279*(5357), 1676–1680. 22

Acuna, M. H., J. E. P. Connerney, N. F. Ness, R. P. Lin, D. Mitchell, C. W. Carlson, J. McFadden, K. A. Anderson, H. Reme, C. Mazelle, D. Vignes, P. Wasilewski, and P. Cloutier (1999), Global Distribution of Crustal Magnetization Discovered by the Mars Global Surveyor MAG/ER Experiment, *Science*, *284*(5415), 790–793. 22

Akasofu, S. I. (1964), The development of the auroral substorm, *Planetary and Space Science*, *12*(4), 273–282. 52

Alfven, H. (1942), Existence of Electromagnetic-Hydrodynamic Waves, *Nature*, *150*(3805), 405–6. 36

André, N., M. K. Dougherty, C. T. Russell, J. S. Leisner, and K. K. Khurana (2005), Dynamics of the Saturnian inner magnetosphere: First inferences from the Cassini magnetometers about small-scale plasma transport in the magnetosphere, *Geophysical Research Letters*, *32*, 1–5. 54

Andrews, D. J., E. J. Bunce, S. W. H. Cowley, M. K. Dougherty, G. Provan, and D. J. Southwood (2008), Planetary period oscillations in Saturn's magnetosphere: Phase relation of equatorial magnetic field oscillations and Saturn kilometric radiation modulation, *Journal of Geophysical Research*, *113*(A9), A09,205. 131

Andrews, D. J., a. J. Coates, S. W. H. Cowley, M. K. Dougherty, L. Lamy, G. Provan, and P. Zarka (2010), Magnetospheric period oscillations at Saturn: Comparison of equatorial and high-latitude magnetic field periods with north and south Saturn kilometric radiation periods, *Journal of Geophysical Research*, *115*(A12), A12,252. 46

Arridge, C. S., N. Achilleos, M. K. Dougherty, K. K. Khurana, and C. T. Russell (2006), Modeling the size and shape of Saturn's magnetopause with variable dynamic pressure, *Journal of Geophysical Research*, *111*(A11), 1–13. 62, 64, 65, 66, 67, 69, 70, 99, 125, 132, 141, 150, 185

Arridge, C. S., C. T. Russell, K. K. Khurana, N. Achilleos, N. André, a. M. Rymer, M. K. Dougherty, and a. J. Coates (2007), Mass of Saturn's magnetodisc: Cassini observations, *Geophysical Research Letters*, *34*, 1–5. 50

Arridge, C. S., K. K. Khurana, C. T. Russell, D. J. Southwood, N. Achilleos, M. K. Dougherty, A. J. Coates, and H. K. Leinweber (2008), Warping of Saturn's magnetospheric and magnetotail current sheets, *Journal of Geophysical Research*, *113*(A8), A08,217. 129, 130, 131, 174

Arridge, C. S., N. André, K. K. Khurana, C. T. Russell, S. W. H. Cowley, G. Provan, D. J. Andrews, C. M. Jackman, A. J. Coates, E. C. Sittler, M. K. Dougherty, and

D. T. Young (2011), Periodic motion of Saturn's nightside plasma sheet, *Journal of Geophysical Research*, *116*(A11), A11,205. 118, 130, 131, 166

Aubry, P., T. Russell, and G. Kivelson (1970), Inward Motion of the Magnetopause before a Substorm, *Journal of Geophysical Research-Space Physics*, *75*(34), 7018–7031. 59, 61, 62

Axford, W. I. (1962), The interaction between the solar wind and the Earth's magnetosphere, *Journal of Geophysical Research*, *67*(10), 3791–3796. 47

Badman, S. V., a. Masters, H. Hasegawa, M. Fujimoto, a. Radioti, D. Grodent, N. Sergis, M. K. Dougherty, and a. J. Coates (2013), Bursty magnetic reconnection at Saturn's magnetopause, *Geophysical Research Letters*, *40*(November 2012), 1027–1031. 54

Badman, S. V., C. M. Jackman, J. D. Nichols, J. T. Clarke, and J.-C. Gérard (2014), Open flux in Saturns magnetosphere, *Icarus*, *231*, 137–145. 54

Bagenal, F., and P. a. Delamere (2011), Flow of mass and energy in the magnetospheres of Jupiter and Saturn, *Journal of Geophysical Research*, *116*(A5), A05,209. 49, 180

Bagenal, F., F. J. Crary, a. I. F. Stewart, N. M. Schneider, D. a. Gurnett, W. S. Kurth, L. a. Frank, and W. R. Paterson (1997), Galileo measurements of plasma density in the Io torus, *Geophysical Research Letters*, *24*(17), 2119. 49

Baker, D. N., T. I. Pulkkinen, M. Hesse, and R. L. McPherron (1997), A quantitative assessment of energy storage and release in the Earth's magnetotail, *J. Geophys. Res.*, *102*(A4), 7159–7168. 52

Baker, V. R. (2006), Geomorphological evidence for water on Mars, *Elements*, *2*(3), 139–143. 22

Baumjohann, W., and R. a. Treumann (1996), *Basic Space Plasma Physics*, September 1982, 329 pp., World Scientific. 36

Berchem, J., and C. T. Russell (1982), The thickness of the magnetopause current layer: ISEE 1 and 2 observations, *Journal of Geophysical Research*, *87*(A4), 2108. 58, 82

Bertucci, C., N. Achilleos, M. K. Dougherty, R. Modolo, A. J. Coates, K. Szego, A. Masters, Y. Ma, F. M. Neubauer, P. Garnier, J.-E. Wahlund, and D. T. Young (2008), The magnetic memory of Titan's ionized atmosphere., *Science*, *321*(5895), 1475–8. 55

Biermann, L. (1951), Kometenschweife und solare Korpuskulastahlung, *Zeitschrift fuer Astrophysik*, *29*, 274–86. 39

Birkeland, K. (1896), Sur les rayons cathodiques sous l'action de forces magnetiques intenses, *Archives des Sciences Physiques*, *4*, 497–512. 39

Birkeland, K. (1908), *The Norwegian Aurora Polaris Expedition 1902-1903 Vol. 1*, H. Aschehoug & Co., Christiania. 39

Birkeland, K. (1913), *The Norwegian Aurora Polaris Expedition 1902-1903 Vol. 2*, H. Aschehoug & Co., Christiania. 39

Boström, R. (1964), A model of the auroral electrojets, *Journal of Geophysical Research*, *69*(23), 4983. 30

Brandt, P. C., K. K. Khurana, D. G. Mitchell, N. Sergis, K. Dialynas, J. F. Carbary, E. C. Roelof, C. P. Paranicas, S. M. Krimigis, and B. H. Mauk (2010), Saturn's periodic magnetic field perturbations caused by a rotating partial ring current, *Geophysical Research Letters*, *37*(22), 1–5. 54, 149

Braun, H., M. Christl, S. Rahmstorf, A. Ganopolski, A. Mangini, C. Kubatzki, K. Roth, and B. Kromer (2005), Possible solar origin of the 1,470-year glacial climate cycle demonstrated in a coupled model., *Nature*, *438*(7065), 208–211. 41

Bunce, E. J., S. W. H. Cowley, C. M. Jackman, J. T. Clarke, F. J. Crary, and M. K. Dougherty (2005), Cassini observations of the Interplanetary Medium Upstream of Saturn and their relation to the Hubble Space Telescope aurora data, *Advances in Space Research*, *38*(4), 806–814. 55

Bunce, E. J., S. W. H. Cowley, I. I. Alexeev, C. S. Arridge, M. K. Dougherty, J. D. Nichols, and C. T. Russell (2007), Cassini observations of the variation of Saturn's ring current parameters with system size, *Journal of Geophysical Research*, *112*(A10), A10,202. 67, 150

Cahill, L. J., and P. G. Amazeen (1963), The Boundary of the Geomagnetic Field, *Journal of Geophysical Research*, *68*(7). 47, 79

Cao, H., C. T. Russell, U. R. Christensen, M. K. Dougherty, and M. E. Burton (2011),

Saturn's very axisymmetric magnetic field: No detectable secular variation or tilt, *Earth and Planetary Science Letters*, *304*(1-2), 22–28. 45

Carbary, J. F., and D. G. Mitchell (2013), Periodicities In Saturns Magnetosphere, *Reviews of Geophysics*, *51*(2012). 45

Carbary, J. F., D. G. Mitchell, S. M. Krimigis, and N. Krupp (2009), Dual periodicities in energetic electrons at Saturn, *Geophysical Research Letters*, *36*(20), 1–6. 46

Chapman, S., and V. C. A. Ferraro (1930), A New Theory of Magnetic Storms, *Nature*, *126*(3169), 129–30. 39, 46, 48

Clarke, K. E., N. André, D. J. Andrews, A. J. Coates, S. W. H. Cowley, M. K. Dougherty, G. R. Lewis, H. J. McAndrews, J. D. Nichols, T. R. Robinson, and D. M. Wright (2006), Cassini observations of planetary-period oscillations of Saturn's magnetopause, *Geophysical Research Letters*, *33*(23), L23,104. 46, 68, 117, 120, 161

Clarke, K. E., D. J. Andrews, C. S. Arridge, A. J. Coates, and S. W. H. Cowley (2010), Magnetopause oscillations near the planetary period at Saturn: Occurrence, phase, and amplitude, *Journal of Geophysical Research*, *115*(A8), A08,209. 46, 68, 117, 120, 143, 160, 161

Collinson, G. A., and D. O. Kataria (2010), On variable geometric factor systems for top-hat electrostatic space plasma analyzers, *Measurement Science and Technology*, *21*(10), 105,903. 83

Coroniti, F. V. (1974), Energetic Electrons in Jupiter's Magnetosphere, *The Astrophysical Journal*, *27*(244), 261–81. 45

Cowley, S. W. H., and E. J. Bunce (2001), Origin of the main auroral oval in Jupiters coupled magnetosphereionosphere system, *Planetary and Space Science*, *49*, 1067–1088. 50, 51

Cowling, T. G. (1933), The magnetic field of sunspots, *Monthly Notices of the Royal Astronomical Society*, *94*, 39–48. 45

de Bergh, C., B. Bézard, T. Owen, D. Crisp, Maillard J-P, and B. L. Lutz (1991), Deuterium on Venus: observations from Earth., *Science (New York, N.Y.)*, *251*(February), 547–549. 22

Decker, R. B., S. M. Krimigis, E. C. Roelof, M. E. Hill, T. P. Armstrong, G. Gloeckler, D. C. Hamilton, and L. J. Lanzerotti (2005), Voyager 1 in the foreshock, termination shock, and heliosheath., *Science (New York, N.Y.)*, *309*(5743), 2020–2024. 38

Delamere, P. a., and F. Bagenal (2013), Magnetotail structure of the giant magnetospheres: Implications of the viscous interaction with the solar wind, *Journal of Geophysical Research: Space Physics*, *118*(11), 7045–7053. 171

Doane, D., and L. Seward (2010), *Applied Statistics in Business and Economics*, 864 pp., McGraw-Hill Higher Education. 111, 157

Doane, D. P., and L. E. Seward (2011), Measuring Skewness: A Forgotten Statistic?, *Journal of Statistic Education*, *19*(2), 1–18. 111, 156

Dougherty, M. K., S. Kellock, D. J. Southwood, A. Balogh, E. J. Smith, B. T. Tsurutani, B. Gerlach, K.-H. Glassmeier, F. Gleim, C. T. Russell, G. Erdos, F. M. Neubauer, and S. W. H. Cowley (2004), The Cassini Magnetic Field Investigation, *Space Science Reviews*, *114*(1-4), 331–383. 79, 80, 81

Dougherty, M. K., K. K. Khurana, F. M. Neubauer, C. T. Russell, J. Saur, J. S. Leisner, and M. E. Burton (2006), Identification of a dynamic atmosphere at Enceladus with the Cassini magnetometer., *Science (New York, N.Y.)*, *311*(5766), 1406–9. 49, 79

Dungey, J. W. (1961), Interplanetary Magnetic Field and the Auroral Zones, *Physical Review Letters*, *6*(2), 47–8. 52, 53, 59

Dunlop, M. W., A. Balogh, P. Cargill, R. C. Elphic, K.-H. Fornaçon, E. Georgescu, and F. Sedgemore-Schulthess (2001), Cluster observes the Earths magnetopause: coordinated four-point magnetic field measurements, *Annales Geophysicae*, *19*(10/12), 1449–1460. 107, 152

Eddy, J. A. (1983), The Maunder Minimum, *Solar Physics*, *89*(1), 195–207. 41

Efron, B. (1987), Better Bootstrap Confidence Intervals, *Journal of the American Statistical Association*, *82*(397), 171–185. 112, 140, 197

Fairfield, D. H. (1971), Average and unusual locations of the Earth's magnetopause and bow shock, *Journal of Geophysical Research*, *76*(28), 6700–6716. 59, 62

Fedorova, A., O. Korablev, A.-C. Vandaele, J. L. Bertaux, D. Belyaev, A. Mahieux, E. Neefs, W. V. Wilquet, R. Drummond, F. Montmessin, and E. Villard (2008), HDO and H2O vertical distributions and isotopic ratio in the Venus mesosphere by Solar Occultation at Infrared spectrometer on board Venus Express, *Journal of Geophysical Research*, *113*(5). 22

Ferraro, V. C. A. (1937), The Non-uniform Rotation of the Sun and its Magnetic Field, *Monthly Notices of the Royal Astronomical Society*, *97*(6), 458–472. 50

Gledhill, J. A. (1967), Magnetosphere of Jupiter, *Nature*, *214*, 155–6. 50

Gurnett, D. A., W. S. Kurth, G. B. Hospodarsky, A. M. Persoon, T. F. Averkamp, B. Cecconi, A. Lecacheux, P. Zarka, P. Canu, N. Cornilleau-Wehrlin, P. Galopeau, A. Roux, C. Harvey, P. Louarn, R. Bostrom, G. Gustafsson, J.-E. Wahlund, M. D. Desch, W. M. Farrell, M. L. Kaiser, K. Goetz, P. J. Kellogg, G. Fischer, H.-P. Ladreiter, H. Rucker, H. Alleyne, and A. Pedersen (2005), Radio and plasma wave observations at Saturn from Cassini's approach and first orbit., *Science (New York, N.Y.)*, *307*(5713), 1255–1259. 46

Gurnett, D. a., A. Lecacheux, W. S. Kurth, a. M. Persoon, J. B. Groene, L. Lamy, P. Zarka, and J. F. Carbary (2009a), Discovery of a north-south asymmetry in Saturn's radio rotation period, *Geophysical Research Letters*, *36*(16), 2–5. 46

Gurnett, D. a., a. M. Persoon, J. B. Groene, a. J. Kopf, G. B. Hospodarsky, and W. S. Kurth (2009b), A north-south difference in the rotation rate of auroral hiss at Saturn: Comparison to Saturn's kilometric radio emission, *Geophysical Research Letters*, *36*(21), 1–4. 46

Hansen, K. C., A. J. Ridley, G. B. Hospodarsky, N. Achilleos, M. K. Dougherty, T. I. Gombosi, and G. Toth (2005), Global MHD simulations of Saturn's magnetosphere at the time of Cassini approach, *Geophysical Research Letters*, *32*(20), L20S06. 69, 71, 120, 123, 163, 173, 184, 185

Hansteen, V. H. (2009), Stellar winds and magnetic fields, in *Heliophysics: Plasma Physics of the Local Cosmos*, edited by C. J. Schrijver and G. L. Siscoe, chap. 9, pp. 225–55, Cambridge University Press, Cambridge. 40

Hill, T. W. (1979), INERTIAL LIMIT ON COROTATION, *Journal of Geophysical Research*, *84*(A11), 6554–6558. 50

Hill, T. W., and F. C. Michel (1976), Heavy ions from the Galilean Satellites and the Centrifugal Distortion of the Jovian magnetosphere, *Journal of Geophysical Research*, *81*(25), 4561–4565. 128

Hill, T. W., A. J. Dessler, and C. K. Goertz (1983), Magnetospheric Models, in *Physics of the Jovian Magnetosphere*, pp. 353–394, Cambridge University Press. 54

Hoffmeister, C. (1943), Physikalische Untersuchungen an Kometen. I. Die Beziehungen des primären Schweifstrahls zum Radiusvektor, *Zeitschrift für Astrophysik*, *22*, 265. 39

Holzer, R. E., M. G. Mcleod, and E. J. Smith (1966), Preliminary Results from the Ogo 1 Search Coil Magnetometer: Boundary Positions and Magnetic Noise Spectra., *Journal of Geophysical Research*, *71*(5), 1481–1486. 47, 79

Horbury, T. S., and a. Balogh (2001), Evolution of magnetic field fluctuations in high-speed solar wind streams: Ulysses and Helios observations, *Journal of Geophysical Research*, *106*(A8), 15,929. 39

Huang, T. S., and T. W. Hill (1989), Corotation Lag of the Jovian Atmosphere, Ionosphere and Magnetosphere, *Journal of Geophysical Research*, *94*, 3761–5. 45

Huddleston, D. E., C. T. Russell, M. G. Kivelson, K. K. Khurana, and L. Bennett (1998), Location and shape of the Jovian magnetopause and bow shock, *Journal of Geophysical Research*, *103*(E9), 20,075. 118, 141, 191

Hultqvist, B., M. Oieroset, G. Paschmann, and R. A. Treumann (1999), Contribution of different source and loss processes to the magnetospheric plasma content, in *Magnetospheric Plasma Sources and Losses*, edited by B. Hultqvist, M. Oieroset, G. Paschmann, and R. A. Treumann, chap. 7, pp. 355–372, Springer Netherlands, Dordrecht, doi:10.1007/978-94-011-4477-3. 49

Jackman, C. M., and C. S. Arridge (2011), Solar Cycle Effects on the Dynamics of Jupiters and Saturns Magnetospheres, *Solar Physics*, *274*(1-2), 481–502. 42, 152

Jackman, C. M., J. a. Slavin, and S. W. H. Cowley (2011), Cassini observations of plasmoid structure and dynamics: Implications for the role of magnetic reconnection in magne-

tospheric circulation at Saturn, *Journal of Geophysical Research*, *116*(A10), A10,212. 159

Jakosky, B. M., and R. J. Phillips (2001), Mars' volatile and climate history., *Nature*, *412*(6843), 237–244. 22

Jarvinen, R., E. Kallio, S. Dyadechkin, P. Janhunen, and I. Sillanp???? (2010), Widely different characteristics of oxygen and hydrogen ion escape from Venus, *Geophysical Research Letters*, *37*(16), 1–5. 22

Jia, X., K. C. Hansen, T. I. Gombosi, M. G. Kivelson, G. Tóth, D. L. DeZeeuw, and A. J. Ridley (2012), Magnetospheric configuration and dynamics of Saturn's magnetosphere: A global MHD simulation, *Journal of Geophysical Research*, *117*(A5), A05,225. 51, 53, 64, 125, 143, 145, 160

Joy, S. P., M. G. Kivelson, R. J. Walker, K. K. Khurana, C. T. Russell, and T. Ogino (2002), Probabilistic models of the Jovian magnetopause and bow shock locations, *Journal of Geophysical Research*, *107*(A10), 1–17. 68, 115, 159, 160, 165

Kanani, S. J., C. S. Arridge, G. H. Jones, A. N. Fazakerley, H. J. McAndrews, N. Sergis, S. M. Krimigis, M. K. Dougherty, A. J. Coates, D. T. Young, K. C. Hansen, and N. Krupp (2010), A new form of Saturn's magnetopause using a dynamic pressure balance model, based on in situ, multi-instrument Cassini measurements, *Journal of Geophysical Research*, *115*(A6), 1–11. 7, 69, 70, 84, 95, 98, 99, 101, 103, 106, 108, 113, 114, 120, 121, 122, 123, 125, 126, 128, 132, 141, 142, 147, 150, 151, 183, 184, 185, 186, 196

Kaufmann, R. L., and A. Konradi (1969), Explorer 12 magnetopause observations: Large-scale nonuniform motion, *Journal of Geophysical Research*, *74*(14), 3609–3627. 48

Kaufmann, R. L., and A. Konradi (1973), Speed and thickness of the magnetopause, *Journal of Geophysical Research*, *78*(28), 6549–6568. 82

Kellogg, P. J. (1962), Flow of plasma around the Earth, *Journal of Geophysical Research*, *67*(10), 3805. 47

Kennel, C. F., and F. V. Coroniti (1975), Is Jupiter's Magnetosphere Like a Pulsar's or Earth's, *Space Science Reviews*, *17*, 857–883. 50

Khodachenko, M., I. Ribas, H. Lammer, J. Grießmeier, M. Leitner, F. Selsis, C. Eiroa, a. Hanslmeier, H. Biernat, C. Farrugia, and H. Rucker (2007), Coronal mass ejection activity of low mass M stars as an important factor for the habitability of terrestrial exoplanets. I. CME impact on expected magnetospheres of Earth-line exoplanets in close-in habitable zones., *Astrobiology*, *129*(1), 207–243. 21

Khurana, K. K., and H. K. Schwarzl (2005), Global structure of Jupiter's magnetospheric current sheet, *Journal of Geophysical Research: Space Physics*, *110*(A7), 1–12. 171, 172

Khurana, K. K., M. G. Kivelson, D. J. Stevenson, G. Schubert, C. T. Russell, R. J. Walker, and C. Polanskey (1998), Induced magnetic fields as evidence for subsurface oceans in Europa and Callisto, *Nature*, *395*(6704), 777–780. 79

Kim, N. H. (2014), *Introduction to Nonlinear Finite Element Analysis*, Springer US. 105

Kivelson, M. G., and X. Jia (2014), Control of Periodic Variations in Saturn's Magnetosphere by Compressional Waves, *Journal of Geophysical Research: Space Physics*, *119*. 169, 170, 171, 172, 175, 189, 190

Kivelson, M. G., and D. J. Southwood (2005), Dynamical consequences of two modes of centrifugal instability in Jupiter's outer magnetosphere, *Journal of Geophysical Research*, *110*(A12), A12,209. 171

Kivelson, M. G., K. K. Khurana, C. T. Russell, M. Volwerk, R. J. Walker, and C. Zimmer (2000), Galileo magnetometer measurements: a stronger case for a subsurface ocean at Europa., *Science (New York, N.Y.)*, *289*(5483), 1340–1343. 79

Krimigis, S. M., T. P. Armstrong, W. I. Axford, C. O. Bostrom, G. Gloeckler, E. P. Keath, L. J. Lanzerotti, J. Carbary, D. C. Hamilton, and E. C. Roelof (1982), Low-Energy Hot Plasma and Particles in Saturn's Magnetosphere, *Science*, *215*(4532), 571–577. 54

Krimigis, S. M., D. G. Mitchell, D. C. Hamilton, S. Livi, J. Dandouras, S. Jaskulek, T. P. Armstrong, J. D. Boldt, A. F. Cheng, G. Gloeckler, J. R. Hayes, K. C. Hsieh, W.-H. Ip, E. P. Keath, E. Kirsch, N. Krupp, L. J. Lanzerotti, R. Lundgren, B. H. Mauk, R. W. McEntire, E. C. Roelof, C. E. Schlemm, B. E. Tossman, B. Wilken, and D. J. Williams (2004), Magnetosphere Imaging Instrument (MIMI) on the Cassini Mission to Saturn/Titan, *Space Science Reviews*, *114*(1-4), 233–329. 84, 86, 87, 88, 89

Krimigis, S. M., D. G. Mitchell, D. C. Hamilton, N. Krupp, S. Livi, E. C. Roelof, J. Dandouras, T. P. Armstrong, B. H. Mauk, C. Paranicas, P. C. Brandt, S. Bolton, a. F. Cheng, T. Choo, G. Gloeckler, J. Hayes, K. C. Hsieh, W.-H. Ip, S. Jaskulek, E. P. Keath, E. Kirsch, M. Kusterer, a. Lagg, L. J. Lanzerotti, D. Lavallee, J. Manweiler, R. W. McEntire, W. Rasmuss, J. Saur, F. S. Turner, D. J. Williams, and J. Woch (2005), Dynamics of Saturn's magnetosphere from MIMI during Cassini's orbital insertion., *Science (New York, N.Y.)*, *307*(5713), 1270–3. 54

Krimigis, S. M., N. Sergis, D. G. Mitchell, D. C. Hamilton, and N. Krupp (2007), A dynamic, rotating ring current around Saturn., *Nature*, *450*(7172), 1050–3. 54, 149, 169

Krupp, N. (2015), Comparison of Plasma Sources in Solar System Magnetospheres, *Space Science Reviews*. 180

Kurth, W. S., T. F. Averkamp, D. a. Gurnett, J. B. Groene, and a. Lecacheux (2008), An update to a Saturnian longitude system based on kilometric radio emissions, *Journal of Geophysical Research*, *113*(A5), A05,222. 46, 117, 119

Lin, R. L., X. X. Zhang, S. Q. Liu, Y. L. Wang, and J. C. Gong (2010), A three-dimensional asymmetric magnetopause model, *Journal of Geophysical Research*, *115*(A4), A04,207. 70, 71, 161

Lindsay, G. M., C. T. Russell, J. G. Luhmann, and L. E. T (1995), Coronal mass ejection and stream interaction region characteristics and their potential geomagnetic effectiveness, *Journal of Geophysical Research*, *100*(A9), 16,999–17,013. 44

Low, B. C. (2001), Coronal mass ejections, magnetic flux ropes, and solar magnetism, *Journal of Geophysical Research*, *106*(A11), 25,141. 44

Luhmann, J. G., and J. U. Kozyra (1991), Dayside pickup oxygen ion precipitation at Venus and Mars: Spatial distributions, energy deposition and consequences, *Journal of Geophysical Research*, *96*(A4), 5457. 22

Marsaglia, G., W. W. Tsang, and J. Wang (2003), Evaluating Kolmogorov's Distribution, *Journal of Statistical Software*, *8*(18), 1–4. 203

Massey, F. J. J. (1951), The Kolmogorov-Smirnov Test for Goodness of Fit, *Journal of the American Statistical Association*, *46*(253), 68–78. 158, 166, 202

Masters, A., D. G. Mitchell, A. J. Coates, and M. K. Dougherty (2011), Saturn's low-latitude boundary layer: 1. Properties and variability, *Journal of Geophysical Research*, *116*(A6), A06,210. 90, 98

Masters, A., J. P. Eastwood, M. Swisdak, M. F. Thomsen, C. T. Russell, N. Sergis, F. J. Crary, M. K. Dougherty, A. J. Coates, and S. M. Krimigis (2012a), The importance of plasma β conditions for magnetic reconnection at Saturn's magnetopause, *Geophysical Research Letters*, *39*(8), L08,103. 53, 105, 121

Masters, A., N. Achilleos, J. Cutler, A. J. Coates, M. K. Dougherty, and G. H. Jones (2012b), Surface waves on Saturn's magnetopause, *Planetary and Space Science*, *65*(1), 109–121. 66, 94, 126

Maurice, S., I. M. Engle, M. Blanc, and M. Skubis (1996), Geometry of Saturns magnetopause model, *Journal of Geophysical Research*, *101*(A12), 27,053–9. 71, 120, 123, 161, 163, 173, 184

Miesch, M. S. (2010), Solar internal flows and dynamo action, in *Heliophysics: Evolving Solar Activity and the Climates of Space and Earth*, edited by C. J. Schrijver and G. L. Siscoe, chap. 5, pp. 99–140, Cambridge University Press, Cambridge, doi:10.1017/CBO9780511760358. 27

Mitchell, D., S. Krimigis, C. Paranicas, P. Brandt, J. Carbary, E. Roelof, W. Kurth, D. Gurnett, J. Clarke, J. Nichols, J.-C. Gérard, D. Grodent, M. Dougherty, and W. Pryor (2009a), Recurrent energization of plasma in the midnight-to-dawn quadrant of Saturn's magnetosphere, and its relationship to auroral UV and radio emissions, *Planetary and Space Science*, *57*(14-15), 1732–1742. 55

Mitchell, D. G., W. S. Kurth, G. B. Hospodarsky, N. Krupp, J. Saur, B. H. Mauk, J. F. Carbary, S. M. Krimigis, M. K. Dougherty, and D. C. Hamilton (2009b), Ion conics and electron beams associated with auroral processes on Saturn, *Journal of Geophysical Research*, *114*(A2), A02,212. 106

Mitchell, D. G., P. C. Brandt, J. F. Carbary, W. S. Kurth, S. M. Krimigis, C. Paranicas, N. Krupp, D. C. Hamilton, B. H. Mauk, G. B. Hospodarsky, M. K. Dougherty, and W. R. Pryor (2015), Injection, Interchange, and Reconnection, in *Magnetotails in the*

Solar System, edited by A. Keiling, C. M. Jackman, and P. A. Delamere, pp. 327–343, John Wiley & Sons, Inc, doi:10.1002/9781118842324.ch19. 54, 149

Ness, N. F. (1965), The Earth's magnetic tail, *Journal of Geophysical Research*, *70*(13), 2989–3005. 50

Ness, N. F., M. H. Acuna, R. P. Lepping, L. F. Burlaga, K. W. Behannon, and F. M. Neubauer (1981), Magnetic Field Studies by Voyager 1: Preliminary Results., *Science (New York, N.Y.)*, *212*, 211–7. 45

Ness, N. F., M. H. Acuna, K. W. Behannon, L. F. Burlaga, J. E. P. Connerney, R. P. Lepping, and F. M. Neubauer (1982), Magnetic field studies by Voyager 2: Preliminary results at Saturn, *Science*, *215*, 558–63. 45

Neugebauer, M., C. T. Russell, and E. J. Smith (1974), Observations of the internal structure of the magnetopause, *Journal of Geophysical Research*, *79*(4), 499–510. 82

Paranicas, C., D. G. Mitchell, E. C. Roelof, P. C. Brandt, D. J. Williams, S. M. Krimigis, and B. H. Mauk (2005), Periodic intensity variations in global ENA images of Saturn, *Geophysical Research Letters*, *32*(21), L21,101. 55

Parker, E. N. (1958), Dynamics of the Interplanetary Gas and Magnetic Fields, *American Astronomical Society*, *128*, 664–75. 39, 40, 42, 43

Paschmann, G., S. Haaland, and R. A. Treumann (2003), *Auroral Plasma Physics*, International Space Science Institute Bern, Springer Netherlands. 54

Petrinec, S. M., and C. T. Russell (1995), An examination of the effect of dipole tilt angle and cusp regions on the shape of the dayside magnetopause, *Journal of Geophysical Research*, *100*(A6), 9559–9566. 60, 165

Petrinec, S. M., and C. T. Russell (1997), Hydrodynamic and MHD Equations Across the Bow Shock and Along the Surfaces of Planetary Obstacles, *Space Science Reviews*, *79*, 757–791. 64

Phillips, J. L., S. J. Bame, W. C. Feldman, J. T. Gosling, C. M. Hammond, D. J. McComas, B. E. Goldstein, M. Neugebauer, E. E. Scime, and S. T. Suess (1995), Ulysses solar wind plasma observations at high southerly latitudes., *Science (New York, N.Y.)*, *268*(5213), 1030–1033. 40

Pilkington, N. M., N. Achilleos, C. S. Arridge, A. Masters, N. Sergis, A. J. Coates, and M. K. Dougherty (2014), Polar confinement of Saturns magnetosphere revealed by in situ Cassini observations, *Journal of Geophysical Research*, *119*, 1–18. 141, 142

Pilkington, N. M., N. Achilleos, C. S. Arridge, P. Guio, A. Masters, L. C. Ray, N. Sergis, M. F. Thomsen, a. J. Coates, and M. K. Dougherty (2015), Internally driven large-scale changes in the size of Saturn's magnetosphere, *Journal of Geophysical Research: Space Physics*, *120*(9), 7289–7306. 170

Pizzo, V. J. (1978), A three-dimensional model of corotating streams in the solar wind. 1: Theoretical foundations, *Journal of Geophysical Research*, *83*(8). 44

Pontius, D. H., and T. W. Hill (2006), Enceladus: A significant plasma source for Saturn's magnetosphere, *Journal of Geophysical Research*, *111*(A9), 1–8. 49

Porco, C. C., P. Helfenstein, P. C. Thomas, a. P. Ingersoll, J. Wisdom, R. West, G. Neukum, T. Denk, R. Wagner, T. Roatsch, S. Kieffer, E. Turtle, A. McEwen, T. V. Johnson, J. Rathbun, J. Veverka, D. Wilson, J. Perry, J. Spitale, A. Brahic, J. a. Burns, a. D. Delgenio, L. Dones, C. D. Murray, and S. Squyres (2006), Cassini observes the active south pole of Enceladus, *Science (New York, N.Y.)*, *311*(March), 1393–1401. 49

Richardson, J. D., and J. C. Kasper (2008), Solar cycle variations of solar wind dynamics and structures, *Journal of Atmospheric and Solar-Terrestrial Physics*, *70*(2-4), 219–225. 153

Robbins, D. E., A. J. Hundhausen, and S. J. Bame (1970), Helium in the Solar Wind, *Journal of Geophysical Research*, *75*(7). 39

Rousseeuw, P. J., and M. Hubert (2011), Robust statistics for outlier detection, *Wiley Interdisciplinary Reviews: Data Mining and Knowledge Discovery*, *1*(1), 73–79. 92

Russell, C., and R. McPherron (1973), The magnetotail and substorms, *Space Science Reviews*, *15*(2-3), 205–266. 52

Russell, C. T., L. K. Jian, and J. G. Luhmann (2013), How unprecedented a solar minimum was it?, *Journal of Advanced Research*, *4*(3), 253–258. 153

Rymer, A. M., A. J. Coates, K. Svenes, G. A. Abel, D. R. Linder, B. Narheim, M. Thomsen, and D. T. Young (2001), Cassini Plasma Spectrometer Electron Spectrometer mea-

surements during the Earth swing-by on August 18, 1999, *Journal of Geophysical Research*, *106*(A12), 30,177. 84

Sachs, A. (1974), Babylonian Observational Astronomy, *Philosophical Transactions of the Royal Society A: Mathematical, Physical and Engineering Sciences*, *276*(1257), 43–50. 73

Schrijver, C. J., and C. Zwaan (2000), *Solar and Stellar Magnetic Activity*, Cambridge Astrophysics, 384 pp., Cambridge University Press, Cambridge. 38

Schwarz, G. E. (1978), Estimating the Dimension of a Model, *The Annals of Statistics*, *6*(2), 461–464. 158

Sergis, N., S. M. Krimigis, D. G. Mitchell, D. C. Hamilton, N. Krupp, B. M. Mauk, E. C. Roelof, and M. K. Dougherty (2007), Ring current at Saturn: Energetic particle pressure in Saturn's equatorial magnetosphere measured with Cassini/MIMI, *Geophysical Research Letters*, *34*(9), L09,102. 57, 84, 105

Sergis, N., S. M. Krimigis, D. G. Mitchell, D. C. Hamilton, N. Krupp, B. H. Mauk, E. C. Roelof, and M. K. Dougherty (2009), Energetic particle pressure in Saturn's magnetosphere measured with the Magnetospheric Imaging Instrument on Cassini, *Journal of Geophysical Research*, *114*(A2), A02,214. 50, 57, 105, 121, 125

Sergis, N., S. M. Krimigis, E. C. Roelof, C. S. Arridge, a. M. Rymer, D. G. Mitchell, D. C. Hamilton, N. Krupp, M. F. Thomsen, M. K. Dougherty, A. J. Coates, and D. T. Young (2010), Particle pressure, inertial force, and ring current density profiles in the magnetosphere of Saturn, based on Cassini measurements, *Geophysical Research Letters*, *37*(2), L02,102. 128

Sergis, N., C. M. Jackman, a. Masters, S. M. Krimigis, M. F. Thomsen, D. C. Hamilton, D. G. Mitchell, M. K. Dougherty, and a. J. Coates (2013), Particle and magnetic field properties of the Saturnian magnetosheath: Presence and upstream escape of hot magnetospheric plasma, *Journal of Geophysical Research: Space Physics*, *118*(4), 1620–1634. 58

Shue, J. H., J. K. Chao, H. C. Fu, C. T. Russell, P. Song, K. K. Khurana, and H. J. Singer (1997), A new functional form to study the solar wind control of the magnetopause size

and shape, *Journal of Geophysical Research-Space Physics*, *102*(A5), 9497–9511. 15, 61, 62, 63, 67, 70, 104, 122, 132, 141, 164, 185

Slavin, J. a., and R. E. Holzer (1981), Solar wind flow about the terrestrial planets 1. Modeling bow shock position and shape, *Journal of Geophysical Research*, *86*(A13), 11,401. 61

Slavin, J. A., E. J. Smith, P. R. Gazis, and J. D. Mihalov (1983), A Pioneer-Voyager Study of the Solar Wind Interaction with Saturn, *Geophysical Research Letters*, *10*(1), 9–12. 59, 60, 61, 62, 65, 67, 125

Slavin, J. a., E. J. Smith, J. R. Spreiter, and S. S. Stahara (1985), Solar wind flow about the outer planets: Gas dynamic modeling of the Jupiter and Saturn bow shocks, *Journal of Geophysical Research*, *90*(A7), 6275. 65

Smith, E. J., L. J. Davis, D. E. Jones, P. J. J. Coleman, D. S. Colburn, P. Dyal, and C. P. Sonett (1980), Saturn: Magnetic Field and Magnetosphere, *Science*, *207*, 407–410. 45

Snyder, C. V., and M. Neugebauer (1963), The Solar Wind Velocity and Its Correlation with Cosmic-Ray Variations and with Solar and Geomagnetic Activity, *Journal of Geophysical Research*, *68*(24), 6361–70. 39

Sonett, C. P., and S. A. Finney (1990), The spectrum of radiocarbon, *Philosophical Transactions of the Royal Society A: Mathematical, Physical and Engineering Sciences*, *330*, 413–26. 41

Sonnerup, B. U. O., and L. J. Cahill (1967), Magnetopause Structure and Attitude from Explorer 12 Observations, *Journal of Geophysical Research*, *72*(1), 171–183. 60

Sonnerup, B. U. Ö., and B. G. Ledley (1979), Ogo 5 magnetopause structure and classical reconnection, *Journal of Geophysical Research*, *84*(A2), 399. 82

Spencer, J. (2011), Watery Enceladus, *Physics Today*, *64*(11), 38. 49

Spreiter, J. R., and A. Y. Alksne (1970), Solar-Wind Flow Past Objects in the Solar System, *Annual Reviews of Fluid Mechanics*, *2*, 313–54. 59, 60

Stallard, T., S. Miller, H. Melin, M. Lystrup, S. W. H. Cowley, E. J. Bunce, N. Achilleos, and M. Dougherty (2008), Jovian-like aurorae on Saturn., *Nature*, *453*(June), 1083–1085. 50

Szita, S., A. N. Fazakerley, P. J. Carter, A. M. James, P. Trávnícek, G. Watson, M. André, A. Eriksson, and K. Torkar (2001), Cluster PEACE observations of electrons of spacecraft origin, *Annales Geophysicae*, *19*(10/12), 1721–1730. 91

Thomsen, M. F., D. B. Reisenfeld, D. M. Delapp, R. L. Tokar, D. T. Young, F. J. Crary, E. C. Sittler, M. a. McGraw, and J. D. Williams (2010), Survey of ion plasma parameters in Saturn's magnetosphere, *Journal of Geophysical Research*, *115*(A10), A10,220. 128, 129, 166

Tokar, R. L., R. E. Johnson, T. W. Hill, D. H. Pontius, W. S. Kurth, F. J. Crary, D. T. Young, M. F. Thomsen, D. B. Reisenfeld, A. J. Coates, G. R. Lewis, E. C. Sittler, and D. A. Gurnett (2006), The Interaction of the Atmosphere of Enceladus with Saturn's Plasma, *Science*, *311*(5766), 1409–12. 49

Tsyganenko, N. A. (1998), Modeling of twisted/warped magnetospheric configurations using the general deformation method, *Journal of Geophysical Research*, *103*(A10), 23,551–63. 174, 176, 190

Tucker, H. G. (1959), A Generalization of the GlivenkoCantelli Theorem, *The Annals of Mathematical Statistics*, *30*(3), 828–30. 111, 202

Ugray, Z., L. Lasdon, J. Plummer, F. Glover, J. Kelly, and R. Marti (2006), Scatter Search and Local Nlp Solvers: A Multistart Framework for Global Optimization, *SSRN Electronic Journal*, *19*(3), 328–40. 133, 134

Vasiliev, S. S., and V. a. Dergachev (2002), The 2400-year cycle in atmospheric radiocarbon concentration: bispectrum of C14 data over the last 8000 years, *Annales Geophysicae*, *20*(1), 115–120. 41

Vasyliunas, V. M. (1968), A survey of low-energy electrons in the evening sector of the magnetosphere with OGO 1 and OGO 3., *Journal of Geophysical Research: Space Physics*, *73*(9). 50

Vasyliunas, V. M. (1983), Plasma distribution and flow, in *Physics of the Jovian Magnetosphere*, edited by A. J. Dessler, pp. 395–453, CUP, New York. 51, 52, 55, 149, 159

Vasylinas, V. M. (2008), Comparing Jupiter and Saturn: dimensionless input rates from plasma sources within the magnetosphere, *Annales Geophysicae*, *26*(6), 1341–1343. 49, 191

Waite, J. H. J., W. S. Lewis, B. a. Magee, J. I. Lunine, W. B. McKinnon, C. R. Glein, O. Mousis, D. T. Young, T. Brockwell, J. Westlake, M.-J. Nguyen, B. D. Teolis, H. B. Niemann, R. L. McNutt, M. Perry, and W.-H. Ip (2009), Liquid water on Enceladus from observations of ammonia and 40Ar in the plume, *Nature*, *460*(7254), 487–490. 49

Walker, R., and C. T. Russell (1995), Solar-Wind Interactions with Magnetized Planets, in *Introduction to Space Physics*, edited by M. G. Kivelson and C. T. Russell, chap. 6, pp. 165–181, Cambridge University Press, Cambridge. 60

Waltz, R., J. Morales, J. Nocedal, and D. Orban (2005), An interior algorithm for nonlinear optimization that combines line search and trust region steps, *Mathematical Programming*, *107*(3), 391–408. 133

Wilcox, J. M. (1968), The interplanetary magnetic field. Solar origin and terrestrial effects, *Space Science Reviews*, *8*, 258–328. 42

Wilcoxon, F. (1945), Individual Comparisons by Ranking Methods, *Biometrics Bulletin*, *1*(6), 80. 109, 195

Woo, R., and S. R. Habbal (2000), Connecting the Sun and the solar wind: Source regions of the fast wind observed in interplanetary space, *Journal of Geophysical Research*, *105*(A6), 12,667. 40

Woo, R., S. R. Habbal, and U. Feldman (2004), Role of Closed Magnetic Fields in Solar Wind Flow, *The Astrophysical Journal*, *612*(2), 1171–1174. 40

Xapsos, M. A., and E. A. Burke (2009), Evidence of 6000-year periodicity in reconstructed sunspot numbers, *Solar Physics*, *257*(2), 363–369. 41

Young, D. T., J. J. Berthelier, M. Blanc, J. L. Burch, A. J. Coates, R. Goldstein, M. Grande, T. W. Hill, R. E. Johnson, V. Kelha, D. J. Mccomas, E. C. Sittler, K. R. Svenes, K. Szegö, P. Tanskanen, K. Ahola, D. Anderson, S. Bakshi, R. A. Baragiola, B. L. Barraclough, R. K. Black, S. Bolton, T. Booker, R. Bowman, P. Casey, F. J. Crary, D. Delapp, G. Dirks, N. Eaker, H. Funsten, J. D. Furman, J. T. Gosling, H. Hannula,

C. Holmlund, H. Huomo, J. M. Illiano, P. Jensen, M. A. Johnson, D. R. Linder, T. Luntama, S. Maurice, K. P. Mccabe, K. Mursula, B. T. Narheim, J. E. Nordholt, A. Preece, J. Rudzki, A. Ruitberg, K. Smith, S. Szalai, M. F. Thomsen, K. Viherkanto, J. Vilppola, T. Vollmer, T. E. Wahl, M. Wüest, T. Ylikorpi, and C. Zinsmeyer (2004), Cassini Plasma Spectrometer Investigation, *Space Science Reviews*, *114*(1-4), 1–112. 82

Zieger, B., and K. C. Hansen (2008), Statistical validation of a solar wind propagation model from 1 to 10 AU, *Journal of Geophysical Research*, *113*(A8), A08,107. 105

Zieger, B., K. C. Hansen, T. I. Gombosi, and D. L. De Zeeuw (2010), Periodic plasma escape from the mass-loaded Kronian magnetosphere, *Journal of Geophysical Research*, *115*(A8), A08,208. 51, 122, 149, 161

Zimmer, C., K. K. Khurana, and M. G. Kivelson (2000), Subsurface Oceans on Europa and Callisto: Constraints from Galileo Magnetometer Observations, *Icarus*, *147*(2), 329–347. 79

To know that we know what we know, and to know that we do not know what we do not know, that is true knowledge

Nicolaus Copernicus